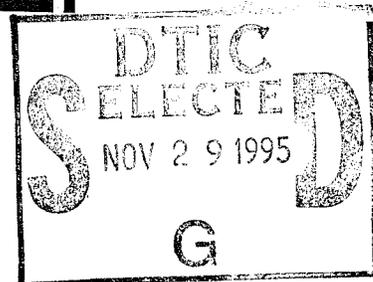# QUANTUM
OPTOELECTRONICS

MARCH 15–17, 1995

DANA POINT, CALIFORNIA

1995 TECHNICAL DIGEST SERIES
VOLUME 14

19951128 026

SPONSORED BY
OPTICAL SOCIETY OF AMERICA

*Summaries of the papers
presented at the topical meeting*

QUANTUM
OPTOELECTRONICS

March 15–17, 1995, Dana Point, California
1995 Technical Digest Series Volume 14

Articles in this publication may be cited in other publications. To facilitate access to the original publication source, the following form for the citation is suggested:

Name of Author(s), "Title of Paper," in *Quantum Optoelectronics*, Vol. 14, 1995 OSA Technical Digest Series (Optical Society of America, Washington DC, 1995), pp. xx-xx.

Optical Society of America

Printed in the U.S.A.

Contents

Accesion For		
NTIS CRA&I		X
DTIC TAB		☐
Unannounced		☐
Justification		
By		
Distribution /		
Availability Codes		
Dist	Avail and / or Special	
A-1		

QUANTUM OPTOELECTRONICS
TECHNICAL PROGRAM COMMITTEE

Larry Coldren, General Chair, *University of California, Santa Barbara*

Claude Weisbuch, General Chair, *CNET, France*

Kenichi Iga, General Chair, *Tokyo Institute of Technology, Japan*

Wayne Knox, Program Chair, *AT&T Bell Laboratories*

Yasuhiko Arakawa, *University of Tokyo, Japan*

Israel Bar-Joseph, *Weizmann Institute of Science, Israel*

Connie Chang-Hasnain, *Stanford University*

Francesco DeMartini, *University of Rome, Italy*

Philippe Fauchet, *University of Rochester*

Kenichi Kasahara, *NEC Corporation, Japan*

Jurgen Kuhl, *Max Planck Institute, Germany*

Nobuyuki Imoto, *NTT, Japan*

John Ryan, *Oxford University, UK*

Richart Slusher, *AT&T Bell Laboratories*

Art Smirl, *University of Iowa, OSA Technical Council Representative*

Joseph Zyss, *CNET, France*

BALLROOMS VI–VIII

8:30am–10:00am
JWA • Nanometer Probing
Gerard A. Mourou, *University of Michigan, Presider*

8:30am (Invited)
JWA1 • Applictions of scanning force microscopy for voltage measurements with high spatial and temporal resolutions, Francis Ho, A. Samson Hou, Bettina A. Nechay, David M. Bloom, *Stanford Univ.* We report on scanning force microscopy measurements with picosecond, and potentially sub-picosecond, temporal resolution by utilizing nonlinear tip-to-sample interactions. **(p. 2)**

9:00am
JWA2 • Ultrafast near-field optical probing, Jason B. Stark, Richart E. Slusher, *AT&T Bell Laboratories;* Umar Mohideen, *UC–Riverside.* We use broadband pulses to image the carrier dynamics of semiconductor microstructures on a submicron spatial scale, with a time resolution of 60 fs. **(p. 5)**

9:15am
JWA3 • Laser-diode-based scanning force microscope and ultrafast sampling probe, John Nees, Douglas Craig, *Univ. Michigan;* Soichi Hama, Shinichi Wakana, *Fujitsu Laboratories Ltd., Japan.* A laser diode is used to sample waveforms on high-speed devices using a highly sensitive photoconductive gate integrated into a scanning force microscope probe. **(p. 8)**

9:30am
JWA4 • STOEM: scanning tunneling optoelectronic microscope, Koichiro Takeuchi, Akira Mizuhara, *Teratec Corp., Japan.* An STM was applied to high-speed sampling measurement using a special probe with a 1.8-ps photoconductive semiconductor switch made of low-temperature GaAs. **(p. 11)**

9:45am
JWA5 • High-frequency on-wafer testing with freely positionable silicon-on-sapphire photoconductive probes, T. Pfeifer, H.-M. Heiliger, H. G. Roskos, H. Kurz, *Rheinisch-Westfälische Technische Hochschule (RWTH) Aachen, Germany.* Freely positionable photoconductive probes based on silicon-on-sapphire are characterized as both generators and detectors of picosecond electric transients. **(p. 14)**

BALLROOMS IV–V

10:00am–10:30am
Coffee Break

BALLROOMS VI–VIII

10:30am–12:00m
JWB • Quantum Devices
Jürgen Kühl, *Max Planck Institute,Germany, Presider*

10:30am (Invited)
JWB1 • Ultrafast all-optical switch with switch-off time unlimited by carrier lifetime, K. Tajima, S. Nakamura, *NEC Corp., Japan.* Experimental results are presented on a modified Mach–Zehnder type all-optical switch. Faster than 8 ps full-switching has been achieved and 1 ps switching at a very high repetition rate is theoretically predicted. **(p. 18)**

11:00am (Invited)
JWB2 • Quantum cascade lasers, F. Capasso, J. Faist, *AT&T Bell Laboratories.* Quantum cascade lasers based on diagonal and vertical intersubband transitions are discussed. Pulsed operation at 100 K with $J_{th} = 3$ kA/cm^2, 60 mW peak power and a slope efficiency of 300 mW/A has been achieved. **(p. 20)**

11:30am
JWB3 • Scaling of Stark-shifted nonlinearities in MQW structures, A. N. Cartwright, X. R. Huang, Arthur L. Smirl, *Univ. Iowa.* Simple rules of scaling the per-carrier nonlinearity in Stark-shifted systems with well number, electric field, amplitude and width of the excitonic transition are demonstrated by measuring this quantity as a function of temperature, bias, and materials system for several multiple quantum well (MQW) structures. **(p. 23)**

11:45am
JWB4 • Dynamic Wannier–Stark effect and superradiance switching in semiconductor superlattices, J. B. Khurgin, S.-J. Lee, *Johns Hopkins Univ.;* N. M. Lawandy, *Brown Univ.* Two novel effects associated with transition from localized to extended states in semiconductor superlattices are introduced. Possible applications in the light sources and detectors are considered. **(p. 26)**

BALLROOMS VI–VIII

12:00m–12:10pm
UEO Closing Remarks and QOE Opening Remarks

12:10pm–1:30pm
Lunch Break

BALLROOMS VI–VIII

1:30pm–3:00pm
QWA • Novel Spectroscopies of Quantum Systems
John Ryan, *Oxford University, UK, Presider*

1:30pm (Invited)
QWA1 • Femtosecond near-field spin microscopy in digital magnetic heterostructures, J. Levy, V. Nikitin, J. M. Kikkawa, D. D. Awschalom, *UC–Santa Barbara;* R. Garcia, N. Samarth, *Pennsylvania State Univ.* Femtosecond-resolved low-temperature near-field scanning optical microscopy is used to spatiotemporally image electronic and magnetic spin dynamics in new magnetically doped heterostructures. **(p. 30)**

2:00pm (Invited)
QWA2 • Near-field spectroscopy of the quantum constituents of a luminescent system, Harald Hess, E. Betzig, T. D. Harris, L. N. Pfeiffer, K. W. West, *AT&T Bell Laboratories.* Luminescent centers of localized excitons with sharp (<0.07 meV) spectrally distinct emission lines were imaged in a GaAs/AlGaAs quantum well by means of low-temperature near-field scanning optical microscopy. **(p. 33)**

2:30pm
QWA3 • Quantum mechanical capacitance in a scanning tunneling microscope, D. Botkin, S. Weiss, D. F. Ogletree, M. Salmeron, D. S. Chemla, *UC–Berkeley.* The nature of the ultrafast response of the tunnel junction in a scanning tunneling microscope is discussed. **(p. 34)**

2:45pm
QWA4 • Photon-assisted tunneling through a quantum dot, S. Jauhar, J. Orenstein, P. L. McEuen, *UC–Berkeley;* L. P. Kouwenhoven, *Delft Univ. of Technology, The Netherlands;* Y. Nagamune, J. Motohisa, H. Sakaki, *Univ. Tokyo, Japan.* We present the first measurements of photon-assisted tunneling through a semiconductor quantum dot. **(p. 37)**

BALLROOMS IV–V

3:00pm–3:30pm
Refreshment Break

BALLROOMS VI–VIII

3:30pm–5:00pm
QWB • Ultrafast Excitonic Nonlinearities and Applications
Philippe Fauchet, *University of Rochester, Presider*

3:30pm (Invited)
QWB1 • Spin quantum beats in quantum wells and wires, Wolfgang W. Rühle, Michael Oestreich, Reinhard Hannak, Albert P. Heberle, Richard Nötzel, Klaus Ploog, *Max-Planck-Institut für Festkörperforschung, Germany;* Klaus Köhler, *Fraunhofer Institut für Angewandte Festkörperphysik, Germany.* Spin quantum beats yield the accurate dependence of the electron g factor in GaAs wells on well width and a huge g factor anisotropy in GaAs wires. **(p. 42)**

4:00pm (Invited)
QWB2 • Coherent nonlinear optical spectroscopy of semiconductor microcavities, Hailin Wang, Jagdeep Shah, T. C. Damen, W. Y. Jan, J. E. Cunningham, *AT&T Bell Laboratories.* Coherent nonlinear optical studies of semiconductor microcavities reveal coherent oscillations and novel dynamical behaviors in a strongly coupled exciton-cavity system. **(p. 45)**

4:30pm
QWB3 • Excitonic versus electronic Bloch oscillations, T. Dekorsy, P. Leisching, R. Ott, H. J. Bakker, H. Kurz, *Institut für Halbleitertechnik II, RWTH Aachen, Germany;* K. Köhler, *Fraunhofer-Institut für Angewandte Festkörperphysik, Germany.* The intraband and interband dynamics of Bloch oscillations are investigated simultaneously. Pronounced differences in frequencies give evidence for Bloch oscillations performed by excitonic and continuum states. **(p. 48)**

4:45pm
QWB4 • AlAs/AlGaAs intracavity saturable Bragg reflector for femtosecond self-starting passive modelocking, W. H. Knox, S. Tsuda, E. A. de Souza, W. Y. Jan, J. E. Cunningham, *AT&T Bell Laboratories.* A new saturable Bragg reflector produces self-starting femtosecond passive mode-locking in a Ti:sapphire laser. The ultrafast excitonic nonlinearity is responsible for the modelocking. **(p. 51)**

BALLROOMS VI–VIII

5:00pm–6:30pm
QOE Postdeadline Paper Session

6:30pm–8:00pm
Conference Reception

BALLROOMS VI–VIII

8:30am–10:00am
QThA • Photonic Bandgaps, Microcavity Physics, and Applications
Kenichi Kasahara, NEC Corporation, Japan, Presider

8:30am (Invited)
QThA1 • Review of photonic bandgaps, E. Yablinovitch, UC–Los Angeles. We discuss the status of photonic bandgap structures from a physics and applications viewpoint. **(p. 56)**

9:00am
QThA2 • Luminescence processes in semiconductor microcavities, R. Houdré, R. P. Stanley, U. Oesterle, P. Pellandini, M. Ilegems, Ecole Polytechnique Fédérale de Lausanne, Switzerland; C. Weisbuch, Ecole Polytechnique, France. We describe the luminescence process in the strongly coupled system consisting of quantum-well excitons and microcavity photons and its possible impace on light-emitting devices. **(p. 57)**

9:15am
QThA3 • Nonlinear vacuum Rabi splitting in semiconductor microcavities, J.-K. Rhee, R. Lai, T. B. Norris, Univ. Michigan; Y. Arakawa, M. Nishioka, Univ. Tokyo, Japan. Using ultrafast techniques, we have observed reduced vacuum Rabi splittings of a strongly coupled semiconductor microcavity in the nonlinear regime. This effect is the manifestation of nonlinear excitonic transitions in the exciton-polariton system. **(p. 60)**

9:30am
QThA4 • Measurements of spontaneous emission factor in electrically pumped microcavity lasers, Rajeev J. Ram, Edgard Goobar, Matthew Peters, Larry A. Coldren, John E. Bowers, UC–Santa Barbara. We report the first measurements of the spontaneous emission coupling efficiency (β) for electrically pumped microcavity lasers. A maximum β of 0.005 was measured at 126 K in a 3-μm diameter device with optimal gain-cavity detuning. **(p. 63)**

9:45am
QThA5 • Radiation pattern of spontaneous emission from microcavity DBR surface emitting lasers, Tetsuko Hamano, Fumio Koyama, Kenichi Iga, Tokyo Institute of Technology, Japan. We first present the far field pattern of spontaneous emission from a microcavity DBR surface-emitting laser and found that it depends on the spontaneous emission spectrum against the fixed cavity resonant modes. **(p. 66)**

BALLROOMS IV–V

10:00am–10:30am
Coffee Break

BALLROOMS VI–VIII

10:30am–12:00m
QThB • New Materials for Quantum Optoelectronics,
Richart E. Slusher, AT&T Bell Laboratories, Presider

10:30am (Invited)
QThB1 • Characterization and device applications of porous silicon, H. Munder, Forschungszentrum Jülich GmbH, Germany. The optical properties of porous Si single layers depend on their microscopic structure. Micro-optical devices like filters can be formed by the use of porous Si multilayers. **(p. 70)**

11:00 am (Invited)
QThB2 • Exciton confinement in organic multiple quantum wells, S. R. Forrest, E. I. Haskal, Z. Shen, P. E. Burrows, Princeton Univ. The absorption, electroabsorption and fluorescence spectra of organic thin films and multiple quantum well structures are found to exhibit excitonic confinement. Applications of these effects to nonlinear optical devices are discussed. **(p. 73)**

11:30am
QThB3 • Ultrathin porous silicon films: physics and device applications, P. M. Fauchet, J. von Behren, L. Tsybeskov, Y. Kostoulas, K. B. Ucer, Univ. Rochester. High-quality submicron-thick porous silicon films have been fabricated and used to demonstrate that this highly luminescent material is an indirect gap semiconductor. **(p. 75)**

11:45am
QThB4 • Polymers in optical microcavities, J. Feldmann, U. Lemmer, R. Hennig, A. Ochse, M. Hopmeier, E. O. Göbel, W. Guss, J. Pommerehne, R. Mahrt, H. Bässler, FB Physik, FB Physikalische Chemie and Wiss. Zentrum f. Materialwissenschaften, Germany. We discuss the possibility to enhance the quantum efficiency of light-emitting polymer devices by placing the polymer material within an optical microcavity. **(p. 78)**

12:00m–1:30pm
Lunch Break

BALLROOMS VI–VIII

1:30pm–3:00pm
QThC • Quantum Dots
Israel Bar-Joseph, Weizmann Institute of Science, Israel, Presider

1:30pm (Invited)
QThC1 • Fabrication and optical properties of quantum confined structures for laser, Yasuhiko Arakawa, Univ. Tokyo, Japan. We discuss optical properties of quantum wires and dots for lasers, including photoluminescence from a single quantum dot, enhanced exciton mobility in quantum wires, and bottleneck problem as well as fabrication technology. **(p. 82)**

2:00pm (Invited)
QThC2 • Optical properties and transport properties of self assembled quantum dots, P. M. Petroff, K. Schmidt, G. Meideiros-Ribeiro, D. Leonard, UC–Santa Barbara. We will discuss the photoluminescence, modulated photoluminescence and transport properties of InAs and InAlAs self assembled quantum dots. We will also show evidence of three dimensional carrier confinement above 77K. **(p. 86)**

2:30pm
QThC3 • 1.32-μm room temperature photoluminescence from InGaAs quantum dots on GaAs, Richard Mirin, James Ibbetson, Kenichi Nishi, Arthur Gossard, John Bowers, *UC–Santa Barbara.* We report 1.32-μm photoluminescence at room temperature from InGaAs quantum dots grown by MBE on GaAs. The luminescence linewidth is only 32 meV, and the integrated intensity is comparable to that of a quantum well. **(p. 87)**

2:45pm
QThC4 • Vertical cavity surface-emitting laser operating in a 12 T magnetic field at 2 K temperature, Ove Lyngnes, Hyatt M. Gibbs Galina Khitrova, Jill D. Berger, Tom R. Nelson, Jr., *Univ. Arizona;* Valerii Zapaskii, *S. I. Vavilov State Optical Institute, Russia.* Strained-layer InGaAs/GaAs quantum wells in 12 T have an almost completely isolated 1-shh magneto-exciton transition. These near-ideal quantum dots exhibit cw lasing with no apparent phonon bottleneck problem. **(p. 90)**

BALLROOMS IV–V

3:00pm–3:30pm
Refreshment Break (Poster Preview)

BALLROOMS VI–VIII

3:30pm–5:00pm
QThD • Physics and Applications of Low-Dimensional Semiconductors
Francesco DeMartini, *University of Rome, Italy, Presider*

3:30pm (Invited)
QThD1 • Quantum wire fractional layer superlattice microcavity lasers, Arturo Chavez-Pirson, *NTT Basic Research Laboratories, Japan.* Using GaAs fractional-layer superlattice (FLS) quantum wires, we have successfully demonstrated room-temperature lasing in a quantum wire microcavity. The efficient coupling of material and cavity states into the lasing process will result in ultimately compact, extremely low current threshold lasers capable of ultra-fast polarization modulation. We discuss the lasing characteristics and the optical properties of the FLS quantum wire. **(p. 94)**

4:00pm (Invited)
QThD2 • Strained InGaAs quantum disk laser with self-organized nanoscale active region, Jiro Temmyo, Eiichi Kuramochi, Mitsuru Sugo, Teruhiko Nishiya, Richard Nötzel, Toshiaki Tamamura, *NTT Opto-electronics Laboratories, Japan.* Self-organization of strained InGaAs on a GaAs (311)B substrate during MOVPE growth is described, and a nanoscale confinement laser with self-organized active region is mentioned. **(p. 97)**

4:30pm
QThD3 • Fabrication and optical characterization of GaAs nano-whiskers, T. Katsuyama, K. Hiruma, T. Sato, K. Ogawa, M. Shirai, K. Haraguchi, M. Yazawa, *Hitachi Ltd., Japan.* Site-controlled GaAs nano-whiskers are demonstrated for the first time. Spectral blue shift and polarization dependence of the photoluminescence show two-dimensional quantum confinement of the whisker. **(p. 100)**

4:45pm
QThD4 • Electronic picosecond-pulse interferometer probing the millimeter-wave response of coupled quantum dots, D. W. van der Weide, R. H. Blick, F. Keilmann, R. J. Haug, K. von Klitzing, K. Eberl, *Max-Planck-Institut für Festkörperforschung, Germany.* A new interferometer using nonlinear transmission lines causes current to flow in coupled quantum dots; radiation is transduced by the structure acting as an antenna. **(p. 103)**

BALLROOMS VI–VIII

5:00pm–6:30pm
QThE • Poster Session

QThE1 • Excitonic spin-flip dynamics under resonant two-photon excitation in quantum wells, A. Lohner, P. Michler, W. W. Rühle, *Max-Planck-Institut für Festkörperforschung, Germany;* K. Köhler, *Fraunhoferinstitut für Angewandte Festkörperphysik,Germany.* Spin-flip dynamics from dark to optically active excitons is studied by two-photon, resonant excitation of exciton luminescence in quantum wells. **(p. 108)**

QThE2 • Dipole emission in two-dimensional photonic band structures, Toshio Suzuki, Paul K. L. Yu, D. R. Smith, S. Schultz, *UC–San Diego.* Dipole emission spectra in two-dimensional periodic structures are computed by the plane wave expansion method, dyadic Green's function, Poynting theorem and triangular interpolation method. **(p. 111)**

QThE3 • Waveguide-coupled microcavity LEDs, Bardia Pezeshki, Jeffrey A. Kash, David W. Kisker, *IBM T. J. Watson Research Center.* We demonstrate microcavity LEDs that emit directly in a waveguide mode, obtaining narrow-band emission at a wavelength that depends on the cavity thickness. **(p. 114)**

QThE4 • Tunable transversely pumped counterpropagating OPOs based on semiconductor structures, Yujie J. Ding, *Bowling Green State Univ.;* Jacob B. Khurgin, Seung-Joon Lee, *Johns Hopkins Univ.* Semiconductor second-order optical nonlinearity in a vertical cavity can be used to achieve first tunable and efficient transversely pumped counterpropagating optical parametric oscillations (OPOs), especially in 3.5–5.5-μm domain. **(p. 117)**

QThE5 • Fast coherent vertical exciton transport in multiple quantum wells, D. S. Citrin, *Univ. Michigan.* The long-range retarded dipole–dipole interaction for planar systems leads to picosecond excitation transfer in short-period multiple quantum wells when a single well is initially excited. **(p. 120)**

QThE6 • Spontaneous emission coupling to the lasing mode in a Fabry–Perot microcavity with high contrast Al_xO_y/GaAs Bragg reflectors, D. G. Deppe, D. L. Huffaker, H. Deng, J. Shin, Q. Deng, *Univ. Texas at Austin.* Data is presented characterizing the spontaneous emission coupling to the lasing mode in a microcavity laser with high contrast Al_xO_y/GaAs Bragg reflectors. **(p. 123)**

QThE7 • Strained InGaAs/AlAs MQW p-i-n modulator with ultrafast recovery, H. S. Wang, P. Li Kam Wa, *Univ. Central Florida;* M. Ghisoni, G. Parry, *Univ. Oxford, UK;* P. N. Stavrinou, *Univ. College London, UK;* C. Roberts, *Imperial College, UK;* A. Miller, *Univ. St. Andrews, UK.* Time-resolved measurements of InGaAs/AlAs multiple quantum well p-i-n modulators gave a 28-ps recovery time while exhibiting a clear quantum confined Stark effect and low photocurrent. **(p. 126)**

QThE8 • Nonlinear optical response of piezoelectric MQWs under bias, X. R. Huang, A. N. Cartwright, D. S. McCallum, D. R. Harken, Arthur L. Smirl, *Univ. Iowa;* J. L. Sánchez-Rojas, A. Sacedón, E. Calleja, E. Muñoz, *Univ. Politécnica Madrid, Spain.* Measurements of the nonlinear response of a piezoelectric multiple quantum well (MQW) as a function of reverse bias voltage demonstrate that the small per carrier nonlinearities measured to date are partially the result of a broadening of the exciton by the huge in-well field, but can be primarily attributed to the quality of the [111]-grown material. **(p. 129)**

QThE9 • Intrinsic and induced anisotropy of the nonlinear absorption in strained [110]-oriented MQWs, X. R. Huang, D. S. McCallum, Arthur L. Smirl, *Univ. Iowa;* D. Sun, E. Towe, *Univ. Virginia.* We present the first measurements of the optically induced and intrinsic anisotropy of the nonlinear absorption in strained [110]-oriented multiple quantun wells (MQWs), and we use these anisotropies to demonstrate a polarization rotation of a modulator with a high contrast ratio. **(p. 132)**

QThE10 • Carrier capture in GaAs quantum wire structures grown on V-groove substrates, S. Haacke, B. Deveaud, D. Y. Oberli, E. Kapon, U. Marti, F. K. Reinhart, *Swiss Federal Institute of Technology, Switzerland.* Carrier capture and relaxation mechanisms are studied in V-groove quantum wires by subpicosecond luminescence. Depending on the sample structure, capture is as fast as 25 ps. **(p. 135)**

QThE11 • Fabrication of GaAs quantum dots grown in two-dimensional V-grooves by MOCVD selective growth, S. Ishida, M. Nishioka, Y. Nagamune, Y. Arakawa, *Univ. Tokyo, Japan.* We propose and demonstrate a novel fabrication technique for GaAs quantum dots, which are grown in AlGaAs two-dimensional V-grooves by MOCVD. **(p. 138)**

QThE12 • Improvement of crystalline quality by strain compensation in InAs$_x$P$_{1-x}$/Ga$_y$In$_{1-y}$P MQWs for 1.3 μm waveguide modulators, X. B. Mei, K. K. Loi, H. H. Wieder, W. S. C. Chang, C. W. Tu, *UC-San Diego.* We show that high-quality InAs$_x$P$_{1-x}$/Ga$_y$In$_{1-y}$P strain-compensated multiple quantum wells (MQWs) on InP substrates for 1.3 μm modulator applications can be grown by GSMBE. We studied the y-dependence of the crystalline quality of 90Å/130Å MQW structures by double-crystal x-ray diffraction. **(p. 141)**

QThE13 • Anisotropy and dispersion of the optical rectification in the symmetric quantum wells, J. B. Khurgin, *Johns Hopkins Univ.* We demonstrate theoretically that the optical rectification and difference-frequency generation nonlinear coefficients, known to exist in the asymmetric quantum wells for certain directions of growth, do not vanish even in the symmetric quantum wells. Practical applications are considered. **(p. 143)**

QThE14 • Pulse propagation and many-body effects in semiconductor four wave mixing, A. Schulze, A. Knorr, S. W. Koch, *Philipps-Univ. Marburg, Germany.* Pulse propagation and many-body effects in semiconductor four wave mixing are studied theoretically for different excitation conditions and sample parameters. **(p. 146)**

QThE15 • Generation of far infrared radiation using compositionally asymmetric MQW waveguides, Babak N. Saif, *Swales & Associates;* Bernard D. Seery, *NASA/Goddard Space Flight Center;* Jacob Khurgin, *Johns Hopkins Univ.;* Colin Wood, *Laboratory for Physical Sciences.* Difference frequency mixing in GaAs/GaAlAs multiple quantum wells (MQW) to produce coherent radiation at 2.5 THz is reported. Two CO_2 lasers are mixed in a 35-μm-thick, doped asymmetric MQW waveguide for efficient phase matching. Waveguide design parameters and experimental results are discussed. **(p. 149)**

QThE16 • Equal pulse correlation in GaAs thin films with near-field microscopy, S. Smith, B. G. Orr, R. Kopelman, T. Norris, *Univ. Michigan.* Using near-field microscopy, local carrier relaxation and diffusion length variations in GaAs and LT-GaAs thin films have been observed with femtosecond time resolution. **(p. 153)**

QThE17 • Quantum fluctuation effects in photon confinement, L. A. Rivlin, *Moscow State Institute of Radioengineering, Electronics, and Automation (MIREA), Russia.* The rest mass of confined photon is an equivalent of the work performed in opposition to the pressure of zero-point vacuum fluctuations during photon confinement into a waveguide mode from the free unbounded space. **(p. 156)**

QThE18 • Calibrated noise measurements in microcavity lasers, Edgard Goobar, Jeff Scott, Gerry Robinson, Yuliya Akulova, Larry A. Coldren, *UC-Santa Barbara.* For the first time to our knowledge calibrated intensity noise measurements of vertical cavity lasers are presented. Partition noise due to polarization degeneracy is found to render excess noise that destroys squeezing. **(p. 158)**

QThE19 • Realization of large subband separation and high power light output in GaAs/AlGaAs two-dimensional quantum well wire laser arrays, Yi Qian, Lianghui Chen, Jingming Zhang, Qiming Wang, Lianxi Zhen, Xiongwei Hu, *Chinese Academy of Sciences, China.* We report GaAs/AlGaAs two-dimensional quantum well wire laser arrays with large subband separation and high power light pulse output at room temperature. **(p. 161)**

5:30pm–6:30pm
Panel Discussion—What's Next in Quantum Optoelectronics?

BALLROOMS VI–VIII

8:30am–10:00am
QFA • Novel Semiconductor Materials and Structures
Nobuyuki Imoto, *NTT, Japan, Presider*

8:30am (Invited)
QFA1 • II–VI semiconductor nanocrystals as isolated quantum dots and in complex structures, Moungi G. Bawendi, *Massachusetts Institute of Technology.* We describe the fabrication and properties of nearly monodisperse CdSe nanocrystals, their assembly into 3-D arrays and their incorporation into organic-based electroluminescent devices. **(p. 166)**

9:00am
QFA2 • Squeezed light generation in semiconductors, A. M. Fox, J. J. Baumberg, M. Dabbicco, B. Huttner, J. F. Ryan, *Univ. Oxford, UK.* We have generated quadrature squeezed light in a semiconductor using the third-order nonlinear susceptibility of ZnS at room temperature with 125-fs pulses at 780 nm. **(p. 168)**

9:15am
QFA3 • Blue-green laser diodes with improved crystal quality by using a strained-layer superlattice for the optical guiding layer, Jun Gotoh, Shinnichi Nakatsuka, Kazuhiro Mochizuki, Masayuki Momose, Akira Taike, Masahiko Kawata, *Hitachi Central Research Laboratory, Japan.* The optical and device characteristics of blue-green lasers fabricated from II–VI semiconductor were improved by using strained-layer superlattices as the optical guiding layers. **(p. 171)**

9:30am
QFA4 • Normal incidence intersubband absorption in vertical quantum wells, V. Berger, *Thomson-CSF, France;* G. Vermeire, P. Demeester, *Univ. Gent, Belgium;* C. Weisbuch, *Ecole Polytechnique, France.* N-doped vertical AlGaAs quantum wells have been grown on a submicron grating. Intersubband absorption at normal incidence is demonstrated in those quantum wells. **(p. 174)**

9:45am
QFA5 • One-dimensional exciton diffusion in GaAs quantum wires, Y. Nagamune, H. Watabe, M. Nishioka, Y. Arakawa, *Univ. Tokyo, Japan.* One-dimensional exciton diffusion in GaAs quantum wires with the lateral width of 7–30 nm was measured by microphotoluminescence measurements at low temperature. **(p. 177)**

BALLROOM FOYER

10:00am–10:30am
Coffee Break

BALLROOMS VI–VIII

10:30am–12:00m
QFB • Micro- and Vertical-Cavity Physics and Applications
Connie Chang-Hasnain, *Stanford University, Presider*

10:30am (Invited)
QFB1 • Theory of semiconductor microcavities and lasers, S. W. Koch, F. Jahnke, H. C. Schneider, *Philipps-Univ. Marburg, Germany.* The photon and carrier dynamics in semiconductor microresonators and microcavity lasers is investigated within a microscopic description of mode confinement, nonequilibrium, and many-body effects. **(p. 182)**

11:00am
QFB2 • Limitations of surface-related optical and carrier losses in microcavity lasers, B. J. Thibeault, T. A. Strand, M. G. Peters, T. Wipiejewski, D. B. Young, J. W. Scott, L. A. Coldren, *UC–Santa Barbara.* A comparison of experimental data with analytical results shows that the viability of microcavity lasers is limited by surface related optical and carrier losses in vertical-cavity surface-emitting lasers. **(p. 185)**

11:15am
QFB3 • Low threshold microcavity lasers using a half-wave cavity spacer, D. L. Huffaker, J. Shin, D. G. Deppe, *Univ. Texas at Austin.* Data are presented characterizing vertical-cavity lasers using a half-wavelength cavity spacer layer. A continuous-wave, room-temperature threshold current of 91 μA is demonstrated. **(p. 188)**

11:30am
QFB4 • Cavity characteristics of selectively oxidized vertical-cavity lasers, Kent D. Choquette, K. L. Lear, R. P. Schneider, Jr., G. R. Hadley, K. M. Geib, S. P. Kilcoyne, *Sandia National Laboratories.* We show that a buried oxide layer forming a current aperture in monolithic vertical-cavity lasers introduces a lateral index variation producing index-guided confinement with a controllable shift in the resonance wavelength in the oxide region, and enables record laser performance. **(p. 191)**

11:45am
QFB5 • Complete polarization control of 8 × 8 vertical-cavity surface-emitting laser matrix arrays, T. Yoshikawa, H. Kosaka, K. Kurihara, M. Kajita, Y. Sugimoto, K. Kasahara, *NEC Corp., Japan.* We completely control polarization of 8 × 8 vertical cavity surface emitting laser (VCSEL) arrays, which have a 6 × 5 μm rectangular post structure. All 64 VCSELs emit linearly polarized light with a polarization angle deviation of only 2.9°. **(p. 194)**

BALLROOMS VI–VIII

12:00m–12:10pm
QOE • Closing Remarks

Nanometer Probing

JWA 8:30 am-10:00 am
Ballrooms VI-VIII

Gerard A. Mourou, *Presider*
University of Michigan

Applications of Scanning Force Microscopy for Voltage Measurements with High Spatial and Temporal Resolutions

Francis Ho, A. Samson Hou, Bettina A. Nechay, and David M. Bloom
Edward L. Ginzton Laboratory, Stanford University, Stanford, CA 94305

Introduction

To keep pace with device technology as it pushes towards 100-nm line widths and gigahertz operating speeds, new measurement tools are needed for studying mesoscopic device physics and for testing and designing the next generation of ultra-dense integrated circuits. A promising new direction is the use of scanning probe microscopes for such measurements, by utilizing probe tip nonlinearities for heterodyning very high-speed signals.[1-6] We have developed such an ultrafast system, based on the scanning force microscope (SFM), that should theoretically be able to map a voltage profile with subpicosecond temporal resolution and sub-micron spatial resolution. Furthermore, it is non-invasive, rugged, and does not require vacuum. By using the square-law force interaction between the SFM and sample for mixing and sampling, we have measured voltage transients as fast as 5 picoseconds. We have also used this system to probe VLSI integrated circuits.

Theory of Operation

Figure 1 shows the concept of an SFM probe system.[1] A scanning force microscope operates by using a CW laser and a position-sensitive detector to sense the deflection of a cantilever to which is attached a sharp tip. We operate an SFM in non-contact mode, in which a gap of approximately 10-100 nm is maintained between the tip and the circuit sample. There is a periodic high-speed voltage V_S on the sample that we wish to measure. We apply a pulse-train sampling voltage V_p to the tip. The voltage across the gap between the tip and the sample is $V_p - V_S$. The measured force is proportional to the square of this voltage and therefore contains a mixing term at an intermediate frequency (IF) corresponding to the offset frequency between V_p and V_S. This IF is chosen low enough so that the cantilever deflection can follow an equivalent-time representation of V_S.

Figure 1. High-speed SFM probe system.

Experiments

To illustrate the operation of the probe, we describe here the results from three experiments. In the first experiment, we probed various signals on an Intel 80486 microprocessor that had been depassivated. (We have also demonstrated non-invasive probing of circuits through passivating layers;[2] removal of passivation for devices that can tolerate it, however, yields improvements in voltage sensitivity and spatial resolution.) The experiment consisted of two parts. In the first part, we operated the microprocessor with a 20 MHz clock and probed the voltages on two metal lines on the microprocessor that carried opposite phases of
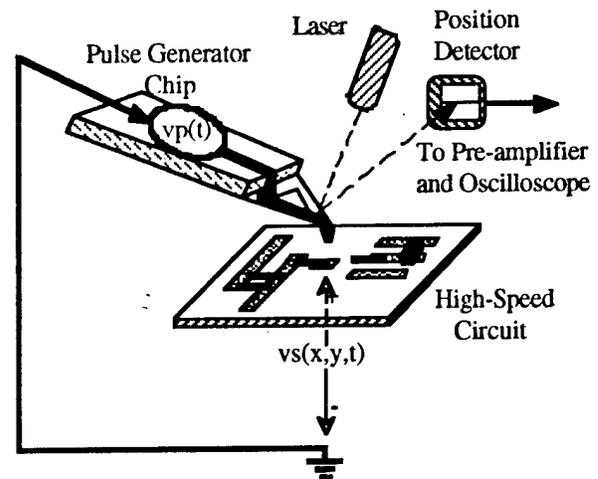
the clock; this is shown in Figure 2. The strobe pulses supplied to the tip were 2 ns in duration, which meant that the time resolution was 2 ns. Next, we operated the '486 in its self-test mode with a 10 MHz clock. In that mode, the microprocessor goes through a pre-defined series of logic states every time it receives a reset signal. By applying a reset every 20 clocks, we were able to measure a repeating self-test sequence, shown in Figure 3, using our probing system. The digital sequence can be easily discerned.
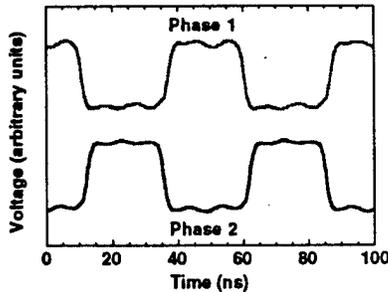

Figure 2. Two clock phases on the 80486 microprocessor.
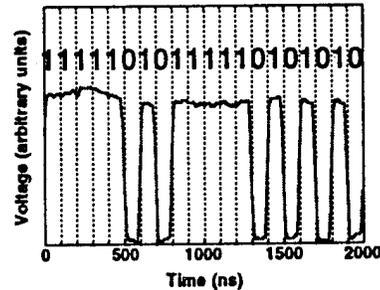

Figure 3. Self-test sequence of the 80486 microprocessor.

A second experiment, in which we probed National Semiconductor's AT/LANTIC (AT local area network twisted-pair interface controller) chip, further demonstrates the usefulness of this probe system for making precise timing and delay measurements. The AT/LANTIC incorporates a clock-recovery phase-lock loop to synchronize incoming ethernet data. A challenge in testing the AT/LANTIC was building the timebase electronics, shown in Figure 4, required for generating sampling pulses with proper timing with respect to the chip. Measured data from the chip are shown in Figure 5. PHCOMP is an asynchronous digital signal that requires about 250 ns to settle to a valid state. The first complete rising edge of PHCOMP (occurring at t=330 ns) is found to be significantly longer (15 ns) than subsequent edges (about 6 ns). The amount of edge broadening is a measure of the jitter in AT/LANTIC's phase-lock loop and also a function of the averaging time for the measurement. In comparison, a second, synchronous signal from the chip (DMUX) showed no significant difference in edge speeds from edge to edge. These results demonstrate the usefulness of the probe system for making precise timing and delay measurements.
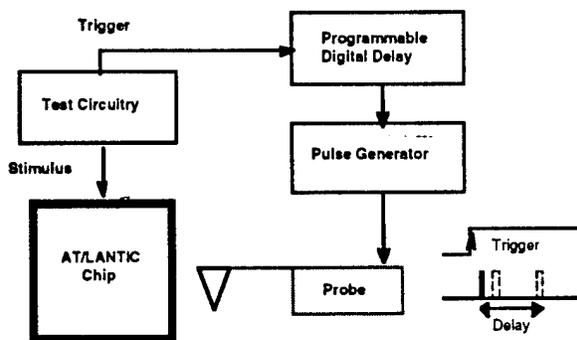

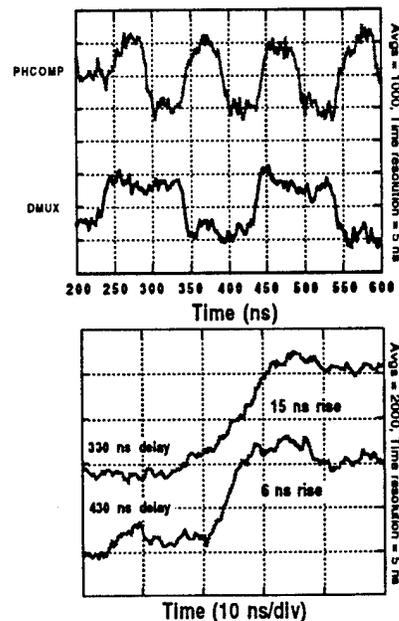**Figure 4.** Timebase circuit for testing the AT/LANTIC.
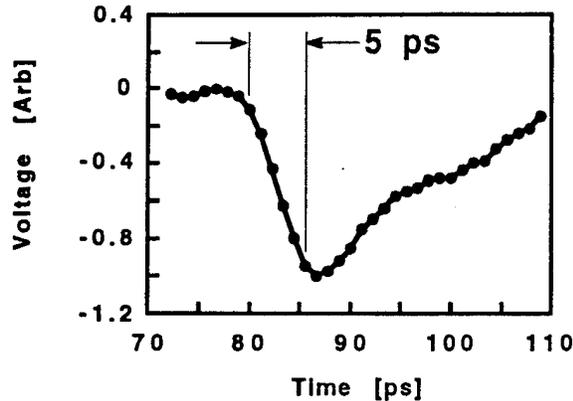

Figure 5. AT/LANTIC measurements.

Figure 6. Probing of nonlinear transmission line.

The preceding experiments were all performed using gold-coated commercially available cantilevers, a scheme which does not work at frequencies greater than a few gigahertz. In order to obtain better temporal resolution, we microfabricated cantilevers with integrated transmission lines. Using these high-speed cantilevers, we were able to observe voltage steps as short as 5 picoseconds on circuits. This is shown in Figure 6. We used nonlinear transmission line (NLTL) circuits, which can generate subpicosecond voltage steps [7], to serve both as the source of the strobe pulses and as the circuit under test. In this experiment, the NLTL circuit and the cantilever chip were wire-bonded together. We anticipate that by integrating the NLTL circuit and the cantilever on the same substrate, we shall obtain sub-picosecond time resolution.

Conclusion

We have measured 5 ps voltage steps using equivalent time sampling, and probed various ICs, including an 80486 microprocessor and a National Semiconductor AT/LANTIC chip. In the future, we anticipate being able to probe with sub-picosecond and nanometer resolution by integrating pulse-generators with microfabricated cantilevers and tips.

References

[1] A.S. Hou, F. Ho, and D.M. Bloom, "Picosecond electrical sampling using a scanning force microscope," Electronics Letters **28**, 2302 (1992).

[2] F. Ho, A.S. Hou, and D.M. Bloom, "High-speed integrated circuit probing using a scanning force microscope sampler," Electronics Letters **30**, 560 (1994).

[3] D.M. Bloom, "Voltage-contrast scanning probe microscopy," Proceedings of the 4th European Conference on Electron and Optical Beam Testing of Integrated Circuits, Zurich, Switzerland 1-3 Sept. 1993. (To be published in Microelectronic Engineering.)

[4] S. Weiss, D.F. Ogletree, D. Botkin, M. Salmeron, and D.S. Chemla, "Ultrafast scanning probe microscope," Appl. Phys. Lett. **63**, 2567 (1993).

[5] K. Takeuchi and Y. Kasahara, "High-speed optical sampling measurement of electrical waveform using scanning tunneling microscope," Appl. Phys. Lett. **63**, 3548 (1993).

[6] G. Nunes Jr. and M.R. Freeman, "Picosecond resolution in scanning tunneling microscopy," Science **262**, 1029 (1993).

[7] M.S. Shakouri, A. Black, B.A. Auld, and D.M. Bloom, "500 GHz GaAs MMIC sampling wafer probe," Electron. Lett. **29**, 557 (1993).

Ultrafast Near-Field Optical Probing

Jason B. Stark
AT&T Bell Laboratories, Murray Hill, NJ 07974
908-582-2173 (voice), 908-582-4702 (fax), jstark@physics.att.com (email)

Umar Mohideen
Department of Physics, University of California, Riverside, CA 92521
909-787-5390 (voice), 909-787-4529 (fax), umar@ucrph0.ucr.edu (email)

Richart E. Slusher
AT&T Bell Laboratories, Murray Hill, NJ 07974
908-582-4094 (voice), 908-582-4702 (fax), res@physics.att.com (email)

Direct measurement of carrier dynamics, using femtosecond light sources, has yielded a wealth of understanding within the field of condensed matter physics[1]. Also, recently, near-field optical probe techniques have enabled optical measurements with spatial resolution below the diffraction limit[2]. An understanding of many scientifically and technologically important issues require a knowledge of the local behavior of carriers within materials and microstructures. We report the development of the required instrumentation, and the first measurement of carrier dynamics with spatial resolution below the diffraction limit and temporal resolution below 60 fs.

The experimental instrumentation consists of a broadband modelocked light source, a pair of acousto-optic modulators (AOMs), and a near-field optical microscope (Fig. 1). Modelocked pulses are separated into pump and probe, and chopped independently by the AOMs. Probe pulses are delivered to the optical fiber probe tip of the near-field microscope, and illuminate the sample. The transmitted light is collected by the objective of a far-field microscope, and delivered, through a multimode optical fiber, to a spectrometer where a photomultiplier tube registers the signal. The pump pulses are delivered through a beam-splitter to the same objective and focused to a far-field spot on the sample. The nonlinear optical response of the sample is recorded as the sample is scanned within the near-field of the fiber probe tip, taking one image for each setting of the time delay between pump and probe pulses. In this way, carrier dynamics within the sample can be imaged as a function of time after excitation, with a time resolution as low as 40 fs, and spatial resolution as small as 50 nm. The results can be displayed as a sequence of animated movie frames.

Infrared optical pulses are generated in a modelocked Ti:Sapphire laser, with a repetition rate of 82 MHz and average power of 400 mW. The spectral bandwidth is adjustable up to a maximum of 100 nm about the 800 nm center. The pulsewidth, from the 3 mm crystal, is below 15 fs. The output enters a two-pass prism-pair dispersive delay line, for compensation of the positive dispersion of the output coupler and subsequent optics. Within this delay line, the beam is spectrally separated into pump and probe. A pair of pick-off mirrors then direct the long-wavelength probe, and short-wavelength pump to the experiment. The pump beam passes through a variable delay line, followed by an AOM, operating at 3.1 MHz. It then enters the far-field microscope, and is reflected downwards from a beam-splitter, through the objective, onto the sample. This far-field pump is focused on the sample to a spot on the order of 5 μm, to uniformly excite the region probed by the fiber tip.
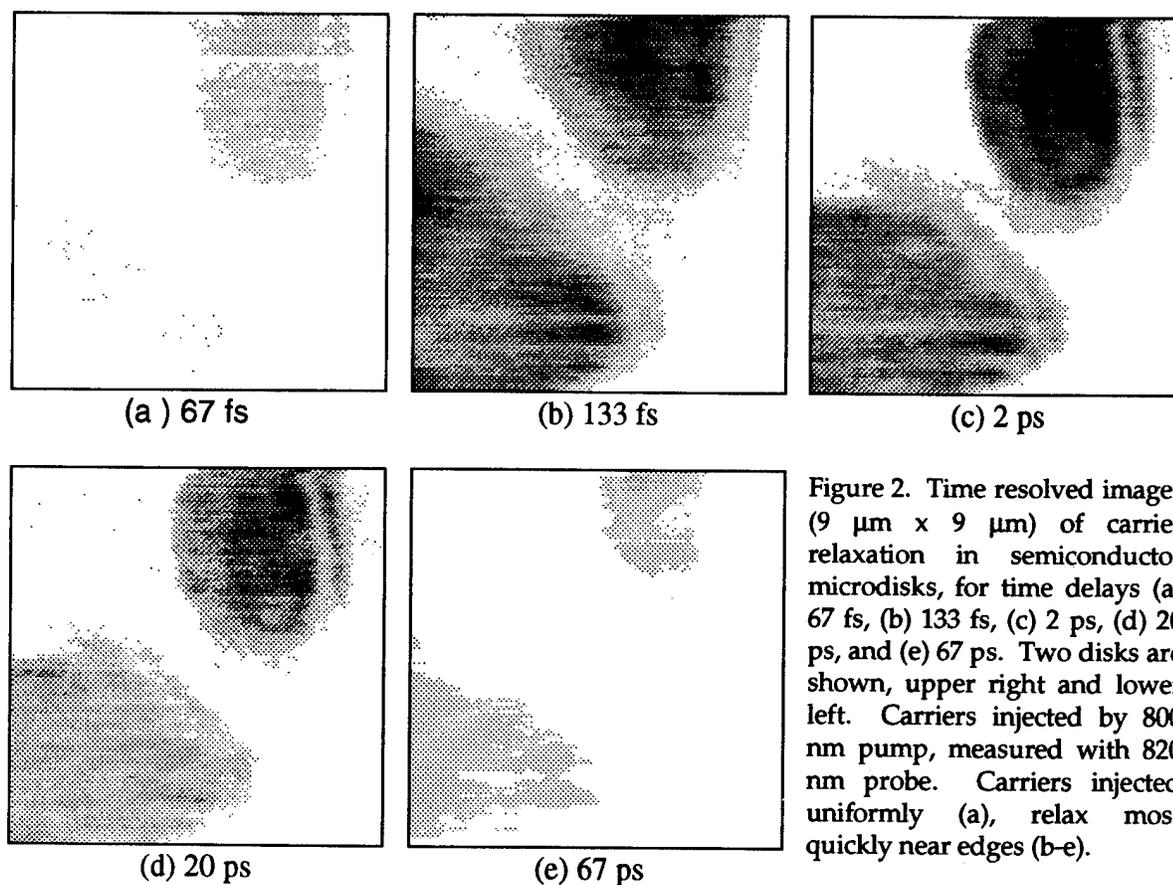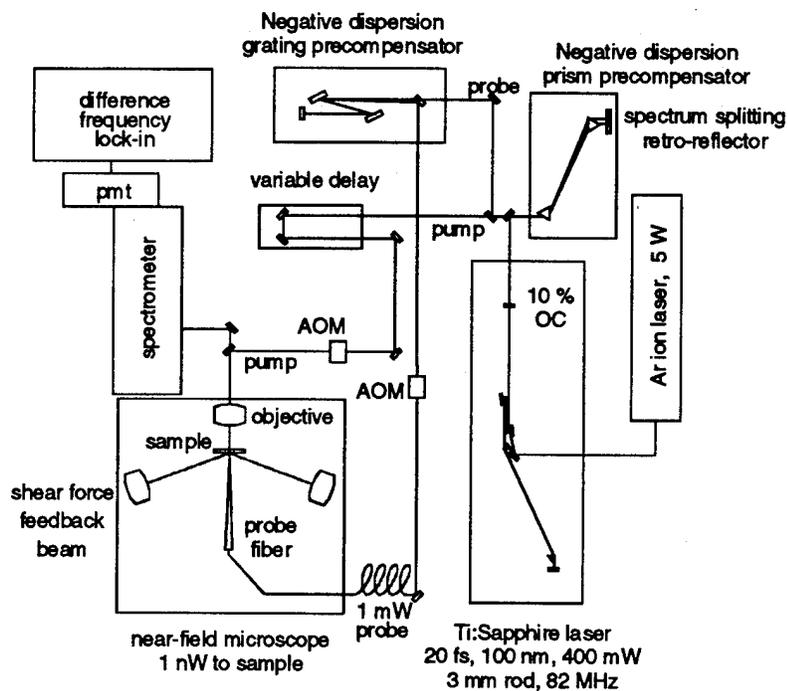
The probe beam enters a second dispersive delay line, using a two-pass grating-pair geometry, to pre-compensate the dispersion introduced during passage through the 1-meter fiber probe tip. The probe beam is modulated at 3.0 MHz. Pulses enter the probe tip and emerge with a pulsewidth of 50 fs. The fiber probe tip is a single-mode optical fiber whose end has been tapered and coated

with aluminum to leave a small aperture, typically 50-100 nm[3]. Light propagating through this aperture is coupled into the far-field and subsequently detected. The coupling efficiency of such tips is typically -50 to -60 dB; the remaining light is absorbed in the aluminum, causing heating, and imposing an upper limit on average power of the order of 1 mW. Light levels in the far-field of the tip are then in the nW regime. The sample is held in the near-field of the fiber tip using a shear-force feedback technique[4], stabilizing the tip-sample separation at around 50 nm. The fiber tip is imaged into a multimode optical fiber, and delivered to a spectrometer to control the probe bandwidth reaching the detector. In a transmission experiment, the absorption of the sample is measured locally by the fiber probe tip, and the sample scanned to form an image. In a nonlinear transmission measurement, the nonlinear response, at the 100 kHz modulation sideband, is recorded simultaneously.

Samples of GaAs quantum wells were etched to produce 150 nm thick disks, of varying diameters from 3 to 10 μm, with eight periods of 10 nm wells separated by 5 nm barriers. The room-temperature excitonic absorption edge is at 850 nm. Measurements made using the full laser spectrum indicate that the carrier recombination in the center of the microdisks is exponential, with a time constant of 500 ps. In the first set of measurements, the pump beam was filtered before the sample, to a 10 nm bandwidth about 800 nm, while the probe was filtered after the sample to 10 nm about 820 nm. In this case the probe measures carriers well above the bandegde, as they relax from their initial distribution, as injected by the pump. Figure 2 shows the nonlinear signal, measured by the probe, in two microdisks (upper right and lower left) of diameters 5 and 10 μm. The image is produced by linearly scanning the X- and Y-voltages on the sample piezoelectric tube (distortions of the circular shape are caused by a nonlinear relationship between the displacement and applied voltage). The nonlinear optical response at 67 fs delay (a) shows the carriers relaxing after excitation by the leading edge of the pump pulse. After 133 fs (b) the nonlinear response is near its peak, indicating a time resolution on the order of 60 fs. After the initial excitation, measurements (c,d,e) at 2, 20 and 67 ps, respectively, show that carriers relax in the microdisks with a time constant on the order of 80 ps. The measured recombination time was 500 ps, with the 80 ps relaxation rate indicating the rate of carrier cooling. Furthermore, carriers near the edges of the microdisks relax most quickly, leaving the nonlinear response peaked strongly toward the center for time delays beyond 1 ps. The spatial resolution in these images, though not rigorously characterized, is on the order of 400 nm. Ultimate resolutions are expected to be under 100 nm.

We demonstrate, for the first time, submicron spatially resolved images of carrier dynamics, with time resolution better than 60 fs. Carriers injected uniformly into the microdisks cool in a time of 80 ps, most quickly near the edges, where they may relax into surface trap states. Studies continue to measure the details of this relaxation, as a function of probe wavelength and with better spatial resolution. Similar studies are under way to study nonequilibrium transport in narrow channel electronic devices, as well as local carrier dynamics in operating semiconductor lasers. Measurements with high spatial and temporal resolution have now evolved from the stage of instrumentation development, to begin producing results having important scientific and technological implications. The rapid development of this field presents many exciting prospects, in the very immediate future, for the study of carrier dynamics in materials and microstructures.

[1]   *Hot Carriers in Semiconductor Nanostructures*, ed. Jagdeep Shah, Academic Press, San Diego, California, 1992

[2]   E. Betzig, J. K. Trautman, Science **257**, 189 (1992)

[3]   E. Betzig, J. K. Trautman, P. D. Harris, J. S. Wiener, R. L. Kostelak, Science **251**, 1468 (1991)

[4]   E. Betzig, P. L. Finn, J. S. Wiener, Appl. Phys. Lett. **60**, 2484 (1992)

Figure 1. Ultrafast near-field probe. Ti:Sapphire laser pulses spectrally split into pump and probe. Probe precompensated for dispersion, pump delayed, each modulated by AOM. Probe coupled into fiber tip, through sample in near-field, into spectrometer. Pump focused onto sample. Difference frequency measured.

(a) 67 fs

(b) 133 fs

(c) 2 ps

(d) 20 ps

(e) 67 ps

Figure 2. Time resolved images (9 μm x 9 μm) of carrier relaxation in semiconductor microdisks, for time delays (a) 67 fs, (b) 133 fs, (c) 2 ps, (d) 20 ps, and (e) 67 ps. Two disks are shown, upper right and lower left. Carriers injected by 800 nm pump, measured with 820 nm probe. Carriers injected uniformly (a), relax most quickly near edges (b-e).

Laser-Diode Based Scanning Force Microscope and Ultrafast Sampling Probe

John Nees and Douglas Craig

University of Michigan, Ultrafast Science Laboratory 2200 Bonisteel Blvd. 1006/IST Ann Arbor MI 48109-2099 USA phone (313) 764-9271 fax (313)763-4876

Soichi Hama and Shin ichi Wakana

FUJITSU Laboratories Ltd. 1-10 Morinosato Wakania Atsugi, Kanagawa 243-01, Japan phone 81-046-248-4311, fax 81-046-248-3896

Introduction

New discoveries in fabrication technology and in device physics have open the way for a class of electronic and optoelectronic devices with nanometer-scale dimensions. These devices offer the opportunity to work with electrons confined to 2-D, 1-D and 0-D in space. In an effort to understand how individual devices work it will be necessary to interrogate individual submicron structures . Aside from the fine dimensions of the contacts used for such measurements it will be necessary to make measurement with very low invasiveness and increasingly, with higher speed. To meet the challenges of new nano-technologies we have developed a probe which demonstrates high impedance voltage measurement using a 0.1-micron contacting tip. The voltage of the tip is photoconductively sampled allowing waveforms to be measured with picosecond resolution [1]. In this paper we describe the operation of the probe using a gain switched laser diode to make measurements which extract only a few fC from the device under test. We also show the probes value as a high-speed, high sensitivity probe for millimeter-wave circuits.

Probe fabrication

The probe is fabricated using Low Temperature grown GaAs (LT GaAs). That is, GaAs grown at 210°C rather than the conventional temperature of 600°C. A micron-thick layer of LT GaAs is grown on a half-micron-thick layer of AlGaAs on a semi-insulating GaAs wafer. Metal, defining the electrodes of a photoconductive switch, is patterned on the LT GaAs layer. The probe's perimeter is patterned by photolithography and defined by front-side etch penetrating through both epi-layers. A self-terminating lift off is used to define a fine probe tip having a tip radius below 0.1 μm[2, 3] The GaAs substrate is chemically removed, freeing the 1.5 μm thick film of LT GaAs and AlGaAs as shown in figure 1. Following this UV curing cement is used to attach the probe to a glass support. and the finished probe is placed on a translation stage for use.
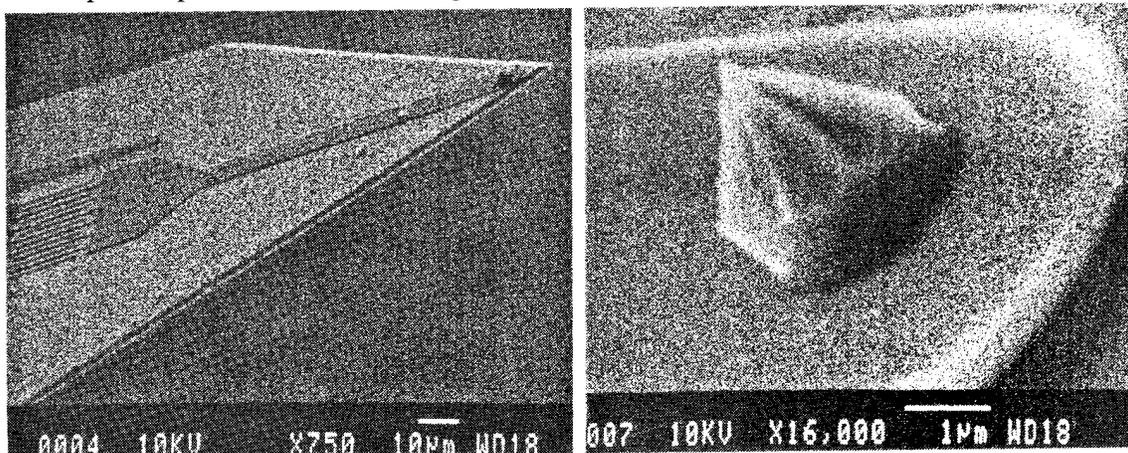

**Figure 1** shows SEM pictures of the scanning force microscope probe and ultrafine tip.

Probe use

The probe is used in a Scanning Force Microscope (SFM) in the place of a conventional cantilever probe. It is mounted and aligned on the SFM stage and an image of the device-under-test is scanned. The probe tip is then positioned at the desired location and pressed into low-force contact with the signal-line to be interrogated. Picosecond resolution is obtained by photoconductively switching charge from the device under test during the picosecond on-time of the probes gate. This samples the electronic waveform on the device-under-test by allowing an amount of current proportional to the waveform voltage to pass on to the detection electronics. The delay of the switching beam is swept to perform equivalent time sampling of the repetitive waveform.

The experiment

A photoconductive SFM probe was made as described above. The gate was illuminated through a fiber-optic connection supported by the substrate used to support the probe on the SFM scanning arm. In the is configuration the probe was scanned over the sample, rather than *vice versa*. In order to measure the effects of parasitic

capacitance on the circuit under test and amplifier was attached to the output of the probe. The *ac* transients measured without illumination of the gate switch agreed with the calculated capacitance of 10 fF. With illumination turned on and a dc voltage applied to the circuit under study a mapping of the tip contact was made over the active area of a test structure. The conductivity mapping was indicative of the uniformity of contact over the surface of the conductor. As may be seen in figure 2(a,b, c, and d) contact with the surface was not continuous during the scan, nor was it repeated from the forward scan (1b) to the reverse scan (1d).
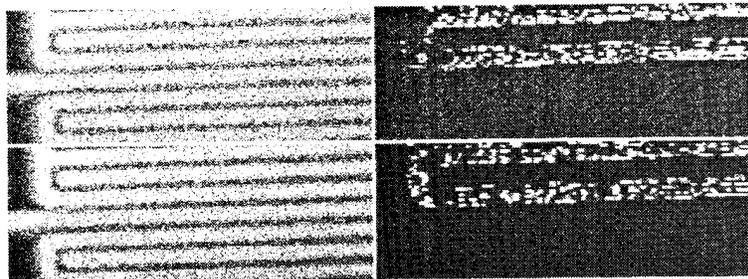
Figure 2 (row 1-a and b, row 2-c and d) shows topographic scans (a and c) of and electrode test pattern and scanned conductivity mapping (b and d) of the circuit. Note that only one loop is connected and that the contact for forward scan and reverse scan are neither identical, nor continuous.
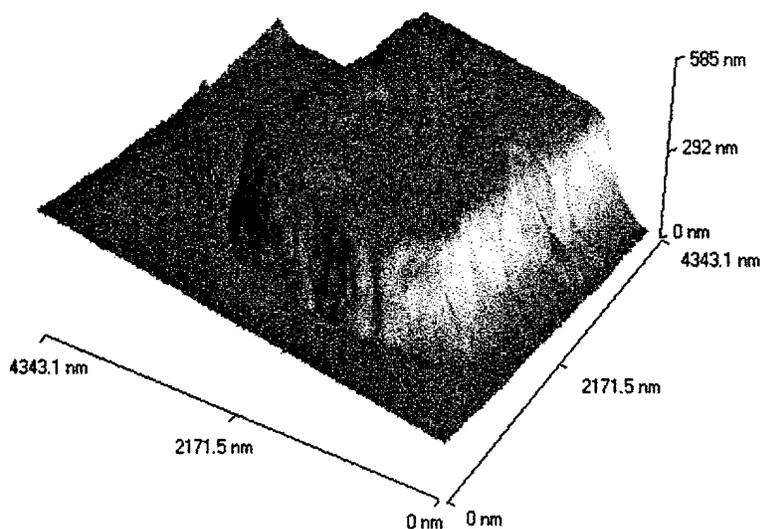
Figure 3 shows the topographic image of a 1.5 micron-wide metal finger on which transients are measured.

In low-force contact, our probe has a dark conductance of 0.05 nS as measured using a Fluke 27 multimeter. The test signal is generated by an electronic pulser and launched onto the device under test by an SMA connector. The measured signal is gated by a 30 x 30-μm photoconductive switch integrated on the LT GaAs probe cantilever and carried on a coplanar stripline to a pre-amplifier and 20 MHz A/D converter. 810-nm, 100-ps optical pulses generated by a Hamamatsu gain switched laser diode are coupled to the probe by the optical fiber mounted with the probe. These pulses are estimated to have fJ of absorbed energy allowing only 5 fC of charge to be removed from the device under test.. Delay between the optical sampling pulse train and the test signal is controlled by a computer controlled electronic delay circuit.

The results

Images scanned by the probe show 10 to 100-nm features. Signal-to-noise equal to unity is seen at 2V with a single shot measurement. With the same degree of invasiveness in the high speed signal single mV sensitivity is achieved at a sampling rate of 3 MHz.
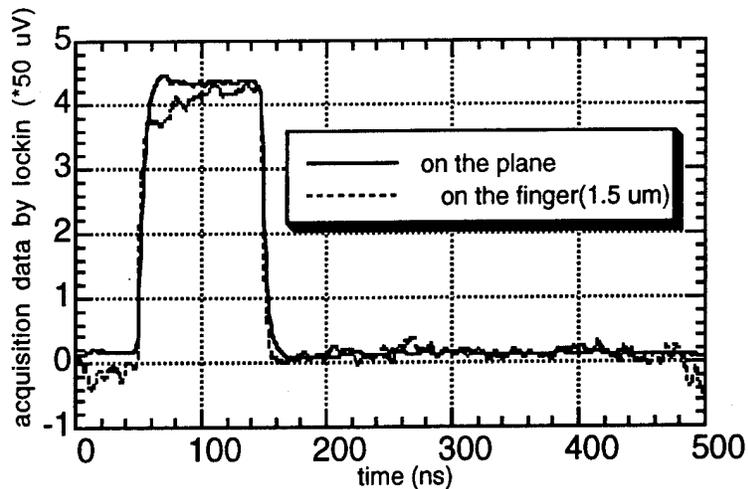
Conclusions and References

Using a probe with demonstrated 2.5 ps temporal resolution and 100-nm spatial resolution we have been demonstrated laser diode-based sampling of integrated circuits. A single shot measurement of 2V sensitivity is possible with the removal of only 5 fC. This probe not only provides a critical solution to the problem of internal circuit testing on VLSI, but it also opens the door to investigation individual mesoscopic devices with unprecedented sensitivity.

The investigation of repeatability and continuity in these measurements is on-going.

D. R. Grischkowsky, *et al* IEEE J. Quantum Electron. QE-24, 221 (1988)

J. Kim, S. Williamson, J. Nees, S. Wakana, and J. Whitaker, Appl. Phys. Lett. 62 (18), 3 May 1993.

C.A. Spindt, L. Brodie, L. Humpfrey, and E. R. E. R. Westerberg, J. Appl. Phys. 47, 5248 (1976).

STOEM: Scanning Tunneling Optoelectronic Microscope

Koichiro Takeuchi, Akira Mizuhara
Teratec Corporation, 2-9-32 Naka-cho, Musashino-shi
Tokyo 180, Japan
FAX:81-422-52-2125, Phone:81-422-52-2102

Introduction

We applied a scanning tunneling microscope (STM) to optoelectronic sampling measurement of high-speed electrical waveform[1]. An optical pulse train was used to turn on and off a photoconductive semiconductor switch (PCSS) made of low temperature GaAs on the STM probe. This special STM can be called scanning tunneling optoelectronic microscope (STOEM).

Because of Great advances in increasing the speed and in decreasing the size of electronic circuits and devices, a new measuring method with high temporal resolution in the order of pico seconds and spatial resolution in the order of sub-micro meters is required. In such high-speed, microscopic measurement, the high frequency signal must be converted to a signal with low frequency in a sufficiently small region at the point to be measured. Furthermore, the measurement must be carried out without mechanical contact or with so soft contact that the probe could not break the surface of devices under test (DUT).

Although an STM has been developed as a microscope with ultra-high spatial resolution since its invention in 1982[2], its property of non-contact and high impedance is also useful for measuring high-speed electrical waveforms. Therefore an STM would be a powerful new instrument offering ultra-high temporal and spatial resolution.

Very recently, some groups have reported novel applications based on such concept[1, 3-5]. Weiss et al.[3] and Nunes et al.[4] measured short electrical pulses using non-linearity of the tunneling current. By using an atomic force microscope (AFM) instead of an STM, Hou et al. [5] measured a high-speed electrical waveform via the mechanical response of the AFM cantilever.

Experiments

Figure 1 shows a schematic view of the probe and the DUT. Our STOEM probe has a photo-conductive semiconductors switch (PCSS) on it. An optical pulse train with 100fs duration from a Ti-sapphire laser is used to turn on and off the PCSS. The periodic frequency of the optical pulse train is 80 MHz + 1kHz, which is synchronized to an external master oscillator, while the fundamental frequency of the DUT signal is 80MHz. The 1kHz frequency difference is the fundamental frequency of the sampled signal to be measured from the current. Therefore the electrical signal is extended 80,000 times along the time axis. This technique is similar to that used for a high-speed oscilloscope and E-O sampling.

Since the band width of the feedback circuit is set to be lower than 1kHz, control of the probe position is not disturbed by the waveform measurement.

The PCSS was fabricated by sputter-evaporating Au/Ti films in interdigitated feature on a semi-insulating GaAs crystal. The line width and the gap distance of the switching region are 5 μ m each. The GaAs photo-conductive layer was grown by MBE at low temperature (<300deg.) to introduce carrier recombination centers[6]. As the result, the PCSS response time was shortened better than 1.8ps. After fabricating the PCSS, the GaAs wafer was cleaved and the metal tip on the cleaved corner was used as the STOEM probe tip. The tip part of the GaAs wafer was removed by wet etching to make the metal tip protruding.

The schematic view of the experimental arrangement for testing the PCSS response is illustrated in figure 2. There are 5mm long coplanar strips (CPS) on a low temperature grown GaAs layer, and an additional electrode connected to the CPS via an interdigitated PCSS. The CPS has design impedance of 50 Ω and consists of two parallel 60 μ m wide strips separated from each other by 5 μ m. The design of the PCSS is the same as that mentioned above.

When a charged strip line is shorted via the photocarriers generated by an laser pulse, an electrical pulse is generated and propagates toward the PCSS. Under this condition we focused sampling pulse beam on the PCSS. Both the 10 mW exiting and 10mW sampling beams were from one Ti-sapphire laser which is the same as that used for the STOEM
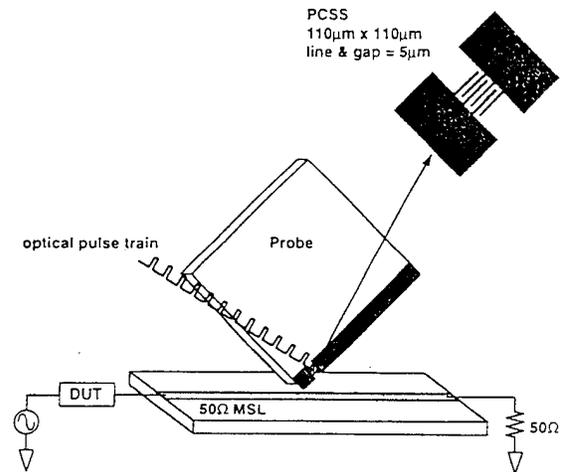

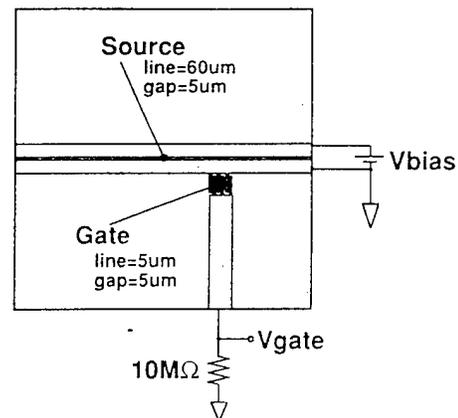Fig. 1 Schematic view of the probe and DUT

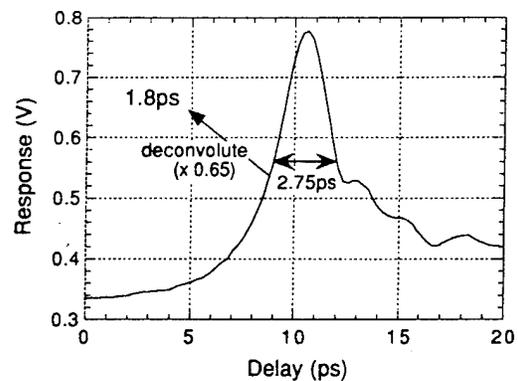Fig. 2 Schematic view of the sample for testing the PCSS response

Fig. 3 Pulse shape of photogenerated pulse. Actual pulse width and PCSS response should be shorter than 1.8ps.

measurement. The focused beam size was approximately 50 μ m in diameter. The sampling beam propagates through a delay line, and we measured the pulse shape of the photogenerated electrical pulse by scanning the delay.

Figure 3 shows a result when the distance between the exciting and sampling beam spots is 300 μ m. Since measured pulse width is 2.75ps, the deconvoluted value is about 1.8ps. Therefore the response time of the PCSS is at least 1.8ps. When the PCSS is used for the measurement using the STOEM, the time resolution is expected to be close to this value. The DC component in figure 3 may be due to unexpected photocarriers generated by sampling beam itself at the gap near the PCSS.

Fig. 4 Pulse shape of the comb generator measured by STOEM.

Using the probe with the PCSS, we measured the pulse shape from a comb generator on a 50 Ω micro strip line made of an Au film. Details of the electronic system setup were described in the previous work [1]. Figure 4 shows the resulted pulse shape with 117ps FWHM. The following oscillation may be due to reflections of the electric pulse. The pulse width is almost the same as the actual value of 113ps.

Conclusion

We fabricated a probe which has a low temperature grown GaAs PCSS. The PCSS response time was 1.8ps. Using this new probe for the STOEM, we measured the pulse shape with 117ps FWHM that is almost the same as the actual value.

REFERENCES

[1] K. Takeuchi and Y. Kasahara, Appl. Phys. Lett. Vol. 63, no. 26, pp. 3548 (1993)

[2] G. Binning, H. Rohrer, C. Gerber, and E. Weibel, Phys. Rev. Lett. Vol. 50, pp. 120 (1983)

[3] S. Weiss, D. F. Ogletree, D. Botkin, M. Salmeron, and D. S. Chemla, Appl. Phys. Lett. Vol. 63, no.18, pp. 2567 (1993)

[4] G. Nunes, Jr. and M. R. Freeman, Science Vol. 262, pp1029 (1993)

[5] A. S. Hou, F. Ho, and D. M. Bloom, Electron. Letters Vol. 28, no. 25, pp. 2302 (1992)

[6] S. Gupta, M. Y. Frankel, J. A. Valdmanis, J. F. Whitaker, G. A. Mourou, F. W. Smith, and A. R. Calawa, Appl. Phys. Lett. Vol. 59, no. 25, pp. 3276 (1991)
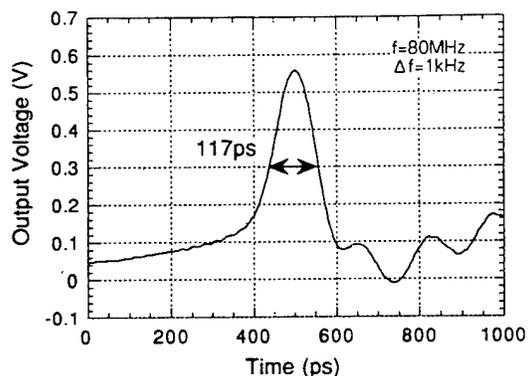
High-Frequency On-Wafer Testing with Freely Positionable Silicon-on-Sapphire Photoconductive Probes

T. PFEIFER, H.-M. HEILIGER, H. G. ROSKOS, and H. KURZ

Institut für Halbleitertechnik II, Rheinisch-Westfälische Technische
Hochschule (RWTH) Aachen, Sommerfeldstr. 24, D-52056 Aachen, Germany
Tel.: +49-241-80-7806 (-7890), Fax: +49-241-8888-246,
Email: roskos@zyklop.basl.rwth-aachen.de

Electronic and optoelectronic devices have become available with cut-off frequencies up to several hundreds of GHz. This technological push necessitates the development of new measurement techniques, because conventional electronic measurement equipment such as network analyzers or sampling oscilloscopes are limited in bandwidth to 40 - 100 GHz.

Considering *optically-assisted* high-frequency measurement techniques, the recent advance in photoconductive (PC) sampling with freely positionable probes significantly extends the potential of on-chip characterization of high-speed devices and circuits [1,2]. The probes are utilized to measure electric voltage transients in direct or tunneling contact with a conductor. The spatial resolution can be pushed far below the micron scale. A sensitivity of 1 µV has been reported for freely positionable PC probes made from LT-GaAs [1]. PC probes based on silicon-on-sapphire (SOS) technology, though inferior in sensitivity to LT-GaAs-based probes, are cheaper and easier to manufacture, and they are optically transparent per se facilitating alignment. In this contribution, we present a detailed characterization of freely positionable SOS PC probes both as *detectors* and *generators* for ultrafast electric signals. The linearity, sensitivity, time resolution and invasiveness are discussed.

Our PC probes utilize a metal-semiconductor-metal interdigitated electrode structure as photoconductive switch (see Fig. 1). To facilitate contacting to a device-under-test (DUT), a 5-µm-high Au-coated Ti tip is located at the end of the short electrode. Fabrication of the finger structure is based on a standard lift-off process for patterning of the Cr/Au metallization on the SOS substrate. The Si layer is implanted with Si^+ and Ne^+ ions to reduce the carrier lifetime. For fabrication of the Ti tip, a special lift-off process with a several-micron-thick photoresist layer was developed [2].
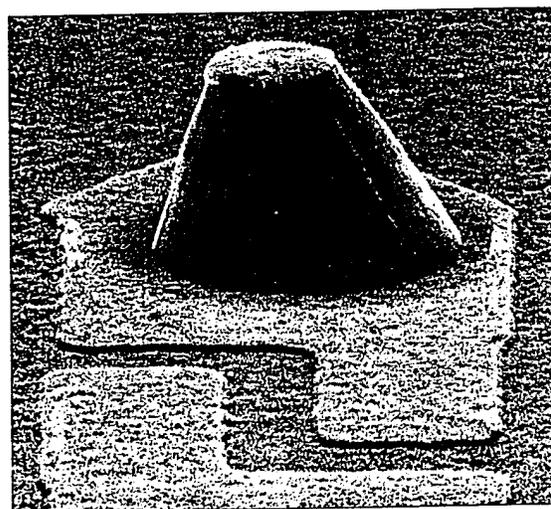

Fig. 1. SEM micrograph of a photoconductive sampling probe with an interdigitated switch. A 5-µm-high Au-coated Ti tip facilitates contacting to a DUT.

The time-resolved characterization is performed with a 100-fs ring dye laser in a pump-probe setup. We utilize a THz dipole antenna [3] and coplanar waveguides (CPWs) with integrated photoconductive switches as DUTs.

In a first series of experiments, electric pulses on an antenna are sampled. The pulses are generated by the switch integrated

into the antenna. The transients are detected close to the generation point with the Ti tip of the PC probe positioned onto one of the arms of the Hertzian dipole of the anntenna [2]. We investigate the response of the PC probe to electric pulses of 40 mV peak amplitude and 1.3 ps duration (FWHM). In these measurements, the intensity of the optical probe beam (beam impinging onto the PC probe) is varied, while the intensity of the pump beam (illuminating the antenna) is kept constant. As a measure for the photo-excitation of the PC probe, we determine the dc photocurrent I_{il} through the PC switch for a fixed bias of 1.5 V. Figure 2 shows
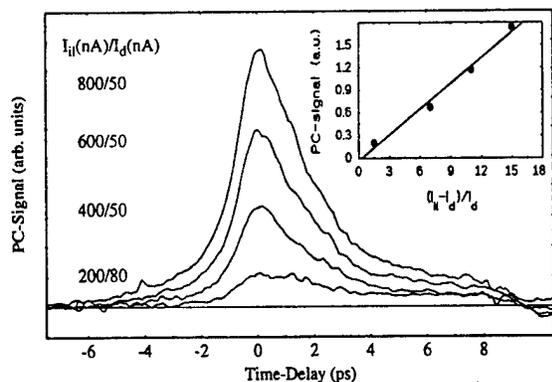
Fig. 2. Time-resolved PC probe signals of 40-mV electric pulses on an antenna. The probe-beam intensity is varied. Inset: dependence of the amplitude of the PC probe signal on the probe photocurrent I_{il}.

transients of the time-resolved experiment for various probe-beam intensities. The data are recorded in single scans (1-s lock-in time constant). The inset displays the peak amplitude of the transients as a function of I_{il}-I_d, with I_d being the dark current in the probe. We make the following observations: (i) No distortion in the shape of the electric pulses is found when the probe-beam intensity is raised. The transients have a duration of 2.7 ps (FWHM). This is longer than the electric-pulse width measured via electro-optic sampling technique (1.3 ps) [2]. A careful analysis of the measured data [2,4] shows that the time resolution of the PC probe is limited by the the lifetime of the carriers in the Si layer of the probe. The lifetime is found to exhibit a bi-exponential

behavior with time constants of 0.6 ps and 2.2 ps. Model calculations [2] predict that a complete suppression of the slow component by optimized ion implantation will result in a time resolution of the probe of approx. 1.5 ps. (ii) The peak amplitude of the transients rises linearly with the illumination intensity of the probe. (iii) The sensitivity of the PC probe can be evaluated from the noise characteristics of the data in Fig. 2. The noise floor is estimated to be approx. 400 μV for a single scan with 1-s lock-in time constant for all values of I_{il}. The sensitivity can be increased with the photoconductance of the PC switch [4]. The photoconductance is determined by the product of the mobility and the density of photoexcited carriers. To increase the sensitivity of SOS PC probes, higher excitation intensities and laser sources with better noise characteristics than that of dye lasers are necessary.
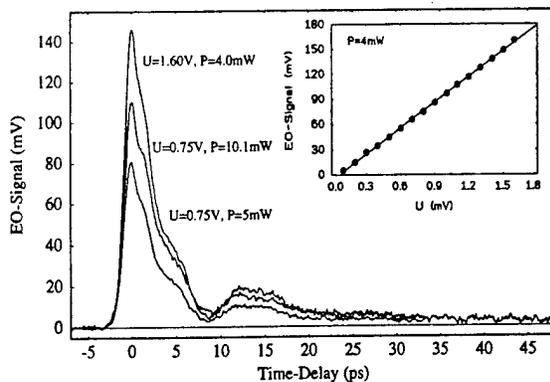
Additionally, we measure the response of the PC probe as a function of the amplitude of the electric transients on the DUT by varying the pump-beam intensity over two orders of magnitude (data not shown here, see [2]). The response of the PC probe reveals a linear dependence on the amplitude of the electric transients.
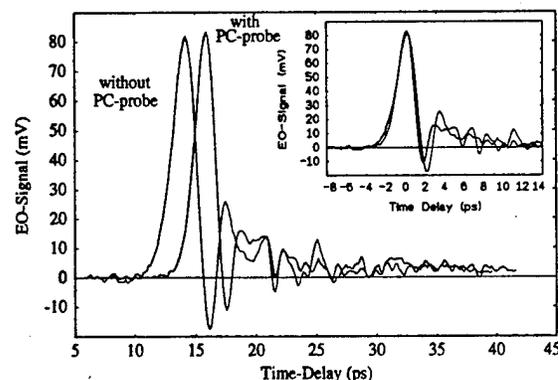
Fig. 3. Electro-optically detected electric pulses on a CPW with and without a PC probe in contact with the CPW. In the inset, the initial parts of the pulses are overlayed.

The invasiveness of our PC probes is investigated by measurements on a SOS CPW (one signal conductor surrounded by two ground conductors, conductor width: 60 μm,

spacing: 30 μm) with integrated PC switch. We detect the electric pulses generated on the CPW behind a point where the tip of a freely positionable probe is in full contact with the signal conductor of the CPW. The transients are traced electro-optically at a point 1.92 mm away from the excitation spot. Fig. 3 shows waveforms detected with and without the PC probe in contact with the CPW 0.73 mm away from the excitation spot. The amplitude of the electric pulse is not measurably affected when the PC probe is brought into contact with the signal conductor. Hence, reflection losses by the PC probe must be small (below the detection limit, i.e. ≤5-10 %). Although the probe apparently does not represent a significant inductive load of the CPW, a weak dielectric invasiveness modifying the effective refractive index of the CPW is found. This is evident in Fig. 3 from the shift of the peak by 1.6 ps towards longer delay times. The shift is explained with a 15-% increase of the refractive index of the CPW by the sapphire substate of the PC probe (substrate width: 1.33 mm). The dielectric invasiveness can be reduced strongly by a larger Ti tip height or by a smaller substrate width.

bring the PC probe into contact with the signal conductor of a 10-mm-long CPW fabricated on GaAs substrate. In contrast to the experiments presented above, the gap of the PC switch is biased and illuminated by the optical pump beam instead of the probe beam. The electric transients launched from the PC probe onto the CPW are detected via electro-optic sampling employing a $LiTaO_3$ crystal positioned onto the CPW approx. 300 μm away from the PC switch. Figure 4 depicts measured electric transients for various bias voltages (U) and average optical pump powers (P) on the PC probe. The amplitude of the generated electric pulses rises linearly with the bias voltage. A duration of the electric pulses of 3.3 ps (FWHM) is obtained. The amplitude of the transients is comparable to that of pulses launched directly from PC switches integrated into CPWs. These results illustrate that freely positionable PC switches can be used as efficient signal generators opening the way for all-photoconductive on-chip testing at any two electrically accessible points on a circuit without the need to integrate PC switches into the circuit.

REFERENCES

[1] J. Kim, S. Williamson, J. Nees, S.-I. Wakana, and J. Whitaker, Appl. Phys. Lett. **62**, 2268 (1993).

[2] T. Pfeifer, H.-M. Heiliger, E. Stein von Kamienski, H. G. Roskos, and H. Kurz, JOSA B (1994), Dec. issue.

[3] H. G. Roskos, Lithu. J. Phys. **34**, 175 (1994).

[4] D. H. Auston, "Picosecond Photoconductors", in Picosecond Optoelectronic Devices, C. H. Lee, ed., (Academic Press, Orlando, 1984), p.73-117.

Fig. 4. Electro-optically detected electric transients generated by a PC probe positioned onto a CPW. The power of the optical pump beam and the bias voltage applied to the PC probe are varied. Inset: Peak amplitude of the electric signals for various bias voltages and a constant pump power of 4 mW.

In a last experiment, we demonstrate that freely positionable PC probes are not only capable to detect but also to generate ps electric transients. For this purpose, we

Quantum Devices

JWB 10:30 am-12:00 m
Ballrooms VI-VIII

Jürgen Kühl, *Presider*
Max Planck Institute, Germany

Ultrafast All-Optical Switch with Switch-Off Time
Unlimited by Carrier Lifetime

K. Tajima and S. Nakamura
Optoelectronics Research Laboratories, NEC Corporation
34 Miyukigaoka, Tsukuba, Ibaraki 305, Japan
Phone +81-298-56-6125 Fax +81-298-56-6125

All-optical switches are expected to become one of key elements in future ultrafast and flexible all-optical communication networks. And it has been generally believed that such all-optical devices would require very fast, as well as very efficient, nonlinear optical material (or phenomena). In fact, the well-known and often discussed figure of merit for nonlinear materials [$n_2/(\alpha\tau)$, where n_2 is the nonlinear refractive index change coefficient, α is the linear absorbance, and τ is the relaxation time] implies that it is the chosen non-linear material that determines the basic device performance such as the switching speed and energy. In this paper, we show that this is not necessarily the case; the speed of a non-linear optical switch proposed by the authors[1,2] is not restricted by the slow relaxation time of high efficiency incoherent nonlinearities.

The proposed all-optical device is schematically illustrated in Fig. 1. This is similar to the well-known Mach-Zehnder (MZ) type device, but it differs in that it has nonlinear materials (waveguides) and control light injection ports in *both* arms. The nonlinear waveguides in both arms are identical. Thus, we call it symmetric Mach-Zehnder (SMZ) all-optical switch. Here we consider the usual case in which the control light photon energy is equal to or slightly lower than the band-gap energy of the nonlinear waveguides in order to efficiently generate photocarriers throughout the waveguides, while the signal light wave-length is much longer than the band-gap wavelength to achieve high transmission. The principle of operation of SMZ is as follows. The optical length of one arm of SMZ is modi-fied by the induced nonlinear refractive index change caused by the first control pulse (leading control pulse) so that the signal output is switched to the other output port (switch-on). If we allow the nonlinear waveguide to relax back to its initial state, then the signal is gradually switched back to the initial port, following carrier recombination, as in the usual MZ all-optical switches[3]. However if the other arm is excited by the second control pulse (trailing pulse) shortly after the first pulse, we expect that the effect of residual nonlinear refractive index change in the first arm to be canceled by that in the second arm. Thus ultra-fast switch-off can be achieved that is not restricted by the slow relaxation time of band-filling nonlinearity.

Experimental results are shown in Fig. 2. In this experiment, a pair of GaAs/AlGaAs waveguides with a core size of $0.5 \times 4 \times 500 \mu m$ are used. The signal and control pulse wavelengths are 900 and 875 nm, respectively. The control light pulse width is ~1.3 ps and the signal light is unmodulated CW light so that bare modulation characteristics of SMZ can be investigated. Fig. 2(a) shows an experimental result in which the time lag between the leading and trailing control pulses (or switching speed) is 56 ps. The square like modulation characteristic is evident. Here a nonlinear phase
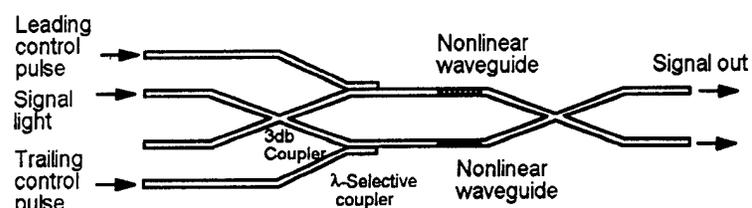

Fig. 1. The symmetric Mach-Zehnder all-optical switch.

shift of π (full switching) was achieved, which was verified by observing the characteristic periodic behavior of all-optical devices[3]. The control pulse energies required for full switching were 4 pJ for one waveguide and 7 pJ for the other, assuming a coupling efficiency of 10 %, estimated from a separate experiment. As the time lag is reduced to 6 ps, a faster switching speed of 8 ps was recorded, as shown in Fig. 2(b). Here the apparent modulation depth is less than 100 % and the square like modulation is no longer observed, because of the insufficient time resolution of the streak camera (~8 ps). Further increase in switching speed was only hindered by the time resolution, but clean square like modulation approaching 1 ps is expected to be possible.

In the above experiment, the control pulse repetition rate was only 82 MHz, allowing the nonlinear waveguides to relax back to the initial state before the next control pulse arrives. If , however, a series of high repetition control pulses are used, then the photocarriers become accumulated in the waveguides to a degree determined by the competition between the carrier generation rate and the carrier lifetime. The average carrier density would exceed 10^{18} /cm^3 for repetition rates greater than 40 GHz, assuming a carrier lifetime of 1 ns and device parameters already cited. Even with this high background carrier density, the switching energy is expected to stay in the same range, because the change in nonlinear refractive index per photogenerated carrier is known[4] to remain in the same range as in the case of low repetition operation ($\approx 3 \times 10^{16}$ / cm^3). Here we assumed the carrier lifetime to be 1 ns, but it is actually a function of carrier density; as the carrier density becomes higher, the recombination process becomes faster. Further, various techniques have been developed to effectively reduce the carrier lifetime. Thus the background density mentioned earlier is probably an overestimation and faster repetition rates should be achievable; that is, if we ignore thermal effects, better than a few hundred GHz is expected for a carrier lifetime of 100 ps, following the earlier discussion. We are now obtaining experimental result which supports these observations and the result will be presented at the conference. We note that this type of strategy for high repetition operation does not work with the normal Mach-Zehnder type all-optical switches.

In conclusion, we have shown that ultrafast switching is possible with the symmetric Mach-Zehnder type all-optical switch, that is not restricted by the slow relaxation time of high efficiency incoherent nonlinearities. A switching speed as fast as 1 ps is expected without sacrificing the high efficiency of band-filling nonlinearity. It is also theoretically shown that a very high repetition rate exceeding hundred GHz is possible.
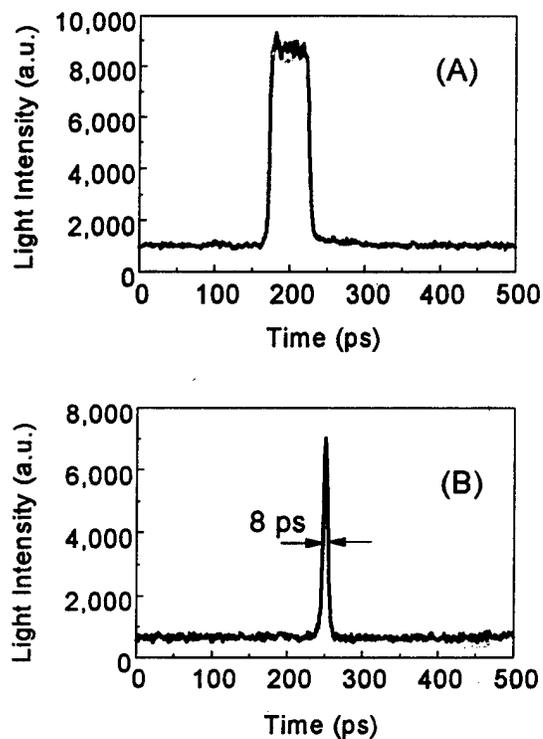
Fig.2. Switching Waveforms

[1] K. Tajima, Jpn. J. Appl. Phys. vol.32, p.L1749, (1993).

[2] S. Nakamura, K. Tajima, and Y. Sugimoto, Appl. Phys. Lett., vol.65, No.3, p.283, 1994.

[3] K. Tajima, S. Nakamura, N. Hamao, and Y. Sugimoto, Jpn. J. Appl. Phys. vol.33, pt. 1, no.1A, p. 144, (1994).

[4] Y. H. Lee, A. chavez-Pirson, S. W. Koch, H. M. Gibbs, S. H. Park, J. Morhange, A. Jeffery, N. Peyghambarian, L. Banyai, A. C. Gossard, and W. Wiegman, Phys. Rev. Lett. vol.57, p.2446, (1986).

QUANTUM CASCADE LASERS

F. Capasso and J. Faist

AT&T Bell Laboratories
Murray Hill, NJ 07974

The recently demonstrated quantum cascade laser is a fundamentally new semiconductor laser.[1-3] It relies on only one type of carrier (unipolar laser) and on quantum jumps of electrons between discrete conduction band energy levels of quantum wells. As such the wavelength can be tailored over a very wide range from the mid-ir (a few microns) to the far-ir (~100 μm) by simply varying layer thicknesses. Two types of quantum cascade lasers will be discussed. In the original structure the relevant intersubband radiative transition is between states centered in different neighboring wells to facilitate population inversion, i.e. the transition is *diagonal* (Fig. 1). In this design, however, the width of the luminescence transition is relatively broad (FWHM~22 meV) due to the interface roughness since electrons traverse several heterointerfaces in the photon emission process. As a consequence the peak gain is reduced. To circumvent this problem we designed the structure of Fig. 2 where electrons make a vertical radiative transition essentially in the same well. This reduces considerably the width of the gain spectrum (FWHM $\simeq$ 10 meV) and therefore the laser threshold current density. To prevent electron escape in the continuum, which is greatly reduced in the case of the diagonal transition, the superlattice of the digitally graded injector is designed to act as a Bragg reflector for electrons in the higher excited state and to simultaneously ensure swift electron escape from the lower states via a miniband facing the latter (Fig. 2). A crucial feature of both structures is that the lower state of the laser transition is separated by an optical phonon ($\simeq$ 30 meV) from the $n = 1$ state. This strongly enhances the scattering of electrons out of the $n = 2$ state. The calculated time is $\tau_{21} \simeq 0.6$ ps which is considerably less than the relaxation time between the $n = 3$ and $n = 2$ state (a few ps) thus creating the population inversion condition. Electrons can in turn tunnel out of the $n = 1$ state in a subpicosecond time to prevent electron build-up.

Quantum Cascade Laser with Diagonal Transition

The AlInAs/GaInAs structure grown by MBE comprises 25 stages, each consisting of a graded gap n-type injection layer and a three coupled-well active region, cladded by AlInAs waveguiding layers.[1-3] The undoped active region includes 0.8 nm and 3.5 nm thick GaInAs wells separated by 3.5 nm AlInAs barriers. 3.0 nm thick AlInAs barriers separate the active regions from the digitally graded n-type doped injectors ($\sim 10^{17}$ cm^{-3}). The samples were processed into mesa etched ridge waveguides and the laser facets were obtained by cleaving. Powers $\simeq$ 30 mW in pulsed operation for a 2.8 nm long device and $\simeq$ 6 mW for a 1.2 mm long device have been obtained at $\lambda = 4.3$ μm and at a heat sink temperature ~100 K. An outstanding feature of this laser is that the gain is much less sensitive to temperature than conventional semiconductor

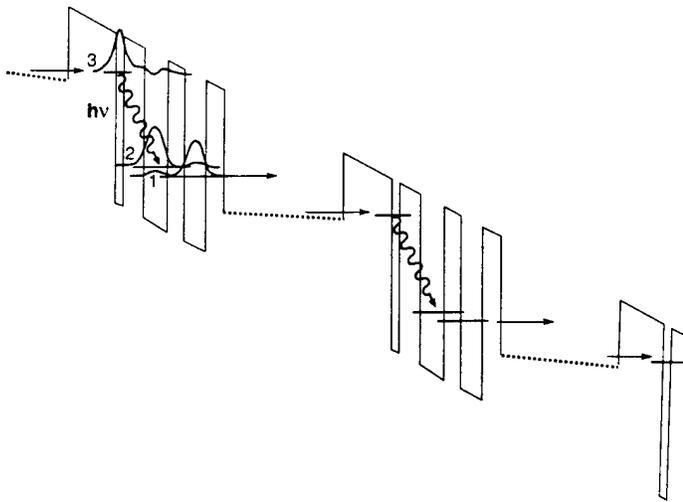Figure 1. Energy diagram of the QC laser under bias showing the diagonal laser transition (wavy arrow). $E_3 - E_2 = 295$ meV.

(a)

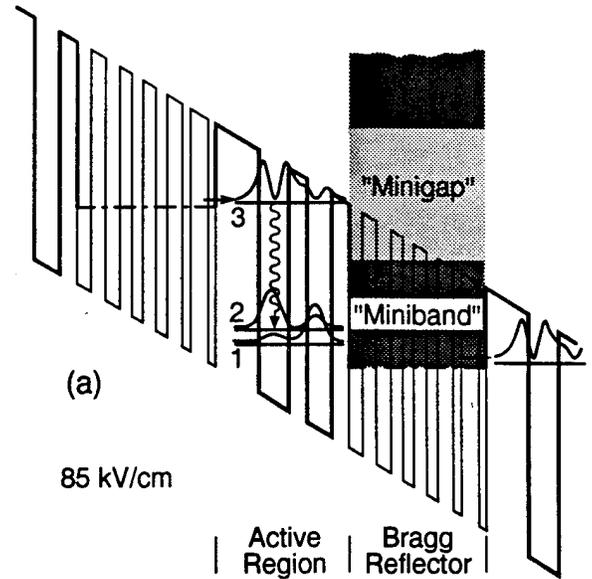85 kV/cm

| Active | Bragg |
| Region | Reflector |

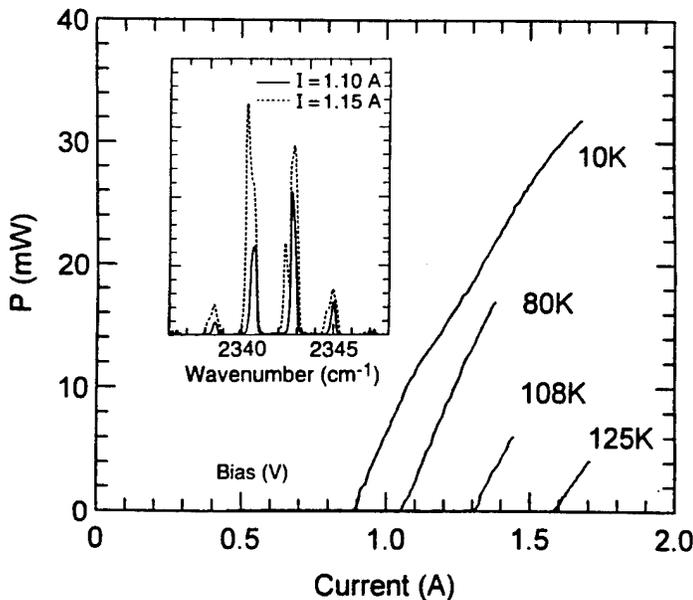Figure 2. Energy diagram of QC laser under bias showing the vertical laser transition (wavy arrow). $E_3 - E_2 = 271$ meV.

Figure 3. Peak optical power from a single facet vs. drive current for a 720 μm cavity length quantum cascade laser with diagonal transition at various heat sink temperatures. The inset shows the high resolution spectrum.
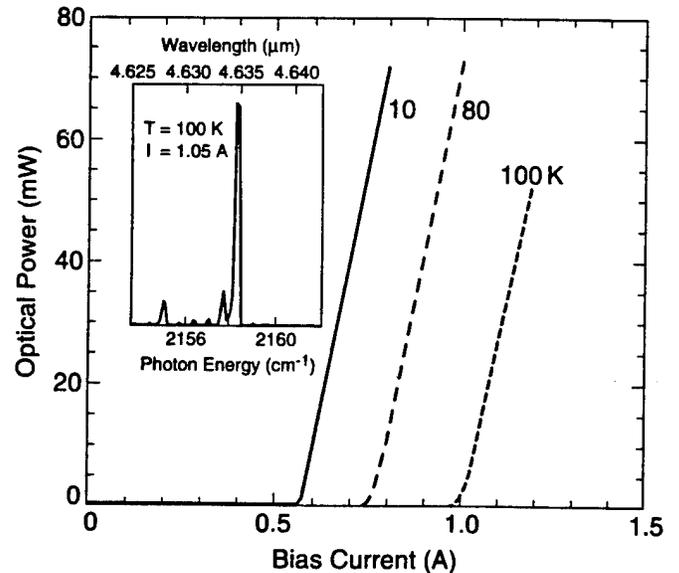
Figure 4. Peak optical output power from a single facet vs. drive current at various heat sink temperatures for the quantum cascade laser with vertical transition. The device is 2.4 mm long. Inset: high-resolution spectra of the sample above threshold.

lasers. The temperature dependence of the threshold indicates an exponential increase $\sim \exp(T/T_0)$ with a $T_0 = 110$ K (Fig. 3). Operating temperatures up to 125 K have been achieved with 5 mW of power (Fig. 3). The threshold is 7.7 kA/cm^2 at ~ 110 K and the measured slope efficiency ~ 50 mW/A per facet. The inset of Fig. 3 shows the high resolution spectrum at two different currents. Well defined longitudinal modes are observed. The mode spacing 2.16 cm^{-1} is in good agreement with the calculated one ($\frac{1}{2nL_{cav}} = 2.13$ cm^{-1} with n = 3.26). The linewidth of the dominant mode is presently limited by heating effects and mode hopping during the pulse. At higher currents an additional transverse mode emerge. The intrinsic linewidth of these lasers in cw single mode operation is expected to be Schawlow-Townes limited, similar to atomic lasers, without the linewidth enhancement factor typical of diode lasers.[1]

Quantum Cascade Laser with Vertical Transition

In this structure (Fig. 2) the 25 active regions consist of a 4.5 nm GaInAs wells coupled to a 3.6 nm well by a 2.8 nm AlInAs barrier. Tunneling injection into the active region is through a 6.5 nm AlInAs barrier and electrons escape out of the n = 1 state through a 3.0 nm AlInAs barrier. The superlattice well and barrier thicknesses are respectively $\ell_w = 2.1, 2.1, 1.6, 1.7, 1.3$ and 1.0 nm and $\ell_b = 2.1, 1.9, 2.0, 2.3$ and 2.7 nm in going from left to right in Fig. 2. The waveguiding cladding regions are similar to those of the diagonal transition structure. After processing, the samples were cleaved in $L_{cav} = 2.4 - 3$ mm length bars. Current pulses of 30 ns were injected in the device with a 20 kHz repetition rate. Fig. 4 displays the peak optical power versus drive current obtained by focusing the light with a f/0.8 optics on a fast HgCdTe detector. The peak optical power is ~ 80 mW at 80 K. The measured slope efficiency is 300 mW/A per facet and essentially temperature independent and corresponds to a differential quantum efficiency per period of 4.5×10^{-2} when corrected for the collection efficiency of the apparatus. The threshold density has a value $J_{th} = 6.7$ kA/cm^2 at 10 K and 3 kA/cm^2 at 100 K. The collaboration of C. Sirtori, D. L. Sivco, A. L. Hutchinson and A. Y. Cho is gratefully acknowledged.

REFERENCES

1. J. Faist, F. Capasso, D. L. Sivco, C. Sirtori, A. L. Hutchinson, and A. Y. Cho, Science, **264**, 553 (1994).
2. J. Faist, F. Capasso, D. L. Sivco, C. Sirtori, A. L. Hutchinson, and A. Y. Cho, Electron. Lett. **30**, 865 (1994).
3. J. Faist, F. Capasso, D. L. Sivco, A. L. Hutchinson, C. Sirtori, Sung N. G. Chu, and A. Y. Cho, Appl. Phys. Lett., Dec. 5, 1994 (in press).

Scaling of Stark-Shifted Nonlinearities in Multiple Quantum Well Structures

A. N. Cartwright, X. R. Huang and Arthur L. Smirl
Laboratory for Photonics and Quantum Electronics
100 IATL, University of Iowa, Iowa City, Iowa 52242
Tel. (319) 335-3460   Fax (319) 335-3462

Optical switching and logic devices require a large optical nonlinearity (absorptive or refractive) per absorbed photon (or injected charge), combined with a rapid excitation recovery time. The accumulated absorptive (or index) changes during a laser pulse are proportional to the shorter of either the pulse duration or the excitation lifetime. Optimally the two are matched, in which case the switching energy (power-time product) is determined primarily by the change in absorption coefficient (or refractive index) per photogenerated carrier-pair. Any mechanism, material or structure that will enhance the per-carrier nonlinear response is therefore of considerable interest. Device structures (such as self-electrooptic effect devices (SEED's), hetero n-i-p-i's, and piezoelectric multiple quantum wells (MQWs)) that rely on the screening of applied, built-in or intrinsic fields are purported to have large per carrier nonlinearities primarily because the carriers generated in a single well can escape and move to screen multiple wells. As a class, we refer to the nonlinearities in such structures as Stark-shifted nonlinearities, since they arise from a reduction in the quantum-confined Stark effect (QCSE) as the field is screened by the photogenerated charge.

Here, we present the results of an extensive experimental investigation and phenomenological theoretical treatment of the per carrier optical nonlinearity in a number of hetero n-i-p-i, SEED and piezoelectric MQW structures. We have investigated how this commonly used figure-of-merit scales with excitonic linewidth, excitonic amplitude, electric field and the number of wells. These studies included the dependence of the per carrier nonlinearity on temperature, on materials system and on sample structure. Moreover, they included structures in which the electric fields were externally applied, built-in and intrinsic. We demonstrate that a single simple expression will account for the scaling of the per carrier nonlinearity with each of the stated parameters. This expression gives us predictive capabilities when designing new structures.

In direct contrast to nonlinearities associated with saturation (or bleaching), a true per-carrier nonlinear cross section cannot be defined for Stark-shifted nonlinearities. However, under a restricted set of conditions (analogous to those necessary for defining a
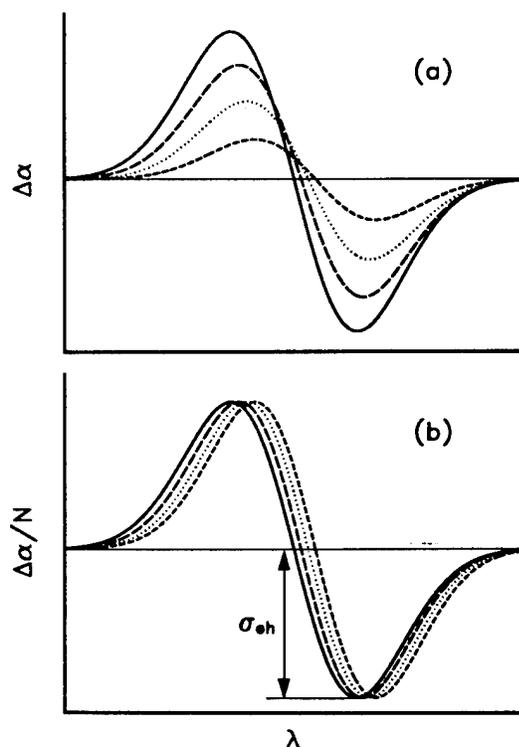

FIG. 1. (a) Change in absorption coefficient, and (b) the per-carrier change in absorption coefficient, $\Delta\alpha/N$, for a Stark-shifted nonlinearity.

bleaching cross section), a useful per carrier figure of merit, σ_{eh}, can be defined for Stark-shifting nonlinearities that obeys very simple scaling rules, as we shall demonstrate. The conditions necessary for defining σ_{eh} are that the photo-generated space-charge field must be small compared to the perpendicular field (whether it is applied, built-in or intrinsic), that each photo-generated carrier must escape the wells and move to screen the field, and that the area under the exciton must remain constant (e.g., bleaching is negligible). Under these conditions, the *peak* amplitude of the change in the absorption coefficient, $\Delta\alpha$, will increase linearly with incident fluence and, therefore, with the number density, N, of photoinjected electron-hole pairs in the well, as depicted in Fig. 1(a). Consequently, the blue shift will be small, and the spectra of the change in the absorption coefficient per carrier, $\Delta\alpha/N$, will have a constant amplitude and shape, but with a zero crossing that shifts linearly with excitation level, as shown in Fig. 1(b). It is this slight shift in the spectra as a function of carrier density that precludes the rigorous definition of a cross section that is constant for a given wavelength, as we do for bleaching. Nevertheless, we can still use the *peak* change in absorption coefficient per carrier as a measure of the strength of the nonlinearity:

$$\sigma_{eh}\,(peak) = \frac{\Delta\alpha_{peak}}{N}. \tag{1}$$

This figure of merit can be expected to obey simple empirical scaling laws, if the blue shift of the exciton (as the result of the screening of the QCSE) is represented as a shifted Lorentzian [1], or Gaussian [2] with amplitude α_0 and a halfwidth at half maximum of Γ_0. Under conditions for which σ_{eh} can be defined, the per carrier figure of merit will have the following form:

$$\sigma_{eh} = \pm \frac{q l_w C}{\varepsilon_s} \frac{m\alpha_0}{\Gamma_0} F(E_\perp)\,, \tag{2}$$

where q is the fundamental charge, m is the number of quantum wells in the intrinsic region, l_w is the width of the quantum well, ε_s is the dielectric constant of the material, $E_\perp$ is the perpendicular field (before screening), and C is a constant that depends on whether the lineshape is Lorentzian or Gaussian. The function $F(E_\perp) = E_\perp$ when the shift in wavelength from the zero field wavelength $\Delta\lambda(E_T) \propto E_T^2$, as it is in the low field limit, and $F(E_\perp) = 1$ when $\Delta\lambda(E_T) \propto E_T$, as it is in the high field limit [3], where $E_T = E_\perp - E_{sc}$ is the photogenerated space charge field.

The scaling of σ_{eh} with number of wells and excitonic amplitude and linewidth is illustrated in Fig. 2. For this demonstration, we measured σ_{eh} in seven separate structures by using a two
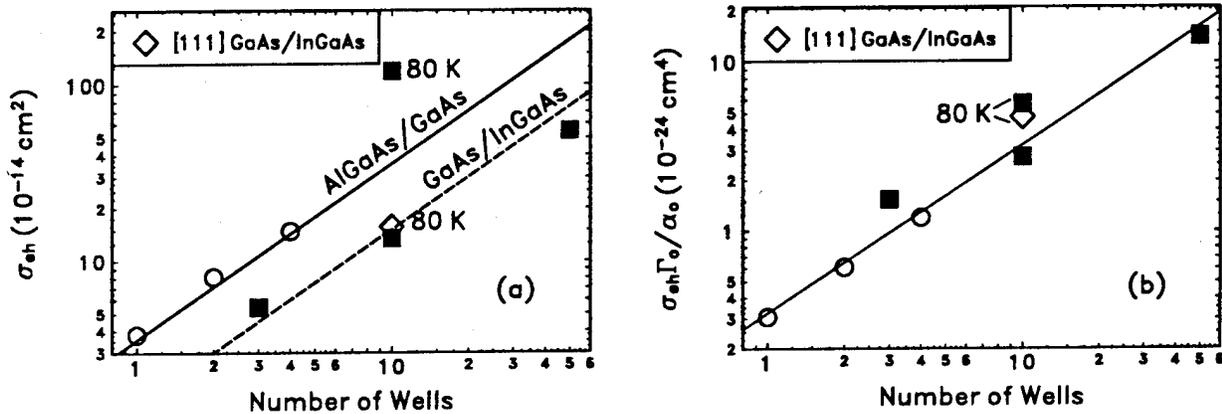

FIG. 2. (a) Measured per-carrier nonlinearity for seven separate structures at the same perpendicular electric field, and (b) the normalized quantity, $\sigma_{eh}\Gamma_0/\alpha_0$, as a function of the number of wells per intrinsic region.

color differential transmission technique. The measurements of the unscaled σ_{ch}'s are summarized in Fig. 2(a). All samples had approximately the same well widths and the same perpendicular fields. These samples included GaAs/AlGaAs hetero n-i-p-i's with 1, 2 and 4 wells per intrinsic region; an InGaAs/GaAs hetero n-i-p-i with 3 wells in the intrinsic region; an InGaAs/GaAs p-i-n MQW structure with 10 wells and one with 50; and a InGaAs piezoelectric MQW p-i-n structure grown in the [111] direction. All of the measurements were at 300 K, except for the two indicated. Notice that the unscaled σ_{ch}'s range over two decades and that they are consistently higher for AlGaAs/GaAs than for GaAs/InGaAs. Nevertheless, all of these σ_{ch}'s lie on a single straight line and are linearly proportional to the number of quantum wells per intrinsic region, as predicted by Eq. (2), when the normalized quantity $\sigma_{ch}\Gamma_o/\alpha_o$ is plotted as shown in Fig. 2(b)!
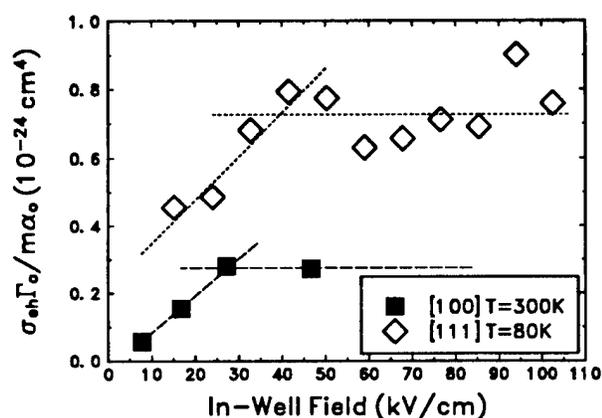
FIG. 3. The dependence of the normalized per-carrier nonlinearity on in-well field.

Finally, to demonstrate the scaling of σ_{ch} with electric field, we measured the σ_{ch}'s of a [100]-oriented InGaAs/GaAs p-i-n with 50 wells and a [111]-oriented InGaAs/GaAs piezoelectric p-i-n with 10 wells as a function of in-well field. For small in-well fields, we expect the shift in center wavelength to vary quadratically with field [$\Delta\lambda(E_T) \propto E_T^2$], and therefore, σ_{ch} should vary linearly with the field [i.e., $F(E_T) = E_T$]. When the normalized quantity $\sigma_{ch}\Gamma_o/m\alpha_0$, where m is the number of wells being screened, is plotted as shown in Fig. (3), the result is a straight line in both cases for in-well fields below ~40kV/cm. By contrast, for large in-well fields we would expect $\Delta\lambda(E_\perp) \propto E_\perp$ and σ_{ch} should be independent of field [i.e., $F(E_\perp) = 1$]. In this regime, the normalized quantity $\sigma_{ch}\Gamma_o/m\alpha_0$ should be a constant independent of field. This is confirmed by the data in Fig. 3.

In summary, we have confirmed the validity of a simple scaling expression that allows one to predictably adjust for changes in well number and electric field in the design of Stark-shifted nonlinear devices, and to predictably correct for operation at other temperatures and predictably scale for conversions between material systems. Moreover, these measurements illustrate that the per-carrier nonlinearity can be improved by optimizing the in-well bias field and by increasing the number of wells per intrinsic region; however, they also demonstrate that when the measured per-carrier nonlinearities are corrected for material quality and temperature (i.e., excitonic amplitude and linewidth) that the per-carrier response does not depend appreciably on material system or on whether the fields are externally-applied, built-in, or intrinsic.

References

1.   G. Lengyel, K. W. Jelley, R. W. H. Engelmann, IEEE *Journal of Quantum Electronics*, vol. 26, pp. 296-304, 1990.
2.   D. S. Chemla, D. A. B. Miller, P. W. Smith, A. C. Gossard, W. Wiegmann, IEEE *Journal of Quantum Electronics*, vol. 20, pp. 265-275, 1984.
3.   W. Chen and T. C. Andersson, Semicond. Sci. Technol. vol. 7, pp. 828-836, 1992.

Dynamic Wannier-Stark Effect and Superradiance Switching in Semiconductor Superlattices

J. B. Khurgin[a], S. J. Lee[a],
N. M. Lawandy[b], S. Li[c]

[a] Department of Electrical
and Computer Engineering
The Johns Hopkins University
Baltimore, MD 21218

[b] Division of Engineering
and Department of Physics
Brown University
Providence, RI 02912

[c] Dept. of Electrical Engineering
University of California
Los Angeles, CA 90024

Figure 1: Energy levels and bands in the SL without (a) and with (b) the optical field. 2a is the unit period of the SL.

We investigate the possibility of observing the transition between the localized states and the extended states in semiconductor superlattices (SL) in the presence of strong external ac field. i.e., the dynamic Wannier-Stark effect [1] and by switching of superradiance.

Let us consider the SL in Fig. 1a. The adjacent wells in this structure consist of materials with different bandgaps. This can be achieved by varying the Al mole fractions in $Al_xGa_{1-x}As$, for example. The SL parameters can be controlled so that the conduction band subbands are nearly in resonance while the valence band energy levels are well separated ($\Delta E_{v,12}^{(0)} \sim 50 meV$). When a strong optical field is applied (see Fig. 1b), the energy levels become "dressed" and the ac Stark effect moves conduction band energy level in well 1 by $(\mu_{cv}\mathcal{E})^2/\delta E$ and the level in well 2 by $(\mu_{cv}\mathcal{E})^2/(\delta E + \Delta E_{v,12} - \Delta E_{c,12}^{(0)})$ where $\mu_{cv} = e < r_{cv} >$ is the dipole matrix element, $\mathcal{E}$ is the optical field, and δE is the excitation detuning. The lower limit on detuning is put upon by absorption that might be caused by the miniband width and the line broadening. Since $\Delta E_{v,12}$ can be large, it is clear that the DWS shift of the level in well 2 is substantially larger than that in well 1. Thus, the energy level separation becomes wider and the miniband widths are substantially reduced, see Fig. 1b. Considering the miniband dispersion relation, as shown in Fig. 2, we see that the DWS effect results in a wider gap at $ka=\pi/2$ and a smaller miniband effective mass. Since the conductivity across the SL is decreased due to the optically-induced miniband effective mass change, a practical scheme to use this structure as an optical detector/switch can be considered.

In order to detect the effective mass change, we can apply a DC field to cause current flow in the SL growth direction. As long as the DC field is small enough not to cause energy level shifts, the Drude conductivity formula can be used. Then, the ac component of the current can be utilized in optical detection in a waveguide whereby the responsivity can be expressed as

$$R = \frac{16\pi\alpha_0}{15\sqrt{3}}Na < r_{cv} >^2 \frac{e\tau}{\hbar}V$$
$$\times \left(\frac{1}{\delta E} - \frac{1}{\delta E + \Delta E_{v,12}}\right)\left(\frac{L}{T}\right)$$

where α_0 is the fine structure constant, L(T) is the waveguide length (thickness), V is the interwell coupling energy, N is the density of conduction electrons, and τ is the momentum

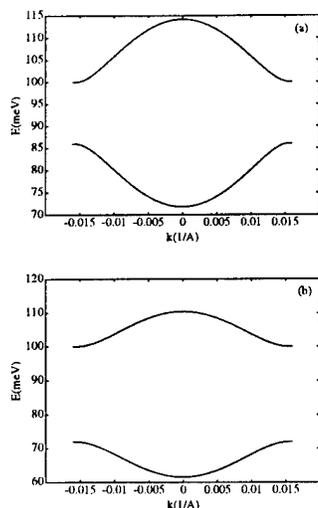Figure 2: Miniband structure with (a) and without (b) the optical field. Note that the field increase the energy gap at $ka = \pi/2$.

Figure 3: (a) Superlattice (SL) with minibands of width 4V. (b) SL with Q > V. Excitons are confined in well regions, but are free to move around in the structure. (c) SL with $F \neq 0$. Exciton are confined in a single well.

relaxation time. The dimensional factors enter only when the light propagates along the interface. When the L/T ratio is equal to 1000, R can be as high as 0.1 A/W, a figure similar to that of a photodiode. Since no light absorption is involved in the process, the DWS detection scheme is suitable for nondemolition measurement. Compared to the "virtual conductivity" scheme [2], far greater responsivity can be obtained in the DWS scheme where the energy is supplied by the DC source [3]. Compared to the quantum wire interferometer method [4], the DWS device seems far easier to implement due to the confinement necessary in one direction and less stringent requirement of electron coherence. Also, using a differential scheme allows substantially reduction of the noise in this device by cancelling out the dc component.

Recently, excitonic superradiant decay in semiconductor quantum wells (QW) has been studied by a number of researchers [5] and

verified experimentally by fast radiative lifetimes obtained in a single GaAs quantum well ($\sim$ 10ps.) under the resonant excitation conditions [6].

In this study, we investigate spontaneous emission properties of the excitonic states in the superlattice (SL) undergoing the Wannier-Stark (WS) transition in the presence of external electric field. In a SL (Fig. 3a), as the period(barrier) increases, the Coulombic attraction energy between the electrons and holes becomes greater than the interwell coupling energy, V. As a result, the wannier exciton in the z-direction becomes Frenkel excitons, indicating that *an electron and an hole are always in the same well, but it is not known in which one* (see Fig. 3b) The oscillator strength (OS) of the exciton then becomes $f_x = N f_o \phi_r^2(0)$ where N is the number of periods and $\phi_r(0)$ the in-plane part of the excitonic wavefunction. We see that there are two enhancement factors - ϕ_r^2 due to the formation of Wannier exciton in the parallel plane and N due to Frenkel exciton in the z direction.

When an electric field F larger than V is applied, the exciton wavefunction gets localized in *one particular* well, with no coherent coupling between adjacent states. Thus, the system can be described by N separate WS ladder wavefunctions, The OS of each state is $f_{WS} = f_0 \phi_r^2(0)$. The total OS of N states in the WS ladder is equal to the OS of the
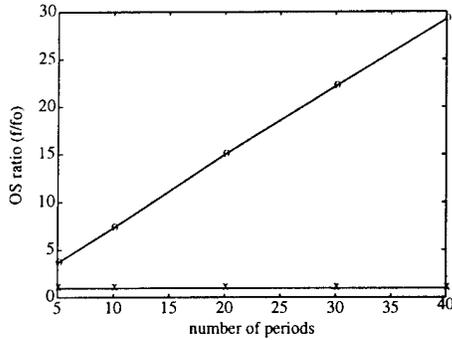
Figure 4: Oscillator strength ratio (f/f_o) vs. number of periods for a barrier width of 50 Å. f denotes the case where the Coulomb attraction is considered and f_0 the case where the Coulomb attraction is neglected. (a) no external bias (b) external bias applied.

superradiant state, indicating that the absorption strength is preserved, but for each particular state the superradiance enhancement is completely gone, thereby slowing down the radiative decay of the WS ladder states by a factor of N. Therefore, a sudden imposition of a relatively weak external field can cause large increase in the radiative lifetime of the SL, opening the possibility of modulating the spontaneous emission in SLs on a picosecond scale, far more efficient than switching of the OS in a single QW [7].

Our calculations are based on the linear combination of 1s exciton states with a single well basis [8] and on the tight-binding method in the non-zero field case for the WS ladder [9]. Fig. 4 shows the OS enhancement ratio after the excitonic effect is considered for both $F = 0$ and $F \neq 0$ cases. It is easily seen that both longitudinal and transverse excitonic components increase the OS dramatically as a linear function of N.

In practice, the enhancement is limited by the SL coherence length, l_c which depends on the presence of scattering mechanisms and factors such as temperature and sample quality. Since the calculated and measured single well decay time is ~ 20 ps. [10], the corresponding value for the SL should be of the order of Thus, aside from observing direct modulation of spontaneous emission by electric field, the enhancement factor could provide a useful measure of the coherence length in SL's.

References

1. R. W. Boyd and M. Sargent III, J. Opt. Soc. Am. B. **5**, 99 (1988).
2. E. Yablonovich, et. al., Phys. Rev. Lett. **62**, 28 (1989).
3. A. Shimizu and M. Yamanishi, Phys. Rev. Lett. **72**, 3343 (1994).
4. A. Shimizu, K. Fujii, and M. Okuda, Phys. Rev. B **40**, 1357 (1989).
5. Eiichi Hanamura, Phys. Rev. B. **38**, 1228 (1988).
6. B. Deveaud, et. al., Surf. Sci. **263**, 491 (1992).
7. I. Suemune, T. Takoka, M. Yamanishi and Y. Lee, IEEE J. **QE-22**, 1900 (1988).
8. S. Li and J. B. Khurgin, Phys. Rev. B **46**, 12535 (1992).
9. J. Bleuse, G. Bastard, and P. Voisin, Phys. Rev. Lett. **60**, 220 (1988).
10. L. C. Andreani, Solid State Commun. **77**, 641 (1991).

Novel Spectroscopies of Quantum Systems

QWA   1:30 pm-3:00 pm
Ballrooms VI-VIII

John Ryan, *Presider*
Oxford University, U.K.

Femtosecond Near-field Spin Spectroscopy in Digital Magnetic Heterostructures

J.Levy, V.Nikitin, J.M.Kikkawa, and D.D.Awschalom
Department of Physics, University of California Santa Barbara, CA 93106
tel. (805) 893-7215   FAX (805) 893-4170
E-mail: jlevy@lotemp.physics.ucsb.edu

R.Garcia, and N.Samarath
*Department of Physics, The Pennsylvania State Univer*sity, University Park, PA 16802
tel. (814) 863-0136   FAX (814) 865-3604

The nature of electronic spin-scattering is central to a wide class of condensed matter systems, ranging from semiconductor quantum wells, magnetic multilayers and granular materials, high-Tc superconductors, Kondo insulators, and magnetic semiconductor quantum structures. The latter class of systems is particularly appealing because one can tailor both the electronic and magnetic properties using MBE techniques. Time-resolved spectroscopies allow one to probe both the electronic and magnetic dynamics within ultrafast timescales, but spatial information is typically diffraction-limited to the wavelength of light. Near-field scanning optical microscopy (NSOM) [1] overcomes this limit, and when combined with femtosecond time resolution and polarization analysis, provides direct information regarding carrier and spin dynamics in both space and time.

For these studies, a new class of MBE-grown semiconductor heterostructures is developed in which magnetic Mn ions are "digitally" introduced in equally spaced MnSe planes within a 120Å wide ZnSe/ZnCdSe quantum well. A strong sp-d exchange interaction between photoexcited electron-hole pairs in the well and paramagnetically aligned S=5/2 Mn$^+$ spins gives rise to anomalously large Zeeman splittings in modest magnetic fields (g_{eff} ~500 at T=4K) [2]. These new structures result in a field-tunable two-level spin system well-suited for exploring spin-dependent electronic interactions.

To investigate the role of defects on spin scattering, localized lattice damage is introduced by implanting samples with 140keV Ga$^+$ ions using a focused ion beam (FIB). A sample patterned with orthogonal stripes, alternatively 300nm and 600nm wide, and separated by 2μm was used for near-field polarization-resolved DC luminescence measurements in the B=0.2T magnetic field at T=5K. As shown in Fig. 1(a), upon excitation with HeCd laser (E=2.805eV) the luminescence intensity detected at E=2.638eV exhibits maxima in the centers of the intrinsic regions and gradually drops down, extending into the implanted areas. The decrease of the luminescence intensity in the implanted regions is attributed to damage-induced non-radiative channels for carrier recombination. The luminescence intensity in the intrinsic regions begins to drop almost 1μm away from the implanted lines. Fig. 1(b) shows the spatially-resolved polarization, $P=(I_+-I_-)/(I_++I_-)$,

where I_+ (I_-) is the luminescence intensity from recombining lower (higher) energy spin down (up) excitons. In marked contrast to the luminescence intensity, the polarization exhibits sharp features at the boundaries between implanted and intrinsic regions.
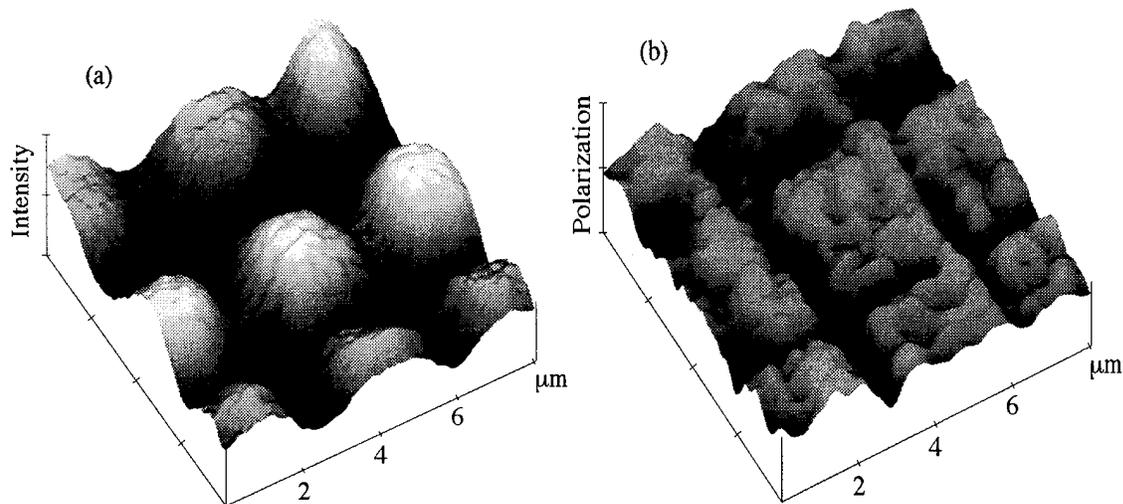

Fig. 1. (a) Spatially-resolved luminescence from a patterned magnetically-doped semiconductor quantum well at B=0.2 T and T=5.0 K, obtained using near-field scanning optical microscopy. Intensity minima appear in the ion implanted regions due to increased nonradiative relaxation channels. (b) Spatially-resolved polarization images show sharp decrease of polarization in the implanted areas.

This difference in profile across the interfaces suggests that spin-scattering in the intrinsic regions is not significantly altered by nearby implanted lattice defects, or by carrier diffusion into implanted regions. However, in order to confirm this picture one must look in the time domain. To investigate the radiative recombination dynamics, the luminescence intensity correlation [3] measurements were performed on a structure patterned with a sequence of parallel stripes of width 800nm, 400nm, 200nm and 100nm, spaced 2μm apart. These measurements yield information about the exciton time-correlation function $G^{(2)}_{ex}=<n_{ex}(\tau)n_{ex}(0)>$. Fig. 2(a) shows the luminescence intensity correlation as a function of both position and time delay τ, with notable differences between implanted and intrinsic
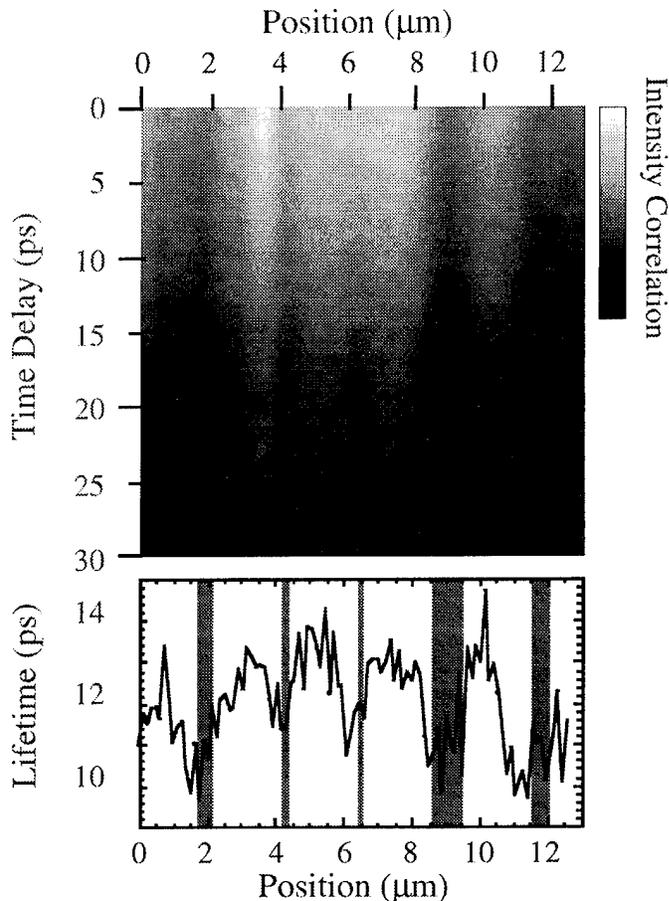
Fig. 2(a) Luminescence intensity correlation as a function of position and time delay τ. (b) Spatially-resolved carrier lifetime extracted from exponential fits.

regions. A carrier lifetime is extracted from an exponential fit to the data at the various positions, and is shown in Fig. 2(b). The lifetime in the implanted regions is reduced compared to the intrinsic regions, dropping to the minima in the middle of the widest implanted area. However, the decrease in lifetime is not sufficient to account for the decrease in luminescence intensity.

In summary, we demonstrate the unique capability of near-field time resolved spectroscopy for the studies of spin-polarized carrier dynamics in quantum semiconductor hetero-structures containing magnetic moments.

References

1. E.Betzig *et al.*, Science 251, 1468 (1991).
2. S.A. Crooker *et al.*, submitted for publication
3. A. Olson *et al,* Appl.Phys.Lett., 41(7) 1982

Near-field optical characterization of quantum wells and nanostructures

Harald F. Hess
AT&T Bell Laboratories
101 Crawfords Corner Road
Holmdel, NJ 07733

A spatial distribution of luminescent centers with sharp (<0.1meV), spectrally distinct emission lines are revealed in a GaAs/AlGaAs quantum wells[1] using low temperature near-field scanning optical microscopy[2], a technique where a subwavelength source and/or detector of light in close proximity (<40nm) to the sample is used to probe with a resolution beyond the diffraction limit. These centers are the energy eigenstate components that comprise the inhomogeneously broadened line shape observed in standard far-field photoluminescence. Measurements as a function of temperature, magnetic field, and well width establish that these centers arise from excitons localized by quantum well thickness fluctuations. For sufficiently narrow wells, virtually all emission originates from such centers. Quantities such as diffusion (both thermal and tunneling), lateral confinement energies, lifetimes, g-factors from magnetic field induced spin splittings, diamagnetic energy coefficients of the luminescent states can now be measured at a site-by-site individual quantum level rather than averaged over a statistical distribution. This information can be used in turn to provide a direct local picture of the interface fluctuations and how they vary under different MBE growth conditions. Near-field microscopy/spectroscopy provides a means to access energies and homogeneous line widths for the individual eigenstates of these centers, and thus allows the luminescent components to be identified and characterized with the extraordinary detail previously limited to the realm of atomic physics.

1. H. F. Hess, E. Betzig, T. D. Harris, L. N. Pfeiffer, and K. W. West, Science 264, 1740 (1194).
2. E. Betzig and J. K. Trautman, Science 257, 189 (1992).

Quantum Mechanical Capacitance in a Scanning Tunneling Microscope

D. Botkin[1] S. Weiss[2], D.F. Ogletree[2] M. Salmeron[2] and D.S. Chemla[1,2]

[1]Department of Physics, University of California at Berkeley, Berkeley, CA 94720

[2]Materials Sciences Division, MS 2-300, Lawrence Berkeley Laboratory. Berkeley, CA 94720

One of the most spectacular manifestations of quantum mechanics is tunneling between closely spaced conductors. The DC I-V characteristics in different types of tunnel junctions, such as metal-vacuum-metal junctions (MVM), metal-insulator-metal junctions (MIM), Josephson junctions, and quantum point contacts in a two dimensional electron gas, are well understood. High frequency transport in these systems is much less understood, and has been the subject of intense research in recent years[1,2].

The recently developed ultrafast scanning tunneling microscope (USTM) [3] is an ideal tool for the study of high frequency transport in the MVM or MIM system in a cross-sectional area on the order of 1 nm^2. In the USTM, an ultrafast photoconductive switch integrated with a scanning tunneling microscope (STM) tip assembly provides an ultrafast gate which temporally resolves the tunneling current. A "pump" laser pulse generates the surface excitation to be studied, and a "probe" laser pulse opens the sampling gate. An intriguing application of the USTM is the creation of movies of surface dynamics. At a fixed time delay between laser pulses, the tip can scan the surface, creating a snapshot of an ultrafast process. Such snapshots, viewed in succession, form a movie of surface dynamics. Before one can attempt to form movies, however, the USTM's response at a single point must be understood.

In what follows, we present experimental measurements of the high frequency response of the tunneling junction of a STM operating in air at room temperature. The tunnel junction is formed between the tip of the STM and the metallic surface of one strip of a coplanar transmission line on the sample. The STM tip position is fixed above a single point on the sample. A laser generates a picosecond voltage pulse on the transmission line, and the resulting tunnel current is monitored in time. The impedance of the tunneling gap can be deduced from the lineshape of the time-resolved tunnel current.

A typical signal measured by the USTM consists of a small AC component which varies with time delay and rides on a large DC background. The background is simply the DC tunneling current used for feedback, determined by the DC bias voltage and gap resistance. Fig 1a shows a 4.5 ps wide tunneling response to a 1 ps excitation pulse on the transmission line. The 10% to 90% rise time is 2 ps. The signal can also be measured while the tip is in ohmic contact, or crashed, with the sample. A typical crashed trace is shown in Fig. 1b. The time-resolved signal appears qualitatively different from the ohmic trace. In fact, the time-resolved signal's close resemblence to the derivative of the ohmic signal, shown in Fig. 1c., suggests that the tunnel junction has a partially capacitive response. However, the magnitude and the tip-sample separation dependence of this capacitive response are very different from that expected for the geometrical capacitance of the junction.

To better quantify the tunneling capacitance, we model the tunnel junction as a resistor, R_t, and a capacitor, C_t, in parallel. With the approximations: (1) that the RC discharge time of the circuit is smaller than the voltage pulsewidth, and (2). that the temporal width of the on cycle of the photoconductive switch is smaller than the voltage pulsewidth, we find that the time resolved signal is given by:

$$S(\tau) \propto S_{cr}(\tau) + T_t \cdot S_{cr}'(\tau) \qquad (1)$$

where $T_t = R_t C_t$ and $S_{cr}(\tau)$ is the crashed response. Eq. (1) states that the time resolved tunnel current can be fitted to $S_{cr}(\tau)$ and its derivative in time delay $S_{cr}'(\tau)$ with a single fitting parameter $T_t = R_t C_t$. This parameter has the dimensions of time delay, and is defined as the tunnel junction RC time constant. Since the tunneling gap resistance is known from DC measurements, we can extract the gap capacitance from the fitting parameter.

Fig. 2 is an example of such a fit. The solid line is the data of Fig. 1a. The fit (gray line) is obtained, according to Eq. (1), from the crashed signal data of Fig. 1b and its derivative in τ. The tunneling capacitance extracted from the fit in Fig. 2 is $C_t = 6.7 \cdot 10^{-19}$ F. In a variety of measurements, we find C_ts varying from 10^{-19} to 10^{-21}F. In contrast, the geometrical tip-sample capacitance is estimated to be larger than 10^{-15} F, even when the radius of curvature of the tip is as small as 1000 Å. The geometrical capacitance of the tip structure measured by conventional means at 20 kHz is 10^{-13} F.

The dependence of C_t on tip-sample separation offers additional insight into the origin of this capacitance. This dependence is measured by retracting the tip and recording the time resolved tunnel current for different tip heights. In Fig. 3, we plot the extracted capacitance for three sets of measurements, each set taken with different combinations of tip and sample metallization or different excitation geometry, as a function of the tunneling gap conductance, G_t. We would prefer to plot C_t as a function of the tip-sample separation, or barrier width, d.
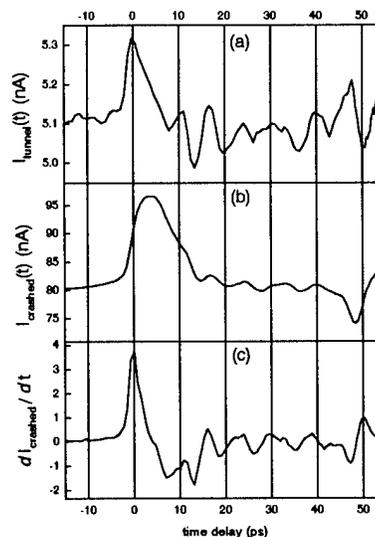
Fig. 1. Time resolved current cross-correlation detected on the tip: (a) in tunneling range (5nA and 80mV settings), and (b) when the tip is crashed into the sample. (c) is the time derivative of (b).
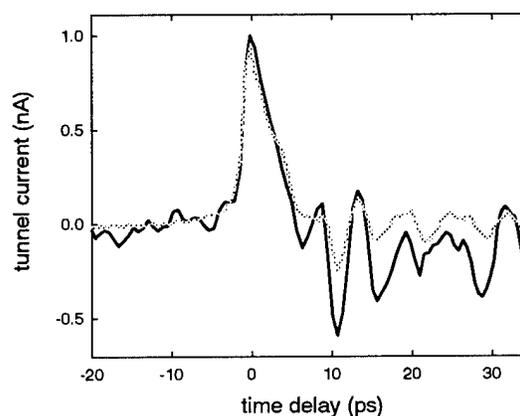
Fig. 2: Fit (solid gray line) to the time resolved data (solid black line) with the ohmic contact signal

However, in ambient conditions, the apparent inverse decay length and apparent barrier width is very different from a clean MVM junction, while the true inverse decay length is still represented by G_t. We find that the tunnel gap time constant, $RC = CG^{-1}$, depends only weakly on the barrier width. Since $G_t = G_0 e^{-\alpha(d-d_0)}$, where α is the inverse decay length, and G_0 is the conductance at a reference barrier width d_0 [4], the measured capacitance must vary as $C_t \propto e^{-\alpha(d-d_0)}$; in contrast, the geometrical capacitance can decrease no more rapidly than 1/d.

We conclude from the above discussion that (1) the time resolved tunnel current has a large capacitive component which originates from the tunneling itself, (2) the extracted capacitance is very small and is not the geometrical capacitance of the junction and (3) the capacitance varies exponentially with barrier width. Therefore, the capacitance has a quantum mechanical origin.

Experimental evidence of quantum reactance in the quasiparticle current in Josephson junctions [1] and in quantum point contacts in two dimensional electron gas systems [2] has been demonstrated only very recently. In both cases, the reactance is explained by the theory of photon assisted tunneling (PAT) [5] as originating from virtual transitions between the two electrodes of the junction. According to the PAT theory, the reactance can be derived from the DC I-V relation by a Kramers-Kroning (K-K) transformation. Since the DC response varies exponentially with tip height, a K-K transformation will preserve this exponential dependence, in accordance with experimental

Fig. 3 Junction capacitance vs. conductance. Data represented by circles taken with brass tip on Au sample. Data represented by diamonds or triangles taken with Pt-Rh tip on Al sample.

observations. Preliminary calculations indicate that the magnitude of the PAT capacitance is comparable to our results. An additional contribution to the quantum reactance can arise from the "electrochemical capacitance" [6] which originates from incomplete screening of the electric field in the metal.

References:

[1] Q. Hu, C.A. Mears, P.L. Richards and F.L. Floyd. Phys. Rev. Lett. **64**, 2945 (1990) and A.H. Worsham, N.G. Ugras, D. Winkler, D.E. Prober, N.R. Erickson and P.F. Goldsmith, Phys. Rev. Lett. **67**, 3034 (1991).

[2] L.P. Kouwenhoven, S. Jauhar, J. Orenstein, P.L. McEuen, Y. Nagamune, J. Motohisa and H. Sakaki, to appear in Phys. Rev. Lett.

[3] S. Weiss, D.F. Ogletree, D. Botkin, M. Salmeron and D.S. Chemla, Appl. Phys. Lett. **63**, 2567 (1993).

[4] J.G. Simmons, J. Appl. Phys. **34**, 1793 (1963).

[5] R. Tucker, IEEE J. Quantum Electron. **QE-15**, 1234 (1979).

[6] M. Büttiker, J. Phys.: Condens. Matter **5**, 9361 (1993).

Photon-Assisted Tunneling through a Quantum Dot

S. Jauhar, J. Orenstein, and P. L. McEuen
Department of Physics, University of California at Berkeley, and Materials Science Division, Lawrence Berkeley Laboratory, Mail stop 2-300, Berkeley, CA 94720

L.P. Kouwenhoven
Department of Applied Physics, Delft University of Technology, 2600 GA Delft, The Netherlands

Y. Nagamune, J. Motohisa[†], and H. Sakaki
Research Center for Advanced Science and Technology, University of Tokyo
4-6-1 Komaba, Meguro-ku, Tokyo 153, Japan

Tel: *(510) 486-5879*
Fax: *(510) 486-5996*

It is now possible to confine electrons in all three dimensions in semiconductors, resulting in the formation of what is commonly called a quantum dot. Electrons in these dots exhibit striking classical and quantum effects. Because of their small size, quantum dots have low capacitance C, which leads to a non-negligible electrostatic energy change upon addition or subtraction of an electron from a dot. This energy e^2/C, typically 0.5 meV, suppresses fluctuations in electron number, allowing for the controlled addition of electrons to the dot by applying a voltage to a gate electrode. Measuring the current through the dot as a function of this gate voltage results in observation of highly regular current peaks, the so-called classical Coulomb Blockade oscillations. As the electrons are completely localized, the energy spacing between levels in a dot may also be relevant. If this energy $\Delta\varepsilon$ is comparable to e^2/C, features may be present in the current due to these so-called 0D states. The interplay between the classical Coulomb Blockade and the quantum states of a dot has been extensively studied by dc transport measurements [1].

The behavior of electrons tunneling through a dot in the presence of an oscillating potential $\tilde{V}\cos(2\pi ft)$ has motivated a spate of recent theoretical work [2,3]. The cornerstone of all of this work is that an oscillating potential can induce an electron to absorb and emit energy quanta hf. Thus, an electron in an initial state of energy ε_i can tunnel through an oscillating barrier to a final state of energy ε_f, where $\varepsilon_f - \varepsilon_i = nhf$ and the integer $n \sim e\tilde{V}/hf$. This photon-assisted tunneling process requires that the applied frequency $f \gg \Gamma$, where Γ is the tunneling rate through the barrier. If $f < \Gamma$, the energies in the dot are only adiabatically modulated. Additionally, we require $e\tilde{V} \sim hf \gg kT$, so that the ac voltage amplitude is strong enough to induce single photon absorption and the temperature is low enough to be able to observe it.

In order to observe photon-assisted tunneling, we have measured the current through a quantum dot while coupling microwave frequencies between 0 and 40 GHz to the dot. A schematic of the experimental apparatus is shown in Fig. 1. The dot is defined by applying negative voltages to two metallic gates deposited over a 0.8 μm-wide wire etched in a GaAs/AlGaAs heterostructure. The two-dimensional electron gas (2DEG) of this heterostructure has a mobility

Fig. 1. Schematic of the apparatus used to couple microwaves to the quantum dot.

of about $10^6 cm^2/Vs$ and an electron density of $3.3 \cdot 10^{15}$ m^{-2} after illumination at 4 K. The device is placed in a dilution refrigerator with a base temperature of 30 mK, and all measurements above 1 GHz are taken with a perpendicularly applied magnetic field of 3.35 T, which corresponds to a filling factor of 4 in the wide 2DEG regions of the device.

We first show, in Fig. 2, the effect of a 10 MHz rf wave on the Coulomb oscillations of the dot. We notice that the peaks broaden as the ac amplitude is increased. This is in excellent agreement with the dashed curves, which are calculated by applying a sinusoidal modulation to the gate voltage of the

unpumped oscillations. As f $\ll$ Γ at 10 MHz, this is precisely the regime where we expect only quasi-static modulation of the dot energies.

Fig. 2. Coulomb oscillations measured while coupling a 10 MHz rf wave to the dot. The dashed curves are calculated.

At much higher frequencies, we find dramatically different behavior. In Fig. 3a, we show a similar set of measurements at three different frequencies of 17, 27, and 36 GHz. Each current peak exhibits a shoulder to the left side. This shoulder is independent of microwave power, and its position shifts to the left as the frequency is increased. This is made clearer in Fig. 3b, in which the

Fig. 3. (a) Current I versus gate voltage V_g on gate 1 at three different frequencies. Dashed curve is without microwaves and solid curves are for increasing power. (b) Derivatives $\partial I/\partial V_g$ of the curves shown in (a). Arrows indicate the photon-induced maxima. Different data sets are offset for clarity.

derivative with respect to gate voltage of each peak is shown. The derivatives of the shoulders yield mini-peaks, and these mini-peaks clearly shift with frequency.

We pool our measurements at applied frequencies between 9 and 36 GHz to produce Fig. 4. In this figure we plot versus the applied photon energy the difference in gate voltage (normalized, to convert it to an energy) between the microwave-induced mini-peaks and the centers of three Coulomb oscillations. The solid line is a linear fit to the points corresponding to the Coulomb peak centered at -31 mV. We find very clearly that the difference ΔV_g^{hf} converted into energy varies linearly with applied frequency.

This linear scaling conclusively demonstrates that photon-assisted tunneling is the origin of the microwave-induced features in the current. To further support this conclusion, we have calculated the response of a typical current peak to 27 GHz microwaves using a model that encompasses photon-assisted tunneling within standard Coulomb Blockade theory[2]. This model has successfully reproduced the shapes of the current peaks in Fig. 3[4].
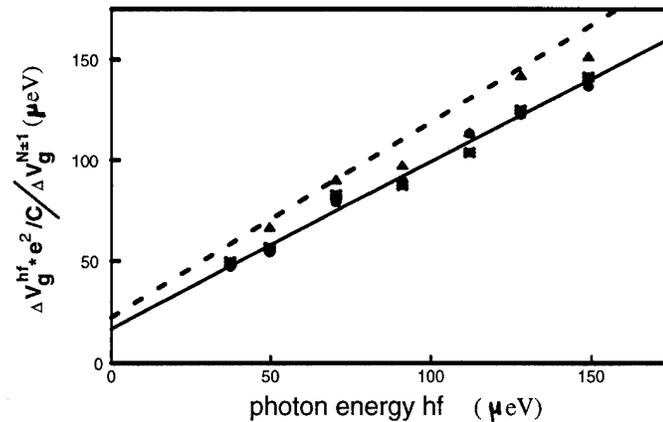
Figure 4. Horizontal axis: Photon energy hf. Vertical axis: ΔV_g^{hf} (properly normalized) is the energy difference between the location of the photon-induced maxima (i.e. arrows in Fig. 3(b)) and the zero-crossing of the dashed curve (without microwaves). ΔV_g^{hf} is determined for 3 different Coulomb peaks (▲ is centered around V_g = -36 mV, ● around -31 mV, and ✳ around -28 mV) from 9 GHz to 36 GHz. The solid line is a fit through the ● points. The dotted line is calculated using the model in Ref. [2].

References:

[1] See for reviews of Coulomb blockade: D.V. Averin and K.K. Likharev, in *Mesoscopic Phenomena in Solids*, edited by B.L. Altshuler et al. (Elsevier, Amsterdam, 1991); and *Single Charge Tunneling*, edited by H. Grabert and M.H. Devoret (Plenum, New York, 1992). See for a collection of quantum dot papers, *The Physics of Few-Electron Nanostructures*, edited by L.J. Geerligs et al. [Physica B **189** (1993)].

[2] L. P. Kouwenhoven, S. Jauhar, K. McCormick, D. Dixon, P. L. McEuen, Yu. V. Nazarov, N. C. van der Vaart, and C.T. Foxon, Phys. Rev. B **50**, 2019 (1994).

[3] M. Büttiker and R. Landauer, Phys. Rev. Lett. **49**, 1739 (1982); P. Johansson, Phys. Rev. B **41**, 9892 (1990); C. Bruder and H. Schoeller, Phys. Rev. Lett. **72**, 1076 (1994).

[4] L. P. Kouwenhoven, S. Jauhar, J. Orenstein, P. L. McEuen, Y. Nagamune, J. Motohisa, and H. Sakaki, accepted in Phys. Rev. Lett.

Ultrafast Excitonic Nonlinearities and Applications

QWB 3:30 pm-5:00 pm
Ballrooms VI-VIII

Philippe Fauchet, *Presider*
University of Rochester

Spin Quantum Beats in Quantum Wells and Wires

W. W. Rühle, M. Oestreich, R. Hannak, A. P. Heberle, R. Nötzel, and K. Ploog

Max-Planck-Institut für Festkörperforschung, Heisenbergstr. 1, D-70569 Stuttgart, Germany

Tel.: +49(711)689-1661, Fax:+49(711)689-1602

Klaus Köhler

Fraunhoferinstitut für Angewandte Festkörperphysik, Tullastr. 72, D-79108 Freiburg, Germany

Recently, the observation of spin quantum beats in time-resolved photoluminescence after picosecond excitation of GaAs quantum wells (QWLs) was reported.[1] A semiclassical description of this novel experiment follows: The circularly polarized laser generates an electron spin polarization in z direction according to the transition rules (Fig. 1). The magnetic field in the perpendicular x-direction forces these spins into a Larmor precession around the x direction, i.e., the electron spin polarization changes periodically with the Larmor frequency between parallel and antiparallel to the z direction. As a consequence, light emitted in z direction periodically oscillates between the two circular polarizations. A typical example is shown in Fig. 2 for a high quality 25nm QWL with an inhomogeneous broadening of the heavy-hole exciton line of $300\mu eV$. [1]

Quantum mechanically, the oscillations are interpreted as quantum beats between Zeeman split electron levels, $s_x = +1/2$ and $-1/2$, which are excited coherently by a short laser pulse. The choice of the circular polarization of the laser then sets the initial condition for the polarization of the luminescence. It is noteworthy, that spin splittings as small as $2.6\mu eV$ are detectable with this method, i.e., splittings which are orders of magnitude smaller than the homogeneous linewidth of the optical transition which is $180\mu eV$ for the 25nm QWL. This method therefore yields a high precision in determination of the Landé g factor, the entity which relates angular and magnetic momentum. At low fields, a linear increase of oscillation frequency with increasing magnetic field strength is observed; the g factor is in this regime independent of B. We restrict
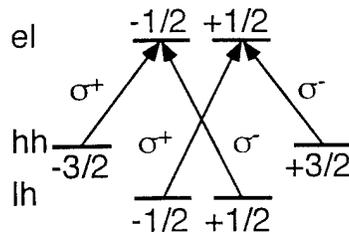
Fig. 1: Level scheme with transition rules.

Fig. 2: Luminescence decay at 2T after circularly polarized excitation of the light-hole exciton. The label I+ (I-) marks the luminescence having the same (opposite) circular polarization as the reflected laser beam.
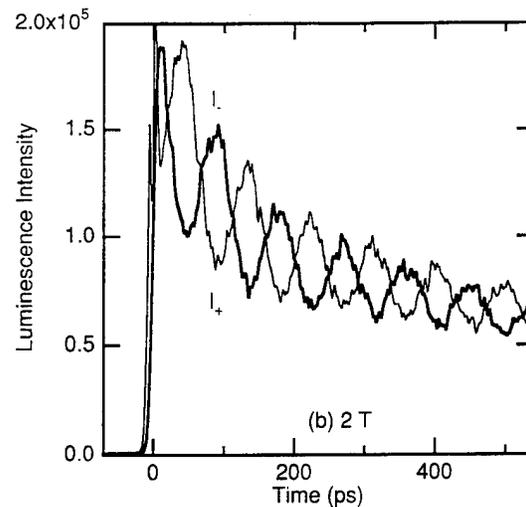
here on this low field regime. Various experiments show, that only the electron spin contributes to the oscillations, even though excitonic recombination is traced, since hole spin relaxation is to fast: i) the oscillations yield the bulk electron g-factor for various semiconductor materials, and ii) the same period is observed in the excitonic recombination, the band-to-acceptor recombination, and in the band-to-band transition of a degenerate electron-hole plasma.

In this contribution, we report on two results: First, an accurate determination of the well width dependence of the g factor in GaAs wells is described. Second, an extreme anisotropy of the g factor in GaAs wires is demonstrated.

The experimental setup consists of a mode-locked, picosecond Ti:sapphire laser or a synchronously pumped DCM dye laser (if shorter wavelengths are needed) for excitation and a streak camera with two-dimensional readout for detection of the luminescence. Spectral and temporal resolution are close to 0.5nm and 10ps, respectively. Sample temperature is about 10K. A superconducting magnet allows application of fields up to 16T.

Three quantum well samples are used to investigate the well width dependence: Sample QWL 35 (35% Al in the 30nm thick barriers) consists of 4 single QWLs with nominal thicknesses of 20, 10, 5, and 1.8nm, sample QWL 30 (30% Al in the 30nm thick barriers) has 20, 10, 5, 2, and 1nm thick QWLs, and sample QWL 27 (27% Al in the 49.2nm thick barriers) has 32.8, 16.4, 8.2, and 1.8nm thick QWLs.

Figure 3 compiles the various g factors for the different well widths measured with the three samples containing different Al fraction in the barriers together with theoretically predicted variations. Please note, that the g factor changes its sign at a well width of about 6nm, however, our experimental method does not yield the sign. The dashed curve is a simple theoretical
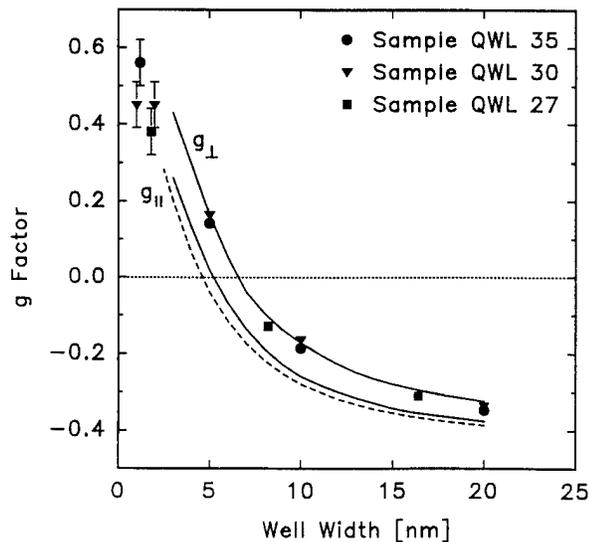
Fig. 3: Dependence of electron g factor on well width. Dashed line: one-band approximation for an Al-fraction of 35% in the barrier. Solid lines: Kane model including anisotropy [3].
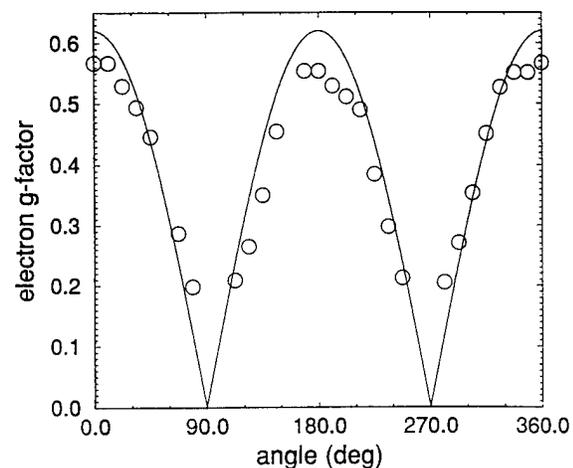
Fig. 4: Electron g factor in the x-y plane at 6T. Circles: experimental data. Solid line: theoretical estimate (without adjustable parameter) according to Ref. [3].

approximation which takes into account that part of the electron wavefunction is in the GaAs well, where the g factor is negative, and that part of it penetrates into the AlGaAs barrier, where the g factor is positive (g(AlGaAs) = +0.54, 0.46, and 0.39 for the samples QWL 35, QWL 30, and QWL 27, respectively). The contribution of the part penetrating into the barriers increases with decreasing well width resulting in the change of the sign of the g factor. [2] The difference for the different Al fractions in the barriers should show up for the smallest well widths: The bulk g factor for the corresponding barrier composition should be obtained for a well width approaching zero. Actually, such a tendency is observed for the smallest well widths in Fig. 3.

The solid lines ($g_{||}$ and $g_{\perp}$) are calculated using a more elaborate three-band Kane model which predicts different g factors for the magnetic field parallel and perpendicular to the growth direction. [3] These different g factors originate from the anisotropy of the quantum well structure. The g factor anisotropy can - within the Kane model - be related to the splitting of the heavy and light hole valence band in the structure. We measure in our experiment the g factor $g_{\perp}$ for B perpendicular to growth direction. The agreement between experiment (symbols) and theory ($g_{\perp}$) is good. In case of a QWL, it is not easy to measure $g_{||}$ with our method.

The challenge remains to measure directly the predicted anisotropy in low-dimensional structures. This becomes possible in case of quantum wires. Our quantum wire sample, QWR, consists of a wire-like superlattice grown on (311) substrates. The in-situ formation of an array of macro-steps during growth results in corrugated superlattices with 4.3nm thick GaAs wires and 4.7nm thick AlAs barriers. Various one-dimensional effects, measured with these wires, as well as a detailed sample description are found in reference 4.

In a QWR, a magnetic field perpendicular to the growth and observation direction either probes the g factor g_1 in wire direction (0 and 180 degrees) or perpendicular to the wire direction (g_2, 90 and 270 degrees). Figure 4 compiles the absolute values of the g factor for various field directions. The solid line is a simple approximation [3], with an anisotropy Δ g of

$$\Delta g = g_1 - g_2 = (2p^2/m_0)(1/E_{hh} - 1/E_{lh}) \qquad (1)$$

and
$$g(\phi) = [(g_1 B \cos \phi)^2 + (g_2 B \sin \phi)^2]^{1/2}, \qquad (2)$$

where ϕ is the angle between the wire direction and the magnetic field, $2p^2/m_0$ is the interband matrix element of the momentum operator, and E_{hh} and E_{lh} are the electron to heavy- and electron to light-hole transition energies. The agreement between experiment and theory is quite good in view of the fact that no adjustable parameter and a very simple theoretical approach are used.

References:
[1] A.P. Heberle, W.W. Rühle, and K. Ploog, Phys. Rev. Lett. **72**, 3887 (94)
[2] M.J. Snelling, G.P. Flinn, A.S. Plaut, R.T. Harley, A.C. Tropper, R. Eccleston, and C.C. Phillips, Phys. Rev. **B44**, 11345 (91)
[3] E.L. Ivchenko and A.A. Kiselev, Sov. Phys. Semicond. **26**, 827 (92)
[4] R. Nötzel, N.N. Ledentsov, and K. Ploog, Phys. Rev. **47**, 1299 (93)

Coherent Nonlinear Optical Spectroscopy of Semiconductor Microcavities

Hailin Wang, Jagdeep Shah, T.C. Damen, W.Y. Jan, and J.E. Cunningham,
AT&T Bell Laboratories, Holmdel, NJ 07733

In semiconductor microcavities, quantization of the photon modes can lead to a unique system where excitons couple coherently to a single mode of photons. In this paper we present the first coherent nonlinear optical study of a composite exciton-cavity system. The results reveal coherent dynamical behaviors that are not accessible to linear measurements.

In general there are two distinct dynamical regimes for the exciton-cavity interactions. In the weak coupling (perturbative) regime, effects of the coherent coupling between the exciton and cavity are negligible. Enhancement or suppression of spontaneous emission rates is expected [1]. In the strong coupling (non-perturbative) regime, the coherent exciton-cavity coupling becomes dominant compared with dissipative decay processes. A normal mode splitting in the linear response of the composite system can be observed [2].

Coherent spectroscopy such as four wave mixing (FWM) is an ideal tool for probing the coherent dynamics of the composite system. By observing quantum oscillations in spectrally-resolved transient FWM response we show for the first time the excitation of a coherent superposition state between the two normal modes of the composite system and demonstrate directly in time domain the coherent energy exchange between the exciton and cavity. Deep quantum oscillations with a period that varies with the normal mode splitting persist even when detuning between the cavity and exciton is much greater than the exciton-cavity coupling rate. The result shows surprisingly that the dynamics of the nonlinear response is in a non-perturbative regime while dynamics of the linear response remains in a perturbative regime, leading to a unique situation where the linear and nonlinear response remains in distinct dynamical regimes. In addition, measurements of the decay of the normal modes also suggest that the strong exciton-cavity coupling leads to mixing of wave functions of localized exciton states.

The microcavity consists of 15 and 20.5 stacks of $\lambda/4$ $Al_{0.11}Ga_{0.89}As/AlAs$ as the top and bottom mirrors, respectively. Two 150 Å GaAs quantum wells are placed at the center (antinode) of a λ cavity. Small variations in the cavity thickness allow us to tune the cavity resonance by moving the laser spot across the wafer while the exciton energy remains nearly unchanged. For FWM measurements (see the inset of Fig. 1 for geometry), 100 fs pulses from a Ti:Sapphire laser are centered at the heavy hole (hh) exciton energy. All measurements were performed at 10 K.

We first compare the linear and nonlinear spectral response of the composite system. Figure 1 shows spectra of the reflected laser pulse and the FWM emission at zero delay when the cavity is nearly resonant with the hh exciton. Both spectra show a normal mode splitting that disappears rapidly with increasing intensities due to saturation of the exciton transition. Figure 2a shows the dependence of FWM spectra on detunings between the cavity and the exciton. To avoid the complication due to light hole excitons, we keep the cavity resonance below the hh exciton energy. Again, two resonances are observed, corresponding to the two resonances in the reflectivity spectrum (see the inset). The resonance at higher energy is exciton-like while the resonance at lower energy is cavity-like. For large detunings the FWM spectrum is completely dominated by the photon-like resonance.

New dynamical behaviors are revealed in the transient FWM response of the composite system. The transient response as a function of the delay between the two incident pulses shown in Fig. 2b is obtained by first sending the FWM signal through a spectrometer centered at the

energy of the corresponding photon-like mode in Fig. 2a. Periodic oscillations are observed in all the temporal responses shown in Fig. 2b. Similar oscillations with an identical phase are also present when we measure the FWM signal at the energy of the exciton-like mode. The period of the oscillation follows exactly the energy separation between the exciton-like and the cavity-like resonance.

There are two very different processes that can lead to oscillations in transient FWM. The first process results from interference of two fields with different frequencies at the detector (polarization beats). The second process results from two optical transitions sharing a common ground state (quantum beats) where the interference takes place in the material and is a direct consequence of the excitation of a coherent superposition state between the two excited states. Since we detect only one frequency component in Fig. 2b, we conclude that oscillations in Fig. 2b are quantum beats and are due to the excitation of a coherent superposition state of the two normal modes.

The quantum beats directly reflect the coherent energy exchange between the photon and exciton. Using the two nearly degenerate eigen states of the uncoupled exciton and photon system $|g,1>$ and $|x,0>$, the wave function of the coherent superposition state can be written as

$$|\psi> = a(e^{-i\Omega_-t} + \alpha e^{-i\Omega_+t})|g,1> + b(e^{-i\Omega_-t} + \beta e^{-i\Omega_+t})|x,0> \tag{1}$$

where $\Omega_\pm$ are the frequencies of two normal modes and a,b, α,β are constants. The wave function corresponds directly to a coherent oscillation of both the exciton and photon population in the cavity. In contrast, oscillations reported in linear measurements (i.e. transient reflectivity) are simply due to interferences of fields with different frequencies in the detector and do not represent the coherent oscillation of the exciton population. In particular, oscillations in linear measurements vanish at large exciton-cavity detunings in contrast to FWM measurements.

When the cavity is far detuned from the exciton resonance, the coupled system is in an adiabatic regime. Very deep oscillations in FWM persist in this regime as shown in Fig. 2b. The persistence of the deep oscillation is very surprising since in this regime the coupling between the cavity and exciton is very weak and effects of the coherent coupling are negligible for linear measurements. Dynamics of linear measurements in this case is dominated by dissipative decay processes and is in a perturbative regime. In contrast, dynamics of the FWM response is still dominated by the coherent exciton-cavity coupling because the nonlinear response results only from the excitonic part of the wave function. We also note that although only a small amount of the exciton wave function is mixed into the cavity like mode, nearly the same amount of excitons is excited in both the cavity-like and exciton-like mode [$\beta \approx 1$ in Eq. (1)] since the photon-like mode is excited much more strongly than the exciton-like mode, which explains the depth of the quantum beats shown in Fig. 2b. FWM signals at the exciton-like mode are very weak due to spectral filtering effects of the cavity.

Figure 2b also shows that the decay time of FWM signals for the photon-like mode decreases from 1.6 ps to 0.5 ps with decreasing detuning, which is unexpected since the intrinsic dephasing rate of the localized exciton is longer than 10 ps, much longer than the cavity life time. In the strong coupling limit, emission and reabsorption of photons by nearly-degenerate excitons can mix the wave function of these excitons, leading to much faster decay of the FWM signal. The decay dynamics of the photon-like modes may be an indication of the cavity-induced state mixing and will be discussed in more detail.

In addition, by treating the composite exciton-cavity as a "molecule" and using the semiclassical Bloch equations we have developed a theoretical description that qualitatively account for the observation of the current measurements [3]. Note that a full quantum theory is still necessary for exploring quantum dynamics that has no classical counter part.

1) Y. Yamamoto, S. Machida, and G. Bjork, in *Coherence, Amplification and Quantum Effects in Semiconductor Lasers*, Y. Yamamoto ed. (Wiley, New York 1991).
2) C. Weisbuch, *et al*, Phys. Rev. Lett. **69**, 3314 (1992).
3) H. Wang, *et al*. submitted for publication.
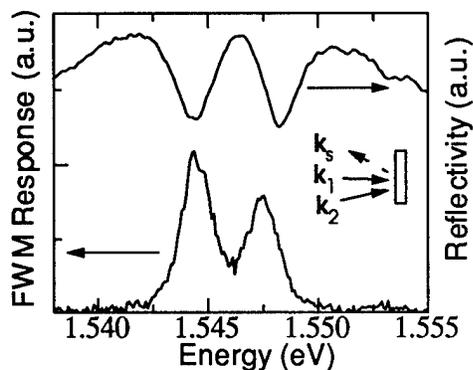
Fig. 1 Spectra of both the FWM emission and reflected laser pulse. The photon flux used for the FWM measurement is $10^{11}/cm^2/pulse$. The reflectivity spectrum is obtained at a much lower intensity.
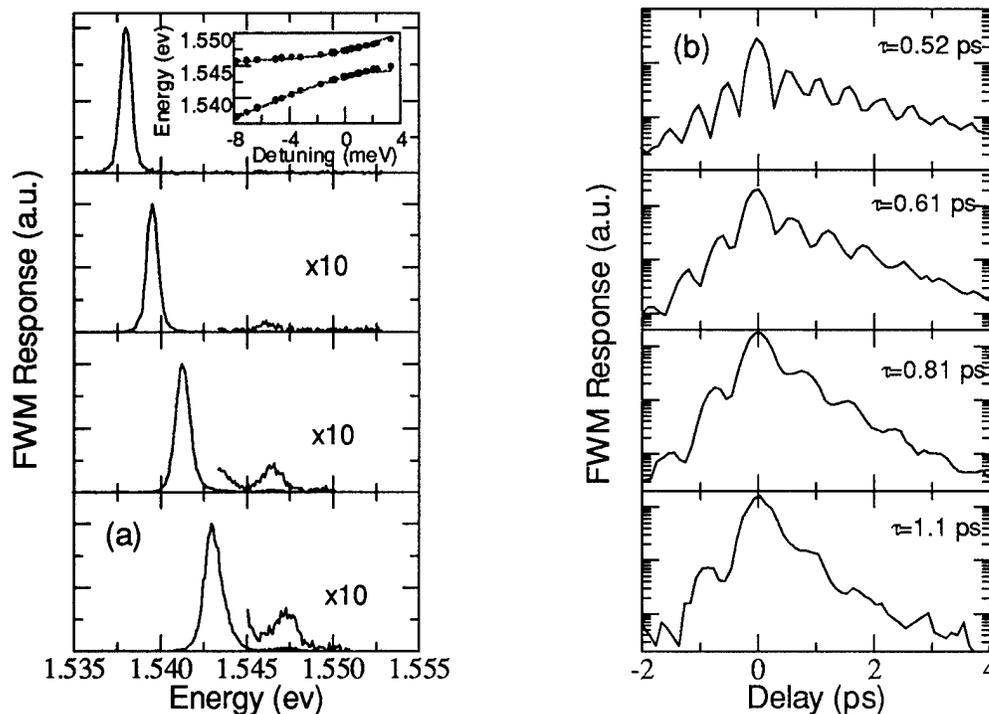
Fig. 2 (a) FWM spectra at zero delay with various exciton-cavity detunings. The inset shows the position of the normal modes in reflectivity spectra as a function of the detuning. (b) FWM signal as a function of the delay between the two incident pulses. The data are obtained at the peak of the corresponding cavity-like resonance in Fig. 2a. τ is the period of the oscillation.

Excitonic versus electronic Bloch oscillations

T. Dekorsy, P. Leisching, R. Ott, H. J. Bakker, and H. Kurz
Institut für Halbleitertechnik II, RWTH Aachen, Sommerfeldstr. 24, D-52056 Aachen,
Germany, phone +49-241-807896, FAX +49-241-8888-246

K. Köhler
Fraunhofer-Institut für Angewandte Festkörperphysik, D-79108 Freiburg, Germany

We present the first comparative study of the interband and intraband dynamics of coherent Bloch oscillations in the Wannier-Stark regime of GaAs/$Al_xGa_{1-x}As$ superlattices. Transmittive electro-optic sampling (TEOS) and degenerate four-wave mixing (FWM) experiments, which are sensitive towards the electronic intraband and excitonic interband dynamics, respectively, are performed simultaneously. Frequency differences in both experiments are observed with a pronounced dependence on the electric field. This effect shows that the Bloch oscillations observed are mainly performed by excitonic states in FWM and by continuum states in TEOS. The observation of non-excitonic Bloch oscillations is of prime importance for electrically driven Bloch oscillations and for the observation of Bloch oscillations at room temperature.

Bloch oscillations (BOs) have been a matter of interest and controverse discussion ever since their first theoretical description [1]. In a semi-classical picture, Bloch electrons perform periodic motions in real- and k-space under the influence of a static electric field. The BO frequency is given by $\nu_{BO}=eFd/h$, where F is the electric field, d the periodicity of the potential, and h Planck's constant. The semi-classical picture was refined by quantum mechanics, where the electron is considered as a wavepacket of Wannier-Stark (WS) states equally spaced in energy by $h\nu_{BO}$ [2]. The breakthrough for the experimental realization of BOs came with the advent of high-quality semiconductor superlattices. where the relatively large superlattice period d reduces the fields necessary to launch BOs with periods shorter than the scattering time [3]. The equivalence between the semi-classical BO picture and the quantum-mechanical description of electronic wavepackets in superlattices has been formally shown by Bastard and Ferreira [4].

The first time-resolved observation of BOs in semiconductor superlattices suceeded in optical experiments employing femtosecond laser pulses. Their broadband spectrum excites a coherent superposition of several WS states, resulting in *quantum beats with the BO frequency* in four-wave-mixing (FWM) experiments [5]. FWM signals arise from third-order *interband* polarizations, which are of excitonic nature [6]. More recently, the emission of THz-radiation from BOs has been observed, being evidence for the *spatial oscillations of the electronic wavepacket* relative to a localized hole [7]. Finally, an electro-optic technique has been developed to investigate the internal field dynamics associated with BOs [8]. Transmittive electro-optic sampling (TEOS) enables to monitor directly the dynamics of the *intraband* dipole moment induced by the spatial motion of coherent electronic wavepackets in amplitude and phase. The method is based on the detection of the optical anisotropy induced by the macroscopic polarization via the Pockels effect. Some of the most interesting questions, which can be addressed by the direct observation of the interband and intraband dynamics of BOs are:

- Are there differences to be observed between the excitonic (interband) and non-excitonic (intraband) dynamics ?
- Do non-excitonic continuum states perform BOs and (if "yes") what is their dephasing?

• How are the differences influenced by the field-dependent localization of the excitonic and/or continuum states performing BOs?

Here, we report on the first simultaneous performance of FWM and TEOS experiments, which allow to answer to the questions above. Fig. 1 depicts FWM and TEOS signals recorded under identical excitation condition at a reverse bias voltage of -0.95 V. The sample is a GaAs/$Al_{0.3}Ga_{0.7}$As superlattice with a width of 19 meV of the first electronic miniband. The lattice temperature is 10 K. The excitation density is 2×10^9 carriers per cm^2 and well. The FWM signal is plotted on a logarithmic scale and the TEOS data on a linear one.

The periodic modulation of the third-order interband polarization in FWM is due to excitonic BOs. The relatively high initial peak compared to the BO induced signal results from the excitation of continuum states that rapidly dephase, even at 10 K [9]. The TEOS data exhibit at zero time-delay a step-like drop due to an instantaneously created polarization in z-direction and an additional coherence peak, that can not be avoided in this geometry [9]. At positive time-delays, the signal is strongly modulated due to BOs. The frequency of BOs as determined by a fast-Fourier-transform (TEOS) and by an accurate determination of the spacing of the maxima and minima in the FWM signal are significantly different: 2.6 THz (10.7 meV) in TEOS and 2.2 THz (9.1 meV) in FWM. We investigate this frequency differences at different reverse bias voltages in the Wannier-Stark regime of the superlattice. The frequency differences observed vanish at small reverse bias and increase at higher reverse bias. Additionally, differences in the dephasing of the intraband and third-order interband polarization are observed.

Fig.1: Simultaneously recorded TEOS (linear plot) and FWM (logarithmic plot) signals at an applied voltage of -0.95 V.

The reason for the frequency differences observed is illustrated in Fig. 2. The BOs result from the coherent superposition of the h0-e0 and the h0-e-1 WS states at higher fields. The heavy holes can be assumed as localized. Neglecting Coulomb interaction between electrons and holes, the frequency/field relation of the BOs performed by electrons in continuum states is given by $\nu_{BO}=eFd/h$. For excitonic BOs, we expect that the exact frequency also depends on the field dependence of the different exciton binding energies of the h0-e0 and h0-e-1 transitions. At high fields, the electronic WS wavefunctions become strongly localized leading to an increase of the exciton binding energy of the h0-e0 transition,
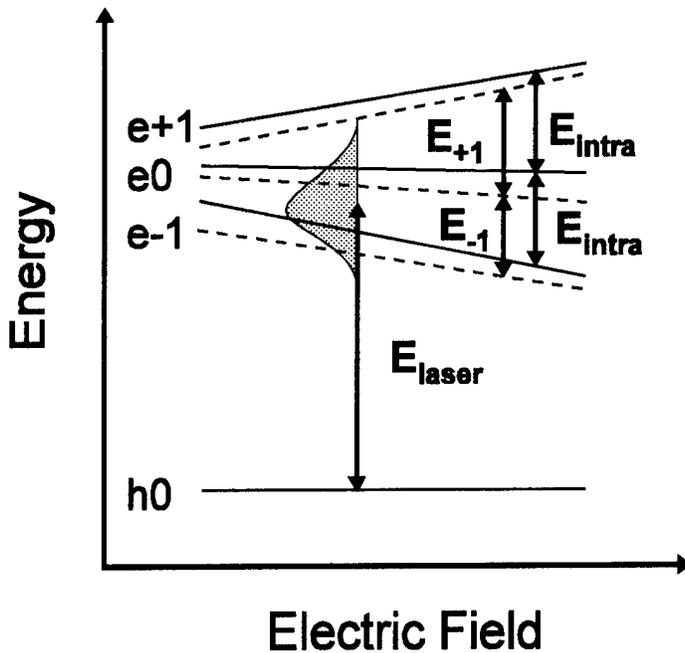
Fig.2: Illustration (not to scale) of the field dependence of the h0-e-1, h0-e0 and h0-e+1 Wannier-Stark continuum (solid lines) and exciton transitions (dashed lines) at higher fields. The energy splitting between continuum states is denoted as E_{intra}, between the h0-e0 and h0-e-1 excitons as E_{-1}, and between the h0-e0 and h0-e+1 excitons as E_{+1}. E_{laser} is the laser energy. Note that $E_{-1} < E_{intra} < E_{+1}$.

while the h0-e-1 transition becomes "indirect" leading to a reduction of the exciton binding energy. Thus the BO frequency in FWM is expected to have a smaller slope compared to the semi-classical frequency/field relation. As a result, the BO frequency of excitonic states will be lower than the BO frequency of the electronic continuum states. The maximum frequency deviation expected from $v_{BO}=eFd/h$ in FWM, is the difference in exciton binding energies of the direct h0-e0 and indirect h0-e-1 transitions at high fields. For the superposition of the h0-e0 and h0-e+1 WS state in the same field regime, higher BO frequencies are expected in FWM than in the semi-classical theory. A more quantitative analysis of the frequency splitting is performed by numerical calculations of the exciton binding energies as a function of the electric field. The results agree well with the experiment. Thus we conlude that BOs oberved in the interband dynamics are mainly performed by excitons, while in the intraband dynamics BOs performed by continuum states are observed. These results are discussed in the context of recent theoretical studies concerning the excitonic nature of the BOs [10,11].

References
[1] F. Bloch, Z. Phys. **52**, 555 (1928); C. Zener, Proc. R. Soc. London A **145**, 523 (1934).
[2] G. H. Wannier, Phys. Rev. **117**, 432 (1960); Rev. Mod. Phys. **34**, 645 (1962).
[3] L. Esaki and R. Tsu, IBM J. Res. Dev. **61**, 61 (1970).
[4] G. Bastard and R. Fereirra, NATO Advanced Institute Series B **206** (Plenum, New York, 1989), p. 333.
[5] J. Feldmann et al., Phys. Rev. B **46**, 7252 (1992); K. Leo et al., Solid State Commun. **84**, 943 (1992); P. Leisching et al., Phys. Rev. B. **50**, in press (1994).
[6] D.-S. Kim et al., Phys. Rev. Lett. **68**, 1006 (1992).
[7] C. Waschke et al., Phys. Rev. Lett. **70**, 3319 (1993).
[8] T. Dekorsy et al., Phys. Rev. B **50**, 8106 (1994).
[9] A. Lohner et al., Phys. Rev. Lett. **71**, 77 (1993).
[10] M. Dignam, J.E. Sipe, and J. Shah, Phys. Rev. B **49**, 10502 (1994).
[11] T. Meier et al., Phys. Rev. Lett. **73**, 902 (1994).

AlAs/AlGaAs intracavity Saturable Bragg Reflector for
Femtosecond self-starting passive mode-locking

W. H. Knox, S. Tsuda, E. A. de Souza, W. Y. Jan and J. E. Cunningham

AT&T Bell Laboratories, Holmdel, NJ 07733

We introduce a new semiconductor structure and demonstrate its use as an intracavity femtosecond mode-locker. The structure consists of an AlAs/AlGaAs quarter-wave dielectric stack grown by molecular beam epitaxy. We insert a single quantum well into a quarter wave layer, as shown in Fig. 1a. The reflectivity spectrum (Fig. 1b) shows a characteristic Bragg reflection with a small dip at the exciton wavelength of 850 nm. This structure provides high reflectivity, low loss, and adjustable saturation intensity, with no further processing required after
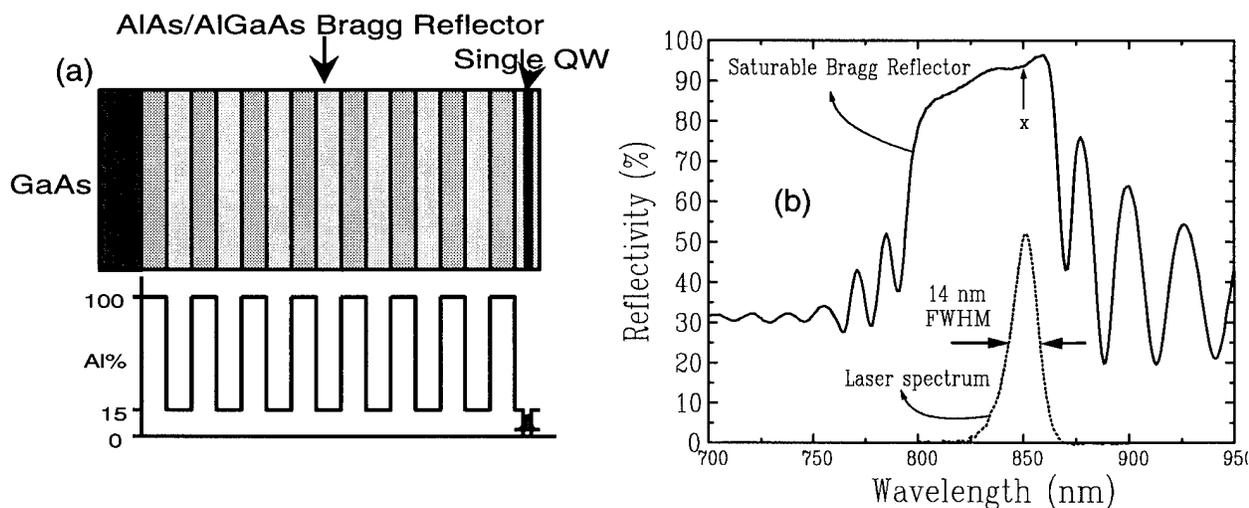
Fig. 1. (a) Saturable Bragg Reflector structure with a stack of AlAs/AlGaAs HL pairs and one single GaAs quantum well buried in the last layer. (b) Reflectivity spectrum of the SBR and the spectrum of the 90 fs pulses.

MBE growth. We refer to it as the "Saturable Bragg Reflector" (SBR), although it could be considered as a *"nonlinear one-dimensional photonic bandgap structure"*. With the Ti:Sapphire laser cavity as shown in Figure 2, we obtain 8 fs pulses when operating in a purely Kerr-lens modelocking regime. When we incorporate the SBR by focusing with a 20 cm radius mirror, we obtain self-starting transform-limited pulses of 90 fs duration. Figure 3 shows a typical autocorrelation trace, and Fig. 1b shows the modelocked spectrum.

3 mm
Ti:sapphire rod

f = 12 cm

M1
flat HR

P1

M2
R=10 cm

M3

Argon

P2

M4

SBR

Output
Coupler
R = 20 cm
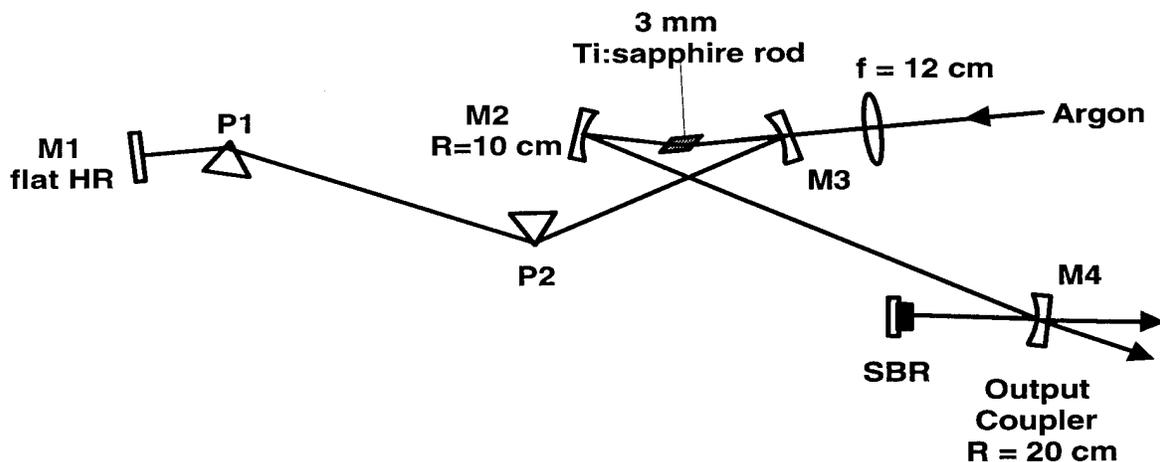
Fig. 2. Cavity setup of the Ti:sapphire laser using an intracavity Saturable Bragg Reflector as a mode-locker.

Previously, Resonant Passive Mode-locking (RPM) [1] showed that a quantum well stack in an external cavity could induce modelocking without introducing any loss into the main cavity. Later, the external cavity was eliminated with the development of the Anti-Resonant Fabry-Perot Saturable Absorber (A-FPSA) [2]. The AFPSA device consists of a quantum well stack covered with a SiO_2/TiO_2 multilayer dielectric stack of ~98% reflectivity. In contrast, the Saturable Bragg Reflector (SBR) achieves modelocking using a single quantum well that is exposed to the entire intracavity intensity. In the present case, the lasing bandwidth is limited by the Bragg reflector bandwidth, which can be increased with different designs.

Autocorrelation
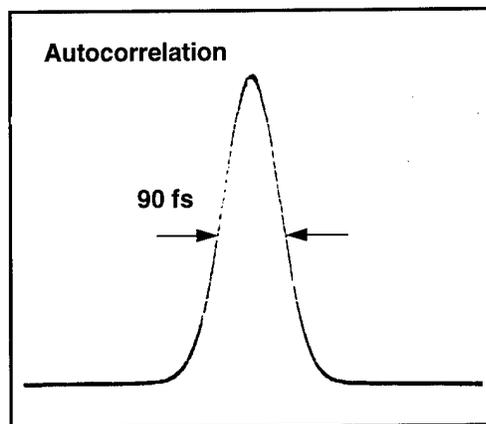
90 fs

Fig. 3. Autocorrelation trace of the 90 fs mode-locked pulse at 850 nm.

We believe that the exciton saturation dynamics in the SBR together with self-phase modulation and group velocity dispersion are responsible for self-starting and femtosecond pulse formation. The range of cavity parameters corresponding to stable femtosecond pulse generation

was considerably greater with the SBR included in the cavity. Therefore, SBR modelocking is much less alignment-sensitive than KLM [3]. This appears to be similar to that obtained with multiple quantum well absorbers in Cr:LiSrAlF$_6$ lasers with conventional reflectors or AFPSAs [4]. Finally, by removing both prisms we obtained stable picosecond pulses.

In conclusion, we have demonstrated a new semiconductor structure for femtosecond self-starting passive mode-locking of lasers. Although we have used the SBR to mode-lock a Ti:sapphire laser, generating stable 90 fs pulses in a TEM$_{00}$ mode, this semiconductor structure can be used to mode-lock other types of lasers. By changing the semiconductor materials and growth parameters it is possible to extend the use of the SBR to other wavelengths.

References

[1] U. Keller, W. H. Knox and H. Roskos, Opt. Lett. **15**, 1377 (1990).

[2] U. Keller, D. A. B. Miller, G. D. Boyd, T. H. Chiu, J. F. Ferguson and M. T. Asom, Opt. Lett. **17**, 505 (1992) ; U. Keller, W. H. Knox and G. W. 'tHooft, IEEE J.Quantum Electron., **28** pp.2123-2133, (1992)

[3] M. M. Murnane, H. C. Kapteyn, J. Zhou, C. P. Huang, G. Taft and M. T. Asaki, 1994 OSA Annual Meeting/ILS -X Program, 95 (1994).

[4] P. M. W. French, R. Mellish, J. R. Taylor, P. J. Delfyett and L. T. Florez, Opt. Lett. **18**, 1934 (1993); U. Keller, 1994 OSA Annual Meeting/ILS -X Program, 90 (1994).

Photonic Bandgaps, Microcavity Physics, and Applications

QThA 8:30 am-10:00 am
Ballrooms VI-VIII

Kenichi Kasahara, *Presider*
NEC Corporation, Japan

Review of photonic bandgaps

E. Yablinovitch
University of California-Los Angeles

We discuss the status of photonic bandgap structures from a physics and applications viewpoint.

Luminescence processes in semiconductor microcavities

R. Houdré[1], C. Weisbuch[2], R.P. Stanley[1], U. Oesterle[1], P. Pellandini[1] and M. Ilegems[1]

1. Institut de Micro- et Optoélectronique, Ecole Polytechnique Fédérale de Lausanne, CH 1015, Lausanne, Switzerland, Tél. : 41-21-6935487, Fax : 41-21-6934525
2. Laboratoire de Physique de la Matière Condensée et Département de Physique, Ecole Polytechnique, F 91128 Palaiseau, France, Tél. : 33-1-45524605, Fax : 33-1-45526139

The interaction of light with semiconductors has always triggered a huge effort both because of its importance in determining fundamental processes and parameters and because of the numerous applications which depend on it. One process of particular importance is luminescence which allows such wide-scale applications as lasers, LEDs and displays.

In the past few years, a new avenue has opened to control and modify the parameters of light-matter interaction : it is that where the light-active material is placed in an optical resonator with dimensions of the order of one optical wavelength[1]. Then, only one or a few optical modes interact with the active material, leading to a strongly modified emission pattern. The goal is here to obtain high-efficiency LEDs by spatially concentrating the emitted light into photon modes which are well-coupled to the useful angle outside the active material. In the limit of emission into only one mode (spontaneous emission factor $\beta = 1$) one obtains a "thresholdless" laser as the light output efficiency in the emission mode remains constant, independant of the light being emitted spontaneously or in a stimulated manner.

In the usual microcavity phenomena the light-matter interaction is weak, i.e. the time evolution of the material system can be described in a perturbative manner, by Fermi's golden rule. The microcavity impact occurs through the modification of the vaccum fields modes : the mode density tends to be more and more spectrally concentrated as the dimensionality of the optical microcavity decreases (fig. 1). At the same time, the vacuum field amplitude of resonant photon modes is increased (by a quality factor Q) while that of the non-resonant modes is decreased by the same factor. Therefore, overall, the light-matter interaction remains roughly the same (the lifetime is hardly changed) and the microcavity mainly acts as a photon mode selector for the spontaneous emission.

Recently, another regime of the light-matter interaction has been evidenced in optical microcavities : the strong-coupling, well known in atomic physics. It relies on the dominance of the interaction of a given atomic level with only one photon mode over all other interactions, be it with other photon modes or other decay mechanisms. In such a case, the light-matter interaction does not lead to a decay of the electronic excitations, but to an oscillation of the strongly coupled atom-photon system between the two coupled states. This is the well-known Rabi oscillation.

Such a situation was shown to occur in semiconductor planar microcavities (figure 2), between imbedded-quantum well (QW) excitons and the resonant photon mode of the cavity[2]. Although exciton and planar microcavity modes have two-dimensional continua, they interact only in a one-to-one correspondance due to the conservation of the in-plane momentum in the optical transition. Therefore a QW exciton with a well-defined momentum interacts strongly with the cavity photon with the same momentum. This leads to the appearance of two mixed normal modes, half exciton and half photons, named cavity-polariton after the similar phenomenon occuring in bulk semiconductors at low temperatures.

The luminescence of such strongly-coupled excitations is of interest for fundamental reasons : how can one describe the luminescence process ? What are its characteristics, such as spectrum and dynamics ? etc... It is also important for applications purposes : as the strong

coupling leads to an oscillation between the exciton and photon states it is no more a mechanism for radiative decay. Light emission will occur when the photon mode decays out of the cavity, due to the mirror transmission or absorption. Such a decay typically occurs in a picosecond, much faster than usual lifetimes in semiconductors. It is therefore of utmost importance to see whether such a fast decay translates into improved luminescence properties or not.

A direct calculation of the emission process looks impractical, as it would require to calculate the exciton emission into all cavity modes and the self-reaction on the exciton, to describe the strong coupling. However, the formalism used to describe polariton emission in bulk materials can be transposed for cavity-polaritons[3]. It assumes that the true excitations of the full system (excitons and cavity photons) are the coupled-mode excitations, the cavity-polaritons.

Then, luminescence is just the phenomenon by which the relaxation-populated cavity-polariton states are coupled to outside photon-modes. We have recently shown that the cavity-polariton states are thermally populated, and that the in-out coupling is the reverse of absorption mechanism[3]. Therefore, the outcoupling coefficient is just the microcavity absorption coefficient, defined and measured as A = 1-T-R, where T and R are the cavity transmission and reflexion coefficients respectively. Of course, the absorption coefficient displays peaks at the coupled-mode energies. Therefore, measuring the photoluminescence spectrum as a function of emission angle allows to determine the cavity-polariton dispersion curve for the in-plane momentum : at a given outside angle one observes the cavity-polariton which has the same in-plane momentum as the emitted photon. The emission spectrum displays peaks at the cavity-polariton energies for that momentum, due to dominant role of the absorption coefficient in determining the spectral lineshape of the emission. Therefore, we can directly measure, point by point, the cavity-polariton dispersion curve[3] (figure 2).

The application of cavity-polariton features to efficient light-emitters is not yet straightforward. If one were able to only excite resonant coupled-modes, one would deal with a β = 1 light emitter as the material would only emit into the resonantly-coupled photon mode. Norris et al.[4] have shown in transient measurements that whereas this is indeed the case when photopumping resonantly, the ultrafast response disappears when pumping non-resonantly, most certainly due to the time required by non-resonant excitons to relax to the fast cavity-polariton modes. In addition, intensity-dependant spectra (figure 3) clearly show that at high-densities, like those required for laser action, phase-space filling leads to the decrease of the exciton oscillator strength and therefore to the collapse of the strong-coupling regime, as evidenced by the transition from an anticrossing to a crossing behaviour of the luminescence peaks in dispersion curves.

In conclusion, we can say that the basics of the luminescence of strong-coupled cavity-polaritons are mostly understood. The translation of this regime into better light emitters will require some newer implementations.

References.

1. See e.g. R.E. Slusher and C. Weisbuch, Solid State Comm. **92**, 149 (1994) and references therein.
2. C. Weisbuch, M. Nishioka, A. Arakawa and Y. Arakawa, Phys. Rev. Lett. **69**, 3314 (1992).
3. R. Houdré, C. Weisbuch, R.P. Stanley, U. Oesterle, P. Pellandini and M. Ilegems, Phys. Rev. Lett. **73**, 2043 (1994).
4. T. Norris et al., QELS'93 and '94, and unpublished.
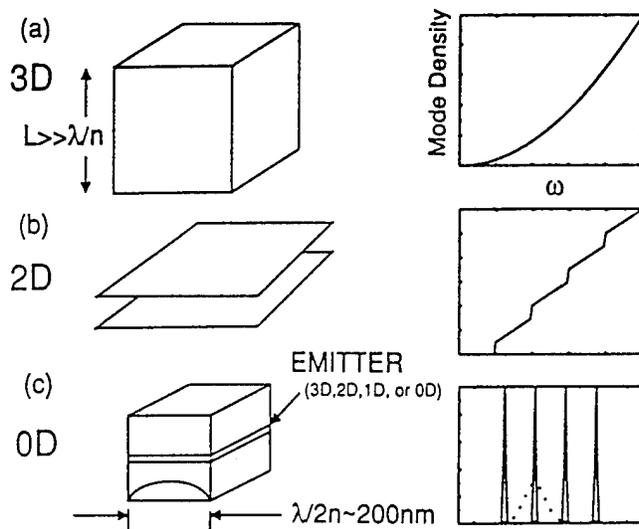
Figure 1 : Microcavity structures and associated density of states.

$$\omega_{\pm} = (\omega_1+\omega_2)/2 \pm (\Omega^2+(\omega_1-\omega_2)^2)^{1/2}$$
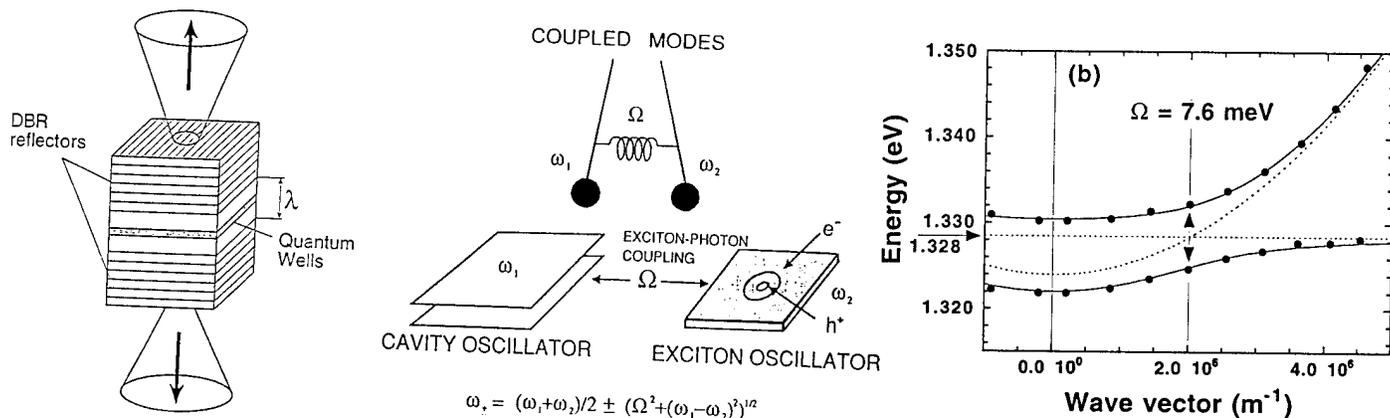
Figure 2 : Schematics of Planar microcavity with embedded quantum wells (left), strongly interacting excitons and photons (center) dispersion curve of coupled excitons and photons (right) [dashed curves : uncoupled dispersion curves ; full curves calculated dispersion curves ; full points : experimental results]
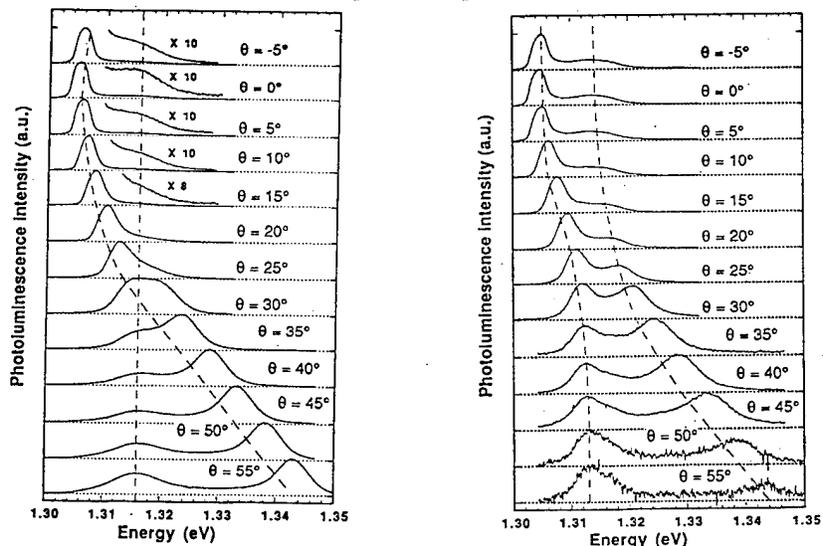

Figure 3 : Angle-resolved photoluminescence under weak and strong excitations. Dashed lines are a guide to the eye to follow the respective anticrossing and crossing behaviour of the dispersion curves.

Nonlinear Vacuum Rabi Splitting in Semiconductor Microcavities

J.-K. Rhee, R. Lai, T. B. Norris, Y. Arakawa,* and M. Nishioka*

Center for Ultrafast Optical Science, University of Michigan
2200 Bonisteel Blvd., Ann Arbor, Michigan 48109, U.S.A.
Tel) (313) 763-4875, Fax) (313) 763-4876
* Institute of Industrial Science, University of Tokyo
7-22-1 Roppongi, Minato-ku, Tokyo 153, Japan

Recently, several research groups have reported investigations of vacuum-field Rabi splittings (VRS) in the linear response of strongly coupled semiconductor microcavities [1–4]. We have previously reported on the dynamics of time-domain vacuum Rabi oscillations, which are most easily understood in the framework of cavity exciton-polaritons, in which the in-plane momentum $k_{\parallel}$ is conserved [2], so that at each $k_{\parallel}$ a single cavity mode interacts with only a single mode of the electromagnetic field (Jaynes-Cummings model). In high Q semiconductor microcavities, the strong coupling between two-dimensional excitons and planar distributed-Bragg-reflector cavity modes results in several-meV splittings observable in the reflectivity or absorption spectrum. In the low excitation regime, the VRS is independent of light intensity incident on the cavity, since the vacuum-Rabi frequency exceeds the externally-driven Rabi frequency (in which case the Jaynes-Cummings model is equivalent to the linear dispersion of the coupled exciton-cavity system). As the incident light intensity is increased, two different effects may be expected to contribute to the nonlinear response. First, as long as the excitonic absorption is equivalent to a two-level system, higher-lying states of the Jaynes-Cummings ladder might be observable. Second, at high intensity phase-space filling and Coulomb screening of the exciton states results in a reduced oscillator strength which leads to a reduced VRS; this effect has no analogue in the case of atom-cavity systems. In this paper, we apply several ultrafast nonlinear techniques to investigate the nonlinear response of semiconductor microcavities.

The $Al_xGa_{1-x}As$-based microcavity sample used in this work is the same as that used for our previous publications, showing 6-meV VRS at 10 K with five 76-Å $Al_{0.2}Ga_{0.8}As$/GaAs quantum wells in the low-excitation regime [1]. In order to observe the nonlinear response, we first investigated the time-integrated reflectance spectra of the microcavity sample with strong impulsive on-resonant excitation: 70-fs laser pulses from a Ti:sapphire oscillator with pulse energy from 0.02 to 200 pJ were tuned to the exciton-cavity resonance and focused on the sample with 150-μm spot diameter at nearly normal incidence. The reflected laser spectra were analyzed with a monochromator; the normalized reflectance spectra are shown in Fig. 1(a). The reflectance spectra were fitted with a superposition of two Lorentzian curves in order to determine the splittings, which are plotted in Fig 1.(b) as a function of excitation optical fluence. In the reflectance spectra, we can clearly see the reduction of VRS at optical fluences higher than 5×10^{10} photons/cm^2. This is the manifestation of a reduced excitonic transition oscillator strength or saturated exciton absorption in the microcavity. The VRS is given by [2]

$$\hbar\Omega = e\hbar\sqrt{\frac{N}{2m\epsilon L_C}f_S}, \tag{1}$$
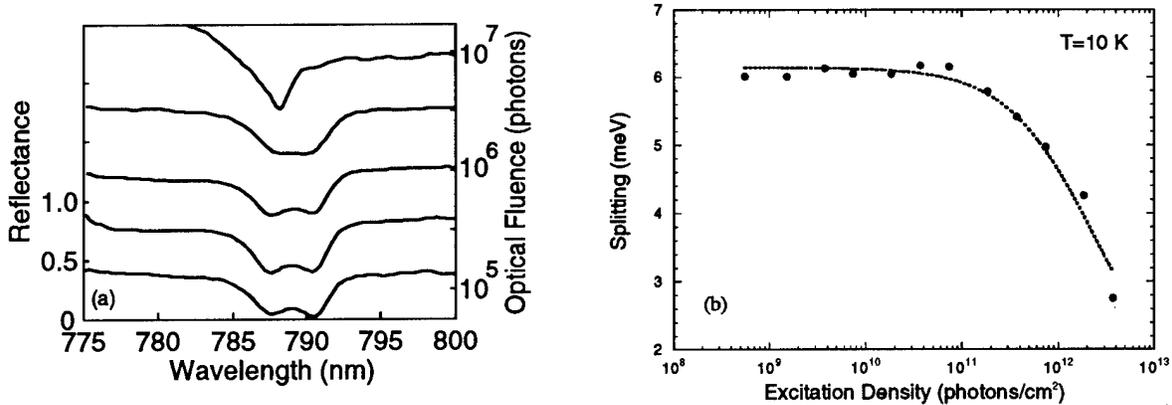
FIG. 1. Normalized reflectance spectra at high optical fluences, (a), and excitation-intensity-dependent VRS, (b), extracted from data (a). The laser was resonant with the exciton–cavity resonance.

where, f_S is the excitonic transition oscillator strength per unit area per quantum well, N the number of quantum wells, and L_C the effective cavity length. In quasi-thermal equilibrium, the areal oscillator strength f_S at higher excitation regimes can be expressed with a well-known simple saturation model by introducing the exciton saturation density n_s [5]:

$$f_S = \frac{f_{S0}}{1 + n/n_s}, \qquad (2)$$

where f_{S0} is the linear areal oscillator strength, and n the EHP density. Note that the VRS is a function of the integrated oscillator strength over the transition linewidth. Thus the VRS is not affected by the peak oscillator strength reduction due to linewidth broadening by exciton-exciton interaction in the low excitation regime ($n < 10^{11}$ excitons/cm^2) [6]. Using (1) and (2), one can find a saturation optical fluence of 9×10^{11} photons/cm^2. From our linear reflectivity spectra and calculated DBR reflectance, we find 18 % absorption of the incidence light. Thus we find for the exciton saturation density $n_s \cong 3 \times 10^{10}$ excitons/cm^2 in good agreement with the theoretical values ($n_s = 2.2 \times 10^{10}$ excitons/cm^2) [5,7]. However, note that the saturation optical fluence is reduced by factor of 4 with respect to the bare QW (without a cavity) due to presence of the cavity.

In order to study the dynamics of nonlinear VRS, we performed pump-probe experiments with on- and off-resonant excitation. For the on-resonance experiment, laser pulses from the Ti:sapphire oscillator were split into pump and probe beams, and the probe spectrum was recorded as a function of delay with respect to the pump. The pump optical fluence for the data shown here was 5.6×10^{10} photons/cm^2. Fig 2.(a) shows typical reflected probe spectra and (b) shows the time-dependent VRS. The initial fast recovery of the VRS is associated with coherent polariton radiation so that most energy stored in the exciton-cavity system is coherently reradiated within the polariton decay time (260 fs) [2]. The VRS then recovers with a time constant of about 35 ps as the incoherent exciton population formed by dephasing decreases due to radiative decay and possibly due to ionization of excitons. Note that the strong coupling between the exciton and cavity enhanced the speed of the nonlinear response even at low temperatures.

In the off-resonant-pump experiment, the pump was selected from a white light continuum generated by a 250-kHz Ti:sapphire regenerative amplifier whose central wavelength was
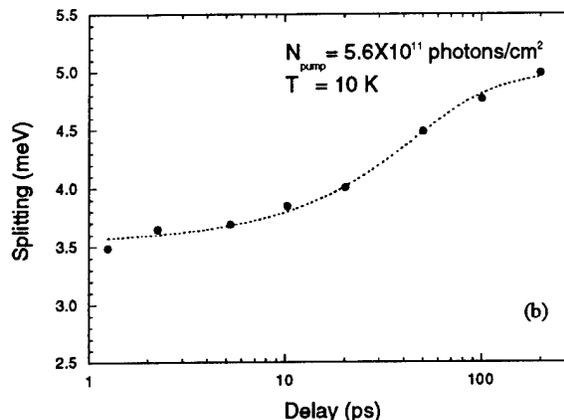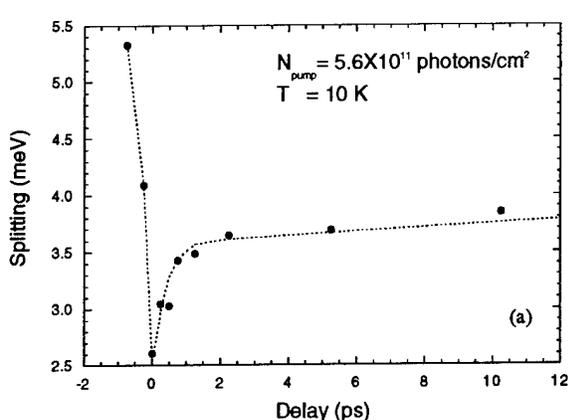
FIG. 2. Time-resolved VRS by pump-probe experiment with on-resonance pump near zero time delay, (a), and in long time delays, (b). VRS's are extracted from normalized reflection spectra of the probe. Dashed curves are guides to the eye.
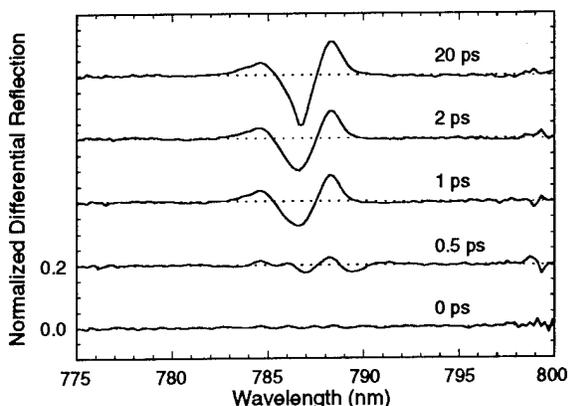
FIG. 3. Time-resolved differential reflection spectra with off-resonant pump. Each curve is normalized with incident probe spectrum. The probe was on-resonance with exciton–cavity resonance. The pump spectrum was selected at 750 nm with 10-nm bandwidth from a white light continuum, so as to excite $Al_{0.2}Ga_{0.8}As$ barrier region. The excitation fluence was 2.7×10^{13} photons/cm^2. The sample temperature was 14 K.

tuned to the exciton-cavity resonance. The pump photon energy was selected just above the high-energy-side edge of the DBR mirror range. This energy level corresponds to the $Al_{0.2}Ga_{0.8}As$ barrier region. Thus we excite EHP in both barriers and quantum wells. Within about 2 ps, free carriers excited in the quantum well relax to the band edge and bleach the exciton oscillator strength. Subsequently, carriers in the barrier region are captured in the quantum wells and slightly increase the degree of saturation in about 50 ps. The relaxation of the saturation in this case is now governed by the carrier lifetime, unlike the resonant-pump case. No evidence was observed in either resonant or off-resonant excitation of higher-lying states of the Jaynes-Cummings ladder.

[1] C. Weisbuch, M. Nishioka, A. Ishikawa, and Y. Arakawa, Phys. Rev. Lett. 69, 3314 (1992).
[2] T. B. Norris, J.-K. Rhee, C.-Y. Sung, Y. Arakawa, M. Nishioka, and C. Weisbuch, Phys. Rev. B 50, to be published in November (1994).
[3] R. Houdré et al., Phys. Rev. B 49, 16761 (1994).
[4] J. M. Jacobson et al., in International Quantum Electronics Conference, Vol. 9, 1994 OSA Technical Digest Series(Optical Society of America, Washington, D.C., 1994), postdeadline paper QPD21, pp. 50–51.
[5] S. Schmitt-Rink, D. S. Chemla, and D. A. B. Miller, Phys. Rev. B 32, 6601 (1985).
[6] D. R. Wake, H. W. Yoon, J. P. Wolfe, and H. Morkoç, Phys. Rev. B 46, 13452 (1992).
[7] K.-H. Schlaad et al., Phys. Rev. B 43, 4268 (1991).

Measurements of Spontaneous Emission Factor in Electrically Pumped Microcavity Lasers

Rajeev J. Ram, Edgard Goobar, Matt Peters, Larry A. Coldren and John E. Bowers

Department of Electrical and Computer Engineering, University of California, Santa Barbara, CA 93106

TEL:(805)893-4235   FAX:(805)893-3262

Enhancement of spontaneous emission coupling (β) into the lasing mode has promised significant reductions in lasing thresholds and absolute intensity noise for microcavity lasers [1,2]. This control is typically achieved by employing high finesse, wavelength scale resonators. Measurements of β have been made in optically pumped devices with various resonator geometries: These include planar DBR resonators (β=0.009 at 4 K [2]), large-diameter post resonators (β=0.004 at 4 K [2]), hemispherical microcavities (β=0.01 at 4 K [3]) and micro-disk lasers (β=0.23 at 77 K [4]). This paper reports the first measurements of β in *electrically* pumped vertical cavity devices as well as the first measurement of β in surface emitting lasers with strong transverse photon confinement.

By definition β is the fraction of spontaneous emission current that is emitted into the lasing mode:
$\beta = (I_{sp}\big|_{laser})/(I_{sp}\big|_{total})$. If we explicitly include the fact that the spontaneous emission rate into the lasing mode is equal to the stimulated emission rate when the cavity contains a single photon, we can express the spontaneous emission factor as $\beta = I_{st}\big|_{p=1}/I_{sp}\big|_{total}$. For the simple case of a linear gain model and a constant carrier lifetime the expression reduces to the well known form [5]

$$\beta = \frac{I_{st}\big|_{p=1}}{I_{sp}\big|_{total}} = n_{sp}\frac{g_o(N-N_o)v_g}{V_{ac}N/\tau_{sp}}$$

$$= \frac{N}{N-N_o}\frac{g_o(N-N_o)v_g}{V_{ac}N/\tau_{sp}} = \frac{g_o v_g \tau_{sp}}{V_{ac}}$$

Under these simplifying assumptions β is found to be independent of carrier density. A realistic gain model, however, shows that β is explicitly dependent on the carrier density and therefore the bias level. Using a logarithmic gain model and bimolecular recombination we see that

$$\beta = \frac{I_{st}\big|_{p=1}}{I_{sp}\big|_{total}} = n_{sp}\frac{g_o \ln(N/N_o)v_g}{V_{ac}BN^2}$$

From this expression we can see that the spontaneous emission coupling factor explicitly depends on the carrier density: as the carrier density increases the spontaneous emission factor decreases. This occurs because the total spontaneous emission rate increases faster than the gain and in addition the increased inversion reduces n_{sp}. We find that the dependence of β on the carrier density overwhelms many of the expected advantages of smaller resonator dimensions.

The measured devices have cylindrical post geometries where the top
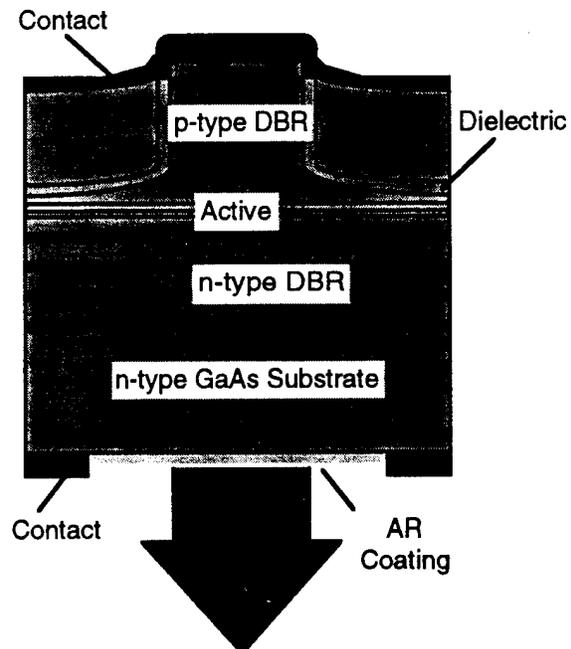
Fig.1 Resonator structure for vertical cavity lasers.

mirror has been etched up to the top cladding layer. This scheme provides

significant optical confinement of the spontaneous emission while avoiding non-radiative surface recombination. The n-type bottom mirror consists of 16.5 AlAs/GaAs periods. A 18 nm linear grading is used between the compositions. The Si doping level is 1×10^{18} cm^{-3} with 5×10^{18} cm^{-3} pulsed doping at the interfaces. The active region consists of 0.12 µm $Al_{0.5}Ga_{0.5}As$ confinement layers surrounding a gain region with three 8 nm $In_{0.185}Ga_{0.815}As$ QWs with 8 nm GaAs barriers. The p-type mirror consists of 30 periods of $Al_{0.67}Ga_{0.33}As$/GaAs layers. In order to flatten the band-gap discontinuity a band-gap engineered 15 nm linear grading with 1×10^{18} cm^{-3} delta doping is used [6]. Finally, the device is capped with 45 nm p^{+} GaAs contact layer. The calculated mirror reflectivities for the top and bottom mirrors are 99.9% and 98.9%, respectively.

The sample is mounted (top-side down) on a cold finger cryostat. A probe mounted on a three axis manipulator is used to test different devices, and a 50 µm multimode optical fiber is positioned under the sample. The fiber, which is typically placed 0.5 mm from the bottom mirror, has a numerical aperture of 0.2. Below threshold this limits the collection of the spontaneous emission to a divergence angle which approximates that of the cavity mode. The spontaneous emission into the lasing mode is measured by

spectrally filtering the light by adjusting the resolution bandwidth (RBW) of an optical spectrum analyzer. The cavity mode and gain peak are optimally aligned at 130 K (Fig. 2). The threshold carrier density is near minimum at this heatsink temperature for both devices. The threshold current density is significantly higher for the smaller devices.

Fig. 3 shows light vs. bias current measurements for a cavity with 3 µm diameter post. Measurements were conducted at 126K and at 71K. In Fig. 4 similar results are shown for a cavity with a 9 µm diameter post. In both measurements the RBW=0.2nm. β at threshold is estimated by measuring the change in the differential efficiency
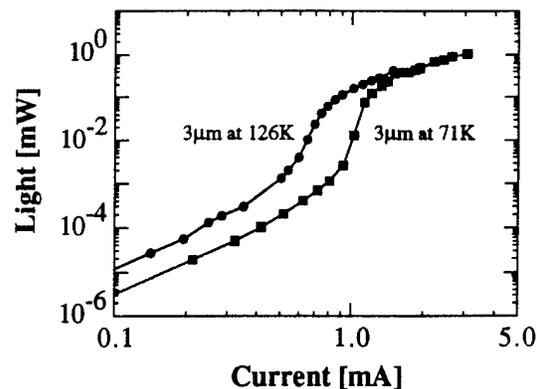
Fig 3. Light versus current for 3 µm diameter devices at heat-sink temperatures of 126 K (optimal detuning) and 77 K.

Fig 2. Threshold current versus heat-sink temperature for 3 µm and 9 µm post diameter structures.
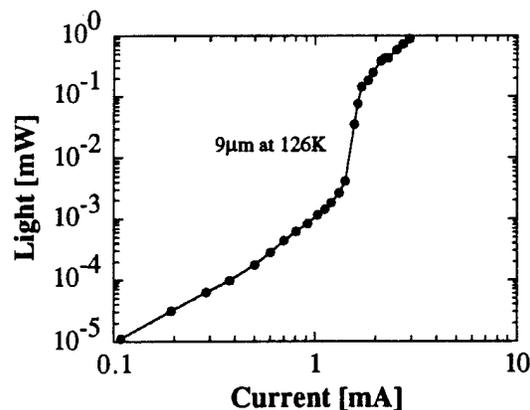
Fig 4. Light versus current for 9 µm diameter devices at heat-sink temperatures of 126 K (optimal detuning).

immediately above and below the lasing threshold. The actual value of β is 0.5 times the change in the differential efficiency since both orthogonal polarizations are collected below threshold whereas lasing occurs in a single polarization. For both devices $\beta \approx 1 - 5 \times 10^{-3}$ is observed, with the 3µm device at 126K having a nominally higher β.

Due to the cavity-gain detuning, operation of the 3 µm device at 71 K almost doubles its threshold current and carrier density. This should render a slight decrease in β. There is an additional decrease in β resulting from the slightly greater gain-cavity detuning at threshold for the 3 µm device at 71 K.

Increasing the device dimension to 9µm is expected to cause more than an order of magnitude decrease in β [7]. The measured values, however, indicate at most a factor of 2 decrease, the dominant cause for this is the significantly lower carrier density in the 9 µm device.

In conclusion, we have measured for the first time the spontaneous emission coupling factor in electrically pumped vertical cavity lasers. The measured values varied from $\beta \approx 1\text{-}5 \times 10^{-3}$ for several device diameters and detunings. It is thought that the small variations in β can be attributed to the increase in carrier density for small resonator diameters. The dependence of β on carrier density presents a serious limitation for practical microcavity devices.

References

[1] Y. Yamamoto, ed. *Coherence, Amplification and Quantum Effects in Semiconductor Lasers*, New York: John Wiley & Sons, 1991.

[2] G. Bjork, *et al.*, "Spontaneous emission coupling factor and mode characteristics of planar dielectric microcavity lasers," *Phys. Rev. A,* vol. 47, 4451 (1993).

[3] F.M. Matinga, *et al.*, "Low-threshold operation of hemispherical microcavity single-quantum-well lasers at 4 K,"

Appl. Phys. Lett., vol. 62, 443 (1993).

[4] R.E. Slusher, *et al.*, "Threshold charactersistics of semiconductor," *Appl. Phys. Lett.*, vol.63, 1310 (1993).

[5] G. Bjork, *et al.*, "Analysis of semiconductor microcavity lasers using rate equations," *IEEE J. Quant. Electron.*, vol. 27, 2386, (1991).

[6] M.G. Peters, *et al.*, "Vertical-Cavity Surface-Emitting Laser Arrays, *SPIE Proceeding Series*, vol. 2147, (1994).

[7] Baba, *et al.*, "Spontaneous emission coupling factor of a microcavity surface-emitting laser," *IEEE J. Quant. Electron.*, vol. 27, 1347, (1991).

Radiation Pattern of Spontaneous Emission
from Microcavity DBR Surface Emitting Lasers

Tetsuko Hamano, Fumio Koyama and Kenichi Iga

P & I Laboratory, Tokyo Institute of Technology

4259 Nagatsuta, Midori-ku, Yokohama 226 Japan

Phone: +1-81-45-924-5026   Fax: +1-81-45-921-0898

I. Introduction

The control of spontaneous emission in microcavity has been extensively studied in order to search for ultimate performances of vertical-cavity surface emitting lasers (VCSELs) such as ultra-low threshold operation [1,2], high-speed modulation and so on. It is interesting to investigate the radiation characteristic from microcavity DBR, and some works on planar microcavity (PLMC) were studied theoretically and experimentally [1-3]. From their results, it is reported that the radiation patterns from PLMC were not isotropic due to the modification of the standing waves in the microcavity, and that the patterns are dependent on the detuning of cavity resonant wavelength and emission peak wavelength. However, we cannot apply such radiation characteristic from PLMC for a microcavity VCSEL that has a finite cavity in all the direction. To study the radiation pattern from a microcavity VCSEL, therefore, we may assume a post-type or pillar-type three-dimensional microcavity (3DMC) whose mesa size is also comparable to several wavelengths long (~a few microns).

In this paper, we present the radiation pattern, especially the far field pattern (FFP) of spontaneous emission from the 3DMC VCSEL calculated by numerical analysis. The FFP is determined by the spectral relation of the (cavity resonant) mode density distribution and the spontaneous emission spectrum. We show that the calculated FFP is dependent on either of mesa size, wavelength detuning, and the spectral width of emission spectrum. This analysis seems similar to the transverse mode analysis of VCSEL but much different by their structures and assumptions.

II. Calculation and Results

Figure 1 shows the structure of 3DMC for calculation, which represents the fabricated VCSEL [4]. In the z direction, it consists of a one-wavelength long cavity, including a single quantum well in the middle sandwiched by a pair of high-reflective semiconductor DBRs. In the xy plane, a square mesa is fabricated whose size is assumed to be around a micron.

The radiation field can be expressed by summing up the electromagnetic waves of all the modes overlapped within the spontaneous emission spectrum. We have already presented the mode density distribution of the 3DMC shown in Fig. 1 in the k space [5, 6], and we have found that there exist Bragg resonant mode, leaky mode and guided mode. Since FFP is observed out of the VCSEL in the air in this case, we take into account of the mode in the diffraction limit determined by the total reflection angle between the semiconductor and the air. We see that the actual spectral width of the spontaneous emission spectrum expressed by Lorentzian function is several 10nm, while the spectral width of the Bragg

resonant mode is around several Å. And its peak mode density is larger than that of leaky modes by factor of 2. That can allow us to neglect to count on the leaky modes and to assume that the radiation field contains only Bragg resonant modes, when the peak wavelength of emission spectrum is fixed around the Bragg resonant modes.

Figures 3 and 4 show the calculated FFP under mesa sizes ~0.8μm square and ~1.3μm square, respectively. The x and y axes represent the angle from the z axis in the air, and the intensity of FFPs is normalized by the peak intensity of the emission spectrum when it is delta function. We also show the schematic relation between the cavity resonant modes and the emission spectra in the figures (in Figs. 2(c) and 3(d)). In these cases, we notice that four Bragg resonant modes contribute to the radiation field from the cavity of ~1.3μm square mesa, while only one from ~0.8μm square.

First, we can compare the FFPs of different mesa sizes under the emission peak wavelength tuned on the (0, 0)-Bragg resonant wavelength and the spectral width of the spontaneous emission spectrum $\Delta\lambda_s$ fixed at 30nm. Since it has only one radiation mode, the microcavity of ~0.8μm square mesa has a single peak FFP, shown in Fig. 2(b). On the other hand, when the cavity has ~1.3μm square mesa, we see that it has also a single peak FFP but not sharper as shown in Fig. 3(c). It is because that the microcavity has three more resonant modes in the shorter wavelength range than (0, 0)-mode's. The radiation field is obtained by the summation of four eigen radiation fields whose combination probabilities are valued by the Lorentzian function of the emission spectrum at their own resonant wavelengths.

Secondly, we can compare under the wavelength detuning. Here, the cavity resonant wavelength is fixed by cavity mesa size, so that the emission peak wavelength is varied in this analysis. The FFPs for ~0.8μm square mesa and $\Delta\lambda_s$=30nm have single peaks along the detuning, as shown in Fig. 2. The FFPs in Fig. 3, however, show that they can be varied along the detuning, since it depends on the overlapped resonant modes.

We also see the variation of FFP against the different spectral width of emission spectrum. Even though the microcavity has multiple radiation modes, we see that the single peak FFP can be obtained under the narrower spectral width.

III. Summary

In summary, we present the FFP of spontaneous emission from 3DMC VCSEL. We find that we can expect the single peak FFP of spontaneous emission due to the three-dimensional microcavity DBR that provides large interval between radiation modes in the k space.

Reference
[1] Y. Yamamoto, S. Machida, K. Igeta and G. Björk: Coherence, Amplification and Quantum Effects in Semiconductor Lasers, ed. Y. Yamamoto (Wiley, New York, 1991) pp. 561-615. [2] M. Yamanishi: Jpn. J. Appl. Phys. 31, 2764 (1992). [3] D. L. Huffaker, C. Lei, D. G. Deppe, C. J. Pinzone, J. G. Neff and R. D. Dupuis: Appl. Phys. Lett. 60, 3203 (1992). [4] J. L. Jewell, S. L. McCall, A. C. Gossard and J. H. English: Appl. Phys. Lett. 51, 94 (1987). [5] T. Baba, T. Hamano, F. Koyama and K. Iga: J. Quantum Electron. 27, 1347 (1991). [6] ibid.: J. Quantum Electron. 28, 1310 (1992).
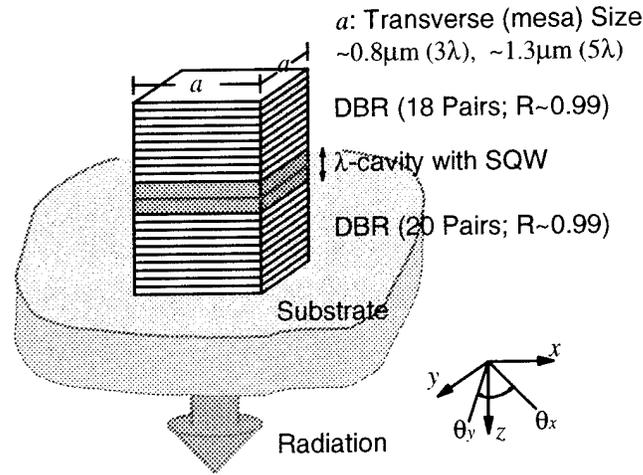
Figure 1: Schematic structure of three-dimensional microcavity DBR surface emitting laser

$a \sim 0.8 \mu m$ @$\Delta\lambda_s$=30nm

(a) λ_s=0.99λ_{00}

(b) λ_s=λ_{00}

(c) Resonant modes and spontaneous emission spectra
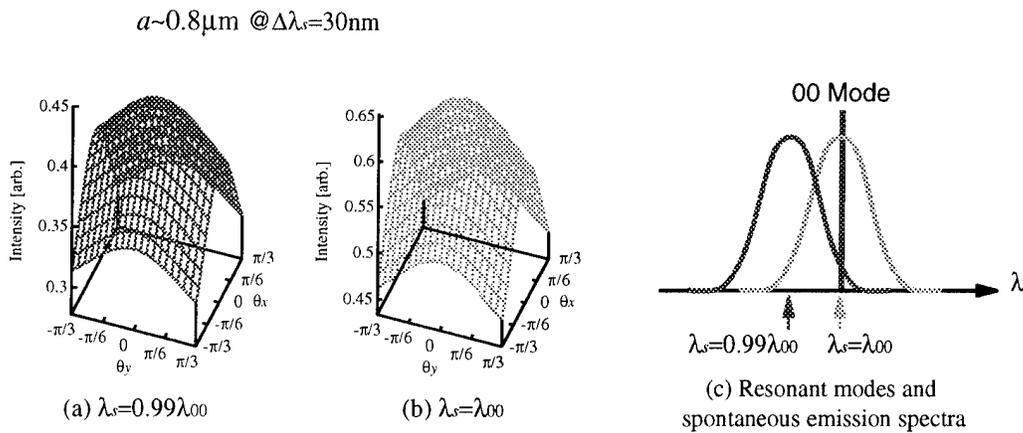
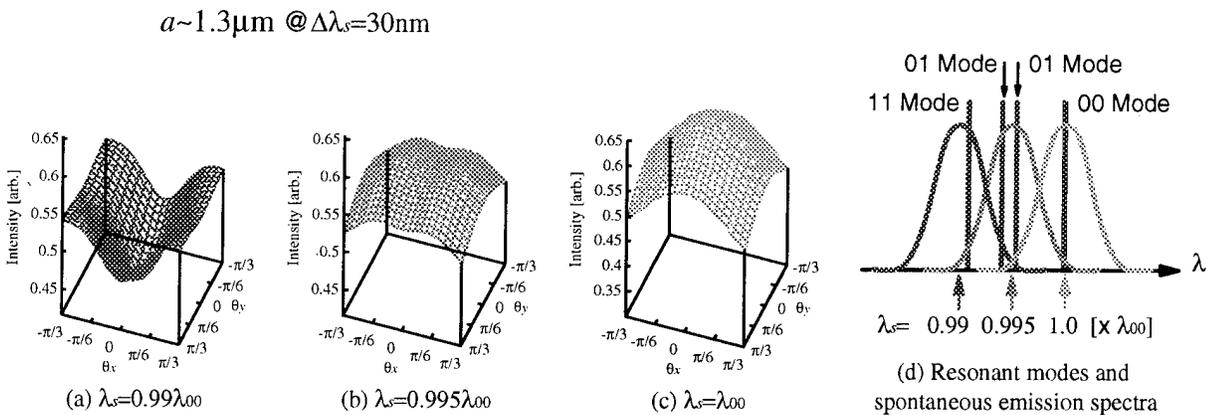Figure 2: Calculated far field patterns of spontaneous emission in the air, from the microcavity of ~0.8μm square mesa

$a \sim 1.3 \mu m$ @$\Delta\lambda_s$=30nm

(a) λ_s=0.99λ_{00}

(b) λ_s=0.995λ_{00}

(c) λ_s=λ_{00}

(d) Resonant modes and spontaneous emission spectra

Figure 3: Calculated far field patterns of spontaneous emission in the air , from the microcavity of ~1.3m square mesa

New Materials for Quantum Optoelectronics

QThB 10:30 am-12:00 m
Ballrooms VI-VIII

Richart E. Slusher, *Presider*
AT&T Bell Laboratories

Characterization and optical device applications of porous silicon

H.Münder

Institute of Thin Film and Ion Technology, Forschungszentrum Jülich GmbH, D-52425 Jülich, Germany

The electrochemical process used to form porous Si layers (PSL) is known for more than 30 years. The spongelike microscopic structure of PSL depends on the substrate properties, the doping concentration and the type of doping, as well as on the etching parameters. The pore size can range from μm to nm depending on the substrate parameters. For a given doping concentration the porosity can be varied by changing the current density. E.g., for $p = 10^{19}cm^{-3}$ the porosity can be varied from about 30 to 80% by changing the current density from 10 to 250 mA/cm^2. The remaining Si structure is still single crystalline. Therefore, PSL have been used as patterned substrates for the heteroepitaxial growth of III-V layers on Si wafers. In addition, PSL can be used for the formation of silicon-on-insulator (SOI) structures.

Until 1990 applied research was mainly motivated by these applications for porous Si. At that time research groups all over the world started to investigate PSL in more detail due to reports showing the photo- and electroluminescence of PSL at room temperature. During the last years more than 15 different models were developed to explain the luminescence behaviour of PSL. Some of these models were based on a certain chemical species in the porous layers. Part of the confusion was due to ageing effects because of the high chemical reactivityand the enormous specific surface of the samples. Careful chemical analysis show that freshly prepared PSL consist only out of Si and H. Nowadays, the discussion focuses on two models - the pure quantum size model and the quantum size model including surface states.

Although the mechanism of the luminescence is not yet clear electroluminescent devices are fabricated. The simple structure of these devices is a microporous layer with a semitransparent top contact. The material for the top contact can be a thin layer of Au or a transparent conductive oxide (ITO). The maximum of the typical electroluminescence spectra is in the red spectral range.

As already mentioned the microstructure depends first on the doping of the substrate and secondly, on the parameters of the etching process. The microstructure of PSL has been investigated by Raman spectroscopy. Due to the small size of the nanocrystallites a strong phonon confinement occurs which results in an asymmetric broadening of the phonon peaks in the Raman spectra. Size distribution functions can be obtained by a detailed analysis of the phonon peak. On p^+-doped substrates the mean diameter of the nanocrystallites is about 6nm whereas on p-doped substrates the mean diameter is less than 3nm. The different microstructures of course result in different optical properties of PSL. E.g., the dielectric function which has been measured by spectroscopic ellipsometry on p^+-doped PSL is dominated by a reduction of the height of the imaginary part. In addition, a broadening of the spectral features compared to the single-crystalline Si is observed. For p-doped PSL a completely new dielectric function is found which is

characterized by a reduction of the height of the imaginary part as well as by a complete lost of the E'_0 and E_1 gap features. These behaviours can not only be studied by spectroscopic ellipsometry but also by reflectance measurements. The spectral shape of the reflectance differs drastically from the one of single-crystalline Si.

For the simulation of the reflectance the complex micro-topology of PSL must be considered. This can only be done within the advanced Bergman effective medium model. However, it has been shown that the dielectric function of Si nanocrystallites can not be described by the dielectric function of crystalline Si. Therefore, a new artifical dielectric function based on the model of Forouhi and Bloomer is used for the Si nanocrystallites in the simulation of the reflectance spectra. By this technique a mathematical description of the optical properties for a set of PSL with various porosities and microstructures is obtained.

The first step towards microoptical devices has been the formation of superlattices with layers of two different porosities and / or microstructures [1,2]. The porosity of PSL formed on homogeneous doped substrates is controlled by the current density during the electrochemical process. Switching the current density periodically between two values will result in a superlattice structure (type I). On the other hand using periodically doped substrates in combination with a constant current density will also result in the formation of a superlattice structure (type II). In the type II structures four layers with different porosities have been found although only two porosities have been expected [3]. This complicated behaviour can be explained due to the high selectivity of the etch process in different doped layers. Therefore, microoptical devices can be better fabricated by changing the current density. For these structures it is possible to simulate the optical behaviour based on the data obtained in the way described before.

Using the technique of changing the current density Bragg reflectors and Fabry-Perot filters have been fabricated. Due to multireflections and interference effects the reflectivity of Bragg reflectors build up by different porous Si layers can be become very high. In the red spectral range reflectance values as high as 99% have been measured. In the infrared spectral range those structures can show values high than Au films. In addition, changing the optical thickness of the different porous layers offers the possibility to design Bragg reflectors for different spectral ranges in an easy controllable manner. Possible applications could be a burried filter under a light emitting PSL. A test structure with a Bragg reflector formed below a high luminescent PSL result in an increase of the PL intensity by a factor of 1.5. This suggests that Bragg reflectors below electroluminescent layers will increase the brightness of those light emitting devices by 50%.

Fabry-Perot filters have also been formed by changing the current density during the formation process of the porous layer. A simple detector structure could be build up by a Fabry-Perot transmission filters above a conventional pn-junction. The optical properties of the filter would be the key factor for the spectral sensitivity of the detector. Reflectance measurements on Fabry-Perot structures show a minimum of reflectivity of 12% at the transmission maximum of the filter

and 86% at the transmission minimum. Due to the fomation of a native oxide film on the pore walls the filter characteristics changes with time. It has been shown that this problem could be solved by a controlled thermal oxidation step. By an oxidation step at 300°C for 20min a long term stability of the optical properties of Fabry-Perot filters has been achived.

Another possible application of porous multilayer systems are waveguides. The waveguiding effect of porous Si multilayers has been shown. This suggests that passive and active microoptical devices can be fabricated on a single Si wafer. Light emitting porous Si structures can be connected to detectors or optical fibres by waveguides build up by porous Si multilayers.

Microoptical devices can be fabricated by using a standard photolithography process. Device structures with lateral diameters less than 10 μm have been fabricated. For such small structures the underetching of the photoresist becomes an important problem. In addition, during the selective area formation of porous Si an inhomogeneous current density occurs. Beside this also the diffusion process of the reactive species in the etch solution becomes important. Both effects result e.g. in higher etching rates at the edges of porous Si microstructures. Therefore, the optical properties of these structures show inhomogeneities. Concepts to optimize the homogeneity of the optical properties have been developed and are still under investigation.

The fabrication of filters, Bragg reflectors and waveguides by using porous Si multilayers show that possible applications of porous Si will not only be related to the electroluminescent properties of this material. The selctive area formation of PSL show that microoptical devices can be fabricated.

REFERENCES

[1]   H.Münder, M.G.Berger, C.Dieker, M.Thönissen, H.Lüth, W.Theiß, P.Grosse, in *Proceedings of 4th International Conference on the Formation of Semiconductor Interfaces*, World Scientific Publishing, Singapore, New Jersey, London, Hong Kong

[2]   M.G.Berger, C.Dieker, M.Thönissen, L.Vescan, H.Lüth, H.Münder, J. Phys. D: Appl. Phys. **27**, 1333 (1994)

[3]   M.G.Berger, M.Thönissen, R.Arens-Fischer, H.Münder, H.Lüth, M.Arntzen, W.Theiß, Thin Solid Films, in press

Exciton Confinement in Organic Multiple Quantum Wells

S. R. Forrest, E. I. Haskal, Z. Shen and P. E. Burrows
Advanced Technology Center for Photonics and Optoelectronic Materials
Department of Electrical Engineering
Princeton University
Princeton, NJ 08544

It has recently been shown that ordered, organic thin films of planar stacking molecules can be grown with monolayer uniformity and control over large substrate distances by the ultrahigh vacuum process of organic molecular beam deposition (OMBD). Due to this ability to grow films with such a high degree of order, it was demonstrated by So, et al[1,2] that multiple quantum well stacks consisting of alternating layers of the archetype compounds, 3,4,9,10 perylenetetracarboxylic dianhydride (PTCDA) and 3,4,7,8 naphthalenetetracarboxylic dianhydride (NTCDA) exhibit exciton quantum confinement. That is, energy shifts in the absorption spectrum, as well as time resolved photoluminescence indicates systematic changes with layer thickness, as the thickness is reduced from 500Å to 10Å. While these early data were compelling, they opened up many questions as to the nature of excitons in closely packed organic molecular systems. Hence, in this work, we have extended this early investigation by measuring the electroabsorption, the absorption and the fluorescence spectra of organic MQW stacks consisting of PTCDA+NTCDA, as well as 3,4,9,10 perylenetetracarboxylic-bis-benzimidazole (PTCBI)+NTCDA. These new investigations provide further information essential to understanding the nature of excitons in these van der Waals-bonded molecular solids.

Measurements of the electroabsorption (EA) spectrum obtained both parallel and perpendicular to the molecular stacking direction indicate that the lowest energy observed excitons in PTCDA are approximately spherically symmetric, with a radius of roughly 13Å. This value is consistent with measurements inferred earlier using the MQW absorption and time-resolved luminescence spectra of So and co-workers[2]. The EA spectra indicate both a mixture of excitonic line broadening due to charge-polarization effects as well as line shifting due to the Stark effect. These data suggest that the lowest energy observed exciton in the spectrum of PTCDA is an extended charge-transfer state. PTCBI excitonic spectra did not show strong EA effects, possibly due to the relatively tightly bound Frenkel-like state which exists in this material. PTCBI differs from PTCDA in that the intermolecular stacking distance and the presence of several different isomorphs of the former compound make it unlikely to support highly extended excitonic states, as is the case for PTCDA.

Further investigations of the low temperature fluorescence (LTF) spectra obtained for PTCDA+NTCDA MQWs indicate a systematic blue shift in the phonon energy of PTCDA, as well as a monotonic shift to higher energy of the full LTF spectrum as the PTCDA layer thickness is decreased. Both of these shifts are found to result from the effects of quantum confinement of the exciton state which, through exciton-phonon coupling, also results in systematic shifts in the intramolecular phonon energy within the PTCDA molecules. A quantitative analysis of the relationship between the Franck-Condon shift and the phonon energy of the dominant vibronic mode in the ground state of PTCDA gives an exciton-phonon coupling constant of $\gamma > 2000$ cm^{-1} which is independent of layer thickness. This independence of γ with layer thickness suggests that the structure of even the thinnest films of PTCDA (10Å) is the same as for much thicker, "bulk-like" films. By

comparison, PTCBI+NTCDA MQW LTF spectra show none of the pronounced energy shifts of the PTCDA+NTCDA spectra, once again suggesting that excitons in PTCBI are tightly bound to the molecules, consistent with their Frenkel-like character.

The extended excitons characteristic of tightly-packed planar molecular structures such as PTCDA strongly suggests that this class of organic molecular crystals might have optoelectronic properties analogous to those of inorganic semiconductor MQWs. Indeed, our theoretical modeling of such systems indicate the possibilities for large nonlinear optical effects which might find use in optical switching applications. The results of these theoretical treatments, as well as the performance of optical devices fabricated from such structures will be presented in this talk.

1. "Quasi-Epitaxial Growth of Organic Multiple Quantum Well Structures by Organic Molecular Beam Deposition," F. F. So, S. R. Forrest, Y. Q. Shi and W. H. Steier, *Appl. Phys. Lett.*, 56, 674 (1990)
2. "Evidence for Exciton Confinement in Crystalline Organic Multiple Quantum Wells," F. F. So and S. R. Forrest, *Phys. Rev. Lett.*, 66, 2649 (1991)

Ultrathin Porous Silicon Films: Physics & Device Applications

P.M. Fauchet, J. von Behren, L. Tsybeskov, Y. Kostoulas and K.B. Ucer

Department of Electrical Engineering
University of Rochester NY 14627

Voice: (716) 275-1487
Fax: (716) 275-2073
email: fauchet@ee.rochester.edu

We have manufactured thin films of light-emitting porous silicon (LEPSi) by electrochemical etching in HF and subsequently lifted them off the silicon wafer by an electropolishing step [1]. The film thickness was varied from 100 μm to 0.1 μm and the porosity ranged from < 40% to ≥ 90%. To insure the structural integrity of the thinner, higher porosity films, they were deposited on sapphire windows where they remain attached by van der Waals or electrostatic forces, in a manner reminiscent of earlier work with ultrathin film of III-V semiconductors [2]. The microstructural, chemical and optical properties of these films have been investigated using a variety of tools, including AFM, XRD, FTIR, cw and time-resolved absorption and luminescence measurements. These films are optically flat, do not scatter light, and show pronounced Fabry-Perot interference fringes in the transparency region which can extend to photon energies well above the bandgap of crystalline silicon (see Fig. 1). The refractive index can be lower than 1.3 for high porosity films, in qualitative agreement with the predictions of a simple effective medium theory.

Figure 2 compares the absorption coefficient of crystalline silicon with that of two LEPSi films. Even after correction for the porosity, the absorption coefficient of the crystalline silicon skeleton is reduced dramatically, as expected from quantum confinement in nanometer-size quantum wires or dots. The peak of the luminescence spectrum usually occurs in the bandtails and has no clear relation to the onset of absorption. This can explained by considering the fact that the absorption is dominated by the largest nanocrystallites (small bandgap), while the luminescence originates from the smallest crystallites (large bandgap). Since we find that the luminescence spectrum is strongly related to the surface chemistry, we conclude that the luminescence does not correspond to band-to-band or free excitonic recombination, but rather involves surface states. In interferometrically flat samples, the broad luminescence spectrum splits into two or more narrow peaks which result from Fabry-Perot resonances (see Fig. 3).

These films have been used to perform femtosecond time-resolved measurements of the carrier dynamics [3]. Figure 4 shows some typical results. We observed induced absorption and not bleaching at all probe wavelengths. This demonstrates that LEPSi remains an indirect gap semiconductor and implies that the high luminescence efficiency does not result from a fast radiative lifetime (the PL lifetime is >> 1 μsec) but rather from an excellent surface passivation

which leads to the absence of non-radiative centers (such as dangling bonds) on the surface. The signal recovery displays two time constants. The subpicosecond recovery is interpreted as trapping by dangling bonds in some of the crystallites. The effective trapping time increases with increasing pumping power. This saturation result from the injection of more than one electron-hole pair per non-radiative recombination center, on average. When this situation is reached, the slow recovery (which appears as a plateau in Fig. 4) becomes markedly faster. We believe that this is evidence for Auger recombination, which is especially efficient when two electron-hole pairs are present in a given nanocrystallite.

Because of their unusual properties, we believe that these LEPSi films can find many uses in technology. Examples of applications include active waveguides, antireflection coatings to low index substrates such as glass, and light-emitting diodes for optical displays. Several examples will be discussed.

References

1. J. von Behren, L. Tsybeskov and P.M. Fauchet, in press
2. T. Gong, W.L. Nighan Jr. and P.M. Fauchet, Appl. Phys. Lett. 57, 2713 (1990)
3. P.M. Fauchet et al, in press
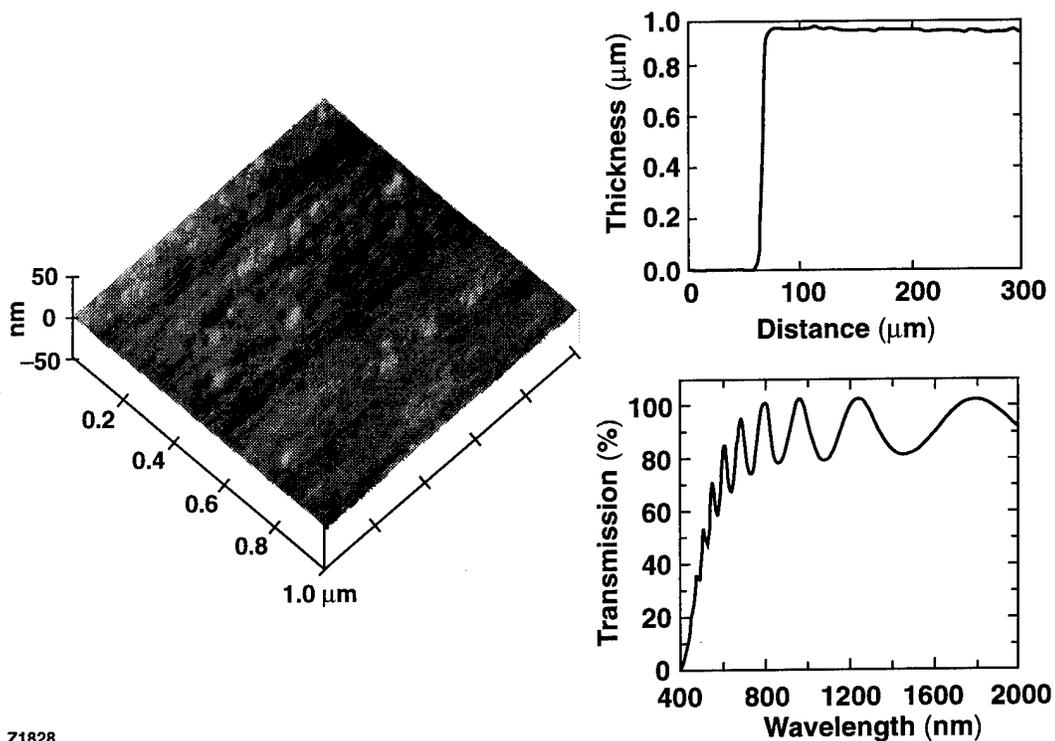
Z1828

Figure 1

Atomic force microscope image, profilometer scan and transmission spectrum of a 0.94 μm thick porous silicon film deposited on a sapphire substrate.
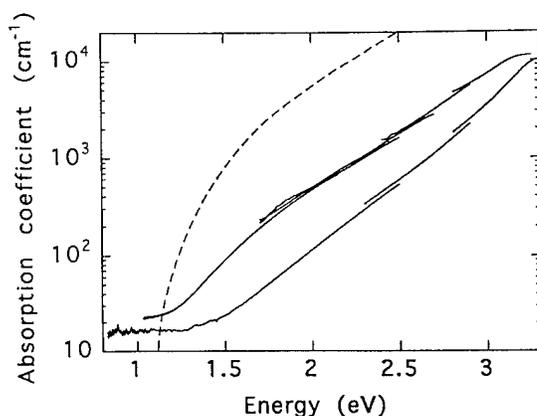
Figure 2

Absorption coefficient of crystalline silicon and two series of LEPSi samples corresponding to a porosity of 40% and 80%. The data are not corrected for the porosity. The effective bandgap increases as the porosity increases, ie, as the average crystallite size decreases. The crystallite size distribution can be inferred from a fit of the absorption spectra. From these fits, we find that the low porosity films contain a significant numbers of large (~10 nm or more) crystallites.
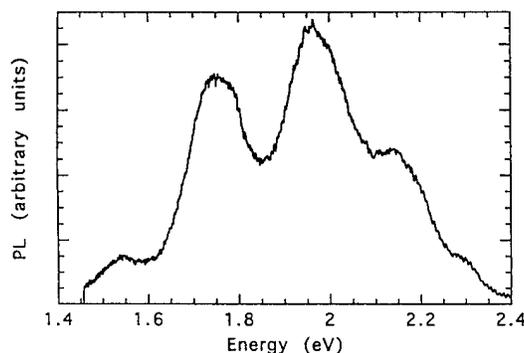
Figure 3

Time-integrated PL spectrum of the film of Fig. 1. The broad spectrum breaks into several peaks produced by multiple interference. The excitation wavelength is 337 nm.
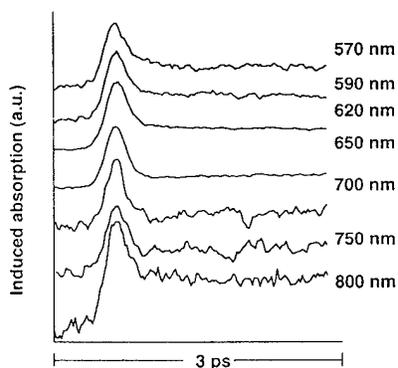
Figure 4

Induced absorption measured for different probe wavelengths after photoinjection with a 100 fs pulse at 2 eV. The film photoluminesces near 1.7 eV and the measurements are performed at room temperature.

Polymers in Optical Microcavities

J. Feldmann, U. Lemmer, R. Hennig, A. Ochse, M. Hopmeier, E.O. Göbel

W. Guss, J. Pommerehne, R. Mahrt, and H. Bässler

FB Physik, FB Physikalische Chemie and Wiss. Zentrum f. Materialwissenschaften

Renthof 5, D-35032 Marburg, Germany

Phone: 49-6421-282122

Fax: 49-6421-287036

The control of the emission properties of light-emitting devices is currently a subject of intense research in the field of inorganic as well as organic semiconductor physics [1]. The possibility to suppress or to enhance the spontaneous emission rate by using optical microcavities [2] is of particular interest, since this can lead to an enhanced light emission [3,4].

In this work we report microcavity effects in two distinct polymer systems. The first system consists of a spin-coated poly(phenyl-phenylenevinylene) (PPPV) layer located between a dielectric mirror and an aluminum mirror. The second system is a spin-coated polymer two-layer structure [5], in which tri(stilbene)amine (TSA) acts as the optically active material. This structure consists of a dielectric mirror with a thin ITO-layer on top, which acts as a hole injector in electroluminescence experiments. Two polymer blend layers have been spin-coated on the ITO-contact. The first hole transport layer is a blend-system of 15% TSA in polysulfone. In a second step we have deposited a thin film of an oxadiazol derivative blended with polystyrene acting as an electron transport layer. Finally, an Al-contact has been evaporated, which serves as the second mirror and as an electron injection contact for electroluminescence experiments.

Both systems show an enhancement of the photoluminescence (PL) within the spectral window defined by the optical $\lambda/2$-mode of the respective cavity. Curve #1 in Fig.1 shows the PL spectrum of a PPPV microcavity sample with a $\lambda/2$-mode at approximately 2.08

eV . The other two curves represent PL spectra of two PPPV reference samples with no mirrors at all (#2) and with only one mirror (#3). Obviously, the PL intensity of the PPPV microcavity sample at 2.08 eV is much higher than the PL intensities of the reference samples at the same photon energy.
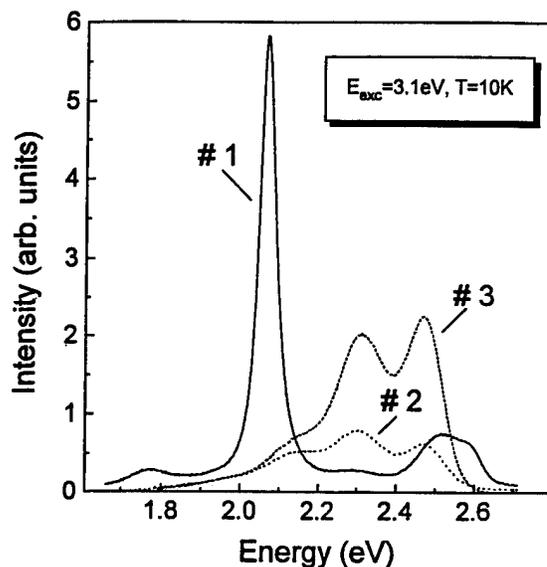
Fig.1: *Time-integrated fluorescence spectra of the PPPV microcavity sample (#1) and of PPPV films of the same thickness without (#2) and with (#3) a backside Al-mirror.*
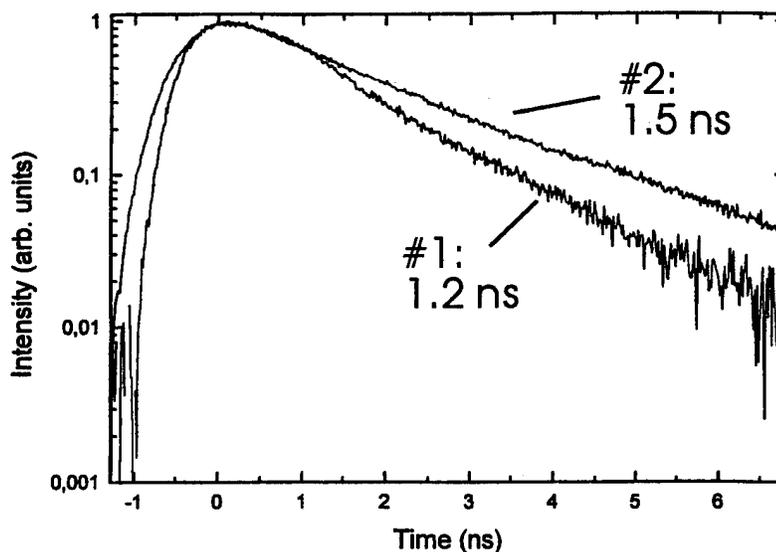
Fig.2: *Time-resolved PL spectra for a detection wavelength of 519 nm corresponding to the cavity mode of the two-layer TSA microcavity and of the two-layer TSA structure without any mirrors.*

Time-resolved PL measurements of the PPPV microcavity and the corresponding reference samples show that the microcavity has no effect on the *overall* lifetime of the PPPV-PL. However, in case of the TSA microcavity a shortening of the PL lifetime is observed. In Fig.2, the PL transients for the TSA microcavity (#1) and for a TSA reference sample without any mirrors (#2) clearly show this effect. The different behavior of the two microcavities is a direct consequence of different ratios between the radiative and the nonradiative recombination rates for the two polymer systems.

For a quantitative understanding of the observed effects the characteristic fluorescence multi-level system, inhomogeneous broadening effects, spectral diffusion and the spatial emission properties have to be taken into account.

We thank the Stiftung Volkswagenwerk for financial support.

1. H. Yokoyama, Science **256**, 66 (1992) and references therein.

2. F. De Martini et al., Phys. Rev. Lett **59**, 2955 (1987) and references therein.

3. A. Ochse et al., International Conference on *Optical Probes of conjugated polymers and fullerenes*, Salt Lake City 1994, to be published in Molecular Cryst. and Liquid Cryst.

4. A. Dodabalapur et al., Appl. Phys. Lett. **64**, 2486 (1994).

5. U. Lemmer et al., submitted for publication.

Quantum Dots

QThC 1:30 pm-3:00 pm
Ballrooms VI-VIII

Israel Bar-Joseph, *Presider*
Weizmann Institute of Science, Israel

Fabrication of Quantum Dots and Nano-scale Observation of Electron-Photon Interaction

Yaushiko Arakawa

University of Tokyo

7-22-1 Roppongi, Minato-ku Tokyo 106 Japan

1. Introduction

Various technological approaches have been performed to fabricate quantum dot structures which are potentially useful for optoelectronic device application and basic physics[1]. One of main goals is to manipulate both electrons and photons in nanostructures and microcavities. Towards this goal, it is important to develop nanofabrication and nano-scale optical characterization techniques.

In this paper we discuss our recent work on the above topics including fabrication of quantum dots, observation of photoluminescence from a single quantum dot, theoretical discussion of phonon bottleneck, fabrication of micorvcavity nanostructure (quantum wire) lasers, and vacuum Rabi-splitting in the microcavities.

2. Fabrication and Spontaneous Alignment of Quantum Dots

The Stranski-Krastanow (SK) growth method is one of promising path for the damage free formation of dot structures [2-4]. The dots are *in-situ* grown without breaking the growth run, maintaining a homogeneous surface morphology and avoiding defect creation. We recently achieved InGaAs quantum dots with the average diameter of 15 nm by MOCVD as shown in Fig.1[5]. We believe this is the smallest quantum dots fabricated by the SK growth mode. The problem inherent in this technique is, however, randomness of distribution of the quantum dots on the surface.

To solve this problem, we demonstrated spontaneous alignment of InGaAs quantum dots using multi-atomic step structures formed in MOCVD growth[6]. In this technique, first, GaAs epilayer with multi-atomic steps along straight lines was grown on vicinal GaAs substrate under appropriate growth conditions. Then the InGaAs quantum dots were grown selectively on the multi-atomic step edges using strain effects. This growth technique results in spontaneously aligned InGaAs quantum dots without any pre-processing technique prior to the growth.

Figure 2 shows AFM images of the quantum dots grown on the [010]-misoriented surface for the InGaAs dots. In the inset, schematic illustration of the growth technique is shown. As indicated in the figure, the InGaAs quantum dots are well aligned at the multi-atomic step edges. The diameter of the quantum dots is less than 20nm.

3. Luminescence form a Signal Quantum Dots

It is important to investigate photon-electron (or exciton) interaction in a single quantum dot. For this purpose the use of the near-field optical microscope is promising to characterize the quantum dot. However, sophisticated experimental system is required and high S/N is difficult to be achieved. On the other hand, the conventional far-field microscope technique is also useful if an appropriate optic system is used. We succeed in observing photoluminescence

from a single quantum dot by using the μ-photoluminescence system and by growing a quantum dot sample in which the distance between each quantum dot is 2μm[7]. Since diameter of the laser beam is focused to be about 0.7μm, only a single quantum dot can be excited in the sample.

Figure 3 shows photoluminescence spectra from a GaAs quantum dot fabricated by MOCVD selective growth technique on SiO2 patterned substrates. The sample was excited by Ar+ laser and detected by photo-multiplier with photon counting mode through a monochromator. As shown in this figure, a single peak is observed with the FWHM of 0.9 meV. By taking excitation power and decay time of photoluminescence into account, the average number of electron-hole pairs is less than one in the single quantum dot. We also succeed in observing time resolved photoluminescence from a single quantum dot using a streak camera with the same μ-photoluminescence system for the first time.

4. Phonon Bottleneck in Quantum Dots: Is this serious problem ?

Inhibition of carrier relaxation into the quantum boxes from barrier region was pointed out a few years ago[8], explaining degradation of luminescence efficiency using this mechanism. However, our theoretical discussion shows that the bottleneck problem can be eliminated through emission of a single LO phonon if the quantum box structures are appropriately designed[9]. The size of the quantum box is designed so that electrons can be directly relaxed into the ground level of the quantum box from the barrier region. In the analysis, instead of Fermi's golden rule, coupled equations in Wigner-Weisskopf theory are used, paying attention to the uncertainty relation between time and energy.

Figure 3 shows the calculated results of the capture rate from barrier region into one quantum box. The results indicate that electrons can interact with LO phonon in wide energy range (~30meV), which implies that energy conservation rule is not maintained in short time regime if the coupling is strong. In addition, the result suggests that extremely precise control of size of the quantum dots is not required. The calculated escape rate is 2×10^{12} 1/s.

5. Fabrication of Microcavity Quantum Wire Lasers

Microcavity structures are expected to substantially reduce the threshold current owing to the controlled spontaneous emission mode. The control of both photon modes and electron modes in confined structures is important for the ultimate light sources. We recently succeeded in fabricating quantum wire laser with vertical microcavity[10].

The quantum wire laser inside the microcavity was fabricated using the selective growth technique. In the microcavity, triangular-shaped $In_{0.3}Ga_{0.7}As$ strained quantum wires are grown between (111)A facets of [011]-oriented GaAs triangular prisms selectively grown on a SiO_2 masked DBR mirror region. The quantum wires are comparatively strained owing to the difference of the lattice constants of GaAs and $In_{0.3}Ga_{0.7}As$. A scanning electron micrograph and a schematic illustration of the cross section of the laser structure are shown in Fig. 2.

The cavity effect is confirmed by measuring photoluminescence with and without the microcavity. A much sharper photoluminescence spectral line was observed from the quantum wires with the microcavity compared to the sample without the cavity. The lasing properties of this sample were measured at 77K, using optical pumping method. Figure 4 shows the output power of the light emitted from the sample as a function of pumping laser power.

6. Vacuum Rabi Splitting in Semiconductor Microcavities

Since the first observation of the vacuum Rabi splitting by our group together with Weisbuch[11], great attention has been received because this is one of relevant new phenomena in the microcavity. The oscillation due to this strong excitonic interaction in the exciton-polariton was also observed in the time domain by Norris and our group[12] Recently nonlinear effects as well as dependence of the interaction on the position and the number of quantum wells were investigated[13,14].

7. Conclusions

Manipulation of photon and electron is important for future quantum optoelectronic devices. Towards this goal, both nano-fabrication and nano-scale characterization techniques are needed to be intensively investigated.

8. Acknowledgment

References

[1] Y. Arakawa and H. Sakaki, Appl. Phys. Lett. **40**, 939 (1982).

[2] C. W. Snyder, B. G. Orr, D. Kessler and L. M. Sander, Phys. Rev. Lett. **66**, 3032 (1991).

[3] S. Guha, A. Madhukar and K. C. Rajkumar, Appl. Phys. Lett. **57**, 2110 (1990).

[4] D. Leonard, M. Krishnamurthy, C. M. Reaves, S. P. Denbaars and P. M. Petroff, Appl. Phys. Lett. **63**, 3203 (1993).

[5] J. Oshinowo, M. Nishioka, S. Ishida and Y. Arakawa: Appl. Phys. Lett **65** (1994) 1421.

[6] M. Kitamura, M. Nishioka, and Y. Arakawa:7th Conf. on Indium Phosphide and Related Material, Sapporo, Japan(1995)

[7] Y. Nagamune, M. Nishioka, and Y. Arakawa: 22nd International Conference on the Physics of Semiconductors(ICPS'94), Vancouver, Canada (1994)

[8] H. Benisty, C. M. Sotomayor-Torrès and C. Weisbuch, Phys. Rev., B **44**, 10945 (1991).

[9] H. Nakayama and Y. Arakawa: 7th International Conference on Superlattices Microstructures and Microdevices(ICSMM-7), p.649, Banff, Canada (1994)

[10] T. Arakawa, M. Nishioka, Y. Nagamune, and Y. Arakawa: Applied Physics Letters, **64**, 2200 (1994)

[11] C. Weisbuch, M. Nishioka, A. Ishikawa, and Y Arakawa, Phys. Rev. Lett. **69**, 3314 (1992)

[12]T. Norris, J-K. Rhee, C-Y. Sung, Y. Arakawa, M. Nishioka, and C. Weisbuch: Phys. Rev. B, **50**, 14663 (1994)

[13] J.K. Rhee, R. Lai, T.B. Norris, Y. Arakawa, and M Nishioka: QTh A3 of this conference

[14] Z.L. Zhang, M. Nishioka, and Y. Arakawa: Appl. Phys. Lett., **64**, 1068 (1993)
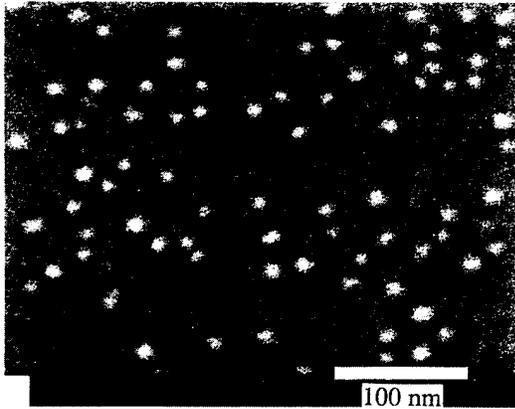
Fig.1: InGaAs quantum dots formed by
MOCVD using Stranski-Kranstanow mode
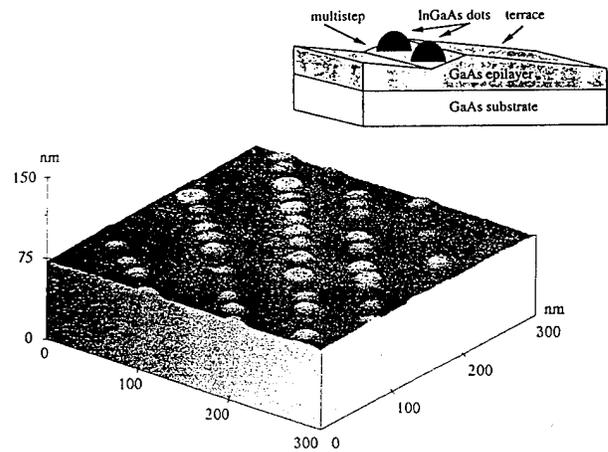
Fig.2: AFM image of the alighned GaAs
quantum dots and schematic illustration..
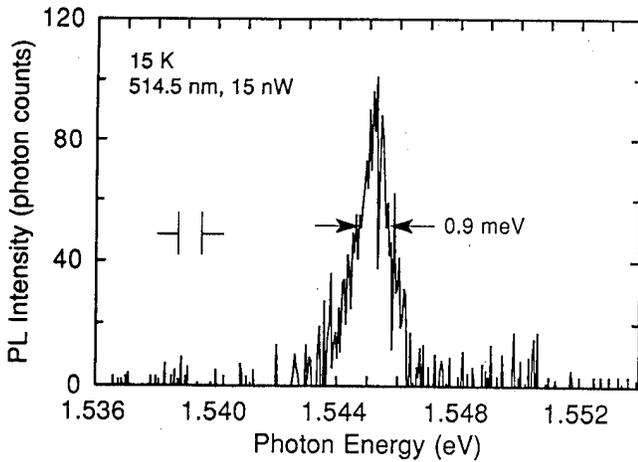
Fig.3: Photluminescene form a single GaAs
quantum dot.
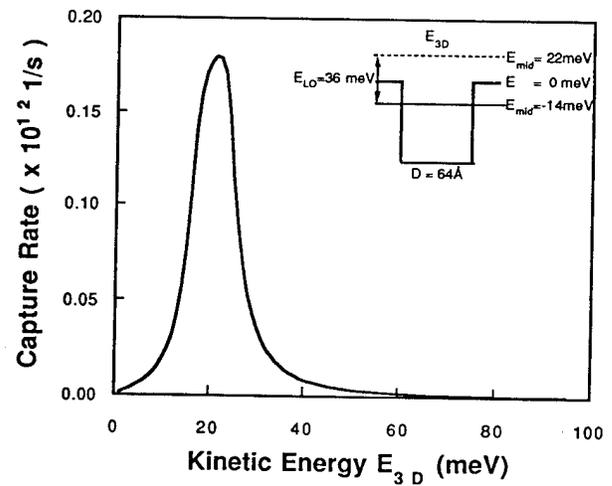
Fig.4: The carriers capture rate from barrier to a
quantum dot as a function of energy of 3D.
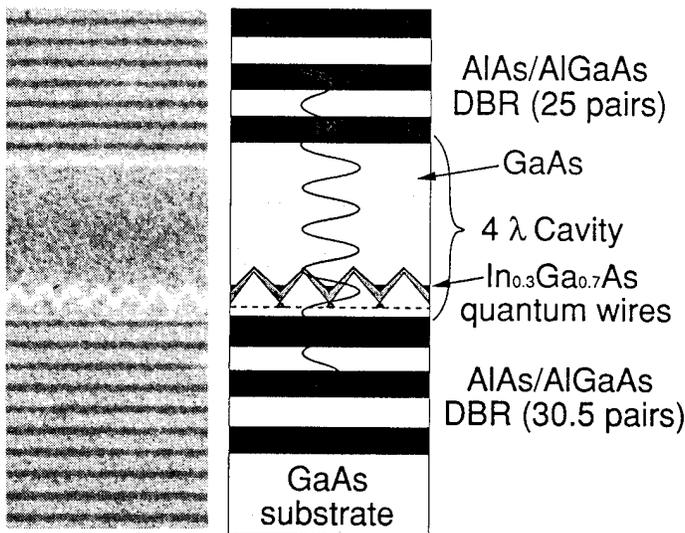
Fig. 5: Schematic illustration of the laser
structure and its SEM micrograph.
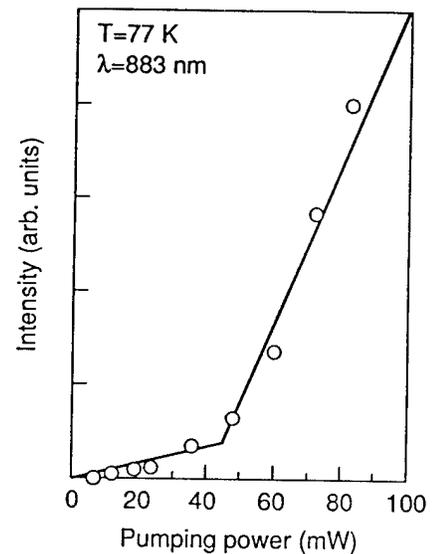
Fig. 6. Light output power from the sample as a
function of pump laser power.

Optical Properties and Transport Properties of Self Assembled Quantum Dots

P.M. Petroff, K. Schmidt, G. Meideiros-Ribeiro, D. Leonard
University of California–Santa Barbara

We will discuss the photoluminescence, modulated photoluminescence and transport properties in InAs and InAlAs self assembled quantum dots. We will also show evidence of three dimensional carrier confinement above 77K.

1.32 μm room temperature photoluminescence from InGaAs quantum dots on GaAs

Richard Mirin[1], James Ibbetson[2], Kenichi Nishi[2], Arthur Gossard[1,2], and John Bowers[1]

[1]Electrical and Computer Engineering Dept. and [2]Materials Dept.
UC Santa Barbara
Santa Barbara, CA 93106

(805) 893-4883
(805) 893-3262 (FAX)

InP is the preferred substrate for long wavelength (1.3-1.55 μm) optoelectronic devices because of the relative ease of growing epitaxial layers of InGaAsP which have the necessary bandgaps and lattice constants. GaAs is not used as a substrate for the growth of these devices because of the difficulty of growing an epitaxial layer of InGaAs with a high enough In content and proper thickness due to the large lattice mismatch. In this paper, we will show that growing InGaAs quantum dots on (100) GaAs substrates allows us to obtain room temperature photoluminescence (PL) at wavelengths as long as 1.32 μm with a full width at half maximum (FWHM) of only 32 meV.

Molecular beam epitaxy (MBE) has been shown to be a viable technique for growing coherently strained InGaAs quantum dots on GaAs substrates[1-2]. The quantum dots are formed when the highly strained InGaAs epilayer partially relieves the strain by forming coherent islands on the surface. In most cases, the deposition of InGaAs is terminated immediately after the transition from layer-by-layer growth to island growth. In the present work, we continue depositing InGaAs well beyond the 2D to 3D transition. This allows us to increase the size of the dots, thus reducing the quantization energy and shifting the optical transitions to longer wavlengths.

The quantum dots presented here demonstrate room temperature PL at 1.32 μm with a FWHM of only 32 meV (Figure 1). As the sample temperature is cooled, the FWHM decreases slightly, reaching a minimum of 29 meV at about 230 K (Figure 2). The FWHM then increases to about 44 meV at about 110 K and remains approximately constant down to the lowest measurement temperature of 1.4 K. The lack of appreciable linewidth narrowing as the sample is cooled indicates that the room temperature linewidth is not due to the thermal distribution of carriers as in a quantum well. Instead, it is due to inhomogeneous broadening which can be attributed to the size distribution of the quantum dots. Nonetheless, this is the lowest reported PL linewidth for quantum dots as grown by MBE. The linewidth broadening as the temperature decreases can be explained by observing that the shoulder towards higher energy becomes more pronounced as the sample is cooled. We believe this shoulder is due to a wetting layer which is commonly observed during

MBE growth of InGaAs quantum dots. In this case, the quantum dots and the wetting layer have different indium compositions, which causes their bandgaps to change at different rates as the temperature is reduced.

In order to get a better understanding of the optical quality of this quantum dot sample, we replaced the InGaAs quantum dot layer with an InGaAs quantum well. Figure 3 shows the integrated intensity versus temperature for the two samples. At temperatures below about 200 K, the quantum dot sample luminesces at least as strongly as the quantum well sample. Even at room temperature, the quantum dot sample is only one order of magnitude weaker in intensity than the quantum well sample. The reason for this temperature-dependent reduction in relative intensity is unclear at this time. It may be due to some defects which are present in the quantum dot sample or to a reduced carrier capture efficiency by the quantum dots.

Atomic force microscopy (AFM) was performed on an identical quantum dot sample, except the growth was terminated immediately after the InGaAs layer was deposited. The sample was kept in ultrahigh vacuum ($< 10^{-9}$Torr) until just prior to the AFM measurements in order to minimize the amount of oxidation. AFM pictures (Figure 4) show that the surface is covered with a high density ($\sim 10^{10}$ cm^{-2}) of dots. The dots are in close proximity to one another. They resemble ellipsoidal sections, with a base diameter on the (100) surface of about 60 nm and with an average height of about 12 nm.

In conclusion, we have demonstrated that room temperature PL at wavelengths as long as 1.32 μm is obtainable from InGaAs quantum dots grown on GaAs substrates. The dots have a room temperature linewidth of 32 meV. This work indicates the possibility of fabricating 1.3 μm lasers on GaAs substrates.

References:
[1] D. Leonard, M. Krishnamurthy, C. Reaves, S. Denbaars, and P. Petroff, Appl. Phys. Lett. **63**, 3203 (1993).
[2] J. Moison, F. Houzay, F. Barthe, L. Leprince, E. Andre, and O. Vatel, Appl. Phys. Lett. **64**, 196 (1994).
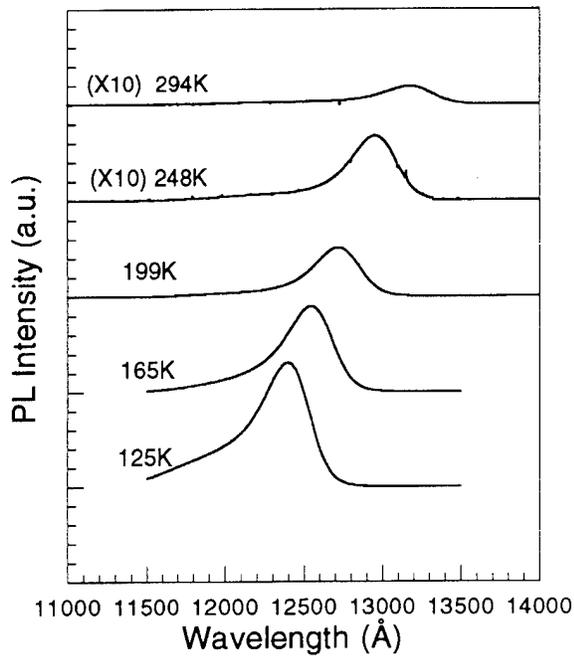
Figure 1: PL spectra taken at several temperatures for InGaAs quantum dots. The excitation intensity is about 0.5 W/cm^2.
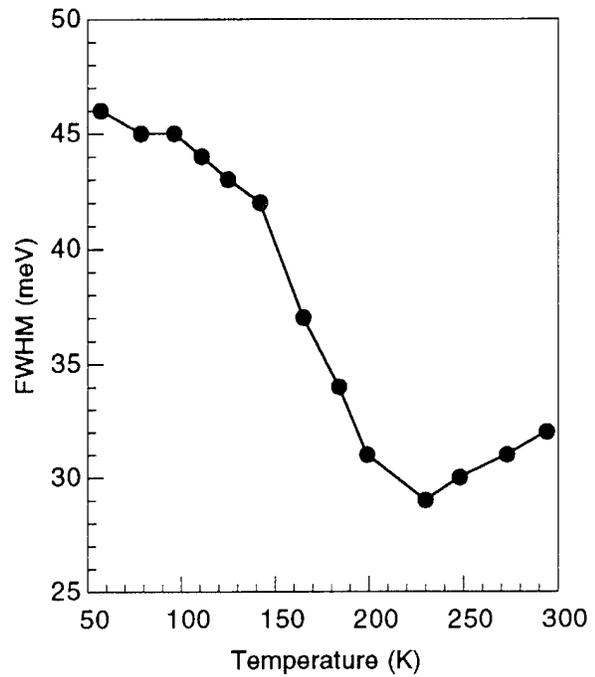
Figure 2: FWHM versus temperature shows an initial decrease as the sample is cooled, but further cooling leads to an increase in the linewidth.
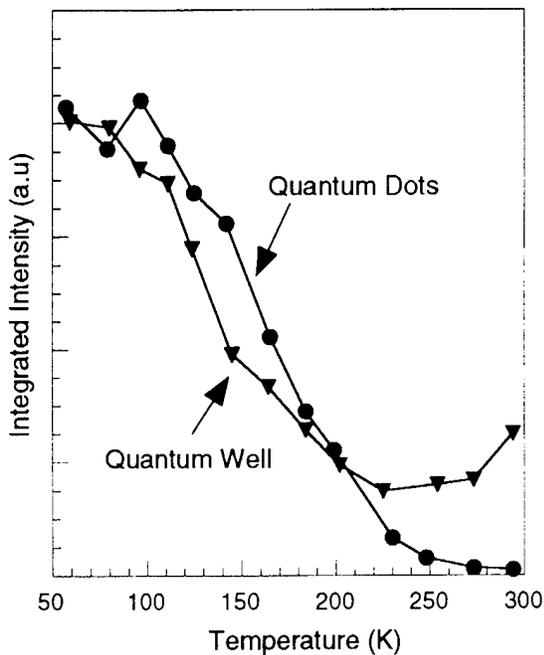
Figure 3: The integrated intensity of an InGaAs quantum dot sample is seen to be comparable to that of an InGaAs quantum well sample.
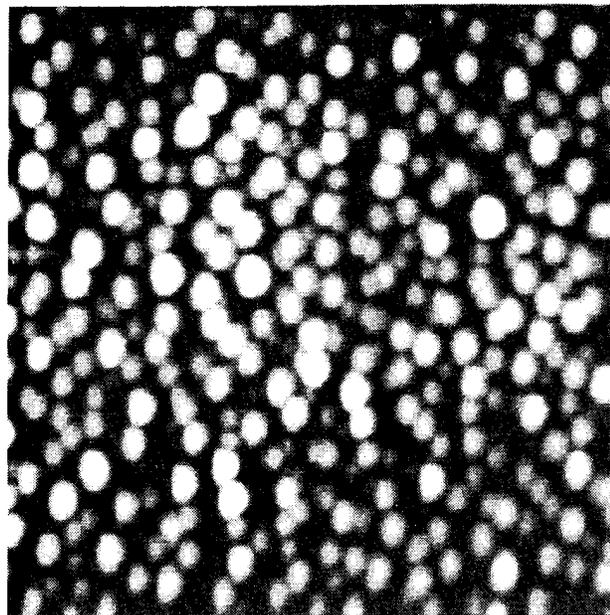
Figure 4: 1 μm X 1 μm AFM of quantum dots

A Vertical Cavity Surface Emitting Laser Operating in a 12 T Magnetic Field at 2K Temperature

Ove Lyngnes, Hyatt M. Gibbs, Galina Khitrova, Jill D. Berger, and Tom R. Nelson Jr.
Optical Sciences Center, University of Arizona, Tucson, AZ. 85721
Ph. (602) 621-2741, FAX (602) 621-4323

Valerii Zapaskii
All-Russian Scientific Center, S. I. Vavilov State Optical Institute
St. Petersburg, 199034 Russia
Ph. (812) 218-1343, FAX (812) 218-1335

Recently, concerns have been raised about the presumed improvement in lasing performance in going from a 2D confined system to a 0D confined system. Stark et al. (1992, 1993) have studied $\approx$ 10 nm GaAs/AlGaAs multiple quantum wells in a perpendicular magnetic field of 12T normal to the quantum wells. Magnetic quantization into equally spaced Landau levels plus the quantum-well quantization along the growth direction result in near-ideal quantum dots. Stark et al. have shown that the 2s magneto-exciton lives $\approx$ 100 ps, i. e., $\approx$ 1000 times longer in 12T than 0T, illustrating the phonon bottleneck. Usually hot carriers in a semiconductor excited well above the bandgap relax by a series of optical phonon emissions, thereby transferring energy rapidly (<1ps) and efficiently to the lattice. Schmitt-Rink et al. (1989), Weisbuch et al. (1991), Bockelmann and Bastard (1990), Benisty et al. (1991), and Inoschita et al. (1992) have emphasized that quantum dot quantization in all three dimensions should result in a phonon bottleneck; i. e., only by accident will the distance between energy levels be equal to the phonon energy. This could degrade the performance of a quantum dot laser considerably.

With this motivation, we designed and grew, by MBE, a VCSEL for 4K operation. It uses 3 $\approx$ 5.5 nm InGaAs/GaAs (x = 0.18) quantum wells in the center of a 1λ GaAs spacer between 24 and 26.5 period GaAs/AlAs top and bottom mirrors respectively. The exciton peak wavelength of the InGaAs/GaAs quantum wells is approximately 920 nm. It can be tuned to some degree due to the thickness variation over the MBE grown sample. The Fabry-Perot peak of the cavity varies even more rapidly with growth thickness, from approximately 925 nm at the center of the growth rotation decreasing to shorter wavelengths outwards on the wafer. The lasing is governed by the Fabry-Perot peak, but only takes place for reasonable overlap between the exciton peak and the Fabry-Perot peak. The structure is optically pumped with a linearly polarized cw Ti:Sapphire laser at λ $\approx$ 835 nm, within the first minimum in the mirror reflectivity and below the absorption edge of the GaAs mirror layers. We also grew a sample with only the InGaAs/GaAs quantum wells and no mirrors in order to study the behavior of the quantum wells in the magnetic field.

Figure 1 show the absorption spectra of the quantum well sample for different magnetic fields. The spectra were recorded in a superconducting magnet at 1.8 K temperature. An unpolarized white-light source was coupled into the magnet dewar through an optical fiber (core diameter 600μm). It is apparent that the conduction band is quantized into Landau levels at high magnetic fields and that the exciton peak shifts by approximately 3.5nm. The large splitting between the 1shh and 2shh Landau levels (approximately 21.5 nm $\approx$ 33.5 meV) is almost as large as the GaAs LO phonon energy. Whether or not optical phonon emission between the 2shh and
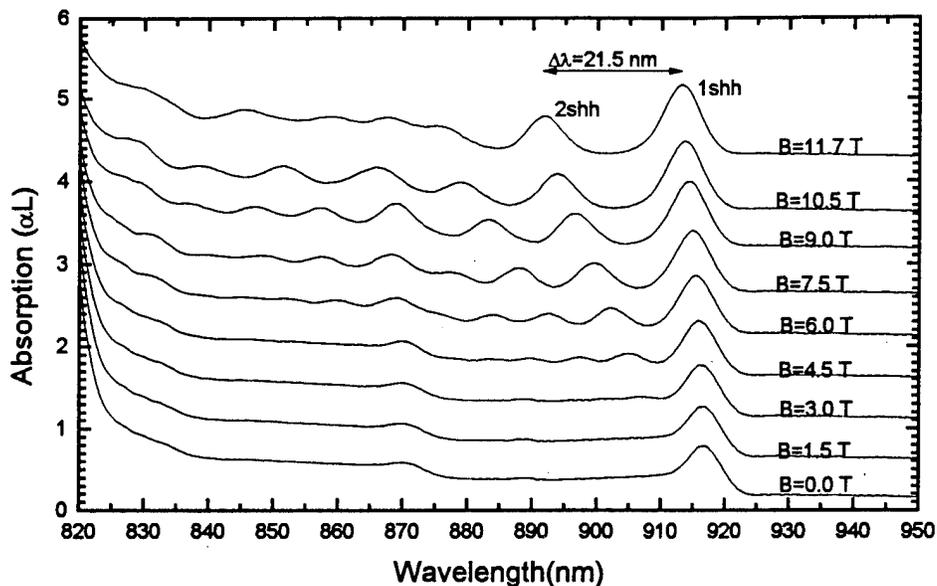
Figure 1: *Absorption spectra of InGaAs/GaAs multiple quantum wells at T=1.8 K for different magnetic field strengths. Curves are displaced by +0.5 for each field strength starting at B = 0.0 T. Not corrected for Fresnel losses.*
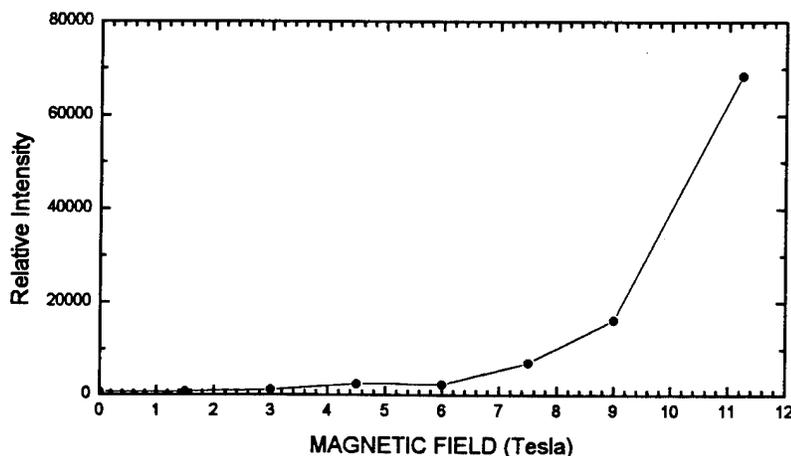
Figure 2: *Relative output intesity of VCSEL as function of magnetic field.. Pump power=53 mW and T= 2.0 K . Pump diameter was approximately 200 μm. Peak wavelength of lasing was 923 nm.*

1shh levels is contributing to the improved laser emission at high field discussed below, can be studied by future time-resolved experiments. Also, the isolated 1shh magneto-exciton peak, made possible by the large strain-induced splitting between light- and heavy-hole valance bands, is attractive for fundamental experiments such as Rabi flopping.

The parameter space governing the lasing performance is rather large: Fabry-Perot peak wavelength, wavelength and power of optical excitation for carrier generation, and magnetic field strength. Figure 2 shows that the output from the VCSEL, for a high pump intencity, increases strongly with the magnetic field. The most likely explanation is that the magnetic field shifts the

exciton energy to a higher energy resulting in a better overlap with the Fabry-Perot peak at this particular location on the sample wafer. This explanation is supported by experiments on a piece closer to the center of the wafer where the Fabry-Perot peak is located at approximately 925 nm; there increasing the magnetic field destroys the lasing because the exciton peak is shifted away from the Fabry-Perot peak. The absorption change with magnetic field at the 835 nm pump wavelength is a secondary effect.

The transition from 2D confinement to 0D confinement is expected to improve the lasing by concentrating the oscillator strength. On the other hand, a phonon bottleneck would decrease the lasing performance. The interplay between these effects, including the case where the difference between the 1shh and 2shh transitions equals one GaAs LO phonon energy, will be elucidated by future studies involving time dynamics(Stark et al. 1992, Akiyama et al. 1994), tuning of the Fabry-Perot peak, etc. The lack of light-hole Landau levels in the vicinity of the lowest InGaAs/GaAs " quantum-dot" heavy-hole Landau levels makes this a particularly attractive system for studying quantum-dot lasing.

In summary, we have demonstrated lasing in a optically pumped VCSEL at 4K and in magnetic fields varying up to 11.7T. We conclude that the phonon bottleneck effect does not prevent cw laser action when 0D confinement is accomplished by the magnetic field. We have also shown that the InGaAs/GaAs quantum wells used as gain medium in the VCSEL, show a splitting almost as large as the GaAs LO phonon energy between the 1shh and 2shh magneto-exciton levels. This almost completely isolates the exciton energy level opening up possibilities for further studies of the exciton peak by itself and relaxation via phonons into the 1shh level.

References:
Akiyama, H., T. Matsusue, and H. Sakaki, "Exciton diffusion and energy relaxation in GaAs quantum wells under a strong magnetic field", 213, IQEC '94 (OSA, Washington, 1994).
Benisty, H., C. M. Sotomayor-Torres, and C. Weisbuch, "Intrinsic mechanism for the poor luminescence properties of quantum-box systems," Phys. Rev. B **44**, 10945 (1991).
Bockelmann, U., and G. Bastard, "Phonon scattering and energy relaxation in two-, one-, and zero-dimensional electron gases," Phys. Rev. B **42**, 8947 (1990).
Inoshita, T., and H. Sakaki, "Electron relaxation in a quantum dot: significance of multiphonon processes," Phys. Rev. B **46**, 7260 (1992).
Schmitt-Rink, S., D. S. Chemla, and D. A. B. Miller, "Linear and nonlinear optical properties of semiconductor quantum wells," Adv. Phys. **38**, 89 (1989).
Schmitt-Rink, S., J. B. Stark, W. H. Knox, D. S. Chemla, and W. Schäfer, "Optical properties of quasi-zero-dimensional magneto-excitons", Appl. Phys. A **53**, 491 (1991)
Stark, J. B., W. H. Knox, and D. S. Chemla, "Femtosecond nonlinear optical response of magnetically confined quantum well excitons," in F. Henneberg, S. Schmitt-Rink, and E. O. Göbel, *Optics of Semiconductor Nanostructures* (Akademie Verlag, Berlin, 1993), p. 399; and references therein; Phys. Rev. Lett. **68**, 3080 (1992); Phys. Rev. B **46**, 7919 (1992); and references therein.
Weisbuch, C., and B. Vinter, *Quantum Semiconductor Structures* (Academic, Boston, 1991), p. 212.

Physics and Applications of Low-Dimensional Semiconductors

QThD 3:30 pm-5:00 pm
Ballrooms VI-VIII

Francesco DeMartini, *Presider*
University of Rome, Italy

Quantum Wire Fractional Layer Superlattice Microcavity Lasers

Arturo Chavez-Pirson, Hiroaki Ando, Hisao Saito, and Hiroshi Kanbe

NTT Basic Research Laboratories

3-1 Morinosato, Wakamiya

Atsugi-shi, Kanagawa, 243-01 Japan

Telephone: 81-462-40-3455

Fax: 81-462-40-4317

e-mail: chavez@wave.ntt.jp

Semiconductor quantum wires are attracting attention not only because they exhibit interesting one-dimensional optical physics but also because they may improve the performance of optical devices. The increased quantum confinement in the quantum wires concentrates the electronic density of states into a narrow wavelength region resulting in enhanced optical properties. For example, lasers using quantum wires are expected to exhibit lower current thresholds, higher modulation bandwidths, and narrower spectral widths compared to quantum well or bulk lasers. This makes quantum wire lasers attractive devices for a variety of applications in communications, optical processing, and optical interconnects.

To achieve the highest efficiency and lowest current thresholds, lasers will have to combine both strong electronic and optical confinement effects. Microcavity structures in principle offer complete optical confinement. In comparison to the usual waveguide structure where the spontaneous emission is distributed over tens of thousands of modes, a wavelength-sized microcavity channels all the light energy into only a few emission modes.

In this presentation we describe the fabrication method and operation of the first quantum wire microcavity laser. [1] This laser integrates a GaAs quantum wire gain medium directly into a dielectric microcavity. It combines the sharply peaked electronic density of states of the quantum wire with the microcavity effect to achieve efficient coupling of both electronic and photonic states into the lasing. We also present the linear and femtosecond nonlinear optical properties of the quantum wires themselves, indicating the effects of the one-dimensional-like quantum confinement. We find that the predicted inhibition of carrier relaxation in quantum wires, the so-called phonon bottleneck, [2] is not significant in our structures and that, in fact, the relaxation is fast (< 300 fs) and efficient.

Semiconductor quantum wires are difficult to fabricate. They must be nanometer-scale, uniformly-sized, densely packed, and free from contamination or defect. We have successfully fabricated quantum wires using fractional layer superlattices (FLS) grown by metalorganic chemical vapor deposition on [001] vicinally oriented GaAs substrate tilted 2° towards the [$\bar{1}$10] crystal orientation. [3] The growth-induced lateral confinement causes optical anisotropies to appear in luminescence, absorption, and gain.[4] Figure 1 schematically indicates how the FLS quantum wire (FLS-QWR) array is formed. The FLS-QWR structure used here consists of 10 periods of 8 nm thick $(AlAs)_{1/4}(GaAs)_{3/4}$ FLS layers having a lateral period of 8 nm. Each wire array is clad by 20 nm thick $(AlAs)_3(GaAs)_2$ short-period superlattice layers that act as barriers for carrier confinement in the [001] direction. The nominal size of the GaAs quantum wire in the [001] and [$\bar{1}$10] directions is 8 nm x 6 nm.

Figure 2 shows the quantum wire microcavity structure with the FLS-QWR array sandwiched between dielectric mirrors. To obtain the lasing performance at room temperature, we optically pump the FLS-QWR with 40 ps pulses from a frequency-doubled Nd-YLF laser. Figure 3 indicates the emission spectrum below and above the lasing threshold. Above threshold the linewidth of the lasing becomes sharp. Figure 4 shows the input-output characteristics indicating a clear lasing threshold even at room temperature for lasing with electric field vector oriented parallel to the wire direction. We have used the anisotropic gain in FLS-QWRs to demonstrate polarization switching in FLS lasers. [4] We discuss this feature and the potential of carrier lifetime-free, cavity lifetime-limited polarization switching.

References

1. A. Chavez-Pirson, H. Ando, H. Saito, H. Kanbe, Appl. Phys. Lett. **64**, 1759 (1994).
2. H. Benisty, C. M. Sotomayor-Torres, and C. Weisbuch, Phys. Rev. **B44**, 10945 (1991).
3. H. Saito, K. Uwai, and N. Kobayashi, Jpn. J. Appl. Phys., **32**, 4440 (1993).
4. A. Chavez-Pirson, H. Ando, H. Saito, H. Kanbe, Appl. Phys. Lett. **62**, 3082 (1993).

(1) Fractional Layer Superlattice Quantum Wire Array
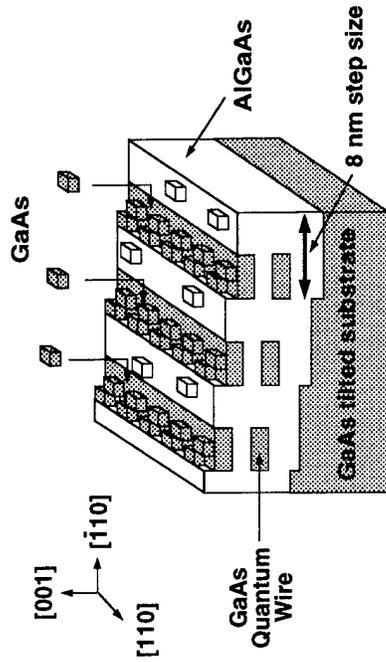
(2) Quantum Wire Microcavity Laser
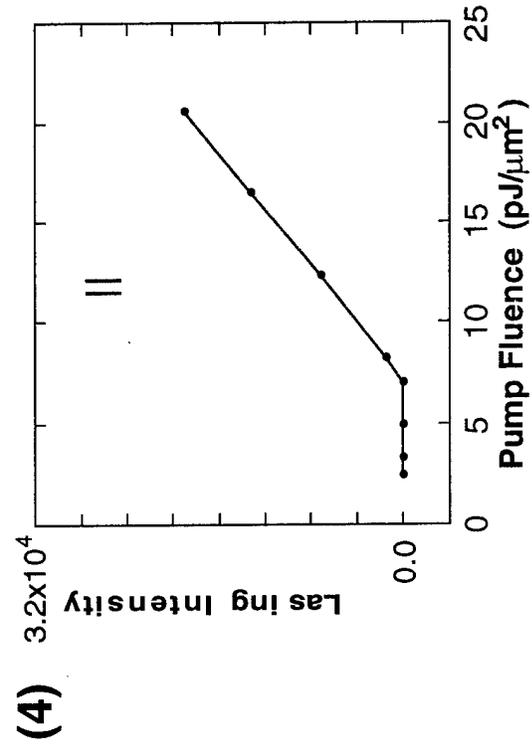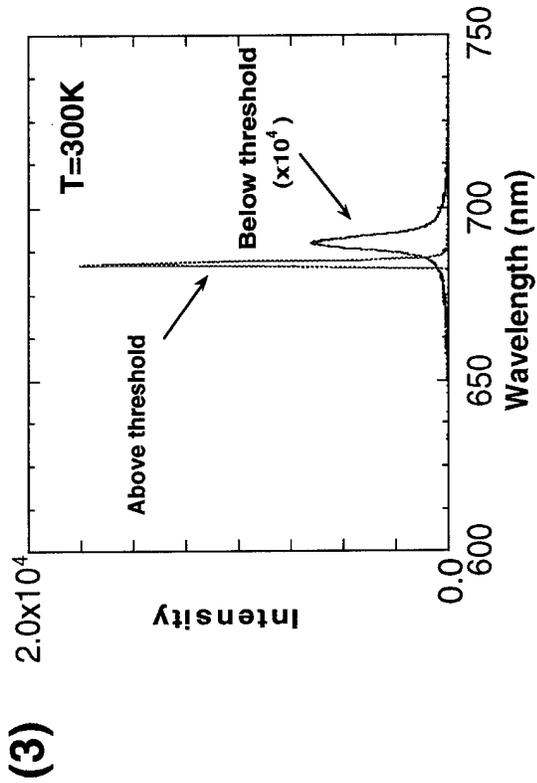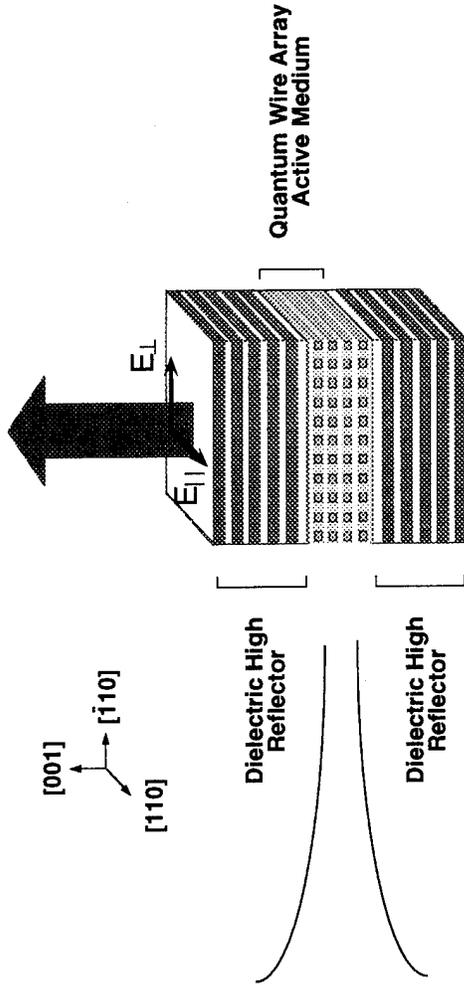
(3)

(4)

Strained InGaAs Quantum Disk Laser with Self-organized Nano-scale Active Region

Jiro Temmyo, Eiichi Kuramochi, Mitsuru Sugo, Teruhiko Nishiya,
Richard Nötzel,[1] and Toshiaki Tamamura

NTT Opto-electronics Laboratories,
3-1 Morinosato-Wakamiya, Atsugi, Kanagawa 243-01, Japan.
([1] Present address: RCIQE, Hokkaido University)
Phone: +81(462)40-2855 , Fax.: +81(462)40-4305
e-mail: temmyo@aecl.ntt.jp

Introduction: Although there have been controversial discussions about the validity of quantum box lasers [1-2], few experimental results have been reported because of the difficulty of fabricating a quantum box structure suitable for laser application [3].

Here we introduce the self-organization phenomena, occuring in strained InGaAs/AlGaAs systems during the interrupted epitaxial growth on GaAs (311)B substrates, to form micro-crystals with built-in quantum disks. We also describe and discuss the performance of a novel strained InGaAs quantum disk laser with a nano-scale active region fabricated by self-organization. The recent activity in other spontaneous nano-scale formation techniques utilizing coherent islanding phenomena is also briefly reviewed.

Coherent Islanding Phenomenon: A coherent islanding phenomenon of strained InGaAs films on GaAs (100) substrates [4], called the Stranski-Krastanow epitaxial growth mode by molecular beam epitaxy, has recently been receiving attention as a useful method for making quantum box structures [5-6], because of its potential for creating damage-free structures. There are some problems, however, such as the inevitable two-dimensional wetting layer residue, poor size-contollability, no ordering, and very narrow range of the growth condition. Unfortunately, no results of room temperature photoluminescence (PL) emission from buried InGaAs islands have yet been reported.

Self-organization Phenomenon: We found, however, a new self-organization phenomenon in the metalorganic vapor phase epitaxy (MOVPE) growth of strained InGaAs /AlGaAs heterostructures on (311)B GaAs substrates [7]. During a short period of growth interruption, with a high substrate temperature, after a thin InGaAs film is grown on an AlGaAs layer, the strained InGaAs film redistributes and separates into well-ordered and high-density nano-scale quantum disks. These disks are directly covered by AlGaAs layers due to mass transport to form the microcrystals (Fig.1). This self-organization phenomenon seems to result

from the barrier height for adatom migration being lower than it is on the (100) surface. The size of the disks can be controlled by adjusting the indium composition and the density can be varied by varying the nominal thickness. The excellent crystal quality and size homogeneity of the quantum disks manifests itself in high PL efficiency and in extremely narrow PL spectra at room temperature [8-9]. The well resolved exciton resonances in photo-excitation spectra indicates the structual perfection and the efficient localization of excitons in our disks [9]. Moreover, we found that the self-organization in strained InGaAs system also occurs on InP (311) substrates [10], indicating that these phenomena on Miller high-index planes might be common to compound semiconductors.

Quantum Disk Laser: We fabricated laser structures containing double-stacked InGaAs quantum disks (DQDs) on a GaAs (311)B substrate and double quantum wells (DQWs) on a conventional (100) substrate, simultaneously. The vertical structure consisted of the separate confinement heterostructure (SCH) with guiding layers, and the active region was composed of double-stacked $In_{0.25}Ga_{0.75}As$ disks with a nominal thickness of 6 nm and $Al_{0.15}Ga_{0.85}As$ barrier and SCH layers between AlGaAs guiding layers. After the deposition of each InGaAs layer, growth was interrupted under an arsine atmosphere for 3 minutes to promote self-organization at a substrate temperature of 750°C. The diameter of the InGaAs quantum disk inside microcrystals was estimated from SEM cross-section observation after slight stain etching to be about 60 nm, but TEM observation with energy dispersive X-ray spectroscopy [9] indicates that the InGaAs disk can be slightly smaller than this. The filling factor was calculated as about 6% on the plane. The full-width at the half-maximum (FWHM) of the PL emission from the quantum disks was about 18 meV at room temperature, which is narrower than that (24meV) of the emission from the (100) wells. The intensity of the emission from the disks was also slightly stronger than that of the emission from the (100) wells. The transverse-mode stabilized ridge waveguide lasers were fabricated using the electron cyclotron resonance (ECR) dry-etching technique and the conventional fabrication process. The ridge was 2 μm wide and the cavity was 900 μm long without facet coating.

The threshold current of the DQD laser was 23 mA, which is considerably lower than that (27 mA) of the (100) DQW laser (Fig.2). The FWHM for the vertical divergence angle of the emission was 25 degrees and that for the horizontal one was 10 degrees for both (311)B quantum disk lasers and (100) quantum well lasers, whereas the optical confinement factors for active volume were quite different for the two lasers. Considering the filling factor of 6% , the low threshold current of quantum disk lasers appears to be related to better optical quality of the disks and might be attributed to some gain enhancement effect, to less guiding loss inside the active region, and to possible cooperative phenomena in disk systems. The estimated lateral size of the disk is not small enough to expect some lateral confinement effects. The quantum efficiency of the DQD lasers was slightly worse than that of the DQW lasers on (100) substrates and tended to saturate, probably because of the reduced active volume. The lasing wavelength

of the quantum disk lasers, about 940 nm, was blue-shifted from that of the (100) DQW lasers. This is consistent with the PL data, and indicates that lasing occurs inside the disks.

Conclusion: The results suggest the possibility of further using this self-organized nanostructure in optical device applications.

References:

[1] M. Asada, Y. Miyamoto, and Y. Suematsu, *IEEE J. Quantum Electron.*, 1986, **QE-22**, pp. 1915-1921.

[2] H. Benisty, C. M. Sotomayor-Terres, and C. Beisbuch, *Phys. Rev. B*, 1991, **44**, pp. 10945-10948.

[3] H. Hirayama, K. Matsunaga, M. Asada, and Y. Suematsu, *Electron. Lett.*, 1993, **30**, pp. 142-143.

[4] S. Guha, A. Mudhukar, and K. C. Rajkumar, *Appl. Phys. Lett.*, 1990, **66**, pp. 2110-2112.

[5] J. M. Moison, F. Houzay, F. Barthe, L. Leprince, E. Andre, and O. Vatel, *Appl. Phys. Lett.*, 1994, **64**, pp. 196-198.

[6] D. Leonard, M. Krisnamurthy, C. M. Reaves, S. P. DenBaas, and P. M. Petroff, *Appl. Phys. Lett.*, 1993, **63**, pp. 3203-3205.

[7] R. Nötzel, J. Temmyo, and T. Tamamura, *Nature*, 1994, **369**, pp. 131-133.

[8] R. Nötzel, J. Temmyo, H. Kamada, T. Furuta, and T. Tamamura, *Appl. Phys. Lett.*, 1994, **65**, pp.457-459.

[9] J. Temmyo, R. Nötzel, H. Kamada, T. Furuta, and T. Tamamura, *Proceedings of 22nd International Conference on the Physics of Semiconductors*, Vancouver, Aug. 1994 (to be published).

[10] J. Temmyo, A. Kozen, R. Nötzel, and T. Tamamura, *Extended Abstracts of the 55th Autumn Meeting, 1994; the Japan Society of Applied Physics*, Nagoya, Sept. 1994, 20a-T-9.

[11] J. Temmyo, E. Kuramochi, T. Nishiya, M. Sugo, R. Nötzel, and T. Tamamura, *Conference Digest of the 14th IEEE International Semiconductor Laser Conference*, Hawai, Sept. 1994, PD4.
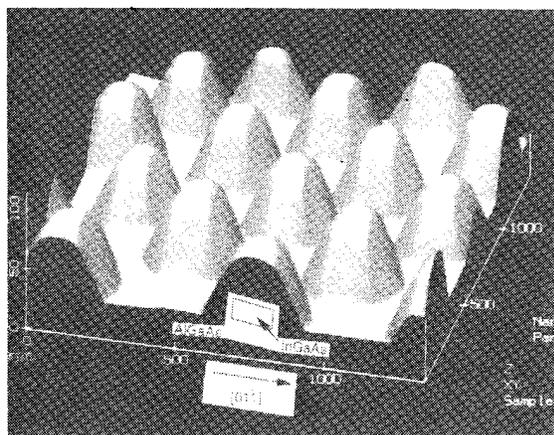
Fig.1 Typical AFM image of the self-organized microcrystals with built-in InGaAs quantum disks on a GaAs (311)B substrate.
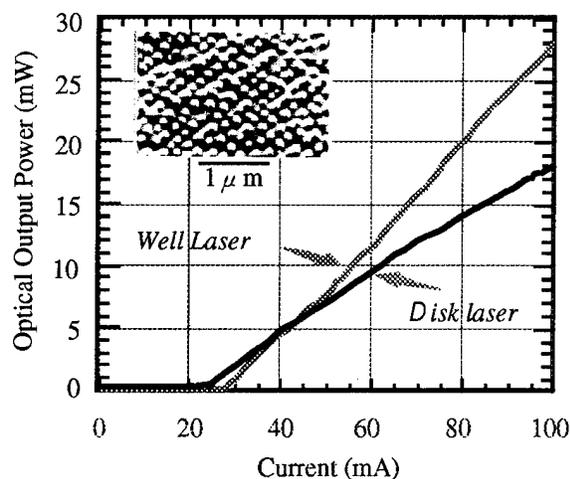
Fig.2 Continuous wave light-current characteristics for a disk laser on (311)B and a well laser on (100) at room temperature. The SEM photograph shows the surface morphology of the self-organized microcrystals as a nano-scale active region.

Fabrication and Optical Characterization of GaAs Nano-whiskers

T. Katsuyama, K. Hiruma, T. Sato, K. Ogawa, M. Shirai, K. Haraguchi and M. Yazawa

Central Research Laboratory, Hitachi Ltd. Kokubunji, Tokyo 185, Japan
TEL:+81-423-23-1111(Ext.3422) FAX:+81-423-27-7801

In recent years there has been considerable interest in the quantum effects of dimensional confinement on the optical properties of semiconductor materials. These confinement effects provide a means of artificially tailoring the optical properties of materials, offering the possibility of producing new optoelectronic devices. For example, modification of the carrier density of states makes it possible to produce semiconductor lasers with lower threshold currents and higher gains[1].

Quantum wire structures showing two-dimensional confinement effects are one of the most interesting microstructures. Recently, we have demonstrated an attractive method of fabricating such quantum wires[2,3]. It is based on selective area growth using reduced-pressure metal-organic vapor-phase epitaxy (MOVPE). Using this method, free-standing wire-shaped nanometer-size GaAs whiskers can be obtained. The advantage of the method is that the inherent nature of whisker growth makes it possible to obtain defect-free nanometer-size whiskers.

In this study, we demonstrate artificial control of the whisker growth position. Such control is essential for various device applications of nano-whiskers. We also describe the optical properties of GaAs nano-whiskers. In particular, the polarization dependence of the photoluminescence is shown in connection with the discussion on the two-dimensional quantum confinement effect.

Typical GaAs whiskers obtained so far are shown in Fig. 1. The growth mechanism of such nano-whiskers can be explained by the Vapor-Liquid-Solid (VLS) model[3]. In this model, the formation of Au-alloy droplets on the substrate is essential for whisker growth. The alloy droplet acts as a catalytic site that promotes the thermal decomposition of the source gas molecules and thus enhances epitaxial growth on the site. In other words, a nano-whisker grows at the alloy droplet site. The actual droplet formation previously studied is based on conventional Au vacuum evaporation, followed by an annealing process. This method, however, leads to a random distribution of the whisker growth positions. Therefore, the location of each Au-alloy droplet must be controlled to fabricate site-controlled whiskers.

The growth procedure for site-controlled whiskers is shown schematically in Fig. 2. We controlled the location by using a SiO2 window mask formed by electron-beam lithography. After patterning of the window on the electron beam (EB) resist layer (PMMA), Au atoms with an average thickness of 1 nm were deposited by vacuum evaporation on both the window region and on the region masked with the resist layer. The EB resist layer was removed together with the Au clusters on the masked region. Next, the sample with the SiO2 mask was annealed at 500 °C for about 10 min. The annealing process formed a single alloy droplet inside the windows only. After removing the SiO2 mask, the sample was placed in an MOVPE chamber to grow the whiskers. Source gases were trimethylgallium and AsH3.

Figure 3 shows a scanning electron microscope image of site-controlled GaAs whiskers grown on a GaAs (111)B substrate. Whiskers with diameters of about 80 nm are exactly placed at the four corners of the 2 μ m $\times$ 2 μ m square. The growth direction of these whiskers is [111]B only; this result coincides well with previous results showing that nano-whiskers grow preferentially in the $\langle 111 \rangle$ As dangling bond direction which is perpendicular

to the (111)B substrate surface[3].

In order to characterize the optical properties of the nano-whiskers, we measured the photoluminescence (PL) spectra of the GaAs nano-whiskers fabricated by the method described above. The lateral size of the whiskers was fixed at 50 nm and the length was typically 1-2 μ m. A GaAs semi-insulating substrate was used to reduce the influence of the emission from the substrate. The excitation source for the PL measurements was provided by a synchronously pumped mode-locked dye laser system which generates 0.5-ps pulses with a 82-MHz repetition rate and 8.5×10^{-7}-J cm^{-2} power density. The power density corresponds to 5×10^{17} -cm^{-3} electron-hole pairs excited in the whiskers. Detection of PL intensity was performed with a synchro-scan streak camera combined with a monochromator.

The PL spectrum for GaAs whiskers measured at 10 K is shown in Fig. 4. The wavelength of the excitation light was fixed at 750 nm. The spectrum of an undoped MOVPE GaAs epi-layer is also shown as a reference. The observed PL bands were fairly wide (about 5 meV) because of the relatively high-density electron-hole pairs. It should be noted that the PL peak of the whiskers is at a higher energy than the peak of the epi-layer sample. The spectral blue shift of the whiskers was thus measured as 2.5 meV. This is considered a result of the two-dimensional quantum confinement (quantum wire) effect.

The polarization dependence of the luminescence was also measured by illuminating the polarized excitation light. Figure 5 shows the PL polarization dependence when excitation polarization is parallel to the whisker axis. As the figure shows, the luminescence whose polarization is parallel to the whisker axis is much stronger than the luminescence whose polarization is perpendicular to the axis. The ratio of *perpendicular* light power to *parallel* light power is measured as 26%. This value is in good agreement with the polarization ratio of 20-30% given by an approximation using a square cross section with an infinite barrier height[4]. Therefore, it again appears that the PL from the GaAs whisker is affected by the two-dimensional quantum confinement effect.

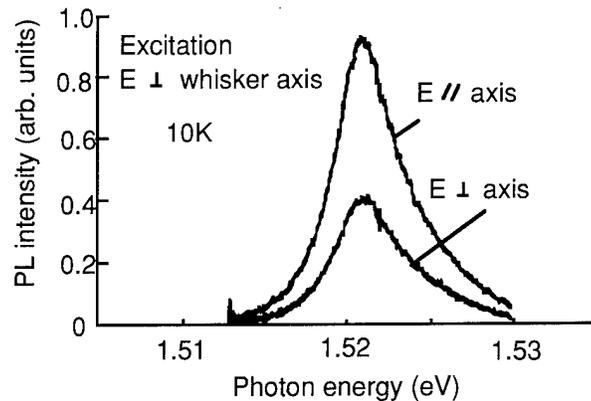On the other hand, the polarization dependence of the luminescence under excitation whose polarization is perpendicular to the whisker axis showed slightly different behavior. Figure 6 shows the results under *perpendicular* excitation. In this case, the ratio of *perpendicular* light power to *parallel* light power increases to about 45%. This implies the existence of energy dissipation related to the polarization rotation in the whisker.

In summary, we demonstrated artificial control of the growth position of GaAs nano-whiskers for the first time. This is done by controlling the location of the Au alloy-droplet, which acts as a seed for whisker growth based on the Vapor-Liquid-Solid growth mechanism. An Au-alloy droplet is fixed on the substrate by using a combination of a SiO2 window mask formed by electron beam lithography and Au vacuum evaporation.

The photoluminescence of the GaAs whiskers was also measured. The spectral blue shift and polarization dependence of the photoluminescence shows the existence of two-dimensional quantum confinement of the carriers in the GaAs nano-whiskers. These results indicate that the nano-whiskers offer high-quality quantum wire structures, which can be applied to opto-electronic devices.

References
[1] Y. Arakawa and A. Yariv, IEEE J. Quantum Electron. QE-22, 1887 (1986).
[2] M. Yazawa, M. Koguchi and K. Hiruma, Appl. Phys. Lett. 58, 1080 (1991).
[3] K. Hiruma, M. Yazawa, K. Haraguchi, K. Ogawa, T. Katsuyama, M. Koguchi and H. Kakibayashi, J. Appl. Phys. 74, 3162 (1993).
[4] C. R. McIntyre and L. J. Sham, Phys. Rev. B45, 9443 (1992).
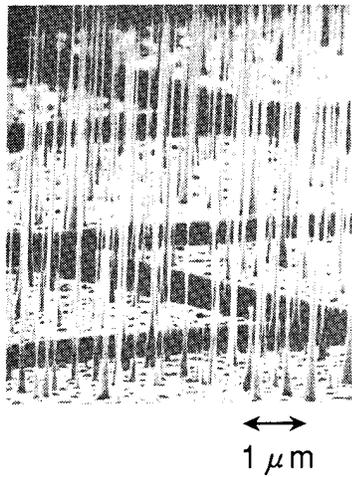
Fig. 1 Typical GaAs whiskers whose growth positions are randomly distributed on the substrate.
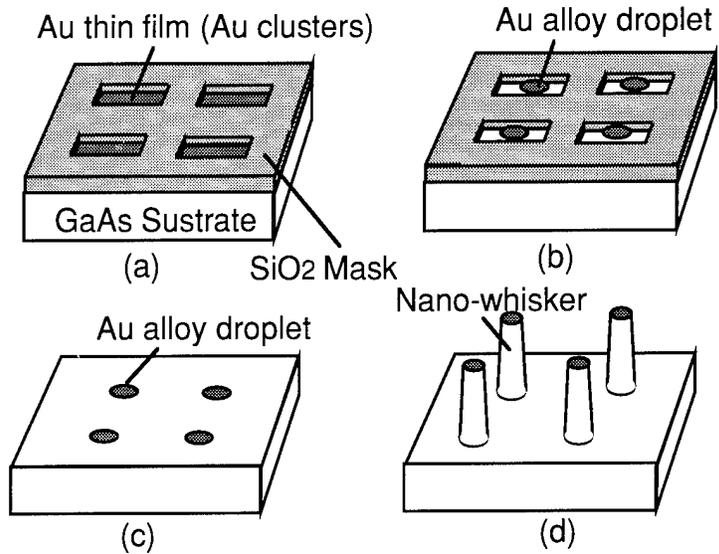
Fig. 2 The growth procedure for site-controlled nano-whiskers. (a) Au thin film (Au clusters) formation inside the window region by Au evaporation and subsequent removal of Au atoms from the masked region, (b) Au-alloy droplet formation by annealing, (c) removal of the SiO2 mask, (d) MOVPE growth of nano-whiskers.

Fig. 3 Scanning electron microscope image of site-controlled GaAs whiskers grown on a GaAs (111)B substrate.
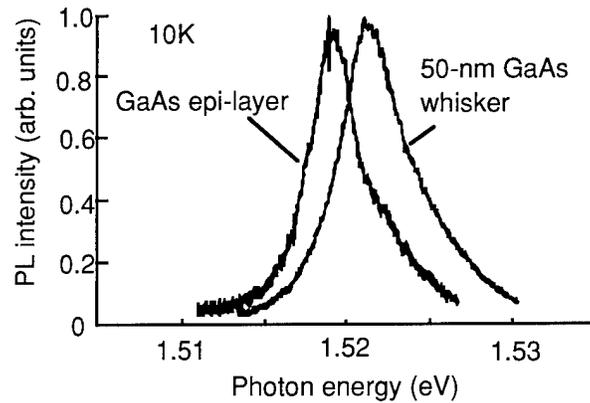
Fig. 4 Photoluminescence spectra for 50-nm GaAs whiskers at 10 K. The result from an undoped MOVPE GaAs epi-layer is also shown as a reference.
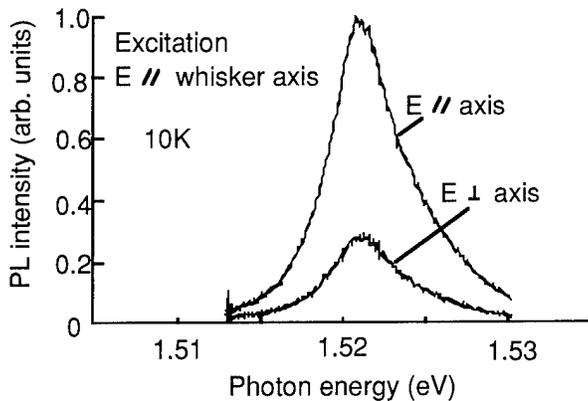
Fig. 5 Polarization dependence of the GaAs whisker photoluminescence under excitation whose polarization is parallel to the whisker axis. The measurement temperature is 10 K.

Fig. 6 Polarization dependence of the GaAs whisker photoluminescence under excitation whose polarization is perpendicular to the whisker axis.

Electronic Picosecond-pulse Interferometer Probing the Millimeter-wave Response of a Quantum-Dot System

D.W. van der Weide, R.H. Blick, F. Keilmann, and R.J. Haug

Max-Planck-Institut für Festkörperforschung

Heisenbergstr. 1, 70569 Stuttgart, Germany

Telephone +49 (711) 689 0 Facsimile +49 (711) 689 1010

Introduction

As a sensing mechanism for broadband (contactless) millimeter-wave spectroscopy of planar mesoscopic systems at cryogenic temperatures, bolometric detection or the photoconductive response of the sample is usually employed. Conventional sources of radiation, such as backward-wave oscillator tubes or Gunn diodes, are then modulated for lock-in detection. In most cases, the output power from these sources varies as they are tuned, changing the thermal load on the system being studied. Furthermore, such conventional sources rarely offer over a decade of frequency coverage, limiting the range available for probing these systems.

Electro-optic switching of photoconductive gaps generates picosecond pulses of radiation, which have been used for broadband probing of the physics of carrier transport.[1] To interfere two such pulses, however, requires a moving mirror for delaying one laser pulse with respect to the other. By contrast, we describe a compact dual-source interferometer which uses pulses generated by two nonlinear transmission line circuits[2] pumped by microwave synthesizers and, consequently, having no moving parts.

We go on to report the response of a quantum-dot sample to the pulsed radiation from this new dual-source interferometer, demonstrating with both simulations and measurements how the source-drain pattern on the sample acts as a transducer of millimeter-wave radiation. We vary the offset frequency of the synthesizers, effectively testing the differential response of the sample beyond 8 kHz.

Pulsing circuits and interferometer

The GaAs IC nonlinear transmission lines (NLTLs) used in this work consist of series inductors (or sections of high-impedance transmission line) with varactor diodes periodically placed as shunt elements. On this structure a fast (~ 2 ps) voltage step develops from a sinusoidal input because the propagation velocity u is modulated by the diode capacitance, $u(V) = 1 \big/ \sqrt{LC(V)}$, where L is the inductance and $C(V)$ the sum of the diode and parasitic capacitance of the line, all per unit length. Limitations of the NLTL arise from its periodic cutoff frequency,

waveguide dispersion, interconnect metallization losses, and diode resistive losses.

In the dual-source interferometer, the output of each NLTL feeds an integrated bow-tie antenna mounted at the focus of a hyperhemispherical high-resistivity silicon lens.[3] These lenses in turn are mounted at the foci of off-axis paraboloidal mirrors. The beams collimated by the mirrors are either transmitted (Source "A") or reflected (Source "B") by a wire-grid polarizing beamsplitter. Each beam then contributes equally to the final, linearly-polarized beam by arrangement of a final wire-grid polarizer mounted at 45 degrees to the beamsplitter [Fig. 1]. Note that, while the prototype construction is already small (~ 17 cm long, 12 cm wide, and 8 cm high), it would be possible to fabricate two antennas and their circuitry on the same substrate, making the whole system extremely compact.
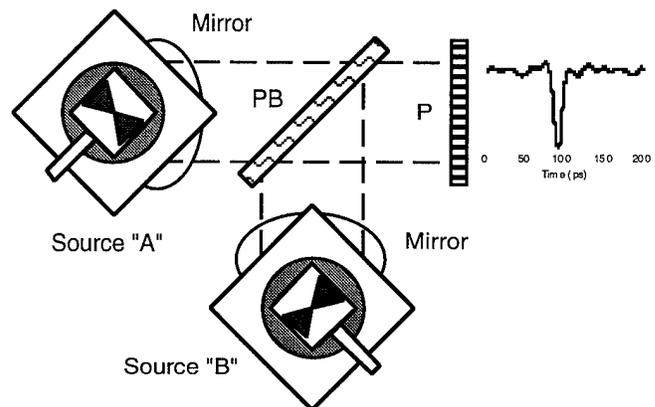
Figure 1. Dual-source interferometer configuration. Each source antenna is at the focus of a paraboloidal mirror and radiates a polarized beam, which is transmitted ("A") or reflected ("B") by the polarizing beamsplitter (PB). The output polarizer (P) selects half the power of each beam. The output waveform as detected by a bolometer is shown.

Each source is fed by a 100–500 mW microwave sinusoid generated by one of two synthesizers, both of which share a common timebase. The output of one synthesizer is offset by $\Delta f << f_0$ ($\Delta f \sim 200$ Hz; $f_0 \sim 7$ GHz), and this offset is used as a trigger for a

spectrum analyzer or a harmonic-selective lock-in amplifier.

Coupled quantum-dot system

The sample consisted of a set of series-connected quantum dots,[4] defined in a mesa-isolated AlGaAs/GaAs 2DEG. The source-drain pattern was ~ 1.1 mm long, and it served as a dipole antenna. Using a full-wave field solver,[5] we simulated the microwave current distribution on the structure for the geometry of the experiment, and found qualitative agreement with our measurements: a peak response

f = 56 GHz

f = 63 GHz

f = 70 GHz
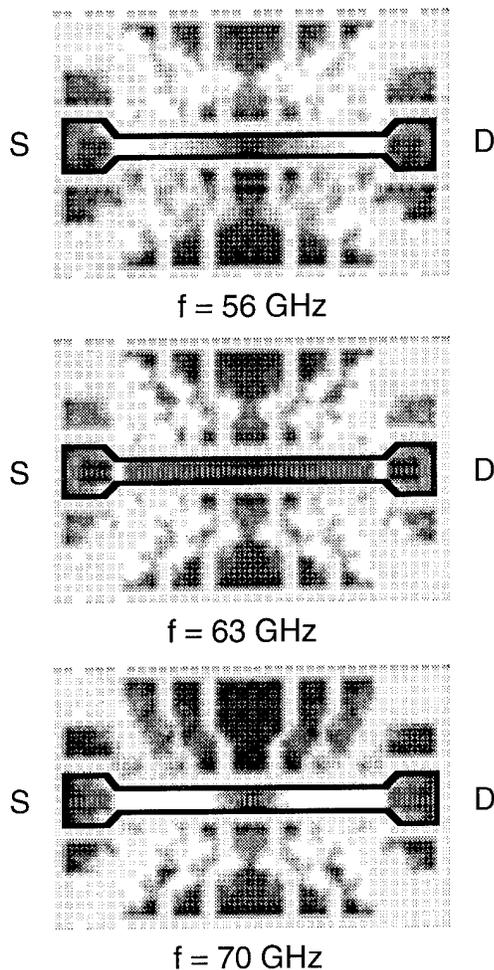
Figure 2. Simulation of radiation-induced source-drain (S-D) current on the quantum-dot structure (other areas are gate fingers; background is GaAs substrate). Light shades are regions of highest current density, with scales (from top to bottom) set to 3.9, 22, and 8.6 A/m, respectively.

of the structure measured at f = 63 GHz (the 9th harmonic of 7 GHz [Fig. 3]) corresponds to a peak in the simulated radiation-induced current density on the source-drain line, as seen in Fig. 2. The peak current density simulated at 63 GHz was ~ 3× more than the value at the neighboring harmonics.

Experimental configuration

The output of the dual-source interferometer was focused by a paraboloidal mirror into a (cold-filtered) light pipe leading to the sample; the bath temperature was T = 350 mK. The sample's radiation-induced drain-source current was amplified and fed into a Fourier-transform spectrum analyzer on which the fundamental frequency displayed corresponds to the fundamental radiation-induced signal; all higher harmonics displayed correspond to higher-order harmonics of the radiation.

Results

A typical output spectrum for two different offset (or intermediate) frequencies (Δf) is shown in Fig. 3 for a microwave fundamental of 7 GHz. The periodicity vs. frequency in the foreground signal is due to the half-wave resonances of the source-drain contact, the primary antenna; its fundamental resonance on GaAs is calculated at ~ 27 GHz. The background signal is obtained by blocking the beam.
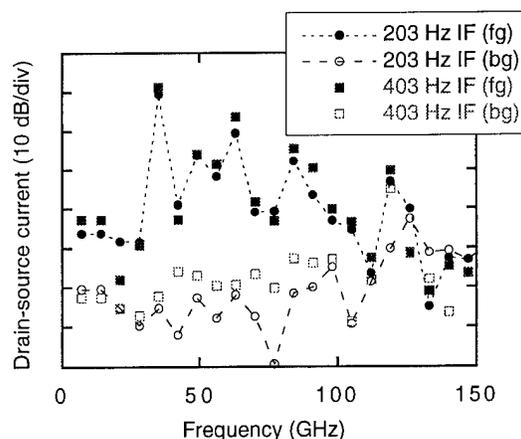
Figure 3. Relative foreground (fg) and background (bg) source-drain current response of coupled quantum dot sample to picosecond pulses at different offset (intermediate) frequencies (IF) and 512 averages. Dotted lines are guides to the eye.

From Fig. 3 we can determine that the sample responds to harmonics up to ~ 140 GHz, the 20th harmonic of 7 GHz, at $\Delta f = 403$ Hz (hence ~ 8 kHz at the 20th harmonic). The rise time of the current preamplifier used on the source-drain signal was 0.01 ms, sufficient for the bandwidth of the source-drain current. While the dual-source interferometer produces measurable harmonics beyond 300 GHz, losses in the light pipe and uncertainties in focusing could contribute to the lower response of the sample.

Conclusions

We have described a new broadband dual-source interferometer for combining picosecond pulses from nonlinear transmission lines driving planar antennas. We have shown that the signal from this instrument is

detected by an asymmetric quantum dot sample as the basis for a forthcoming detailed study of the millimeter-wave induced transport of carriers in this sample.

Acknowledgments

References

[1] S. Verghese, et al., Appl. Phys. Lett. **64**, 915 (1994).
[2] D.W. van der Weide, J.S. Bostak, B.A. Auld, and D.M. Bloom, Appl. Phys. Lett. **62**, 22 (1993).
[3] D.W. van der Weide, to appear in J. Opt. Soc. Am. B (December, 1994).
[4] R.H. Blick, et al., submitted to Phys. Rev. Lett. (June, 1994).
[5] *EM* 2.4 (Sonnet Software, Inc., Liverpool, NY).

Poster Session

QThE 5:00 pm-6:30 pm
Ballrooms VI-VIII

Excitonic spin-flip dynamics under resonant two-photon excitation in quantum wells

A. Lohner, P. Michler, and W. W. Rühle

Max-Planck-Institut für Festkörperforschung, Heisenbergstraße 1, D-70569 Stuttgart, Germany

Tel: +49/711-6891664, Fax: +49/711-6891662

K. Köhler

Fraunhoferinstitut für Angewandte Festkörperphysik, Tullastraße 72, D-79108 Freiburg,

Germany

The detailed dynamics of resonantly excited nonthermal excitons in quantum wells has been investigated recently [1,2]. Various fit parameters were necessary to describe the time evolution of the heavy-hole exciton luminescence. Comparable and therefore not easily distinguishable rates for the radiative recombination, the spin relaxation, and the momentum relaxation of excitons were obtained. In particular, the flip of the spin of optically active ($J=\pm1$) into optically inactive ($J=\pm2$), "dark" excitons plays an important role in the analysis since these dark excitons serve as a huge, invisible reservoir in the overall dynamics.

Here we report on a new, more direct approach to study specifically this spin-flip process: Dark excitons are resonantly created by two-photon absorption and their transformation by spin-flip into optically active excitons is traced via time-resolved luminescence. The measurements were performed with a tunable 100 fs Optical Parametric Oscillator synchronously pumped by a Ti:Sapphire laser. Heavy-hole, $J=\pm2$ excitons are resonantly excited in a 50 Å GaAs/AlGaAs quantum well by two-photon absorption with a photon energy of $E_{ph}=$ 0.821 eV. The sample was kept at about 15 K. The heavy-hole, $J=\pm1$ exciton luminescence was detected with a streak camera with S20 cathode. This setup works perfectly since the streak camera is completely insensitive in the wavelength regime

of the exciting laser but very sensitive at the photon energy of the luminescence.

Figure 1a shows the temporal evolution of the heavy-hole exciton luminescence at 1.642 eV after linearly polarized two-photon excitation. The unpolarized luminescence rises to maximum in 20 ps and decays with a time constant of 204±5 ps. For comparison, Fig. 1b shows the time evolution of the heavy-hole exciton luminescence (solid line) after resonant, single-photon excitation (E_{ph}= 1.642 eV). The rise time is limited by the time resolution of our experimental setup. The luminescence decreases initially with a time constant of about 6 ps and decays then exponentially with a decay time of 220±5 ps. The initial decay of exciton luminescence with single photon is qualitatively similar to recent results ,[1] although in our case this decay is by a factor of 2 faster.

Dark excitons are created by a two-photon absorption process due to the optical selection rules. The luminescence in Fig. 1a results from excitons which changed their spin from J=±2, to J=±1 excitons. Therefore, the measured time evolution of luminescence is at short times mainly determined by the spin-flip transformation of excitons. We fit the time evolution of the luminescence with a model containing three terms. The first term corresponds to the integration of the laser pulse (see dotted line in Fig.1b), and the third part is the slow decay at long times. The second term is closely related to the spin-flip time and contains the only free fitting parameter. This fit to the experimental data is shown as a solid line in Fig. 1a and yields a time constant for the exciton spin-flip of about 20±5 ps. This time is substantially shorter than the spin-relaxation time reported in Ref. [1], but closer to theoretical predictions.[2] However, a quantitative comparison is difficult since the thickness of our quantum well is smaller.

[1] A. Vinattieri, Jagdeep Shah, T. C. Damen, D. S. Kim, L. N. Pfeiffer, and L. J. Sham, Solid State Commun. **88**, 189 (1993) and A. Vinattieri, Jagdeep Shah, T. C. Damen, K. W. Goosen, L. N. Pfeiffer, M. Z. Maialle, and L. J. Sham, Appl. Phys. Lett. **63**, 3164 (1993)

[2] M. Z. Maialle, E.A. de Andrada e Silva, and L. J. Sham, Phys. Rev. **B 47**, 15776 (1993)
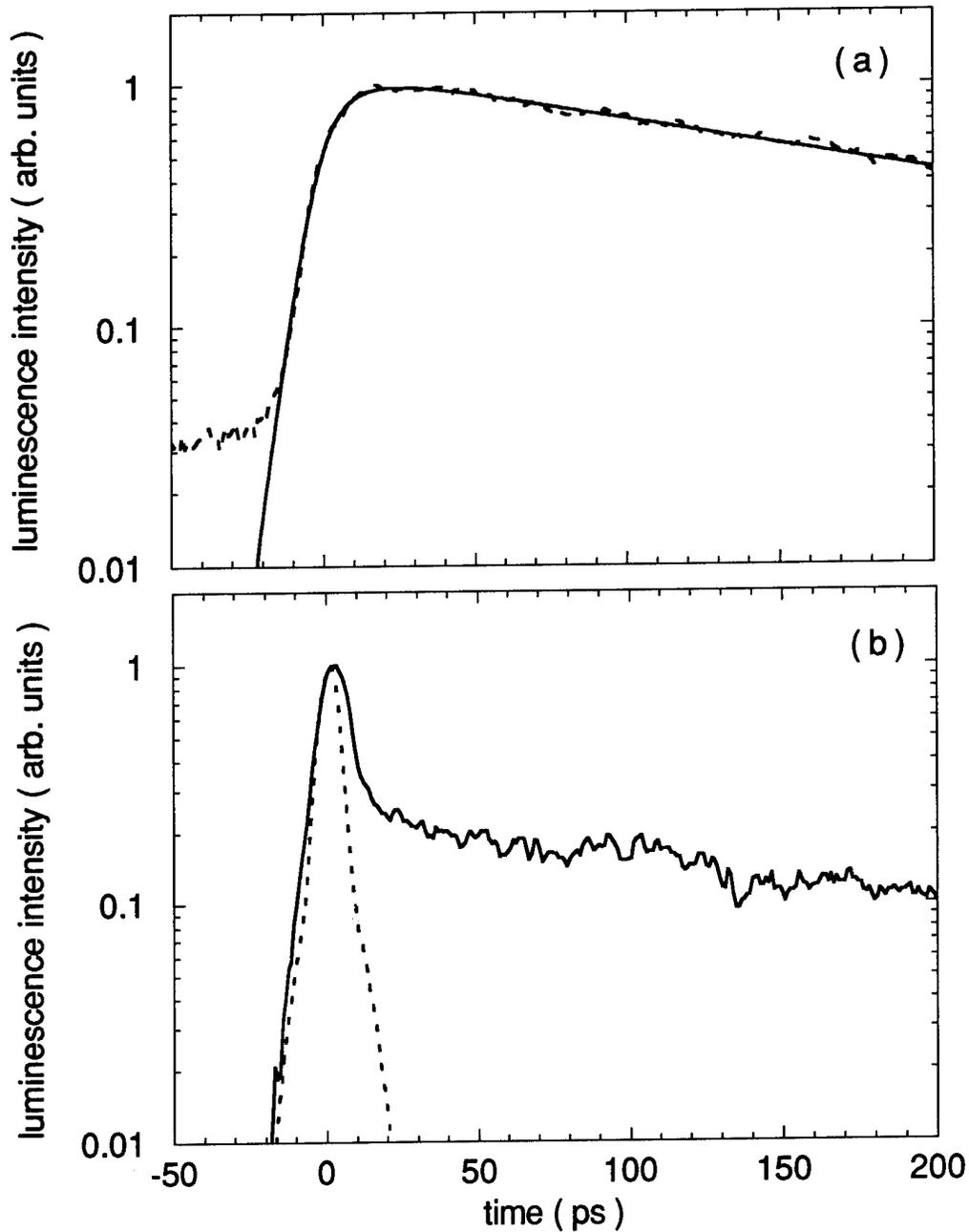
FIG. 1. (a) Temporal evolution of resonantly excited heavy-hole exciton lumines-
cence (dashed line) at 1.642eV after two-photon absorption of femtosecond infrared pulses
(E_{ph}= 0.821 eV). The solid line represents the result of our model calculation.

(b) Time evolution of the heavy-hole exciton luminescence for single-photon excitation
(E_{ph}= 1.642 eV). The dashed line represents the temporal trace of the 100 fs laser pulses
as obtained with the time resolution of the streak camera system.

Dipole Emission
in Two-Dimensional Photonic Band Structures

Toshio Suzuki and Paul K. L. Yu
Department of Electrical and Computer Engineering

D. R. Smith and S. Schultz
Department of Physics

University of California, San Diego
La Jolla, California 92093-0407
(619)-534-6180
FAX (619)-534-2486

For non-conducting passive two-dimensional dielectric periodic structures, the wave equation with a source term $J(x,y,t)$ for an electric dipole can be written as,

$$\nabla\times\nabla\times\mathbf{E}(x,y,t) + \frac{1}{c^2}\varepsilon(x,y)\frac{\partial^2}{\partial t^2}\mathbf{E}(x,y,t) = -\mu_0\frac{\partial}{\partial t}\mathbf{J}(x,y,t) \tag{1}$$

where $\mathbf{J}(x,y,t) = \mathbf{J}(x,y)J(t) = I_0\Omega\mathbf{d}\,\delta(x-x_0)(y-y_0)\theta(t)\,e^{-i\Omega t}$. $\qquad$ (2)

The dyadic Green's function $\overline{\mathbf{G}}(x,y,t; x',y',t')$ satisfies,

$$\nabla\times\nabla\times\overline{\mathbf{G}}(x,y,t; x',y',t') + \frac{1}{c^2}\varepsilon(x,y)\frac{\partial^2}{\partial t^2}\overline{\mathbf{G}}(x,y,t; x',y',t') = \overline{\mathbf{I}}\delta(x-x')\,\delta(y-y')\,\delta(t-t'). \tag{3}$$

$\overline{\mathbf{G}}(x,y,t; x',y',t')$ can be constructed with the eigen solutions of the homogeneous wave equation,

$$\nabla\times\nabla\times\widehat{\mathbf{E}_0^n}(x,y,t) + \frac{1}{c^2}\varepsilon(x,y)\frac{\partial^2}{\partial t^2}\widehat{\mathbf{E}_0^n}(x,y,t) = 0 \tag{4}$$

The eigen solutions of (4) with properly normalized eigenvectors can be readily obtained by the plane wave method.

By applying the dyadic Green's function $\overline{\mathbf{G}}(x,y,t; x',y',t')$ and (4), the analytic expression for emission power of the electric dipole can be derived similarly to the three-dimensional case. Because of periodic nature of photonic crystals, the entire two dimensional k-space can be divided in many identical domains to the 1st Brillouin zone. Thus, the dipole emission power becomes

$$P_{\text{lattice}}^{2D} = \frac{I_0\Omega\mu_0c^2\pi}{2(2\pi)^2}\left[\int_{\text{1st BZ}} dk_x dk_y \sum_{n=1}^{NP}\left|\mathbf{d}\cdot\widehat{\mathbf{E}_{z\,0}^n}(x_0,y_0,k_x,k_y)\right|^2\delta[\Omega-\omega_n(k_x,k_y)]\right] \tag{7}$$

This surface integral can be transformed into the line integral as,

$$P_{Lattice}^{2D} = \frac{I_0 \Omega \mu_0 c^2 \pi}{2(2\pi)^3} \sum_{n=1}^{NP} \int_{\substack{\Omega = \omega_n(k_x, k_y) \\ 1st\ BZ}} \frac{dl}{|\nabla \omega_n(k_x, k_y)|} \left| d \cdot \widehat{E_{z\ 0}^n}(x_0, y_0, k_x, k_y) \right|^2 . \tag{8}$$

The line integral in (8) is numerically evaluated by the triangle interpolation integration method. (for three-dimensional cases, tetrahedron method). In the triangle method, the irreducible Brillouin zones in the k-space are divided into NT triangles in which energy contours are linearly interpolated.

The two-dimensional square lattice (lattice constant=a) with dielectric cylinders (ε=9, radii=0.378a) is investigated, since the periodic structures can be experimentally well verified in the microwave frequency. The band diagram for propagating modes and complex band structure at X point with the imaginary k-vector in (1,1) direction (both for TE polarization) are plotted in Fig 1. (a) and (b) respectively. In Fig 1. (c), we show the calculated density of states. The corresponding dipole emission power (computed) at the center of dielectric cylinders with dipole moment (0,0,1) is given in Fig 1. (d). The computations suggest complete suppression of dipole emission in the photonic band gaps and strong enhancement around the band edges.

References

(1). Toshio Suzuki and Paul. K. L. Yu, "Emission power of an electric dipole in the photonic band structure of the FCC lattice." To be published in Opt. Soc. Am. B.

(2). Toshio Suzuki and Paul. K. L. Yu, "Dispersion relation at L point in the photonic band structure of the FCC lattice with active or conductive dielectric media." To be published in Opt. Soc. Am. B.

(3). Toshio Suzuki and Paul. K. L. Yu, "Tunneling in the photonic band structures." Submitted to Opt. Soc. Am. B.

(4). J. P. Dowling and C. M. Bowden, "Atomic emission rates in inhomogeneous media with application to photonic band structures." Phy. Rev. A **46** (1), 612 (1992).
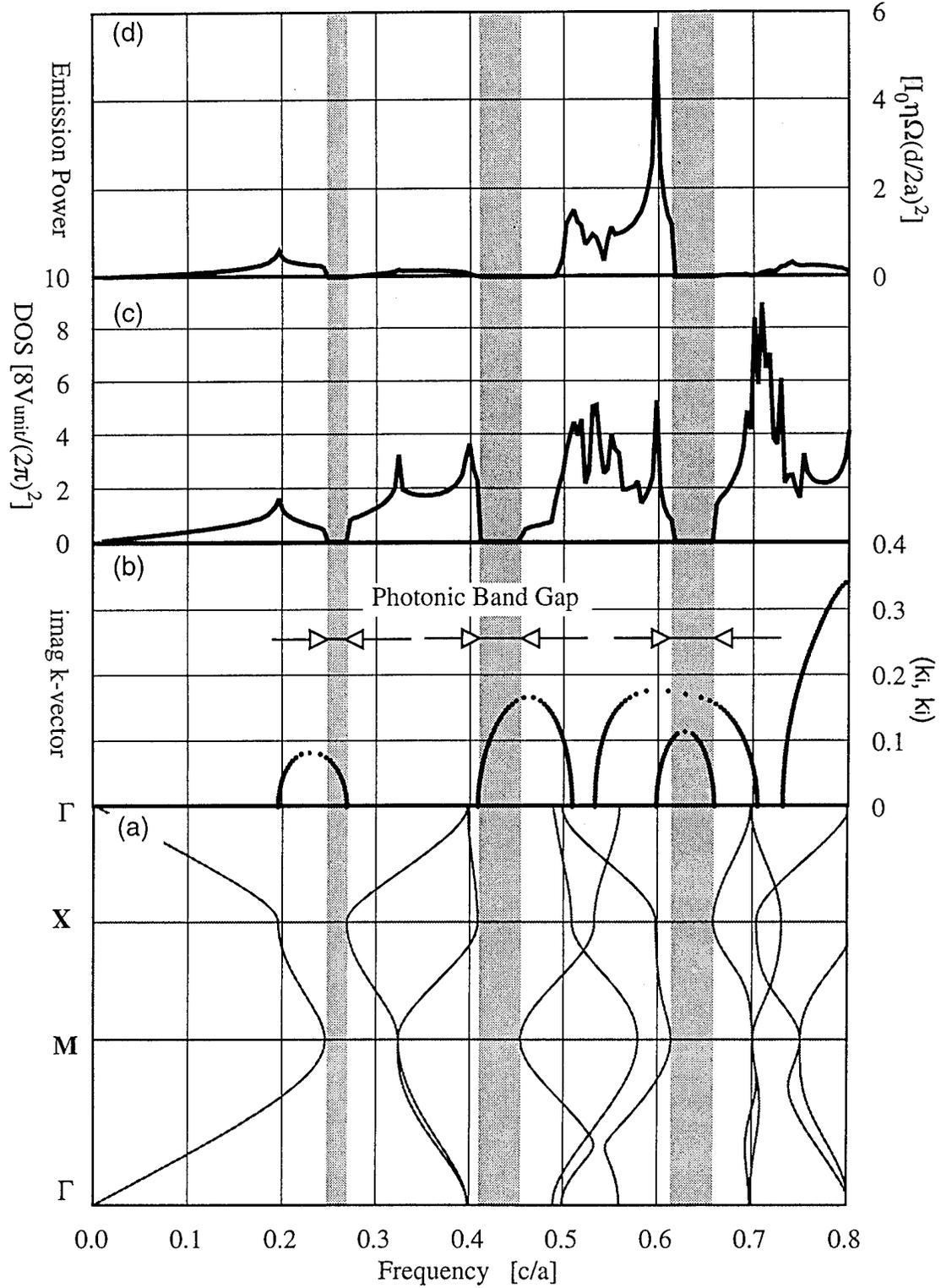
Waveguide-Coupled Microcavity LEDs

Bardia Pezeshki, Jeffrey. A. Kash, and David. W. Kisker
IBM Research Division, T. J. Watson Research Ctr., Yorktown Heights, NY 10598
Tel: (914) 945-1443, FAX: (914) 945-2141

The ability to modify the spontaneous emission of an atom in a micro-cavity has introduced a new degree of control which may have profound significance for opto-electronic devices[1]. In compound semiconductors, distributed Bragg mirrors on the two sides of an active quantum well lead to narrow-band emission in the cavity mode[2]. Generally, these cavities are optimized for normal incidence geometry, and the light is monitored perpendicular to the layers. However, at room temperature, and under strong pumping conditions, the light is emitted in a broad range of wavelengths. The presence of the microcavity causes each wavelength to be generated at a different angle and thus the narrow band emission wavelength changes with angle. In this work we show that micro-cavities can be optimized to emit at an angle that corresponds to a waveguide mode, and thus they can directly couple to an adjacent waveguide. Since the emission bandwidth depends directly on the cavity thickness, one can use a taper in the device to controllably generate many wavelengths into the same waveguide. Such a device could be used for multi-wavelength communication through the same optical fiber.

Such a device is shown schematically in Fig. 1. The multi-layer mirrors above and below the quantum well define the resonance condition. The mirrors are doped p-i-n to allow current injection into the quantum well. A ridge waveguide is formed from a low index material above the mirrors, and the light can couple from the semiconductor cavity to this waveguide through the top Bragg mirror. The reflectivity of this top mirror is set to control the coupling between the waveguide and the resonator, and determines the wavelength resolution of the device. Energy lost through the bottom mirror, however, must be minimized and the reflectivity of the bottom mirror must be sufficiently high. For multi-wavelength operation, a growth-induced taper in the cavity causes the emission wavelength into the waveguide to be dependent on position. Contacts spaced adjacent to the waveguide allow current injection at different points and cause emission at different wavelengths. A proton implant step isolates the diodes.
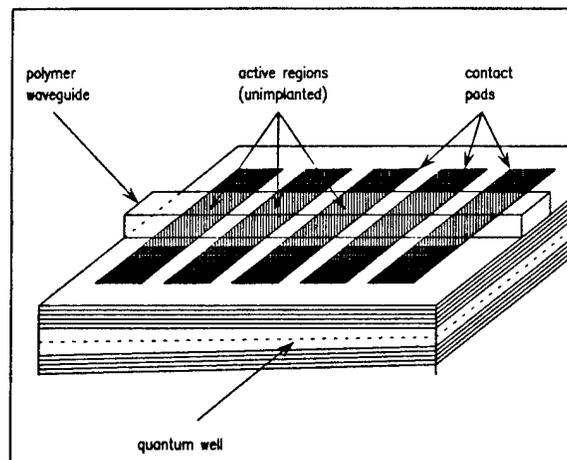
Figure 1: Device Schematic. The microcavity containing the QW is optimized to emit directly into the top waveguide.

The microcavity itself resembles another waveguide, and the whole structure is very similar to an asymmetric directional coupler. This lower micro-cavity waveguide, instead of conventional total internal reflection mirrors, uses anti-resonance quarter-wave layers to confine the light. It is well known that such asymmetric couplers have a frequency-selectivity that increases with the asymmetry[3]. The photon or cavity lifetime determines the coupling length, as the light is propogating at an angle. Thus the same device can be interpreted in both waveguide and resonator terms. We previously used a coupled-waveguide ray diagram approach to estimate both the wavelength resolution and the coupling length of such devices[4].

Devices were fabricated by OMVPE, using $Al_{0.3}Ga_{0.7}As/AlAs$ quarter wave mirrors and a 7.5nm thick GaAs QW. The bottom mirror consisted of 30.5 periods, the top mirror of 6 periods, and the cavity was one wavelength thick, with the quantum well at the center. The layers were optimized to be most reflective at approximately 30 degrees to the normal in the AlGaAs layers. This angle corresponded to the fundamental mode of the top polymer waveguide. After growth, the wafer was implanted twice, once to provide current funneling from the contacts to the region direcly below the polymer waveguide, and the second time to isolate the top diode regions from each other. An ohmic alloyed AuGe layer was then evaporated on the backside of the wafer, and ohmic 200 mm long TiAu contacts were patterned on the front side, spaced 20 mms apart. A 10 mm wide and 5 mm thick polymer waveguide was fabricated by spinning on and developing a UV-sensitive polymer. The device was then cleaved to about a centimeter in length, packaged, and contacts about 1.5mm apart were wire bonded to outside electrical leads.

Figure 2: Observed luminescence from the thin side of the device as different diodes are pumped.

To test the device, we simply positioned a multi-mode fiber at the cleaved polymer end, and observed the luminescence using a pulsed current source and an optical spectrum analyzer. Current was injected into both contacts on either side of the waveguide. Fig. 2 shows the experimentally obtained spectra from the end of the waveguide as different diodes were pumped. The emission wavelength shifted according to the growth induced taper in the OMVPE layers. The amplitude was roughly constant from diode to diode, indicating negligable loss in the top waveguide, and relatively flat intrinsic QW luminescence. The observed power that was coupled to the fiber was relatively small, about a micro-watt at 100 mA continuous injection. Observing from the thin side of the wafer, we note that the luminescence peaks are asymmetric, with a slower drop off on the long wavelength side. Fig. 3 shows the effect of varying injection conditions. In this case, we changed the duty cycle of the current pulses to keep the total injected carriers constant, and observed the relative efficiency. When the injected current is small, only a small amount of power is coupled to the top waveguide. This efficiency peaks at about 100mA and falls off at very high current levels. The spectrum also exhibits the narrowest linewidth of about 1.3nm at about 100mA. The shape of the luminescence changed as we examined the light emission from the other side of the device. The luminescence from the thick side exhibited the slower drop off on the short wavelength side, and was also a little broader.

Figure 3: Effect of varying drive current on the output spectrum and relative efficiency.

The performance of these LEDs can be compared to our previously developed first order theory.

Without a taper, in a lossless device, we'd expect the linewidth to be set by the reflectivity of the top mirror and the difference between the indices of the polymer waveguide and the semiconductor cavity. A six period mirror would yield a reflectivity of 98.8%, a FWHM of about 0.5nm, and a coupling length of 200 microns. The difference between the expected and measured FWHM maybe partially attributed to the taper, causing a broadening in one shoulder, and the non-ideal experimental conditions. For example, our theory was developed for coupling to a single mode waveguide, while the 10 mm wide polymer waveguide supports many lateral modes, each with a slightly different propogation constant.

The coupled output power is quite weak since there is no waveguide defined in the microcavity itself. The resonance condition from the two Bragg mirrors establishes a relationship between wavelength and azimuthal emission angle, creating a two dimensional step-like photonic density of states. Only a small fraction (< 1%) of this light travels in the direction of the top polymer waveguide and can couple out of the resonator. Laterally defining a waveguide in the resonator would not only increase this acceptance angle, but provide photonic quantization in the lateral direction, preventing emission at undesired angles. Including the acceptance angle limitation, our efficiency is about the same as the vertical micro-cavity LEDs previously demonstrated.

The asymmetric shape of the luminescence and the current dependent efficiency can be explained using higher order effects. For the light to efficiently couple to the top waveguide, it requires the loss to be small over the coupling length. As the current injection increases, we reduce the loss in the quantum well and improve this coupling. This effect was previously observed in an optically pumped device containing six quantum wells, where the higher loss led to good coupling only at very high pumping rates. The asymmetry is caused by amplification in the 200 micron region. When observing from the thin side, shorter wavelengths have a longer distance to travel and be amplified before reaching the resonance condition and coupling to the top waveguide; thus there is more intensity from the shorter side of the peaks. The intensity does not linearly increase at high current densities since the

Figure 4: Comparison of luminescence from two sides of the chip (Amplitudes not to scale).

states at the transition energy defined by the cavity resonance are already filled and inverted, thus the total power output is clamped and the relative efficiency decreases. Heating and carrier dependent index changes deteriorate the performance, increasing broadening and causing wavelength shifts.

In summary, we have shown that microcavity LEDs can be optimized to emit into a waveguide mode, enabling new designs for wavelength-dependent devices. Further optimization should increase the performance of such devices.

[1] Y. Yamamoto and R. E. Slusher, Physics Today June 1993 p 66.
[2] U. Keller, G. R. Jacobovitz-Veselka, J. E. Cunningham, W. Y. Jan, B. Tell, and K. F. Brown-Goebeler, Appl. Phys. Lett. 62, p. 3085 (1993).
[3] B. Broberg, B. S. Lindgren, M. G. Oberg, and H. Jiang, J. Lightwave Tech. LT-4 p. 196 (1986).
[4] B. Pezeshki, F. Tong, J. A. kash, and D. W. Kisker, to appear in IEEE J. Light. Tech. 12 (1994).
[5] B. Pezeshki, J. A. Kash, D. W. Kisker, and F. Tong, Appl. Phys. Lett. 65 p. 138 (1994).

Tunable Transversely-Pumped Counterpropagating Optical Parametric Oscillators Based on Semiconductor Structures

Yujie J. Ding
Department of Physics and Astronomy and Centers for Materials and Photochemical Sciences
Bowling Green State University, Bowling Green, OH 43403.
Jacob B. Khurgin and Seung-Joon Lee
Department of Electrical and Computer Engineering
The Johns Hopkins University, Baltimore, MD 21218.
Tel. (419) 372-8785. Fax (419) 372-9938.

Since backward parametric oscillations were proposed [1] in the parallel propagation configuration, such a fundamental nonlinear process has never been observed due to the lack of appropriate materials for achieving quasi-phasematching. Recently, following Ref. [2], quasi-phasematching were achieved based on GaAs/AlGaAs multilayers [3] or asymmetric quantum-well domain structures [4-6]. Here, for the first time to the best of our knowledge, we propose to use second-order optical nonlinearities of multilayers or asymmetric quantum-well domain structures in a vertical cavity to achieve tunable and efficient transversely-pumped counterpropagating optical parametric oscillations (TPCOPOs). Similar to Refs. [3-6], the quasi-phasematching can be achieved in these structures by spatially modulating the second-order susceptibility along the growth direction. The threshold pump power for the TPCOPOs is

$$P_{th} = \frac{n_1 n_2 n_3 \lambda_1 \lambda_2}{4\eta_0 [\chi_0^{(2)}]^2} \frac{(1 - \sqrt{R_1 R_2})^2}{1 - R_1} \frac{W}{L} \frac{d_{eff}}{d} \tag{1}$$

where W, d, d_{eff}, and L are the width, thickness, effective thickness, and length of the waveguide, respectively, R_1 and R_2 are the reflectivities of the vertical mirrors, n_1, n_2, n_3 are the refractive indices at ω_1 (λ_1), ω_2 (λ_2), and ω_3 (λ_3), $\chi_0^{(2)}$ is the amplitude of the spatially-modulated second-order susceptibility, and η_0 is the vacuum impedance. If there is no horizontal cavity, the conversion efficiency and output power are plotted vs. the pump power, in Fig. 1(a). There is an optimal pump power $P_3 \approx 3.36 P_{th}$ at which the efficiency reaches the maximum value of $\eta_{max} \approx 43.5\%$. *We can see that without mirror feedback for the oscillating waves their amplitudes start from zero at their respective input planes and reach the maximum values at the output planes.* This is similar to the backward parametric oscillations in the parallel propagation configuration in Ref. [1], but fundamentally different from the conventional OPOs [7] in the collinear propagation configuration where oscillations cannot occur without the mirror feedback. If $P_3 \gg 3.36 P_{th}$, there is a huge build-up of the oscillating fields inside the material, that are more or less constants along the propagation direction of the signal or idler except near small regions at both ends of the material. The conversion efficiency from the fields at ω_1 and ω_2 to the field at ω_3 (sum-frequency generation) is high since the overlap between two oscillating fields is large. This process saturates TPCOPOs.

One of the most important applications of the TPCOPOs is to generate tunable output from the signal and idler. This can be done by changing the incident angle of the pump wave around the direction normal to the surface plane. Based on the phasematching condition along the propagation direction of the signal or idler, the minimum and maximum output wavelengths can be determined to be

$$\lambda_{min} = \lambda_3 (n_1 + n_2)/(n_2 + 1) ; \quad \lambda_{max} = \lambda_3 (n_1 + n_2)/(n_1 - 1). \tag{2}$$

Consider GaAs/Al$_{0.8}$Ga$_{0.2}$As multilayers, $\lambda_3 \approx 0.9\,\mu m$, $R_1 = R_2 \approx 99.99\%$, $d_{eff}/d \approx 10$, $W \approx 1\,\mu m$, $L \approx 1\,cm$, and $\chi_0^{(2)} \approx 10^{-10}\,m/V$, $P_{th} \approx 819\,mW$, $\lambda_{min} \approx 1.4\,\mu m$, and $\lambda_{max} \approx 2.6\,\mu m$. Consider ZnSe/ZnS multilayers, $\lambda_3 \approx 0.49\,\mu m$, and $R_1 = R_2 \approx 99.99\%$, $P_{th} \approx 107\,mW$, $\lambda_{min} \approx 0.7\,\mu m$, and $\lambda_{max} \approx 1.6\,\mu m$. Consider GaAs/AlAs asymmetric coupled quantum-well domain structure, $\lambda_3 \approx 10\,\mu m$, $\chi_0^{(2)} \approx 30 \times 10^{-9}\,m/V$ [4], $R_1 = R_2 \approx 99.9\%$, and $W \approx 10\,\mu m$, $P_{th} \approx 99.6\,mW$, $\lambda_{min} \approx 15\,\mu m$, and $\lambda_{max} \approx 29\,\mu m$. For achieving high-power output, we should design the structure resulting in the high threshold pump power to achieve η_{max}.

In the presence of the horizontal cavity with the reflectivities $R_{3,4} \approx 1$, the conversion efficiency and output power are plotted vs. the pump power in Fig. 1(b). The threshold pump power is $P_{th}' = 16(1 - R_{3,4})^2 P_{th}/\pi^2$ for nondegenerate TPCOPOs and $P_{th}' = 4(1 - R_{3,4})^2 P_{th}/\pi^2$ for degenerate TPCOPOs. The conversion efficiency reaches maximum value of 25% when $P_3 = 4P_{th}'$. The lower maximum conversion efficiency is due to the saturation of the TPCOPO by more efficient sum-frequency generation. If $R_{3,4} \approx 99\%$, the threshold pump powers based on three structures discussed above can be 33 μW, 4.4 μW, and 4 μW, respectively. For efficiently achieving the low-power output, we should use a horizontal cavity resulting in the low threshold pump power to achieve η_{max}'. If we want to achieve 10 μW output, $P_3 = P_{out}/\eta_{max}' \approx 40\,\mu W$ and $P_{th}' = P_3/4 = 10\,\mu W$. Our parametric processes can be then used to amplify the low-power signal from the parametric oscillator to the required level through multi-stage amplifiers. To achieve high-power and tunable output in the mid-IR domain, we use GaAs/Al$_{0.8}$Ga$_{0.2}$As multilayers. Assuming $\lambda_3 \approx 2\,\mu m$, $R_1 \approx R_2 \approx 99\%$, $W \approx 20\,\mu m$, $R_{3,4} \approx 95\%$. The threshold pump power is 33 W. To achieve the maximum conversion efficiency, $P_3 = 4P_{th}' \approx 131\,W$. The total output power is then 33 W. Based on Eqs. (2), the maximum tuning range of the output wavelength is 3.1-5.8 μm. The proposed TPCOPOs may eventually become the only tunable and high-power laser sources in this domain.

One of the advantages of the transverse-pumping geometry is that we can generate efficient parametric oscillations for a large wavelength range of the pump wave. If the conversion efficiency decreases from its optimal value 25% to 20%, and for $d \approx 1\,\mu m$, and $\lambda_0 \approx 0.9\,\mu m$, we can tune the pump wavelength within the bandwidth $\Delta\lambda \approx 1309\,\text{Å}$. Such a large usable bandwidth is possible only for transverse-pumping geometry. Because each TPCOPO can be miniature, a large number of the TPCOPOs can be fabricated into a one-dimensional array on one wafer.

[1] S. E. Harris, Appl. Phys. Lett. 9, 114 (1966).

[2] N. Bloembergen, U.S. Patent No. 3 384 433 (1968).

[3] R. Normandin et al., Electr. Lett. 26, 2088 (1990). D. Vakhshoori et al., Appl. Phys. Lett. 59, 896 (1991).

[4] S. Li and J. Khurgin, Appl. Phys. Lett. 62, 1727 (1993).

[5] J. B. Khurgin and Y. J. Ding, Opt. Lett. 19, 1066 (1994).

[6] J. B. Khurgin, Phys. Rev. B38, 4056 (1988); S. Janz et al., Opt. Lett. 19, 622 (1994).

[7] S. E. Harris, Proc. IEEE 57, 2096 (1969).
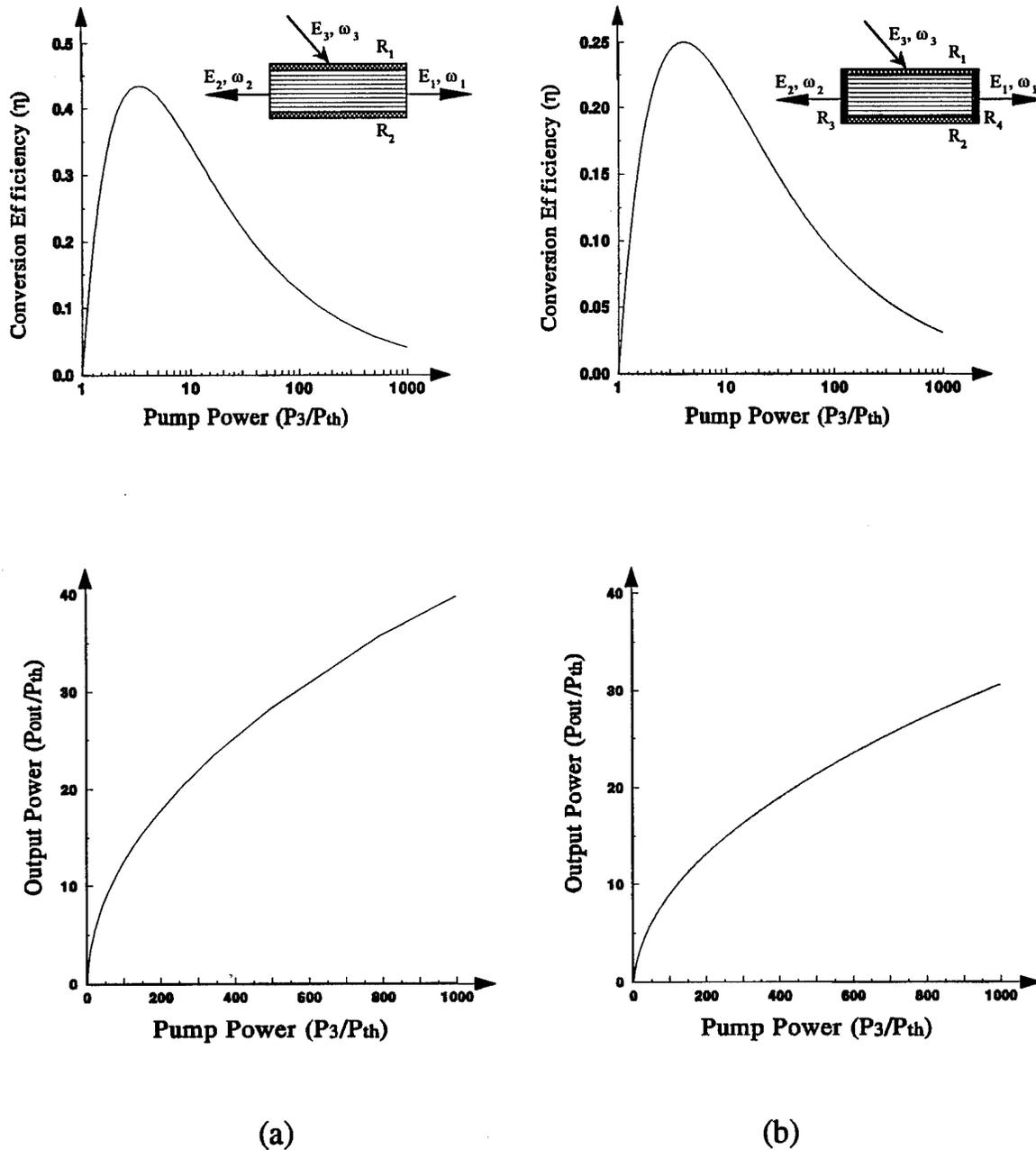
Fig. 1   The conversion efficiency (top) and output power (bottom) vs. the pump power: (a) without and (b) with the horizontal cavity. Insets: the proposed structures and wave propagation configurations for (a) and (b).

Fast Coherent Vertical Exciton Transport
in Multiple Quantum Wells

D. S. Citrin
Center for Ultrafast Optical Science, The University of Michigan
2200 Bonisteel Boulevard, Ann Arbor, Michigan 48109-2099
Tel: (313) 747-0971, Fax: (313) 763-4876

In superlattices in which the barriers are sufficiently narrow and low, the low-temperature vertical transport of excitons is due to quantum-mechanical tunneling between successive quantum wells (QW).[1] For structures with wide and high barriers [multiple QW's (MQW)], the interwell coupling is due to the dipole-dipole interaction.[2] The context for treating coherent effects of this sort is exciton-polariton theory.[3] Exciton transport has been of interest in various molecular systems,[4] where the picture is of incoherent Förster transport.[5]. The MQW provides a tailor-made system of which an individual structure can be studied, while data on molecular systems must be frequently interpreted in terms of ensembles. There has been little experimental or theoretical[6] work on this type of vertical transport in MQW's, although incoherent transport in such structures has been the subject of one study.[7]

In the present work we study the coherent vertical transport of excitons in MQW's. We find that in planar systems there is a possibility of rapid coherent excitation transfer between different QW's. We consider the dynamics subsequent to the introduction of an initial exciton population into a single QW within the MQW. Schemes for doing so by means of incoherent excitation are discussed. Thus, the envisaged experiment involves initial conditions markedly different from light-propagation studies. The dynamics are governed by the coherent radiative decay (spontaneous emission) of excitons and reabsorption elsewhere in the structure. At low-temperature, where the occupied exciton states have very small in-plane momentum (direct-gap case), it is essential to consider the effects of retardation, *i.e.* the full dynamical dipole-dipole interaction must be taken into account, since for small in-plane wavevectors $k_\parallel$ the interwell coupling including retardation is long-ranged, whereas the neglect of retardation arbitrarily introduces a finite spatial range to the interwell coupling. The Green's functions (GF) describing exciton polaritons contain all the dynamical information in the model.[8] We consider an infinite, periodic MQW composed of symmetric, identical QW's, and assume the width L_z of the individual QW's is much less than the wavelength in the background dielectric medium corresponding to the optical transition of interest. The GF for the exciton's transition dipole moment in QW n following excitation with in-plane wavevector $k_\parallel$ in QW 0 is $D_n(t, k_\parallel)$. The population in QW n is then given by $N_n(t) = |D_n(t, k_\parallel)|^2$. The GF is diagonal in the normal-direction planewave basis $\{|q\rangle\}$,[8] and the dynamic dipole-dipole coupling, both intra and interwell, is characterized by a self-energy $\hbar\Sigma^{(1)}F_q$ where $\hbar\Sigma^{(1)}$ is the single-QW radiative self-energy. [See Ref. [8] for the explicit expression.]

The interwell coupling is given in direct space by $F_n = \exp\{-\alpha|n|L\}$ and in q-space by $F_q = \sinh y/(\cosh y - \cos\phi)$ where $y = \alpha L$, $\phi = qL$ with L the periodicity in the z direction, $\alpha = (k_\parallel^2 - \kappa^2)^{1/2}$ the z-component of the wavevector of the mediating electromagnetic field, and $\kappa = E_{ex}(k_\parallel)/(\hbar c)$ with $E_{ex}(k_\parallel)$ the exciton energy. For $k_\parallel > \kappa$, α is real indicating that the interaction is mediated by an evanescent electromagnetic field and the coupling strength falls off exponentially. For $k_\parallel < |\kappa|$, however, the relevant values of α are imaginary (propagating field), and the coupling is long-ranged. The coupling energy $\hbar\Sigma^{(1)}F_{lm}$ is thus of a very different form from the Förster result coupling between point dipoles (r^{-6}). The long-range nature of the coupling for the MQW is due to the fact that all electric-field lines originating in one QW eventually intersect another. We now consider two limiting cases. (i) $k_\parallel > \kappa$, $y \gg 1$. This reduces to the case of nearest-neighbor dipole-dipole coupling between QW's (instantaneous limit, IL). (ii) $y \ll 1$ (long-wavelength approximation, LWA).

(i) For $k_\parallel \gg |\kappa|$, retardation is negligible. The IL corresponds to an interwell interaction mediated by virtual photons through the evanescent electric fields associated with large-wavevector polaritons. For $k_\parallel \gg |\kappa|$, $\hbar\Sigma^{(1)}, y \in \Re$. Since $y \gg 1$ by assumption, $\sinh y, \cosh y \gg 1$ and $F_q \approx \tanh y [1 + \operatorname{sech} y \cos\phi]$. $N_n(\tau_A) = |D_n(\tau_A)|^2$, where $G_A = \tanh y \operatorname{sech} y \hbar\Sigma^{(1)}$ and $\tau_A = G_A t/\hbar$ is

the scaled time, is plotted in Fig. 1(a). One finds for $\tau_A \ll 1$,

$$N_n(t) \approx \begin{cases} 1 - \frac{1}{2}(G_A t/\hbar)^2, & n = 0 \\ \frac{1}{4}\frac{(G_A t/\hbar)^{2|n|}}{(|n|!)^2}, & n \neq 0 \end{cases} \tag{1}$$

As $t \to 0$, the time derivative of $N_n(t) \to 0$. This leads to a time delay for the transfer of excitation to QW n as seen in Fig. 1(a). For $\tau_A \gg |n|$, we obtain the long-time behavior

$$N_n(t) \approx (2\hbar/\pi G_A t) \cos^2(G_A t/\hbar - \pi|n|/2 - \pi/4). \tag{2}$$

Thus, for large τ_A the time scale for the loss of population in a given QW is $\hbar/G_A$.

(ii) The LWA is valid at all $k_\parallel$ if $k_\parallel L \ll 1$. We have $F_q \approx y/(1 - \cos\phi)$. $N_n(\tau_B) = |D_n(\tau_B)|^2$ is shown in Fig. 1(b) where $\tau_B = G_B t/\hbar$ and $G_B = \hbar\Sigma^{(1)}y$. In the short-time limit $\tau_B \ll 1$, we obtain

$$N_n(t) = \begin{cases} 1 - 2\sqrt{\frac{G_B t}{\pi\hbar}}, & n = 0 \\ \frac{2G_B t}{\pi\hbar}, & n \neq 0 \end{cases} \tag{3}$$

The time derivative of the population at $t = 0$ does not vanish (for $n = 0$ it diverges), unlike for the IL. For $n \neq 0$, the initial rise is independent of n. Thus, the long-range character of the coupling between QW's gives rise to fast excitation transfer, in contrast to what was seen in the IL. The long-time limit $\tau_B \gg |n|$ gives

$$N_n(t) \approx 2\hbar/\pi G_B t. \tag{4}$$

Apart from the oscillatory factor in (i), the long-time dynamics are thus formally similar to what was found above in the IL. Because the LWA is a continuum limit, we do not expect the oscillatory part which arises from the discreteness of the MQW.

We summarize. (i) The IL corresponds to the neglect of retardation. In the extreme limit, we have $G_A \sim e^{-\nu}\hbar\Sigma^{(1)}$ and the dominant coupling is between nearest-neighbor QW's $n = \pm 1$, and the expressions for the GF are well known. The IL involves large-wavevector excitations which cannot couple directly with the free-space optical field. Time-domain techniques related to attenuated total-internal-reflection spectroscopy and near-field optical microscopy show promise to access these modes. For GaAs/AlGaAs-based structures, typically $|\Sigma^{(1)}|^{-1} \approx 10$ ps near $k_\parallel = 0$. $\hbar/G_A \sim e^{k_\parallel L} 10$ ps $\gg 10$ ps, and excitation transfer is slow. Consequently, excitons satisfying the IL in MQW's based on GaAs/AlGaAs or other direct-gap semiconductors are likely to dephase more quickly. Moreover, there will be a population of small-$k_\parallel$ states whose dynamics are not described by the IL. An alternative for the study of the IL is the use of indirect-gap type-I–exciton systems such as InAs/GaAs under proper strain conditions.

(ii) Unlike (i), the LWA can be studied directly in the far field (in $k_\parallel < \kappa$), since the exciton-like states here couple directly with the free-space modes of the electromagnetic field. As in (i), the time scale $\hbar/G_B \gg |\Sigma^{(1)}|^{-1}$. Still, because G_B does not depend upon L exponentially, the time scale can be fast. For example, for a GaAs/AlGaAs MQW, $\kappa_{ex}^{-1} \approx 400$ Å. If $L = 150$ Å ($L_z = 80$ Å, say), then $\hbar/G_B \approx 27$ ps if $|\Sigma^{(1)}|^{-1} = 10$ ps. Moreover, we point out the very rapid rise dynamics shown in Fig. 1(b). Thus, long-range coupling is conducive to fast excitation transfer. This is desireable for switching applications, although the population decay is slow. This problem is not expected to be as severe in MQW's composed of just a few QW's where the radiative depletion of the coherent exciton population is on the 10 ps time scale.

Figure 2 shows proposed excitation and detection schemes for coherent vertical exciton transport. In Fig. 2(a), QW B is tuned so its hh resonance lies between the hh and lh excitons of QW's A and A'. (A'''s hh is resonant with A). The excititing pulse is then tuned to the hh absorption of B, which then transfers excitation to A'. Similarly, for detection, the hh resonance of A and A'' lies between the hh and lh resonances of C. One then time resolves the emission from the hh exciton in C.

We conclude with the remarks that the infinite-range coupling in planar systems is an essential feature; the neglect of retardation leads to spurious qualitatively different dynamics in the LWL.

In finite MQW stacks the dynamics will also contain an oscillatory component due to the reflection off the last QW's. In addition, we expect the rapid excitation transfer will also be present in the finite stacks, without the long population decay in infinite structures, thus making the phenomena under investigation of interest for applications in optical switching.

This work was supported by the National Science Foundation under STC PHY 8920108.

References

[1] B. Deveaud, *et al.*, Phys. Rev. Lett. **58**, 2582 (1987); A. Nakamura, *et al.*, Solid State Commun. **71**, 553 (1989).

[2] T. Förster, Z. Naturf. **4a**, 321 (1949).

[3] J. J. Hopfield, Phys. Rev. **112**, 1555 (1958).

[4] I. Yamazaki, *et al.*, in *Primary Processes in Photobiology*, edited by T. Kobayashi (Springer, Berlin, 1987).

[5] M. Hauser, U. K. A. Klein, and U. Gösle, Z. Physik. Chem. NF. **101**, S255 (1976); A. Blumen and G. Zumofen, J. Chem. Phys. **75**, 892 (1981); J. Baumann and M. D. Fayer, J. Chem. Phys. **85**, 4087 (1986).

[6] L. G. Gerchikov and A. V. Subashiev, Solid State Commun. **90**, 57 (1994).

[7] A. Tomita, *et al.*, in *Quantum Electronics and Laser Science Conference*, 1992 OSA Technical Digest Series, Vol. 13 (Optical Society of America, Washington, DC, 1992), pp. 116-118.

[8] D. S. Citrin, Phys. Rev. B **47**, 3832 (1993); Solid State Commun. **89**, 139 (1994).

Fig. 1 The exciton population in QW n as a function of scaled time. (a) IL, (b) LWA.
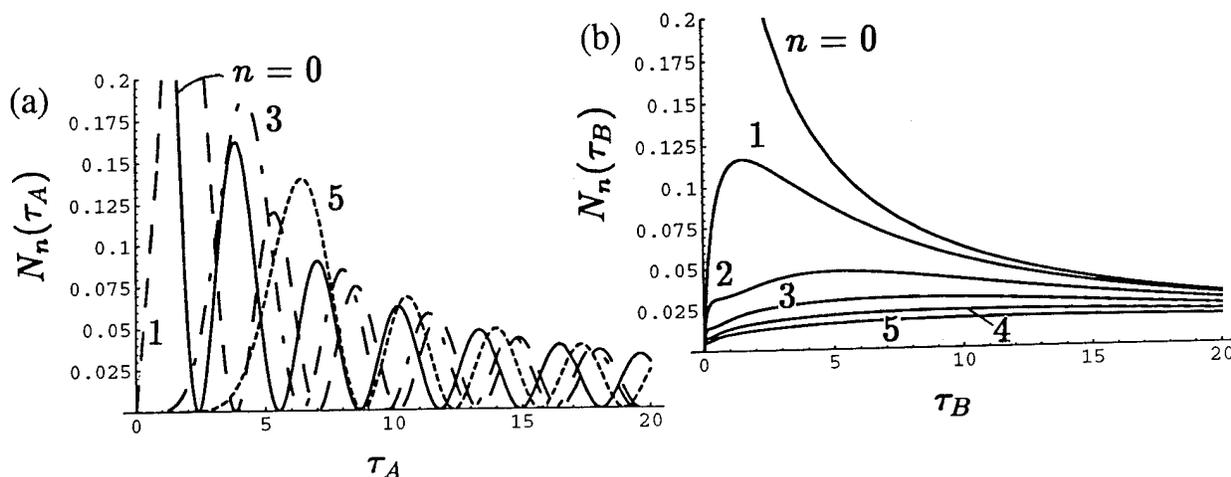
Fig. 2 (a) Excitation scheme; (b) detection scheme.
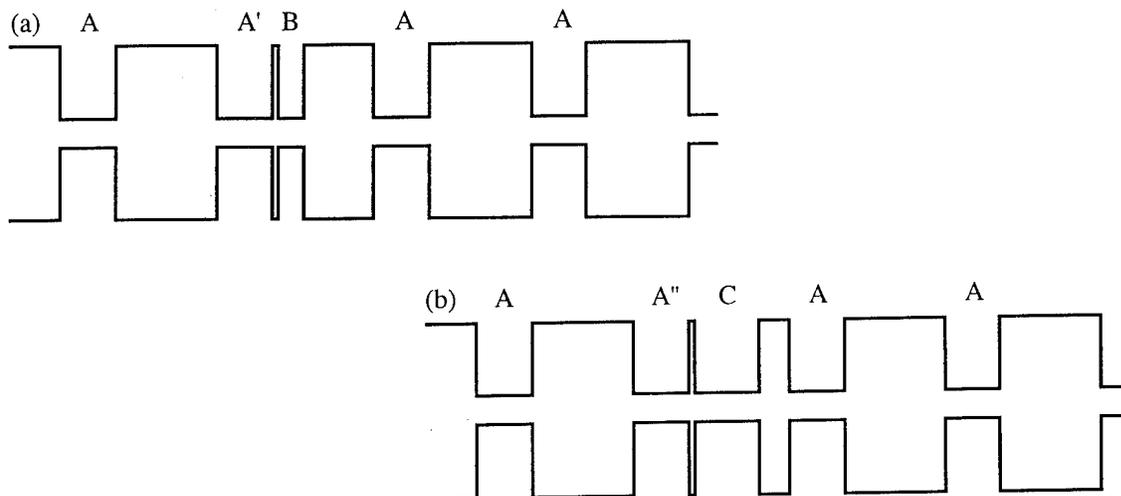
Spontaneous Emission Coupling to the Lasing Mode in a Fabry-Perot Microcavity with High Contrast Al$_x$O$_y$/GaAs Bragg Reflectors

D.G. Deppe, D.L. Huffaker, H. Deng, J. Shin, and Q. Deng

Microelectronics Research Center
Department of Electrical and Computer Engineering
The University of Texas at Austin, Austin, Texas 78712-1084
Phone: (512) 471-4960
Fax: (512) 471-8575

There has been recent interest in studies of the influence of controlled spontaneous emission on the operating characteristics of lasers and light emitting diodes. Most cavity designs used in such work can be distinguished as either planar and of the Fabry-Perot type, or as possessing additional confinement in the lateral direction. For both cavity types the mirror design based on distributed Bragg reflectors (DBRs) plays an important role. Since the actual cavity length is set by light penetration into the mirrors, both the cavity length and the mirror reflectivity are set by the DBR design, which in turn sets the lateral mode profile for the planar cavity. In this talk we will present data characterizing the operation of a Fabry-Perot microcavity laser fabricated using high contrast DBRs of Al$_x$O$_y$/GaAs. The mirrors are formed by the selective conversion of AlAs into Al$_x$O$_y$ using "wet oxidation" [1], resulting in the laser structure as illustrated in Fig.1. Four Al$_x$O$_y$/GaAs pairs are used on both the top and bottom (substrate) sides to form the laser cavity. In the actual laser cavity the oxidized mesa as illustrated in Fig.1 is 100μm in diameter while the lasing mode area is less than 10μm, so that the laser cavity is in fact planar. The resulting lasing characteristics of this cavity with high contrast DBRs are compared with those of a similar planar cavity design which uses the more typical AlAs/GaAs Bragg reflectors. For this second laser the upper reflector consists of sixteen pairs of AlAs/GaAs while the lower reflector (substrate side) consists of twenty-four pairs of AlAs/GaAs.
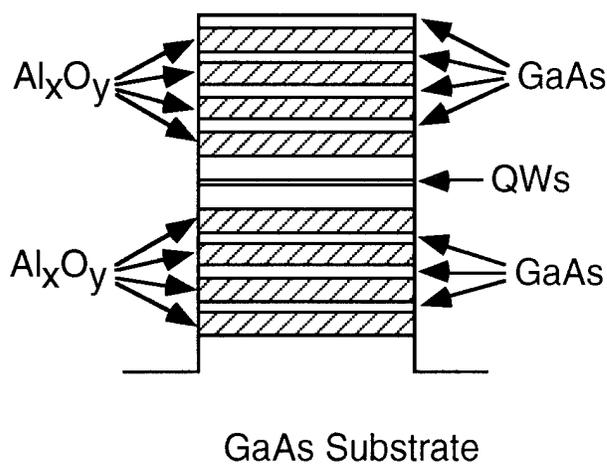
Figure 1: Schematic cross-section of the Fabry-Perot microcavity based on Al$_x$O$_y$/GaAs DBRs.
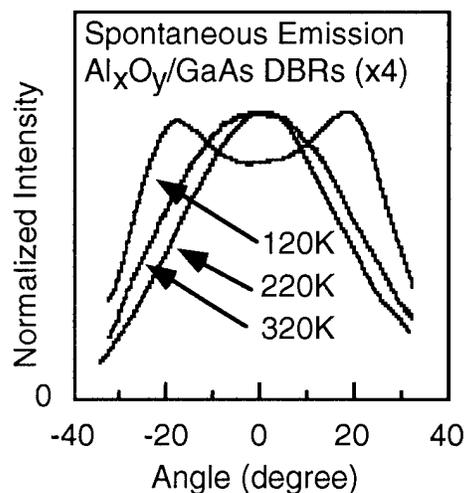
Figure 2: Angular spontaneous emission characteristics versus temperature for the cavity with Al$_x$O$_y$/GaAs DBRs.

Both lasers studied contain similar active regions formed by a one-wavelength thick cavity spacer containing three InGaAs quantum wells (QWs) placed at the center. The QW

thicknesses and compositions yield a bulk room-temperature emission peak of $\lambda \sim 0.98 \mu m$. The lasers are characterized in terms of their lasing threshold dependence on temperature, the spontaneous emission patterns versus temperature, the angular distribution of the lasing modes, and the temporal responses of the lasers under gain-switched operation. The measured temperature characteristics are used to find the optimized temperature for tuning the lowest order passive cavity mode for each laser to its QW emission peak. Figure 2 shows the measured angular radiation patterns for spontaneous emission taken at several temperatures for the cavity which uses the Al_xO_y/GaAs DBRs. Considerable modification of the spontaneous radiation pattern is observed, which is due to the short effective cavity length as compared to the total coherence length (spectral width) of the emission. These spontaneous emission characteristics can be compared with those for the AlAs/GaAs cavity as shown in Fig.3, which possesses a longer effective cavity length and results in little modification of the spontaneous emission. For this cavity the spontaneous emission is broader and nearly unchanged for the temperature range measured.

The angular lasing characteristics for both cavities are shown in Fig.4 for quasi-continuous wave (CW) operation (optical pump pulse widths of ~100ns), at each cavity's respective minimum threshold temperature. The corresponding lasing wavelengths are ~0.95μm for the Al_xO_y/GaAs cavity, and ~0.97μm for the AlAs/GaAs cavity. The pump spot size in both cases is ~8μm diameter. Figure 4 shows the increased angular range due
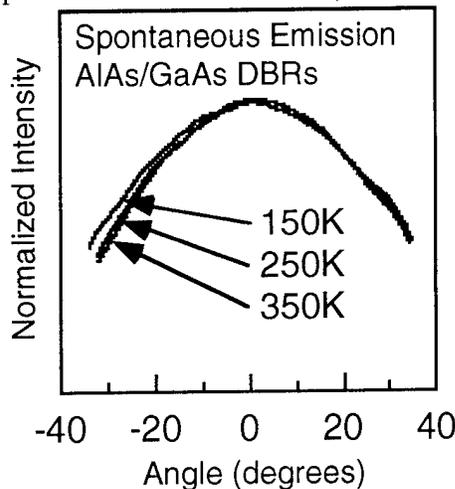
Figure 3: Angular spontaneous emission characteristics versus temperature for the cavity with AlAs/GaAs DBRs.
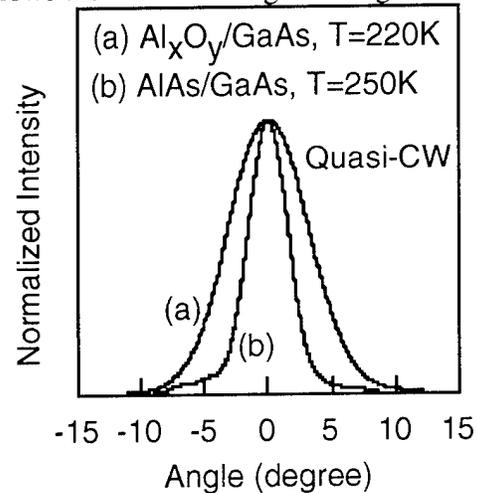
Figure 4: Angular lasing characteristics for the Al_xO_y/GaAs and AlAs/GaAs cavities at their respective minimum threshold temperatures.

to the effective shorter cavity length of the Al_xO_y/GaAs mirrors. The angular characteristics of the lasing mode are fairly well explained in trend by DeMartini and coworkers' [2] and Ujihara's [3] descriptions of the minimum sized single-wavelength mode in a Fabry-Perot microcavity, for which the area scales with the wavelength, cavity length, and mirror reflectivity as given by $A_{min} \sim (\lambda \cdot L)/(1-R)$. For the laterally distributed gain region, the spectral width of the lasing mode is within the spectral bandwidth of the mode area described by A_{min}, making the single wavelength description of the angular characteristics valid. Therefore, the shorter effective cavity length for the Al_xO_y/GaAs DBRs can be expected to increase the angular range of the lasing mode.

On the other hand, the effective mode area for the spontaneous emission is limited by the spectral bandwidth of the spontaneous emission, which includes spectral modes outside the bandwidth of the mode of A_{min}. The detailed analysis for planar Bragg

reflector microcavities based on the Fourier decomposition of the spectral modes is given in Ref.[4], and predicts a decreased angular width for a shorter cavity, in contrast to the single mode case of A_{min}. This agrees with the experimental data of Fig.2, as compared to Fig.3, for which the shorter cavity with Al_xO_y/GaAs DBRs produces a narrower angular emission for spontaneous emission for the tuned cavity. The angular spontaneous emission coupling to the lasing mode therefore depends on the spontaneous spectrum.

To further study the frequency dependence of the angular emission we present in Figs. 5 and 6 the temporal response and radiation patterns for gain switched operation for the Al_xO_y/GaAs microcavity. The laser is excited with a 300fs pulse from a Ti:Sapphire laser. Streak camera measurements given in Fig.5, along with the far-field radiation patterns given in Fig.6, show that as the lasing pulse width is decreased by increasing the pump power, the radiation pattern broadens due to the frequency dependent coupling of the transverse cavity modes to the lasing mode. In contrast, similar data for the AlAs/GaAs microcavity shows that both the pulse width and the far-field radiation patterns both saturate for gain-switched pump powers close to threshold. The minimum pulse width measured for the AlAs/GaAs microcavity is 40ps.
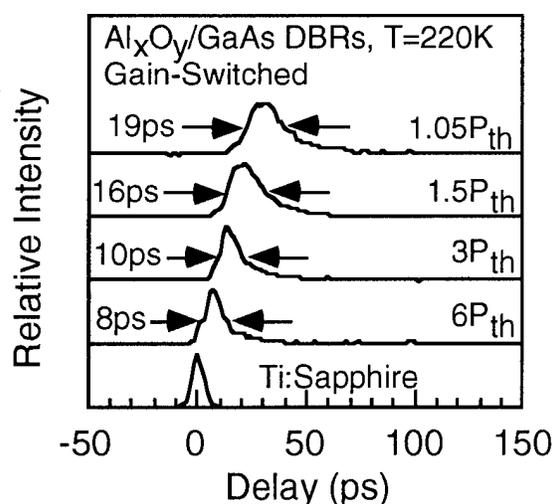
Figure 5: Temporal response of the Al_xO_y/GaAs microcavity under gain-switched operation.
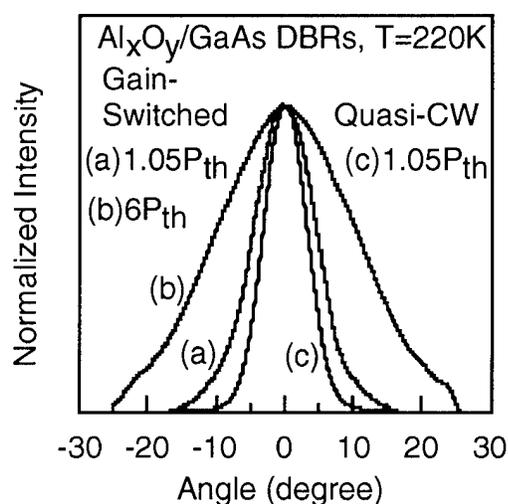
Figure 6: Angular lasing characteristics for the Al_xO_y/GaAs under gain-switched operation.

In addition to the experimental data presented characterizing the lasing mode we will also present the calculated predictions of the modified spontaneous emission for a cavity with such high contrast mirrors, along with the fractional coupling to the lasing mode which arises due to the lateral distribution of the gain region.

References

[1]   J.M. Dallesasse, N. Holonyak, Jr., A.R. Sugg, T.A. Richard, and N. El-Zein, Appl. Phys. Lett. **57**, 2844 (1990).

[2]   F. DeMartini, M. Marrocco, and D. Murra, Phys. Rev. Lett. **65**, 1853 (1990).

[3]   K. Ujihara, Jpn. J. Appl. Phys. **30**, L901 (1991).

[4]   D.G. Deppe, C. Lei, C.C. Lin, and D.L. Huffaker, J. Mod. Opt. **41**, 325 (1994).

Strained InGaAs/AlAs MQW *pin* Modulator with Ultrafast Recovery

H.S.Wang, P LiKamWa
Center for Research and Education in Optics and Lasers (CREOL)
University of Central Florida, Orlando, Florida, 32826, USA

M Ghisoni, G Parry
Interdisciplinary Research Centre for Semiconductor Materials
Department of Engineering Science
University of Oxford, Parks Road, Oxford, OX1 3PJ, UK

P N Stavrinou
Department of Electronic and Electrical Engineering,
University College London, Torrington Place, London, WC1E 7JE, UK

C Roberts
Interdisciplinary Research Centre for Semiconductor Materials
Blackett Laboratory, Imperial College, Prince Consort Road, London, SW7 2BZ, UK

A Miller
Department of Physics and Astronomy, University of St Andrews,
North Haugh, St Andrews, Fife, NK16 9SS, UK
Tel: +44 334 463122
Fax: +44 334 463104

The lattice mismatched, InGaAs/(GaAl)As multiple quantum well (MQW) system is currently of interest for optical modulator applications around 1 μm. Most work to date has concentrated on the low barrier, InGaAs/GaAs system[1,2]. Here we investigate, InGaAs/AlAs using time resolved ultrashort pulse laser techniques in order to assess the suitability of this system for applications as high speed modulators based on the quantum confined Stark effect (QCSE) and saturable absorbers for mode-locked lasers. It is shown that this material system may offer advantages for optical modulator applications because an ultrafast recovery can be combined with low photocurrent to reduce power dissipation in a material which retains strong excitonic absorption features and clear QCSE.

A fundamental limit to the speed of MQW optical modulators is set by the decay time of any photogenerated carriers within the quantum well structure[3]. Recovery times may depend on recombination, thermionic emission and tunneling from the wells. A number of groups have investigated InGaAs/Al$_x$Ga$_{1-x}$As with x < 30%, however, high barrier InGaAs/AlAs *pin* modulators have been reported only recently[4]. The depth of the wells for InGaAs/AlAs (~0.5eV for electrons) is approximately 10 times higher than InGaAs/GaAs, which predicts a long room temperature thermionic emission time for electron and holes of ~26μs. On the other hand, relatively short carrier lifetimes (on the order of 0.5ns) are characteristic of InGaAs/(Al)GaAs MQW structures (an order of magnitude shorter than typically observed in the GaAs/AlGaAs system).

The MQW *pin*-diode structure used in this work was grown by molecular beam epitaxy (MBE) on an n^+ GaAs substrate. The central intrinsic region contained 10 periods of 100Å-wide $In_{0.1}Ga_{0.9}As$ quantum wells (in-plane strain $\approx 0.7\%$) separated by 60Å AlAs barriers bounded by two undoped 0.4µm $Al_{0.3}Ga_{0.7}As$ regions. The sample was processed into 400x400 µm mesa photodiodes using standard photolithographic. Photocurrent spectra show a strong e1-hh1 excitonic transition at 904nm with no electrical bias. On application of an electric field, the peak moves to longer wavelengths and loses oscillator strength. The large confining potential experienced by the electron and hole wavefunction results in the exciton remaining resolvable for applied fields in excess of 200kV/cm. The magnitude of the photocurrent was low even at these large fields, due to the difficulty of carrier escape from the deep wells. A Ti:sapphire laser provided sub-100fs pulses at 80MHz in a conventional pump-probe arrangement.
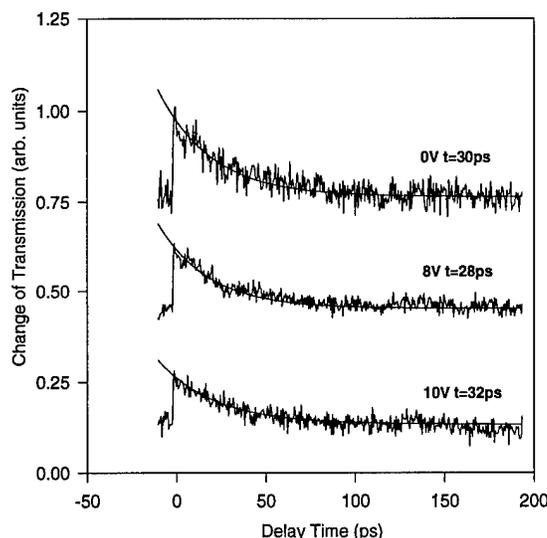
Figure 1 Pump-probe measurements at three different reverse bias voltages with 10pJ pulses.

Figure 1 shows the transmitted probe signal at a wavelength of 904nm, as a function of time delay at 800µW average pump power. Since this wavelength corresponds to the peak of the exciton absorption feature, the initial increase in signal is caused by bleaching of the exciton absorption by photogenerated carriers via phase-space-filling and Coulomb screening[5]. The recovery of the signal is determined by the rate that electrons disappear from the bottom of the quantum wells. The observed relaxation time was 30ps at low optical excitation energies. There is very little variation of the observed relaxation time with electric field. Measurements at wavelengths on either side of the exciton peak showed no obvious dynamical effects that could be attributed to field screening of the QCSE. This contrasts with GaAs/AlGaAs *pin* modulators which show a strong field dependence.

Since InGaAs/AlAs has very high barriers, escape from the wells is minimal. Thermionic emission times are long, and the electric field required for resonant tunnelling to occur is beyond the break-down voltage of the diode. This leads to the conclusion that the signal decay is not

caused by carriers escaping from the wells. The most likely explanation for the ultrafast recovery is carrier trapping or recombination due to defects at the interface surfaces. The incorporation of impurities during growth of AlAs is well known, in particular that of oxygen which acts as a non-radiative centre[6]. This is consistent with measurements, shown in figure 2, made at different pump pulse energies corresponding to initial carrier densities of 10^{10} to 10^{11} cm^{-2}. The recovery time becomes significantly longer at higher excitation densities due to saturation of the levels. Thus higher pumping levels will have longer relaxation times because of the partial filling of the defect sites.
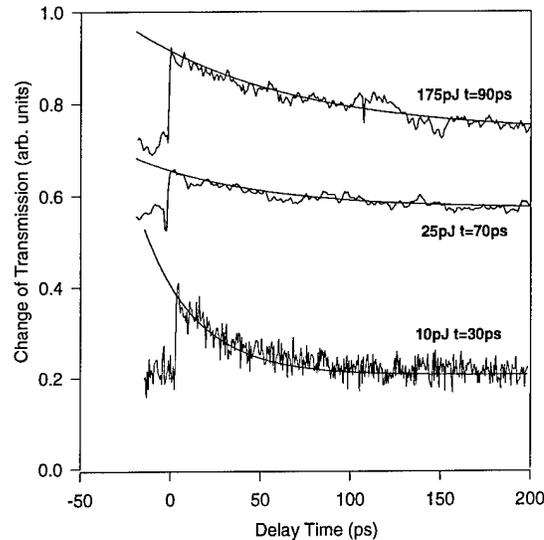
Figure 2 Pump-probe measurements at three different pump power levels at fixed voltage..

In conclusion, we have performed, to our knowledge, the first ultrashort pulse measurements on a strained, InGaAs/AlAs MQW *pin* diode modulator. We have demonstrated that this system offers an ultrafast recovery due to non-radiative recombination while retaining good excitonic absorption and quantum confined Stark effect properties essential for a high performance optical modulator. The shortest recovery time measured for this device was 28ps. For optical modulator applications, the low photocurrent reduces heating effects within the device and avoids space charge effects at high optical excitation, such that it should be possible to construct a modulator with high speed and low power dissipation.

References

1.   T.K. Woodward, T. Sizer II, D.L. Sivco, A.Y. Cho *Appl. Phys. Lett.* **57** 548 (1990)
2.   A. Stohr, O. Humbach, S. Zumkley, G. Wingen, G. David, D. Jager, B. Bollig, E. C. Larkins, J. D. Ralston *Opt. Quant. Electron.* **25** S865 (1993)
3.   D. C. Hutchings, C. B. Park, A. Miller *Appl Phys Lett* **59** 3009 (1991)
4.   M. Ghisoni, G. Parry, L. Hart, C. Roberts and P. N. Stavrinou, in press *Appl. Phys. Lett.*
5.   S. Schmitt-Rink, D.S. Chemla, D.A.B. Miller *Adv. Phys.* **38** 89 (1989)
6.   T. Someya, H. Akiyama, Y. Kadoya, T. Noda, T. Matsusue, H. Noge and H. Sakaki, *Appl. Phys. Lett.* **63** 1924 (1993)

Nonlinear Optical Response of Piezoelectric Multiple Quantum Wells Under Bias

X. R. Huang, A. N. Cartwright, D. S. McCallum, D. R. Harken and Arthur L. Smirl
Laboratory for Photonics and Quantum Electronics, 100 IATL, University of Iowa, Iowa City, IA 52242
Tel. (319) 335-3461   Fax (319) 335-3462
and
J. L. Sánchez-Rojas, A. Sacedón, E. Calleja and E. Muñoz
Dpto. Ing. Electrónica, Univ. Politécnica de Madrid, Ciudad Universitaria, 28040-Madrid, Spain
Tel. 34.1.336 73 21   Fax 34.1.336 7323

Strained multiple quantum wells (MQWs) that are grown on [111]-oriented substrates have huge intrinsic piezoelectric fields along the growth directions and are attractive for a number of novel nonlinear optical, electronic and electro-optical device applications (e.g. blue shifting SEEDs[1]). Unfortunately, until recently, very little was known about the nonlinear properties of these piezoelectric MQWs. The existence[2] of piezoelectric fields in strained [111]-oriented InGaAs/GaAs QWs and the screening[3] of these fields by photo-excited carriers had been demonstrated. In addition, the nonlinear responses of piezoelectric MQW structures to steady-state[4] and pulsed[5] optical excitations had been reported. However, prior to our recent work, the shot-to-shot accumulation of carriers (which are long-lived because they are spatially separated) had prevented the time resolution of the nonlinear optical and carrier dynamics in piezoelectric MQWs. In the last few months, by placing piezoelectric MQWs in p-i-n structures that were carefully designed to reduce the carrier lifetime, we have finally begun to temporally resolve the nonlinear response. For example, we have been able to definitively demonstrate that the bandstructure of our samples are mechanically clamped, not free; that the nonlinear response is dominated by long range screening of the in-well piezoelectric field by carriers that have escaped the wells and not by in-well screening as originally proposed,[6] and that the per-carrier nonlinear response is more than an order of magnitude smaller than that in [100]-oriented structures, not an order of magnitude larger as originally purported.[4]

All of our previous measurements of piezoelectric MQWs were performed without the benefit of an externally applied bias. Consequently, the in-well fields were much higher in the [111]-oriented samples than in similar [100]-oriented samples, under typical bias conditions. The question then arises as to whether the smaller per-carrier nonlinearities measured in the piezoelectric samples are the result of broadening by the huge in-well fields, whether they can be attributed to material quality, or whether they are the result of some intrinsic difference in the nonlinear mechanisms. Here, in order to address this issue, we perform the first side-by-side comparison of a pair of otherwise identical strained [111]- and [100]-oriented MQWs as a function of bias voltage. By so doing, we are able to measure the per-carrier nonlinear response of each sample at comparable in-well fields and to eliminate field-induced broadening from the comparison.

The two samples used in this work were grown side-by-side in the same chamber. Each consists of a strained $In_{0.15}Ga_{0.85}$/GaAs MQW embedded in the intrinsic region of a p-i-n structure (p-i-(MQW)-n). One was grown on an n^+ [100]-substrate, and the other on a n^+ [111]B-oriented substrate. In the [111]-oriented sample, the piezoelectric field in the QWs opposes the p-i-n electric field, and as a result, the total in-well field (which is the difference between the piezoelectric field and the p-i-n field) is ~100 kV/cm. In the [100]-oriented sample, the only field across the QWs is the p-i-n field, which is about 25 kV/cm. Consequently, under a reverse bias, the total in-well field in the [100]-oriented sample will increase and that in the [111]-oriented sample will decrease. The shift in the excitonic peak of each sample with bias voltage is illustrated in Fig. 1.

The figure-of-merit that we choose to use for comparing the nonlinear response of these two samples is the peak change in the absorption coefficient per carrier (caused by the screening of the quantum confined Stark effect by the photo-excited carriers): $\sigma_{eh} \equiv \Delta\alpha(peak)/N$, where N is the number of
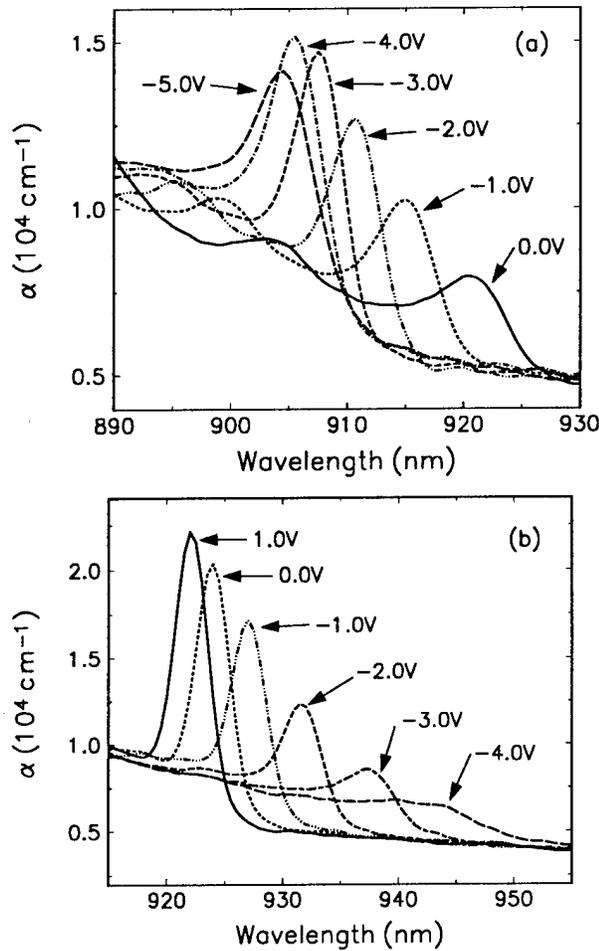
Fig. 1. Linear absorption spectra for (a) the [111]-
and (b) [100]-oriented samples under bias.

photogenerated carriers. In separate work, we have established that (in the low excitation regime where σ_{eh} can be defined) σ_{eh} follows the following phenomenological scaling expression:

$$\sigma_{eh} = C\frac{\alpha_0}{\Gamma}F(E_\perp),\qquad(1)$$

where C is determined by the number and width of the wells and is a constant here and where α_0 is the height and Γ is the width of the excitonic absorption peak, $E_\perp$ is the net nonoptically-induced in-well electric field (i.e., it includes the piezoelectric, p-i-n and externally applied fields). When $E_\perp$ is small (< ~30 kV/cm), there is a quadratic relation between the excitonic shift and $E_\perp$, and therefore, $F(E_\perp) = E_\perp$. For sufficiently large net in-well fields (>> 30 kV/cm), the exciton will shift linearly with field and $F(E_\perp) = 1$. For even larger fields, the scaling rule given by Eq. (1) is no longer valid as oscillator strength is transferred to the continuum and forbidden transitions. Consequently, it is very difficult to compare σ_{eh}'s for the [111]- and [100]-oriented samples when the in-well fields are dramatically different. However, if we apply a bias voltage to each sample and manipulate the total in-well fields to make them equal, then we can compare the nonlinear optical responses of the [111]- and [100]-oriented samples under conditions where $F(E_\perp)$ is the same for each sample. Under these circumstances, any differences in σ_{eh} must be attributed to differences in the excitonic amplitudes and linewidths (materials quality) or to differences in the excitonic areas (oscillator strength).

The quantity σ_{eh} was extracted from two-color differential transmission measurements performed using 2 ps pulses from two synchronized, independently-tunable mode-locked dye lasers. For these measurements, the pump was fixed above the heavy-hole exciton and the probe tuned across the exciton. The σ_{eh}'s measured for each sample are plotted as a function of net in-well field in Fig. 2. Several features are worth noting. First, notice that σ_{eh} for the [100] MQW is much larger than for the [111] sample for modest, but equal, in-well fields. This feature suggests that the remaining difference in the σ_{eh}'s for the two samples can be attributed directly to the "intrinsically" broader exciton in the [111] sample (which may be an indication of material quality). Next, notice that the general trends are the same for each sample. Specifically, for in-well fields < 35 kV/cm, σ_{eh} increases roughly linearly with the field, consistent with negligible broadening of the exciton with field and with a quadratic shift of the exciton with field [i.e., with $F(E_\perp) = E_\perp$]. Above ~35 kV/cm, σ_{eh} decreases with increasing in-well field, consistent with a field-induced broadening of the exciton and with a linear shift in the excitonic line center [i.e., with $F(E_\perp) = 1$]. Finally, notice that at the highest in-well fields, when field-induced broadening is expected to dominate, that σ_{eh} becomes the same for each orientation.

Fig. 2. Measured σ_{eh} for the [111]- (solid diamond) and [100]-oriented (empty box) samples.

These tendencies are made clearer if we plot the normalized quantity $\sigma_{eh}\Gamma/\alpha_0$ to remove the effect of excitonic broadening, as we have done in Fig. 3. Notice that the quantity $\sigma_{eh}\Gamma/\alpha_0$ is roughly the same for each sample. Since the oscillator strength (as represented by the area under the excitonic peak) is approximately the same for each sample and since the in-well fields are equal, this result further substantiates that the smaller σ_{eh} obtained for the [111]-oriented material (shown in Fig. 2) is mainly associated with the larger excitonic linewidth in the [111] sample and that this larger linewidth is most probably related to less than optimized material quality.

Consequently, we conclude from these measurements that the per-carrier nonlinear optical response of piezoelectric MQWs can be optimized by properly adjusting the net in-well fields. Specifically, σ_{eh} can be improved by a factor of ~3 by choosing an operating bias of ~35 kV/cm. We also conclude that we can expect further improvement (perhaps as much as a factor of 6) in the per-carrier nonlinear optical response of piezoelectric MQWs with optimized growth conditions, but that the per carrier nonlinearities will probably not exceed those of [100] materials. Nevertheless, these materials are likely to continue to gain attention because of the additional design flexibility that the in-well piezoelectric fields provide. For example, in [111] structures, because of the presence of the in-well piezoelectric field (that can be arranged to oppose the p-i-n field), it is always possible to engineer the bandstructure to provide the optimal in-well bias conditions (~35 kV/cm) without an externally applied bias, while often this is not possible in [100] structures.

Fig. 3. The normalized quality $\sigma_{eh}\Gamma/\alpha_0$ for [111]- (solid diamond) and [100]-oriented (empty box) samples.

References

1. K. W. Goossen, E. A. Caridi, T. Y. Chang, J. B. Stark, D. A. B. Miller, and R. A. Morgan, *Appl. Phys. Lett.* **56**, 715 (1990).
2. E. A. Caridi, T. Y. Chang, K. W. Goossen, and L. F. Eastman, *Appl. Phys. Lett.* **56**, 659 (1990).
3. T. S. Moise, L. J. Guido, R. C. Barker, J. O. White, and A. R. Kost, *Appl. Phys. Lett.* **60**, 2637 (1992).
3. I. Sela, D. E. Watkins, B. K. Laurich, D. L. Smith, S. Subbanna, and H. Kroemer, *Appl. Phys. Lett.* **58**, 684 (1991).
5. A. N. Cartwright, D. S. McCallum, T. F. Boggess, A. L. Smirl, T. S. Moise, L. J. Guido, R. C. Barker, and B. S. Wherrett, *J. Appl. Phys.* **73**, 7767 (1993).
6. D. L. Smith and C. Mailhiot, *Phys. Rev. Lett.* **58**, 1246 (1987).

Intrinsic and Induced Anisotropy of the Nonlinear Absorption in Strained [110]-Oriented Multiple Quantum Wells.

X.R. Huang, D.S. McCallum, and Arthur L. Smirl

Laboratory for Photonics and Quantum Electronics, 100 IATL, University of Iowa, Iowa City, IA 52242
Tel.: 319 335 3461; Fax.: 319 335 3462

D. Sun and E. Towe

Department of Electrical Engineering, University of Virginia, Charlottesville, VA 22903
Tel.: 804 924 3960; Fax.: 804 924 8818

Recent theoretical studies [1,2] and experimental measurements [3,4,5] have shown that there is a large inherent anisotropy in the absorption coefficient of excitons in biaxially strained quantum wells (QWs) grown on (110) surfaces. Due to the symmetry properties of the excitonic wavefunctions, there is no such anisotropy in the absorption spectra of unstrained or biaxially strained QWs grown on (100) or (111) surfaces. Such an anisotropy in the absorption coefficient can be exploited to construct optical switches or modulators. For example, a contrast ratio of 330:1 between on and off states has been achieved in uniaxially strained [100]-oriented QW structures using 100 wells. [6] In this work, we present the first measurements of optically-induced and intrinsic anisotropies in the nonlinear absorption of a biaxially strained, [110]-oriented MQW structure using picosecond pump-probe and differential transmission spectroscopy. We also demonstrate how the polarization rotation associated with these anisotropies can be used to construct an all optical on/off switch or modulator with a contrast ratio of 25:1 using only 50 wells.

The structure studied here was a pseudomorphic InGaAs/GaAs p-i(MQW)-n grown on a semi-insulating substrate which was oriented 6 degrees away from [110] towards the [111]B direction. This substrate orientation was chosen to obtain good material quality during growth. The intrinsic region of the p-i(MQW)-n contains 50 periods of 6 nm wide $In_{0.13}Ga_{0.87}As$ QWs separated by 8 nm wide GaAs barriers. The lattice mismatch between wells and barriers resulted in a biaxial in-plane strain of 0.93 % in the quantum wells. The n and p doped layers were thick enough that a potential of 1.4 V (the bandgap for GaAs) could develop between the n and p doped layers. Although mesas with electrical contacts had been fabricated on the p-i(MQW)-n, no electrical contacts were made to these during the measurements described herein. The optical anisotropy of the as-grown QWs was demonstrated by measuring the room temperature absorption spectra for linear polarizations along the [$\bar{1}$10] and [001] directions. The results are shown in Fig. 1, together with the difference between the two absorption spectra. The maximum difference of absorption coefficients between orthogonal directions is 6.6 x 10^3 cm^{-1} at 924 nm. Light which is initially polarized at 45° to the [$\bar{1}$10] and
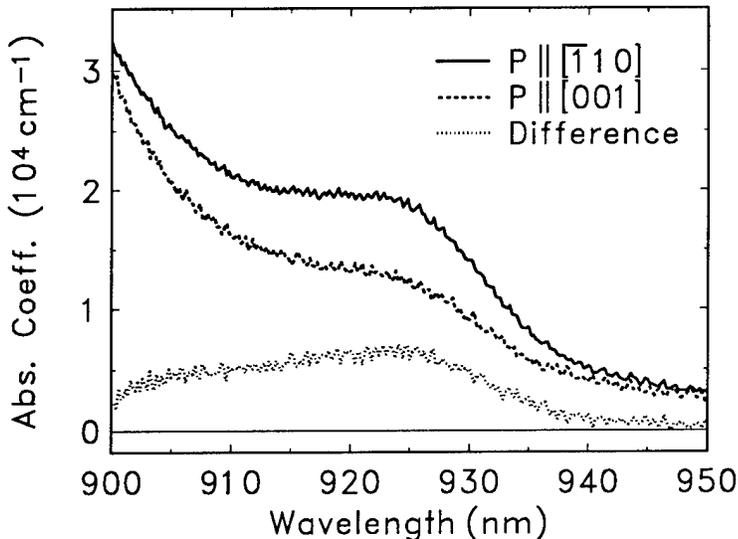
Fig. 1   Absorption spectra of the [110]-oriented MQW for light polarized along the [$\bar{1}$10] and [100] directions. Difference between these two spectra.

[001] directions will have its plane of polarization rotated upon passage through the MQW because the component light polarized along the [$\bar{1}$10] direction will be preferentially absorbed with respect to the orthogonal component. The maximum measured polarization rotation of a weak probe initially polarized at 45° to the [$\bar{1}$10] and [001] directions was 2.5°, which is consistent with the measured absorption anisotropy.
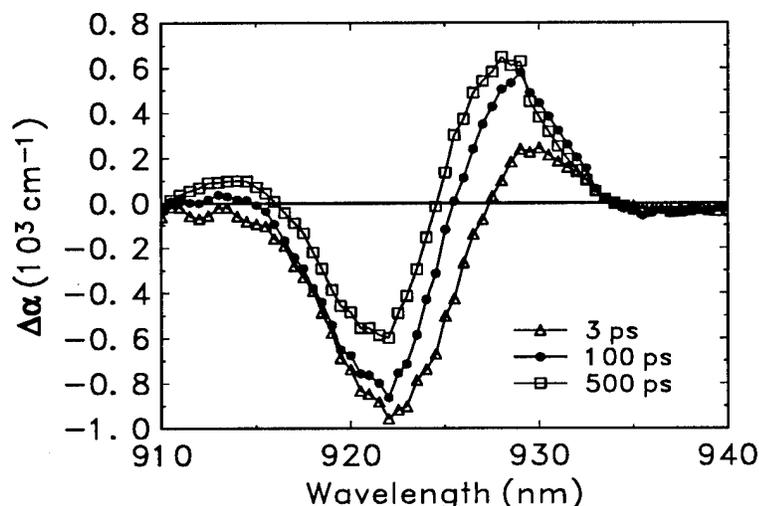
Fig. 2   Absorption coefficient change of the [110]-oriented MQW for selected probe delays.

The temporal evolution of the optical nonlinearity was studied with a picosecond pump-probe technique. Carriers were injected into the QWs with a strong pump pulse, and the resulting absorption coefficient change was measured with a weak probe pulse. The pump and probe pulses were generated by the same cavity-dumped, tunable dye laser, which emitted 2 ps pulses at a repetition rate of 147 kHz. This low repetition rate was chosen to allow near complete recovery of the MQW between pump pulses. A variable delay in the probe beam path allowed the absorption coefficient change to be measured at different times after the arrival of the pump pulse. Selected results are shown in Fig. 2, for a pump pulse of fluence 3.0 μJ/cm^2. It can be seen from Fig. 2 that 3 ps after the arrival of the pump pulse, the $\Delta\alpha$ spectrum is dominated by a single negative peak. By 100 ps after the arrival of the pump pulse, the $\Delta\alpha$ spectrum has evolved into the negative lobe and positive lobe characteristic of a red-shifted exciton. The 3 ps spectrum is consistent with bleaching of the exciton by the carriers which have been optically injected into, and which remain in, the QWs. The time taken for the change in the form of the $\Delta\alpha$ spectrum is consistent with the photogenerated carriers escaping from the QWs and drifting to the doped regions, where they reduce the p-i-n electric field. However the existence of a red-shifted exciton implies that there has been an increase in the electric field in the QWs. This apparent contradiction is resolved by recalling that the substrate is slightly misaligned towards the [111]B direction, and consequently there is a component of biaxial strain normal to the [111]B direction. The strain normal to the [111]B direction results in a piezoelectric field in the growth direction of the QWs. [7] This piezoelectric field is in the opposite direction to the p-i-n electric field, and the piezoelectric field and p-i-n field largely cancel in the QWs. When carriers move to the doped regions, the p-i-n electric field is screened, cancellation no longer occurs, and the total electric field in the QWs increases, which causes a red shift.

We demonstrated operation of a polarization rotation modulator using the inherent anisotropy of the [110] oriented MQW. The modulator is sketched in the inset to Fig. 3, and is an adaptation of the pump/probe geometry described earlier, with the addition of a quarter wave plate and analyzer after the MQW. In this case, the pump beam was generated by a second cavity-dumped, tunable dye laser, which was operated at 900 nm. The pump pulse was arranged to arrive at the MQW 30 ps before the probe. The "off" state of the modulator was obtained by adjusting the analyzer and quarter wave plate to minimize transmitted light in the absence of the pump beam. The quarter wave plate was necessary because the anisotropy of the absorption coefficient is accompanied by an anisotropy of the refractive index, which causes the light transmitted through the MQW to be elliptically polarized. The "on" state of the modulator
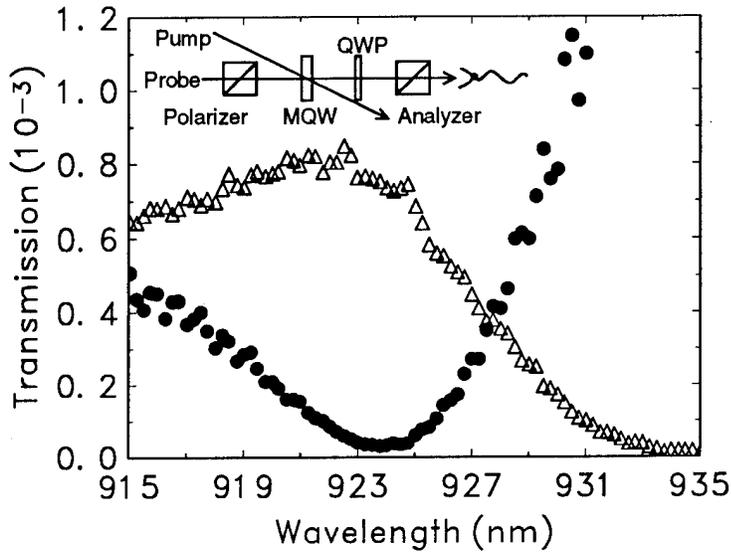
Fig. 3 Transmission of the [110]-oriented polarization rotation modulator with the pump on (triangles) and the pump off (circles). The inset shows the configuration of the modulator.

is obtained by injecting carriers into the MQW with the pump beam. These carriers partially bleach the exciton, which causes a change in the amount by which polarization of the probe beam is rotated on passage through the MQW, and a corresponding increase in the transmission through the analyzer. The transmission of the analyzer in the on and off states is plotted as a function of wavelength in Fig. 3. The contrast ratio is obtained by dividing the transmission in the on state by the transmission in the off state. The maximum contrast ratio is 25:1, which is obtained at 924 nm. For this set of measurements, the pump fluence

was 37 μJ/cm^2, which bleaches the excitonic absorption by ~ 15 %. This fluence is sufficient to completely flatten the conduction and valence bands in the intrinsic region. We therefore expect that the change in the excitonic absorption coefficient, and hence the anisotropy, are dominated by excitonic bleaching.

Although the peak contrast ratio obtained here is only 25:1, compared with the 330:1 reported for uniaxially strained [100]-oriented MQWs,[6] it should be noted that the [100]-oriented structure contained twice as many QWs. In addition, the measurement of the [100]-oriented MQW was made at 200 K, whereas our measurement was made at room temperature. When compared on a per-unit length basis at room temperature, the biaxially strained [110]-oriented MQW is expected to show similar performance to the uniaxially-oriented [100]-oriented structure. The [110]-oriented MQW modulator has the significant advantage that it requires no post-growth processing, unlike the [100]-oriented modulator, which requires several post-growth processing steps before the anisotropy is obtained.

References

1. Y. Kajikawa and M. Hata, Superlattices and Microstructures **12**, 355 (1992).
2. S. Nojima, Jpn. J. Appl. Phys. **31**, L765 (1992).
3. D. Gershoni, I. Brener, G.A. Baraff, S.N.G. Chu, L.N. Pfeiffer, and K. West, Phys. Rev. B **44**, 1930, (1991).
4. Y. Kajikawa, M. Hata, T. Isu, and Y. Katayama, Surf. Sci. **267**, 501 (1992).
5. D. Sun, E. Towe, M.J. Hayduk, and R.K. Boncek, Appl. Phys. Lett. **63**, 2881 (1993).
6. H. Shen, M. Wraback, J. Pamulapati, M. Dutta, P.G. Newman, A. Ballato, and Y. Lu, Appl. Phys. Lett. **62**, 2908 (1993).
7. D. Sun and E. Towe, Jpn. J. Appl. Phys. **33**, 702 (1994).

Carrier capture in GaAs quantum wire structures grown on V-groove substrates

S. Haacke, B. Deveaud, D.Y. Oberli, E. Kapon, U. Marti, F.K. Reinhart

Institute of Micro- and Optoelectronics, Department of Physics,
Swiss Federal Institute of Technology
1015 LAUSANNE, Switzerland

Tel (41) 21 693 36 49   Fax (41) 21 693 45 25

Carrier capture in quantum wells (QWs) has been intensively studied in the past years, especially concerning the dependence of the capture time on QW and barrier dimensions [1]. On the other hand, little is known about the carrier transfer and capture times into one-dimensional (1D) quantum wires (QWRs). In particular, in structures such as crescent-shaped QWRs grown on V-groove substrates, in which the carriers are transferred via both 3D barrier and 2D QW regions surrounding the wires, the carrier capture into the QWRs can be quite complex.

An ultra-fast carrier capture time (some tens of ps or less) is important for two reasons. First, for the determination of the intrinsic exciton lifetime in QWRs, the processes of capture and radiative decay (of the order of a few hundreds of ps) have to be clearly separated in time. Second, for laser or other device applications, slow carrier capture might limit the direct modulation bandwidth. The present paper shows that such fast carrier capture times (25 ps) are present in QWRs grown on sub-μm pitch V-arrays. Much slower carrier capture is measured in larger pitch samples.

The QWR structures investigated here are grown by organometallic chemical vapor deposition (OMCVD) or molecular beam epitaxy (MBE) on grooved (100) GaAs substrates. For the OMCVD samples the grooves were etched along the [01$\underline{1}$] direction with a short pitch of 240 nm or a large pitch of 3.5 μm. When thin GaAs layers are deposited on top of the $Al_{0.5}Ga_{0.5}As$ barrier layer, crescent-shaped QWRs form as a result of migration and accumulation of Ga atoms at the groove's bottom. For the same reason vertical QWs (VQW) of $Al_{0.5}Ga_{0.5}As/Al_yGa_{1-y}As$ (y<0.5) grow, embedded in the $Al_{0.5}Ga_{0.5}As$ layers, below and on top of the QWR (see fig. 1). In addition, GaAs QWs are present on the {111}A slopes of the groove (side-wall QWs) and on the horizontal plateaus (horizontal QWs). The thickness at the QWR center and the effective width are 2.8 nm and 14 nm, respectively, in the small pitch sample.

The carrier capture processes have been studied by photo-luminescence (PL) up-conversion. Previous results published in Ref. 2 could thus be extended thanks to the better time resolution of 500 fs which enables us to study ultra-fast carrier capture. Figure 2 shows a PL spectrum of a short pitch OMCVD sample at T=20 K recorded with a delay of 10 ps after the exciting pulse (at 2.116 eV). The high-energy transition at 2.016 eV originates from the horizontal and from the side-wall GaAs QWs with a thickness of $\approx$1 nm. The peak around 1.95 eV is attributed to the VQWs, whereas the dominant emission centered at 1.795 eV stems from the QWRs [3]. The shoulder at 1.84 eV reveals filling of the second QWR subband. The energy positions are in agreement with the corresponding transtions observed in PLE spectra and calculated with a $1/\cosh^2$ potential for the lateral confinement [4]. It should be stressed that the QWRs investigated show clearly a one-dimensional confinement. The carrier capture therefore involves transfer from 2D QWs into 1D QWRs.

PL transients recorded at the different transition energies (avoiding band-filling like in fig. 1) reveal a decay time for the QWR of τ_{QWR}= 305$\pm$5 ps (in agreement with [2]), for the GaAs QWs τ_{QW}= 160$\pm$10 ps, and finally τ_{VQW}= 25$\pm$5 ps for the PL decay of the VQWs (Figure 3). The short decay of the VQW is attributed to the very efficient carrier transfer into the

QWR. This fast carrier capture is apparently limited by carrier diffusion since the maximum distance carriers have to traverse in the VQWs before reaching the QWR ($\approx$100 nm) are of the same order as typical carrier diffusion lengths.

The longer decay time of the GaAs QWs is typical for QWs of a few nm thickness [5]. It is not significantly reduced by an eventual carrier transfer into the QWR. We can therefore conclude that the transfer between the GaAs QWs and the QWR is quite ineffective. TEM images show indeed that these QWs are almost separated from the QWRs as a result of the strong tapering of the side-wall QWs [2,4]. This narrowing seems to impose a severe barrier for the carrier transport into the QWRs.

The carrier transfer between the VQW and the QWR is also observed in the large pitch sample, however on a much longer time scale. The PL decay time of the VQWs is found here to be τ_{VQW}= 260 ps. Since the relative intensity of the GaAs QWs and the QWRs is constant at any time, both regions are apparently disconnected, also in the large pitch structures. These results confirm earlier CL measurements on comparable QWR structures [3].

The QWRs in the *MBE grown samples* are sandwiched between $(AlAs)_n/(GaAs)_m$ superlattices (SL) [6]. Carriers transfer from a n=4/m=8 SL into the QWRs with a time constant of $\approx$ 1 ns. The transfer time is reduced to typically 50 ps if an n=2/m=4 SL is chosen. This result can be understood in terms of an improved transport of heavy-holes in the second type of SL.

In summary, we have measured carrier capture times in QWR structures grown on V-groove substrates. Very efficient carrier transfer within 25 ps between the 2D vertical QWs and the 1D QWRs is observed in OMCVD grown samples with a 240 nm pitch. The carrier transfer from the horizontal and side-wall QWs is much less effective.

References

[1] D. Morris, B. Deveaud, A. Regreny, and P. Auvray, Phys. Rev. **B47**, 6819 (1993) and references therein.
[2] J. Christen, M. Grundmann, E. Kapon, E. Colas, D.M. Hwang, and D. Bimberg, Appl. Phys. Lett. **61**, 67 (1992).
[3] E. Kapon, M. Walther, J. Christen, M. Grundmann, C. Caneau, D.M. Hwang, E. Colas, R. Bhat, G.H.. Song, and D. Bimberg, Superl. & Microstr. **12**, 491 (1992).
[4] M. Walther, E. Kapon, D.M. Hwang, E. Colas, and L. Nunes, Phys. Rev. **B45**, 6333 (1992).
[5] J. Feldmann, G. Peter, E.O. Göbel, P. Dawson, K. Moore, and C. Foxon, Phys. Rev. Lett. **59**, 2337 (1987).
[6] U. Marti, M. Proctor, R. Monnard, D. Martin, F. Morier-Genoud, F.K. Reinhart, R. Widmer, and H. Lehmann, Am. Soc. Conf. Proc. **227**, 80 (1991).

Figure captions

Fig. 1: Schematic of the periodic QWR structure showing the layer sequence and the disposition of the GaAs quantum wires (QWRs), the GaAs quantum wells (QWs) and the vertical AlGaAs QWs.

Fig. 2: PL spectrum of the short pitch sample at T=20 K recorded 10 ps after excitation. Transitions according to the GaAs QWs, the vertical QW and the QWR are identified. Arrows indicate the position of the QWR subbands l=1 and l=2 as measured by PL excitation [4]. Notice the population of the l=2 subband.

Fig. 3: PL decay of the vertical QW and the GaAs QW with the respective decay times of τ= 25 and 160 ps.
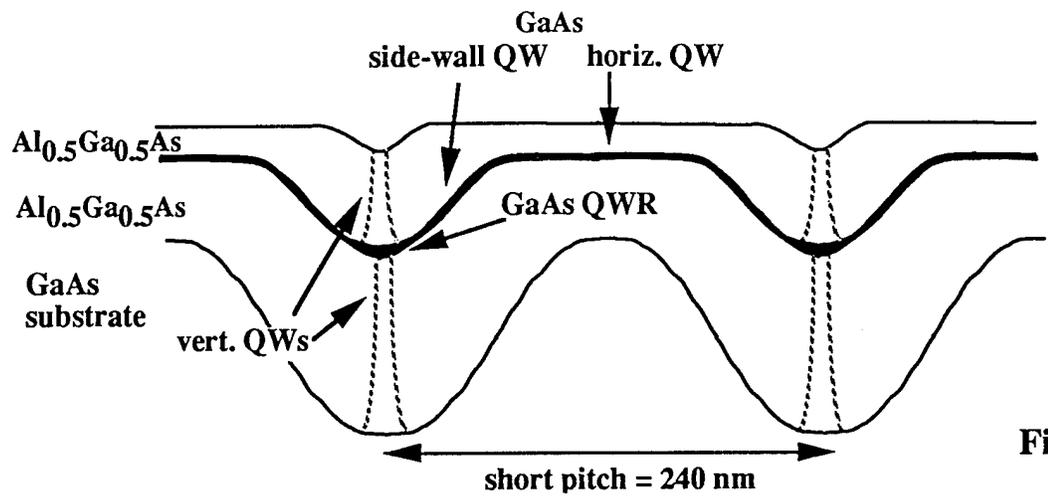
Fig. 1
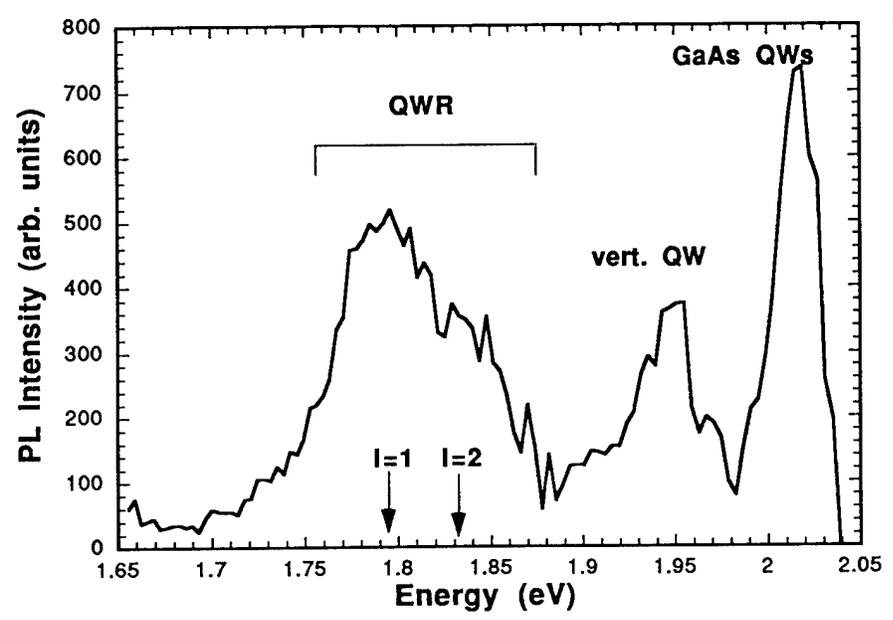
Fig. 2
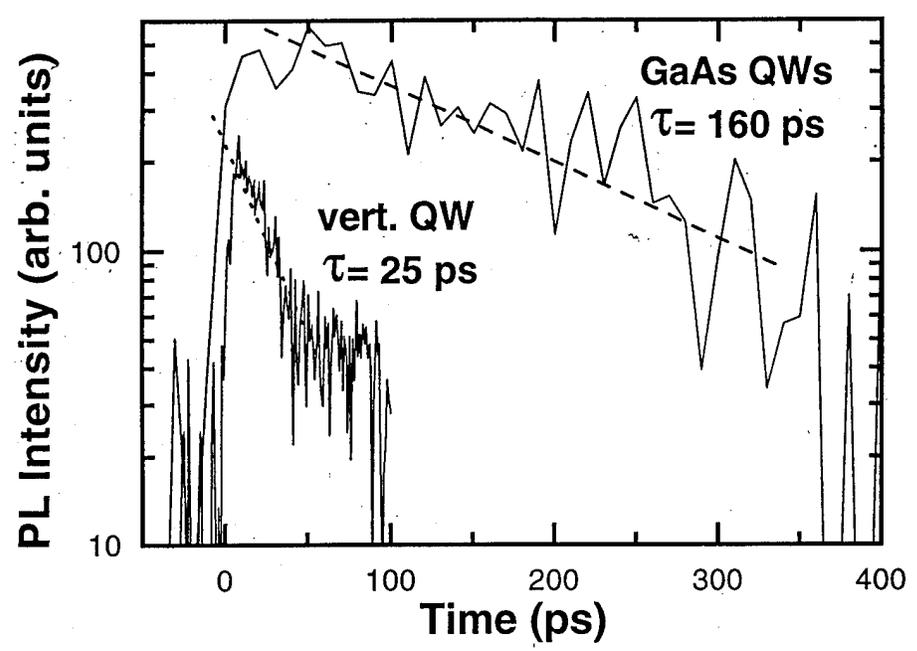
Fig. 3

Fabrication of GaAs Quantum Dots Grown in Two-dimensional V-Grooves by MOCVD Selective Growth

S. Ishida, M. Nishioka, Y. Nagamune, and Y. Arakawa

Institute of Industrial Science, University of Tokyo,

7-22-1 Roppongi, Minato-ku, Tokyo 106, Japan

1. Introduction

A reduction of dimensionality of the electron motions in quantum nano-structures allows new device concept as well as new physics[1,2]. For this purpose, various efforts have been devoted to the fabrication of the quantum dot structures. For example, the use of Stranski-Krastanow growth mode is promising to realize uniform and small quantum dot structures[3,4]. However, in this technique, it is difficult to control the position. On the other hand, the GaAs quantum dots on AlGaAs plinths which was grown on SiO2 patterned substrate was realized by MOCVD selective growth technique with a lateral width of 25nm[5]. In this method, the position of the quantum dots is controlled. But, non uniformity of size of the quantum dots due to the size fluctuation of the SiO2 pattern is unavoidable.

In this paper, we propose and demonstrate a novel technique for the fabrication of the quantum dot structures using MOCVD. The GaAs quantum dots are grown in AlGaAs two-dimensional V groove (2DVG) structures which are composed of (111)A and (111)B-facets of GaAs. The AlGaAs 2DVG is formed by the MOCVD selective growth on SiO2 patented substrate. This fabrication technique is an extension of the growth for the quantum wires on V-groove structures which were formed by selective growth on SiO2 patterned substrates[6]. Since the quantum dots are grown in the 2DVGs, size fluctuation is expected to be much suppressed. It should be noted that the 2DVGs can not be formed by chemical etching technique because of anisotropy of etching rate.

The results show successful formation of the quantum dots of 40x40x30 nm^3 with controlled position and high uniformity. Photoluminescence (PL) properties are also discussed.

2. Fabrication Procedure

Figure 1 shows schematic illustration of the 2DVGs which are composed of (111)A and (111)B-facets. The 2DVG structures are formed using selective growth technique on SiO2 patterned substrates. When the SiO2 line is in parallel with the orientation of <001>, a V groove which is composed of (111)A-facet can be formed above the SiO2 line[4]. Similarly when the SiO2 line is in parallel with <011>, a V groove on which (111)B-surface is appearing is formed. Therefore, by forming SiO2 window patterns, 2DVGs can be realized by growing four dot-like structures. Figure 2 shows illustration of formation of the 2DVGs by the growth of dot-like structures which have (111)A and (111)B-facets on patterned substrates. Details are described in the next section.

The followings are summary of the fabrication process. Before starting the MOCVD growth, a SiO2 layer with a thickness of ~20nm was formed by plasma-CVD on (100) GaAs

substrate. Grating patterns of PMMA photoresist with a period of 80 nm were defined on SiO2 layer by electron beam lithography. The diameter of the windows and periodic is 80 nm and 120 nm. The resist pattern was transferred to the under SiO2 layer using wet chemical etching with buffered HF (17%). Figure 3 shows SEM micrograph of photoresist pattern.

The growth process by MOCVD is as follows. The AlGaAs is grown in the window region of the SiO2 pattern selectively. A AlGaAs dot-like structure is formed in each window. By continuing the growth, lateral growth occurs above SiO2 region with appearance of (111)A and (111)B facets. As a result, A 2DVG is formed among four dot-like structures. Figure 4 shows SEM micrograph of AlGaAs 2DVGs. Then, by switching the growth layer from AlGaAs to GaAs, quantum dot structures were grown at the bottom of 2DVGs. By switching the material from GaAs to AlGaAs again, the quantum dots were embedded. Growth temperature and V/III ratio were 700 C and 100, respectively.

In order to have the 2DVGs, additional careful consideration is necessary. GaAs has an anisotropy in the growth rate depending on the crystal orientation. If the window pattern is along <011> and <011> orientation, (111)A or (111)B facets of GaAs adhere to the nearest structure. Therefore, the windows should be shifted to <011> or <011> with half periodic length.

3. Characterization of the Quantum Dots

Figure 5 shows SEM micrograph of cross section of GaAs quantum dots grown in 2DVGs. The GaAs dots are embedded in AlGaAs layer. As indicated in this photograph, the quantum dots are successfully formed and the size of dot is about 40x40x30 nm^3.

Figure 6 shows photoluminescence spectra of the quantum dots measured at 15 K by the use of Ar+ laser light with the wave length of 514.5 nm. The beam spot size was about 5 μm in diameter, and the power is about 2 mW before it was collected. Figure 6 shows the spectra. The PL peak at 817.5 nm is corresponding to the quantum dot structures. The PL peak at 820 nm is the GaAs bulk transition. As shown in this figure, the blue shifts are 2.5 nm. The shifted energy of the PL of the quantum dots is about 5 meV.

4. Conclusion

In conclusion, we propose and demonstrate a novel fabrication technique for GaAs quantum dot structures which are grown in AlGaAs 2DVGs by MOCVD. Each GaAs quantum dot is formed in the 2DVGs which are composed of (111)A and (111)B facets of four dot-like structures selectively grown on SiO2 patterned substrate. The size of the quantum dots is about 40x40x30 nm^3 with the energy shift of PL peak of 5meV. This fabrication technique is promising to realize quantum dots with controlled position and high uniformity of size.

References
[1] Y. Arakawa and H. Sakaki, Appl. Phys. Lett. **40**, 939 (1982)
[2] Y. Arakawa, K. Vahala, and A. Yariv,Appl. Phys. Lett., **45**, 950 (1984)
[3] D. Leonard, M. Krishnamurthy, C.M. Reaves, S.P. Denbaars, and P. Petroff: Appl. Phys. Lett., **63**, 3203 (1993)
[4] J. Oshinowo, M. Nishioka, S. Ishida and Y.Arakawa : Appl. Phys. Lett **65** (1994) 1421
[5] Y. Nagamune, S. Tsukamoto, M. Nishioka, and Y. Arakawa, Appl.Phys.Lett. **64**, .2495 (1994)
[6] S. Tsukamoto, Y. Nagamune, M. Nishioka, and Y. Arakawa, Appl. Phys. Lett. **62**, 49 (1993)
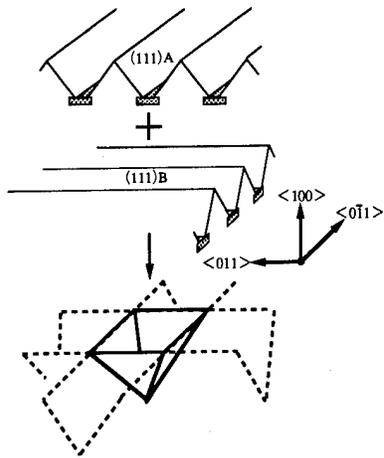
Fig.1: Scematic illustration of two-dimensional V-grooves (2DVGs) which are composed of (111)A and (111)B-facet.
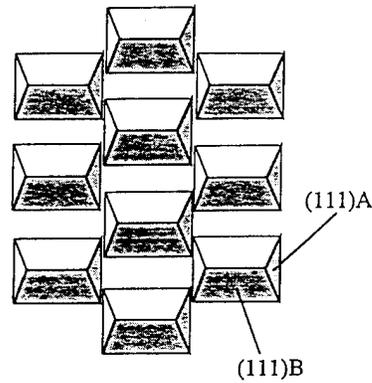
Fig.2: Formation of 2DvGs by the growth of dot structures which have (111)A and (111)B-facets on pattern substrstes. A 2DVG is formed among for dot structures.
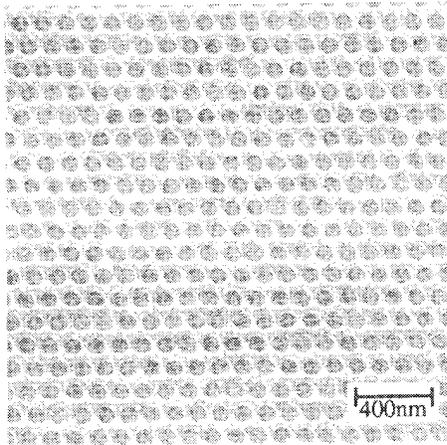
Fig.3: SEM micrograph of photoresist pattern. The diameter and period of windows were 90nm and 130nm, respectiveiy.
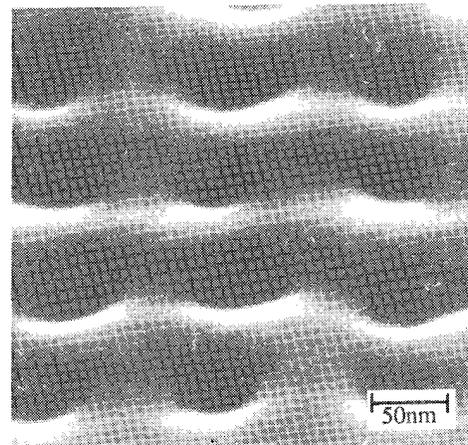
Fig.4: SEM micrograph of AlGaAs 2DVGs
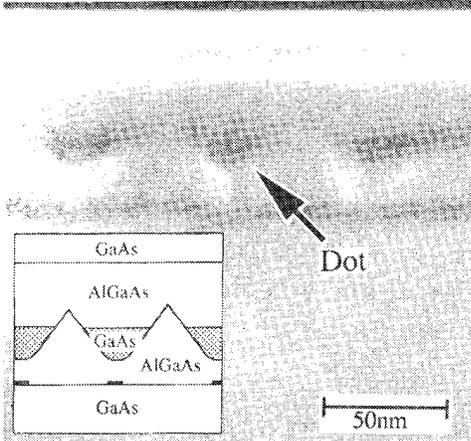
Fig.5: SEM micrograph of cross section of GaAs quantum dots grown in 2DVGs. TheGaAs dots are embedded in AlGaAs layer. The size of the quantum dots is 40x40x30 nm3.
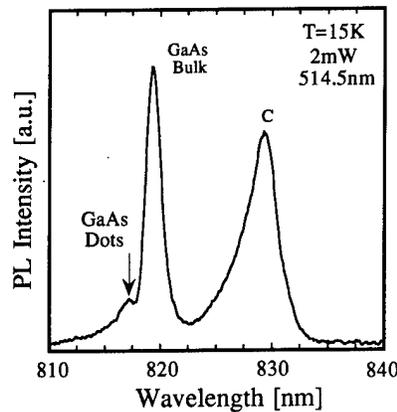
Fig.6: Photoluminescence spectra of the quantum dots.

IMPROVEMENT OF CRYSTALLINE QUALITY BY STRAIN COMPENSATION IN $InAs_xP_{1-x}/Ga_yIn_{1-y}P$ MULTIPLE QUANTUM WELLS FOR 1.3 μm WAVEGUIDE MODULATORS

X. B. Mei, K. K. Loi, H. H. Wieder, W. S. C. Chang and C. W. Tu
Department of Electrical and Computer Engineering, University of California, San Diego, La Jolla, CA.

We have successfully improved the crystalline quality and reproducibility--by strain compensation--of $InAs_xP_{1-x}/Ga_yIn_{1-y}P$ multiple quantum wells (MQWs) on InP substrates for 1.3μm modulators.

The samples were grown by gas-source molecular beam epitaxy (GSMBE) in a modified Varian GEN-II MBE system, which uses elementary Ga and In as the group III sources and P_2 and As_2 from cracked phosphine and arsine, respectively, as the group V sources. The growth temperature was 460°C.

With .strain compensation the alternatively growth of compressively and tensilely strained layers reduces the difference between the lattice constant of the substrate and the average lattice constant of the stack, and thus makes the structure more stable against dislocation generation. We call the point where this difference equals zero the ideally compensated point. For an uncompensated $InAs_{0.4}P_{0.6}/InP$ 90Å/130Å MQW structure, the largest number of peruids that can be grown without broadening of the satellite peaks in X-ray rocking curves is between 5 and 7. On the other hand, as is shown in Fig. 1, the X-ray rocking curve of a strain-compensated structure with as many as 50 periods of $InAs_{0.4}P_{0.6}/Ga_{0.17}In_{0.83}P$ 87Å/120Å MQWs shows very sharp satellite peaks of up to the seventh order. Different Ga compositions, 0.09, 0.13 (the ideally compensated point) and 0.17 were used in three 11-period MQWs samples. Excellent X-ray rocking curves were obtained from all of them, and almost no difference in the widths and numbers of the satellite peaks was found. This suggests that for a certain number of periods, the structural parameters, e.g., the composition and the layer thickness, can vary in a relatively wide range around the ideally compensated point without degrading the crystalline quality.

Low-temperature photoluminescence of a 50-period strain-compensated sample shows a narrow exciton peak, with a full width at half maximum of only 4 meV, indicating that the interfaces are very smooth and the optical property is excellent.

A p-i-n waveguide structure consisting of 21 periods of 93Å/130Å $InAs_{0.4}P_{0.6}/Ga_{0.13}In_{0.87}P$ MQWs is grown. The surface-normal electro-

absorption exhibits a large quantum-confined Stark effect (QCSE) near 1.3 μm (Fig. 2). At zero field, the half width at half maximum of the exciton peak is 6.5 meV. The energy shift under a field of 5×10^5 V/cm is 52 meV. Furthermore, a large change of the absorption coefficient ($\Delta\alpha$) of 6000 cm^{-1} is obtained at a detuning energy of 13 meV and under a bias of 8×10^4 V/cm. The $\Delta\alpha/\alpha_0$ (where α_0 is the α at zero field) is as high as 30 at a detuning of 28 meV under a bias of 1.2×10^5 V/cm. These results indicate that strain-compensated MQWs have a very small residual absorption beyond the exciton peak and thus are very suitable for optical modulator applications.
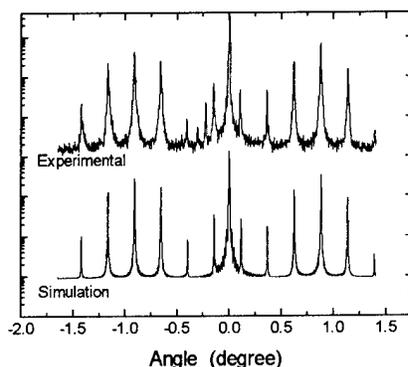
FIG. 1. (Top) Double-crystal X-ray rocking curve of a 50-period InAs$_{0.4}$P$_{0.6}$/In$_{0.83}$Ga$_{0.17}$P 86Å/120Å strain-compensated MQW structure and (Bottom) simulation based on the dynamical theory.
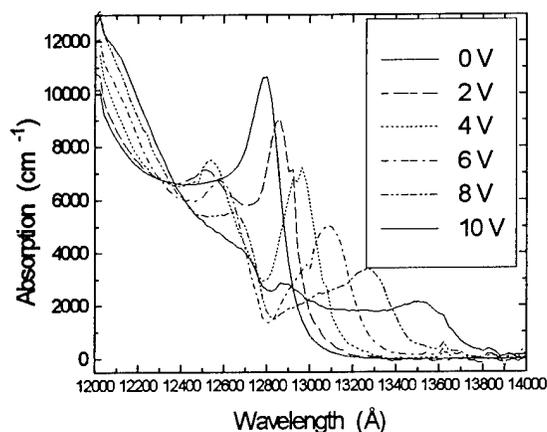
FIG. 2. Electro-absortion spectra of a 21-period InAs$_{0.4}$P$_{0.6}$/Ga$_{0.13}$In$_{0.87}$P 93Å/130Å strain-compensated MQW structure.

Anizotropy and dispersion of the optical rectification in the symmetric quantum wells

J. B. Khurgin
Department of Electrical and Computer Engineering
The Johns Hopkins University
Baltimore MD 21218

Generation of the far-infrared light by the optically excited semiconductors have been reported by numerous groups of researchers [1, 2] While such various mechanisms as current surge and the depletion field-induced optical rectification (OR) have been proposed, recent results [3] have shown that the bulk OR accounts for a major portion of the observed teraherz signal. Recently [4] we have evaluated the OR coefficients of the bulk zinc-blende semiconductors excited *above* the bandgap and obtained the results in agreement with the experimental data. We have shown that the OR has its origin in the asymmetry of bonding orbitals in the valence band.

In the present work we expand the bond-orbital treatment to the *symmetric, unbiased* quantum wells (QW) and show that dispersion, anisotropy and dynamics of the teraherz radiation are all altered drastically as the result of the bonding orbitals mixing induced by the confinement.

We have considered GaAs QW grown on (100), (011), and (111) surfaces, and evaluated the OR coefficients in the system of coordinates associated with the direction of growth. The results are shown in Fig.1 One can see drastic difference between the differently-oriented QW's. In the (100) oriented material four bonding orbitals are equally mixed in the ground heavy hole state, The optical rectification coefficient is zero at the absorption edge and then grows rather slowly. Only two components: $\chi^{(2)}_{zxy}$ and $\chi^{(2)}_{xzy}$ are substantial.

In the (011) oriented material two of the bonding orbitals contribute to the heavy hole and the other two to the light hole. As a result large $\chi^{(2)}_{xxx}$ and $\chi^{(2)}_{xyy}$ components of the OR coefficient are present, and due to the heavy-light hole splitting the reversal of sign of the OR coefficient is possible! The presence of large $\chi^{(2)}_{xxx}$ component is beneficial for the teraherz radiation generation, when the optical radiation impinging onto the surface is polarized

in the plane of QW's

In the (111) oriented material the light hole state consists nearly exclusively from only one bonding orbital, and the heavy hole state consists mostly of the other three orbitals. The OR coefficients were found to be the highest for the QW's of this orientation although they are not the most convenient for the teraherz radiation in the surface-emitting configuration. On the other hand the largest coefficients $-\chi^{(2)}_{xzz}$ and $\chi^{(2)}_{zzz}$ are perfect for the difference frequency generation in the waveguide configuration.

We also show that the strain can produce effect similar to confinement that can explain the reversal of sign in the THZ radiation observed in [2].

References

[1] S. L. Chuang, S. Schmitt-Rink, B. I. Greene, P. N. Saeta, and A. F. J. Levi, Phys. Rev. Lett. 68, 102 (1992)

[2] X-C Zhang, Y. Jin, K. Yang and L-J Scholwalter, Phys. Rev. Lett. 69, 2303 (1992) and references therein

[3] P. N. Saeta, B. I. Greene and S. L. Chuang, Appl. Phys. Lett., 63, 3482 (1993)

[4] J. B. Khurgin, "Teraherz radiation via above the gap optical excitation of the semiconductor structures", to be published in Dec.1994 issue of JOSA B
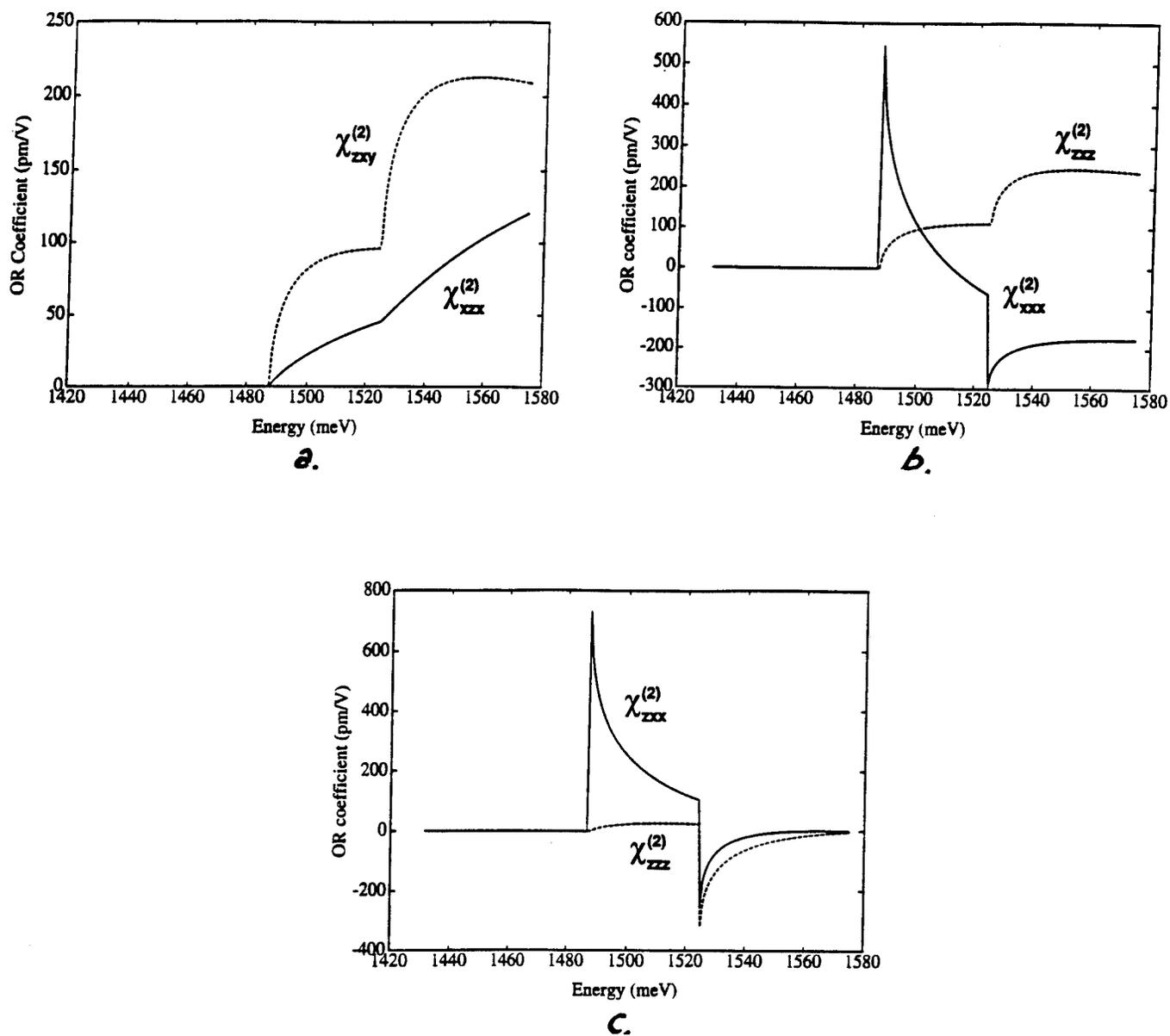
Fig.1 The frequency dependence of the optical rectification coefficient in the 100Å GaAs QW.

   a. (100) orientation

   b. (011) orientation

   c. (111) orientation

Pulse Propagation and Many-body Effects in Semiconductor Four Wave Mixing

A. Schulze, A. Knorr and S.W. Koch

Fachbereich Physik und Wiss. Zentrum für Materialwissenschaften

Philipps-Universität Marburg

35032 Marburg, Germany

The simultaneous influence of pulse propagation and Coulomb many-body interaction in Four Wave Mixing experiments is theoretically studied using the Semiconductor-Maxwell-Bloch equations. In this framework, the propagation of the optical fields and the microscopic interaction of the light with the semiconductor are treated consistently. The Maxwell equation is used as a reduced wave equation and the many-body Coulomb interaction are treated at the level of a screened Hartree-Fock approximation including phenomenological decay terms. We have analyzed the interplay of the propagation and Coulomb effects by calculating the Four Wave Mixing signal (FWMS) for different sample lengths and various excitation conditions, i.e. for pulses with different intensities at the exciton and in the continuum.

The time resolved FWMS for excitation with low intensity pulses spectrally centered at the 1s exciton is governed by the exciton polariton dynamics and exciton exciton interaction[1]. Here, the modulation of the FWMS is determined by the propagation of the FWMS itself. We observe for small samples an increase of the decay of the signal and for longer samples the developement of polariton nodes. An analytical formula to determine the increase of the decay time is proposed. In this regime, propagation effects are the origin of signatures of the FWMS comparable to those generated by many-body Coulomb interaction, i.e. for negative delay times τ of the insident pulses the signal amplitude is increased and for longer samples we observe delayed signal components. Our approach allows to distinct how many-body and propagation effects contribute to the FWMS.

If the intensity of the incident pulses is increased the time resolved FWMS developes for small samples where propagation can be neglected in addition to the FWMS at time τ an echo like structure due to bandgap renormalization[2]. Including the propagation effects

for longer samples the echo like component increases and the signal component at τ is decreased (see Fig.1). This surprising effect is not due to the propagation of the FWMS itself, but due to the balance of signal generation and absorption of the incident pulses.
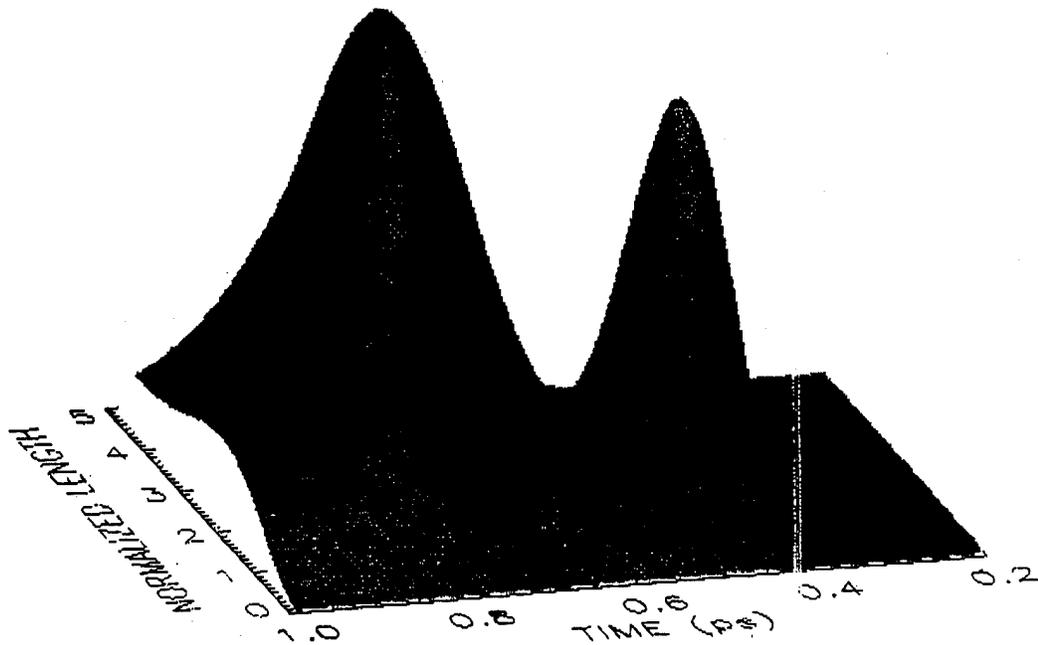
Fig.1: FWMS for an excitation of the 1 s exciton resonance with increased intensity. The incident pulses arrive at 0 ps and 0.4 ps.

A further increase of the intensity of the incident pulses leads to an increase of the echo component at the expense of the component at the delay time τ for small samples. The absorption of the incident pulses causes a decrease in the bandedge shift after a certain sample length. Therefore, for longer samples the developement of a signal at τ can be observed, which is generated by the absorbed incident pulses. In conclusion, we present a detailed study of semiconductor four wave mixing which allows to determine the contributions of many-body and propagation effects to the total four wave mixing signal.

[1] D. Fröhlich, A. Kulik, B. Uebbing, A. Mysyrowicz, V. Langer, H. Stolz, and W. von der Osten, Phys. Rev. Lett. **67**, 2343, (1991);

T. Rappen, G. Mohs, M. Wegener, Phys. Rev. B **47**, 9658 (1993)

[2] M. Lindberg, R. Binder, and S. W. Koch, Phys. Rev. A **45**, 1865 (1992)

W. Schäfer, F. Jahnke, S. Schmitt-Rink, Phys. Rev. B **47**, 1217 (1993)

Generation of Far Infrared Radiation Using Compositionally-Asymmetric Multiple Quantum Well Waveguides

by

Babak N. Saif
Swales&Associates
5050 Powder Mill Rd.
Beltsville, MD 20705
301-572-1223

Bernard D. Seery
NASA/Goddard Space Flight Center
Space Technology Division
Greenbelt, MD. 20771
301-286-8943

Jacob Khurgin
The Johns Hopkins University
Electrical and Computer Engineering Department
Baltimore, MD. 21218
410-516-7518

Colin Wood
Laboratory for Physical Sciences
850 Greeneed Drive
College Park, MD. 20740
301-935-6473

NASA's Earth and space science missions have motivated the investigation of methods to produce coherent radiation in the 1-3 terahertz (THz) spectral region, corresponding to 100-150 μm wavelength, for use as local oscillator sources in high resolution laser heterodyne spectrometers . Scientific applications of this technology include measurements of the hydroxyl radical (OH) at 2.5 THz in Earth's upper atmosphere, which is important because of its role in the destruction of ozone. In addition, astrophysicists are interested in spectroscopy of the interstellar molecular cloud in this previously unexplored region of the electromagnetic spectrum. However, these measurements nessitate a space-based instrument because the lower atmosphere is largely opaque in this spectral region.

Recently there have been two research groups in addition to ours which are investigating difference frequency mixing in GaAs photovoltaic and photocurrent devices.[1,2] We have measured in excess of 12 μW of far infrared radiation, an order of magnitude higher than reported previously, due largely to the higher intrinsic nonlinear conversion efficiency, phase matching, and better energy coupling efficiency in our waveguide device.

Our GaAs/GaAlAs multiple quantum well mixer device was grown by molecular beam epitaxy (MBE). The large dipole moment characteristic of intersubband transitions was 'engineered' by growing epitaxial layers that comprise the compositionally asymmetric multiple quantum wells. The quantum wells, shown schematically in figure 1, were optimized to have only two intrasubband transitions within the conduction band, separated by 150 meV. The asymmetry resulted in an estimated second order nonlinear susceptibility, $\chi^{(2)}(\omega_1 - \omega_2, \omega_1, \omega_2)$, of 10 nV/m. In order to provide efficient interaction between the pumps and the nonlinear medium, field confinement and long interaction length were deemed necessary. These requirements suggested a waveguide implementation, providing a means for efficient phase matching. Because of the long wavelength (118 μm) of the output radiation, phase matching required 25 - 50 μm thick epi layers.

Once the MBE growth process was complete, the sample was thinned by polishing to 35 μm and cleaved to 500 μm (length) x 5000 μm (width). Two CO_2 lasers, separated in frequency by 2.5 THz, were

used as input pumps to the MQW mixer. The respective wavelengths were 9.67 µm and 10.55 µm. An infrared two-element beam expander/collimator assembly expanded and collimated the beams prior to the concave mirror used to focus the light into the waveguide (see figure 2). A quartz crystal with an attenuation of 10^6, placed prior to the pyroelectric detector, was used to discriminate between the desired far infrared radiation and unwanted infrared pump radiation. The experimental results are shown in figure 3, a plot of the far infrared output radiation versus the input infrared laser power. A quarter waveplate was used to verify that the effect observed was in fact the far infrared radiation signature and not spurious thermal radiation resulting from the lack of a thermal heat sink. Both lasers must be TM-polarized to excite intersubband transitions, according to theory (see figure 3). When the lasers are orthogonally polarized, the output power drops off dramatically, as can be seen in the lower data set in the figure. This, and the fact the output power is proportional to the product of the input laser powers, unmistakably demonstrates the nonlinear mixing origin of the far infrared output radiation.

References:
1. Sirtori, C., F. Capasso, J. Faist, L. N. Pfeiffer, and K. W. West, Conference on Lasers and Electro-Optics '94, paper QMB6.

2. Brown, E. R., K. A. McIntosh, F. W. Smith, M. J. Manfra, and C. L. Dennis, Applied Physics Letters, 62 (11), 1206, March 15, 1993.

3. Khurgin, J., J. Opt. Soc. Am. B, 6, 1673, (1989).
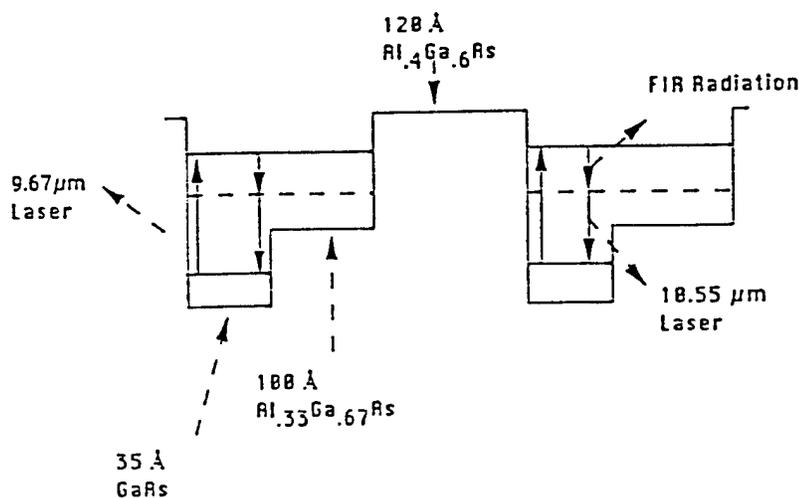
Figure1 .The Asymmetric Multiple Quantum Wells
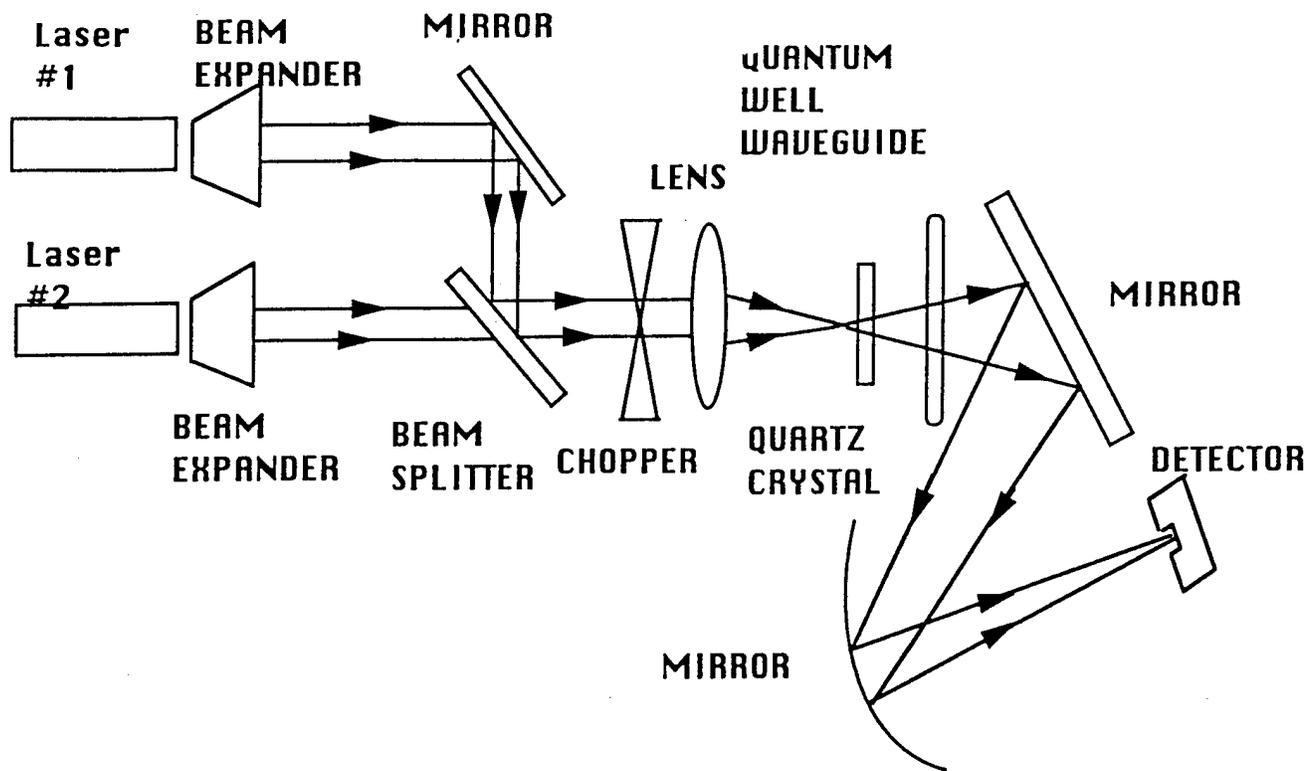
Figure 2. Difference Frequency Experimental Set Up
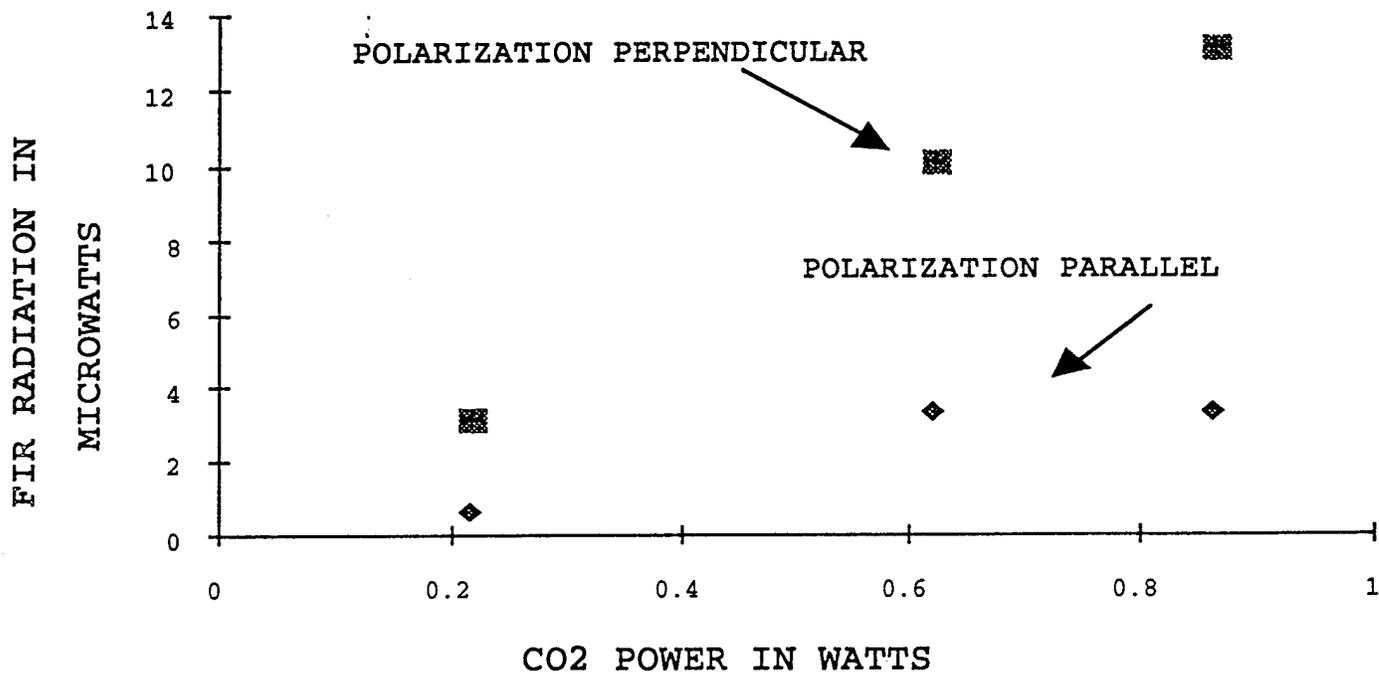
Figure 3. FIR Radiation Output .US. A Co2 Laser

Equal Pulse Correlation in GaAs thin films with Near-field Microscopy

S. Smith, B.G. Orr, R. Kopelman & T. Norris
The University of Michigan
Center for Ultrafast Optical Science
Ann Arbor, Michigan 48109
PHONE: (313) 763-4875, FAX: (313) 763-4876

We are developing a femtosecond Near-field Scanning Optical Microscope (NSOM) with the aim of probing ultrafast optoelectronic processes in semiconductor materials and devices with sub-wavelength spatial resolution. Here we present preliminary results from an Equal Pulse Correlation[1] (EPC) measurement in GaAs thin films (1 μm thick) taken using our near-field microscope. These results demonstrate the possibility of making highly localized, femtosecond carrier relaxation and/or carrier diffusion measurements in a semiconductor thin film.

Our NSOM uses the tapered fiber probe developed by Betzig et. al.[2], through which we send two equal intensity pulses as shown in figure 1. The well known saturation of the absorption in an optically thin semiconductor film leads to an increased transmission which is symmetric about time zero. As discussed in the original paper by Tang et. al.[1], the signal can be interpreted as a convolution of the pulse autocorrelation and a double-sided decaying exponential, where the decay is attributed to hot carrier relaxation. In the geometry of our experiment, we expect an additional contribution due to carrier diffusion since the volume being sampled is much smaller than typical diffusion lengths in GaAs.
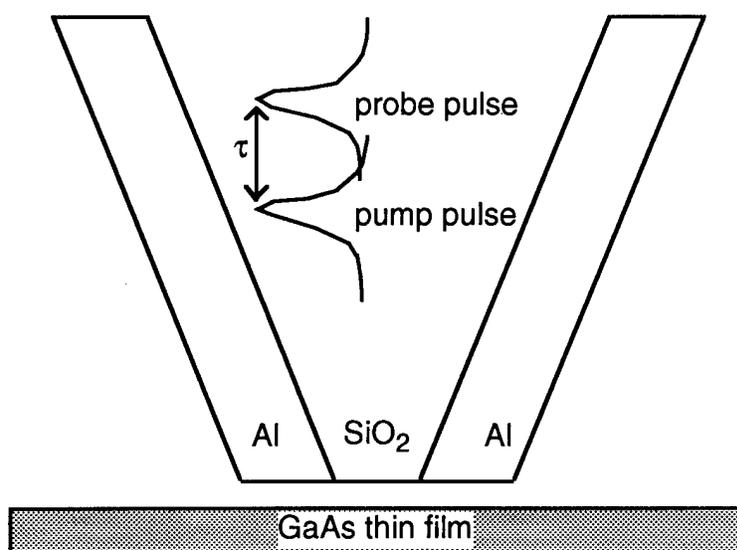
Figure 1: The tapered Aluminum-Glass-Aluminum structure of the Near-field tip forms a subwavelength aperture through which both the pump and probe are sent with variable time delay τ.

The "pump" and "probe" beams (they are actually equivalent) are acousto-optically modulated at 2.01 and 2 MHz, then combined colinearly before entering the fiber. The dispersion due to the 80cm length fiber that is an integral part of the NSOM tip is compensated for using a grating pair (600 lines/mm). The EPC signal is proportional to the intensity squared, and thus appears at the sum and difference frequencies, the lower of which is detected by a lock-in amplifier.

Figure 2 shows the EPC at two remote locations in a 1 μm thick Low Temperature grown GaAs (LT-GaAs) film taken using our NSOM. The autocorrelation through an identical length fiber without an NSOM tip is also shown for comparison. We observe variations in both relaxation time and signal amplitude. These variations can be related to the local density of states and the proximity of material defects and thus are a signature of the local environment on a submicron scale.

Figure 3 shows a comparison of the EPC taken with our NSOM in standard epitaxially grown GaAs and LT-GaAs 1μm thick films. The GaAs EPC width is much narrower, even though the conduction band lifetime in LT-GaAs is known to be much
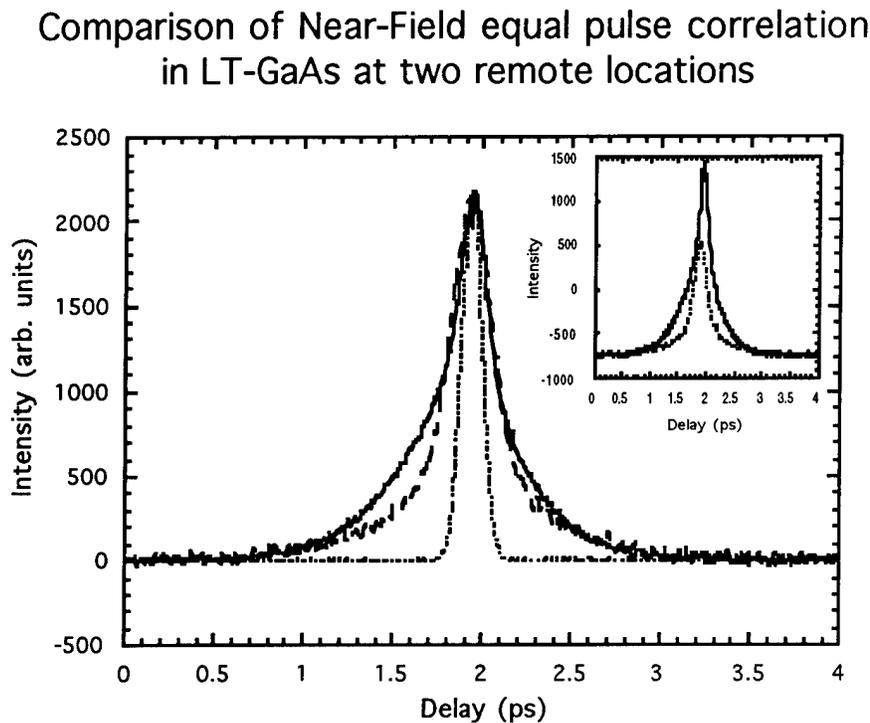
Figure 2: Near-field equal pulse correlation at two remote locations in a 1μm thick LT-GaAs film (outer two traces). Inner trace is the autocorrelation of the pulse. Inset: equal pulse correlations before normalization.

shorter than in GaAs. One possible reason for this could be the effect of carrier diffusion away from the volume being probed. Our current understanding of LT-GaAs assumes a high density of defects and thus a decrease in the mobility and diffusion length. This in turn would show a slower relaxation component due to diffusion for the LT-GaAs, which is consistent with what is observed.

Comparison of Near-Field equal pulse correlation in GaAs and LT-GaAs
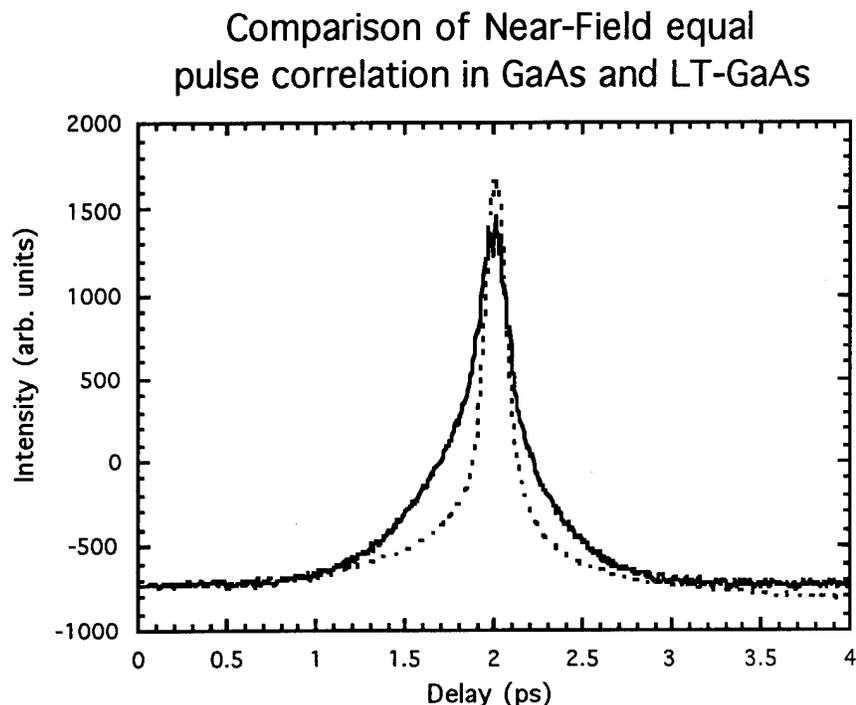
Figure 3:   Near-field equal pulse correlation in GaAs and LT-GaAs. The GaAs correlation is the narrower of the two.

It should be noted that the aperture size in these measurements was undetermined; however, an estimate based on the output power observed compared to that of other NSOM tips of known size is 250 nm (0.3λ for the wavelength used). The obtainable resolution of NSOM in this application will be limited by signal to noise considerations, and has yet to be determined. Our results suggest it is possible to study carrier dynamics in thin films on the femtosecond timescale with submicron spatial resolution not obtainable with diffraction limited optics.

References

(1) C.L. Tang & D.J. Erskine, Phys. Rev Lett. 51 (9), 844 29 Aug (1983).

(2) E. Betzig et. al., Science Vol. 251, 1468 (1991).

QUANTUM FLUCTUATION EFFECTS IN PHOTON CONFINEMENT

L.A.Rivlin

Moscow State Institute of Radioengineering, Electronics, and Automation
[MIREA]
78 Vernadsky Ave., Moscow, 117454, Russia
Phone & FAX: (7-095) 434 9317

We consider the field evolution in a waveguide with mirror walls during adiabatic variation of its cross-section starting from the free unbounded space. The rigorous calculation shows that the energy of a cut-off frequency quantum is equal to the work performed in this confinement process in opposition to the radiation pressure of zero-point vacuum fluctuations, having the initial frequency equal to zero. This statement lends the clear physical meaning to known analogy between the cut-off frequency and the photon rest mass in a waveguide put forward by de-Broglie: the rest mass is an equivalent of mentioned energy (work) and ultimately come from the simplest form of electromagnetic matter - the static fluctuation field of vacuum. The cut-off wavelength is merely the Compton wavelength of a photon confined in a waveguide.

In this context the so-called longitudinal and transverse masses of the photon coincide with corresponding expression of the special theory of relativity. The formula for longitudinal mass follows strictly from the time derivative of the waveguide propagation constant. The transverse mass acquires a meaning only if we consider a joint acceleration of a field and of the waveguide in a direction normal to its axis. The transverse mass merely is equal to the difference between the radiation-pressure forces exerted by the field of a mode containing a single photon on opposite waveguide walls, divided by the transverse acceleration.

The similar force difference in the bent waveguide determines the photon mass in the expression for centrifugal force.

The photon with rest mass defined as above behaves in the field of gravity just like the ordinary massive particle. This statement became clear from the gedanken-experiment with a vertical waveguide: the dependence of waveguide cross-section dimensions and of a wave frequency on the gravitational potential leads to the change of propagation constant quite similar to the change of the momentum of a heavy particle moving vertically. In a particularly interesting case the wave propagation upward along the vertical waveguide ceases that corresponds to stopping at the uppermost point of the path of a massive body, which is thrown upward and has exhausted its initial momentum.

The non-zero mass of a confined photon is due to the presence of a transverse standing wave in the waveguide and arises from this "stopped" field component. In general the photon mass is equal to zero only if a photon is represented by an ideal unbounded single plane wave. Any real electromagnetic wave is spatially bounded and possesses a standing component causing the effect of non-zero mass. We are essentially seeing the uncertainty relation at work.

Moreover the concept of confined photon rest mass leads to evolving the zero-mass wave equation into a one dimensional equation of the Schroedinger type for the massive particle without introducing the non-zero mass a priori.

The general conclusion is: the rest mass energy originates from the work done in "scraping together" (confining) the matter that makes up the particles from the infinite free space.

Calibrated Noise Measurements in Microcavity Lasers

Edgard Goobar, Jeff Scott, Gerry Robinson, Yuliya Akulova and Larry A. Coldren

Dept. of Electrical and Computer Engineering
University of California Santa Barbara, CA 93106
Fax: (805) 893 4500
Tel: (805) 893 2875

During recent years the intensity noise in semiconductor lasers has received considerable attention. This is mainly due to the theoretical predictions [1] and experimental results [2-7] indicating that sub-shot-noise levels, amplitude squeezing, can be obtained if the pump noise is suppressed using a high impedance injection current. Recent results indicate, however, that multimode operation in semiconductor lasers may render increased noise levels in spite of the low pump noise [4-7]. The intensity noise of vertical-cavity surface emitting-lasers VCSELs has been reported in refs. [8] and [9]. In [8] the polarization stability of GaAlAs-GaAs VCSELs was examined and the effect of mode partition between the two polarizations was observed. However, to the best of our knowledge, measurements where the VCSEL noise is directly compared to the fundamental shot-noise level have not yet been reported.

In this work, calibrated intensity noise measurements of InGaAs-GaAs VCSELs are presented. The noise of intra-cavity contacted VCSELs ranging from 5μm to 15μm in diameter is compared to the shot-noise limit as measured with a light emitting diode (LED).

The 5μm devices have been shown to be strongly single mode and we therefore expected them to exhibit amplitude squeezing. It is found, however, that the noise of our devices exceeds the shot-noise limit by more than 10 dB. In order to investigate the origin of this excess noise, measurements were also performed selecting the different polarizations. In spite of a 30 dB side mode suppression ratio (SMSR), the 5 μm lasers showed a

significant amount of noise in the polarization orthogonal to the lasing mode. From the polarized measurements the normalized cross-correlation between the two degenerate polarization modes is calculated and found to be on the order of -0.4 to -0.7. This confirms that the excess noise is caused by incomplete cancellation of the fluctuations in the two polarizations.
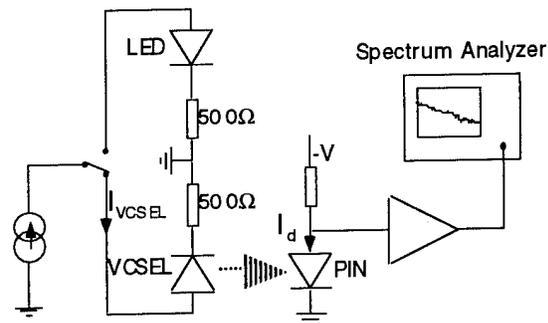
Fig. 1 Schematic view of the measurement set-up.

Fig. 1 shows a schematic view of the measurement set-up. The VCSELs are top emitting intra-cavity contacted devices [10]. The active region is formed from three 80Å $In_{0.2}Ga_{0.8}As$ quantum wells with 80Å GaAs barriers. The DBR mirror layers are formed from AlAs/$Al_{0.1}Ga_{0.9}As$ pairs. The lower mirror consists of 28.5 periods while the upper mirror consists of 15 periods. An array of lasers was wire-bonded and mounted on a 40 pin dual-in-line chip carrier, which was then mounted on a printed board together with an LED (Hamamatsu L2656). The condition to obtain sub-shot noise current injection is $4kT/R \leq 2qI_{VCSEL}$ [2]. Since $I_{VCSEL} \approx 3$-6mA, a 500 Ω series resistance is used to ensure pump noise suppression. The intensity noise is detected with a but-

coupled Si PIN photodetector detector (Hamamatsu S1722-01) which was mounted slanted in order to avoid spurious backreflections to the lasers. The signal is amplified with a low noise amplifier and measured with an electrical spectrum analyzer. The same detector is later moved over to the LED in order to measure the shot-noise limit at the same photodetector current. The detector was very linear up to 4.5mA photodetector current, which was the highest photodetector current we could measure biasing the LED slightly below its maximum rated current. The shot-noise statistics of the photodetector current was verified in a similar way as in ref. [11]. Introducing neutral density filters with increasing degree of attenuation in front of the LED, it was verified that the shot noise signal was independent of the attenuation.
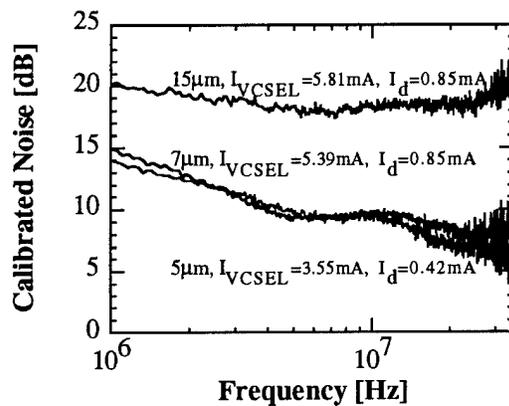
Fig. 2 Intensity noise normalized to the shot-noise limit for 15μm, 7μm and 5μm diameter devices.

Typical intensity noise characteristics, normalized to the shot-noise, are shown in Fig. 2. The upper trace is for a 15μm device biased at $I_{VCSEL} \approx 2.6\ I_{th} = 5.8$mA. The photodetector current was in this case $I_d = 0.85$mA. The other two traces are for 5μm and 7μm devices, respectively, biased at $I_{VCSEL} \approx 7.7\ I_{th} = 5.39$mA and $I_{VCSEL} \approx 5\ I_{th} = 3.55$mA and at the detector currents $I_d = 0.85$mA and $I_d = 0.42$mA, respectively. In the frequency range of our measurements the lasers exhibit noise in excess of their respective shot-noise levels.

In order to examine the origin of this result the optical spectrum of the 5μm device was measured through a Glan-Thompson polarizer at the same biasing level. In the spectra (not shown here) a 30 dB SMSR is observed when the polarizer was rotated between the two polarization states. In spite of the relatively high SMSR there is a significant amount of noise in the polarization orthogonal to the main mode.
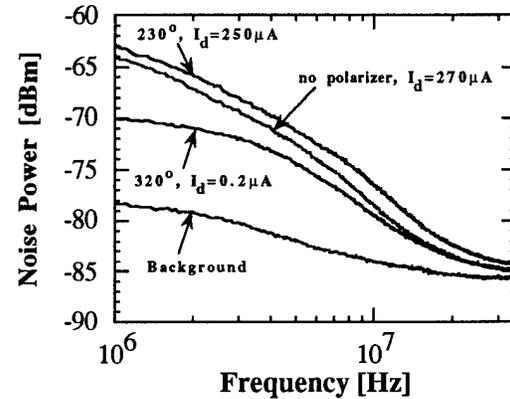
Fig. 3 Intensity noise of the 5μm device measured through a Glan-Thompson polarizer.

This is verified in Fig. 3, where the intensity noise measured through the polarizer is presented. Due to coupling losses the detector current is now $I_d = 0.25$mA or $I_d = 0.2$μA, depending on the angle of the polarizer. When the polarizer is removed and $I_d = 0.27$mA the noise is lower than with of the polarizer, which is a clear indication of mode partition noise.

In the presence of two orthogonal polarization modes, the photodetector current can be described as:

$$I_d(t) = I_x(t) + I_y(t)$$

were $I_d(t)$ is the total detector current and $I_x(t)$ and $I_y(t)$ are the components due to the two polarization modes. The power spectral density of $I_d(t)$ is therefore:

$$S_d(f) = \int_{-\infty}^{+\infty} \langle I_d(t)I_d(t+\tau)\rangle e^{-i2\pi f\tau} d\tau$$

$$= S_x(f) + S_y(f) + 2S_{xy}(f)$$

were $\langle\ \rangle$ indicates time averaging and $S_x(f)$, $S_y(f)$ and $S_{xy}(f)$ are the power spectral densities and the cross-power spectral density of the two polarization modes, respectively. Using the measurement data the normalized cross-power spectral density can be calculated as:

$$C_{xy}(f) = \frac{S_{xy}(f)}{\sqrt{S_x(f)S_y(f)}}.$$

In Fig. 4, the normalized cross-spectral density of the two polarization modes of the 5μm device is shown. It confirms that the two polarization modes are negatively correlated, but since $C_{xy}(f) \neq -1$ the fluctuations of the two modes do not cancel totally and therefore prevent us from seeing squeezing.
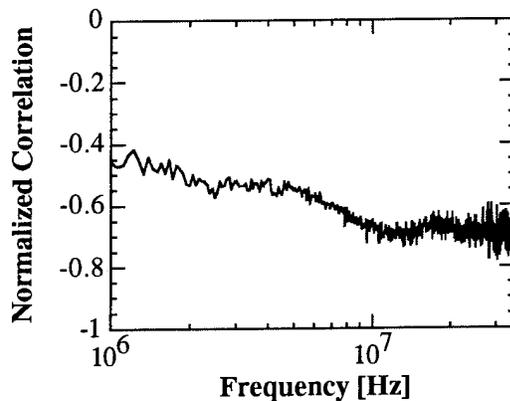
Fig. 4 Normalized cross-correlation between the two degenerate polarization modes in the 5μm device.

In conclusion, calibrated noise measurements show that our VCSELs exceed the shot noise limit by more than 10 dB. The single mode devices have a relatively high SMSR. Still, partition noise due to polarization degeneracy is found to render excess noise that destroys squeezing. This result is in qualitative agreement with results reported for in-plane lasers in refs. [4-7], were the degradation of the SMSR rendered increased intensity noise. The introduction of some polarization selective mechanism might be necessary in order to overcome this limit.

[1] Y. Yamamoto, S. Machida and O. Nilsson, Phys. Rev. A, **34**, 4025 (1986).

[2] S. Machida and Y. Yamamoto, Phys. Rev. A, **35**, 5114 (1987).

[3] W. H. Richardson, S. Machida, Y. Yamamoto, Phys. Rev. Lett., **22**, 2867 (1991).

[4] S. Inoue, H. Ohzu , S. Machida and Y. Yamamoto , Phys. Rev. A, **46** 2757 (1992).

[5] M. J. Freeman, H. Wang, D. G. Steel, R. Craig and D. R. Scifres, Optics Lett., **18**, 379 (1993).

[6] M. J. Freeman, H. Wang, D. G. Steel, R. Craig and D. R. Scifres, Optics Lett., **18**, 2141 (1993).

[7] H. Wang, M. J. Freeman, and D. G. Steel, Phys. Rev. Lett., **71**, 3951 (1993).

[8] F. Koyama, K. Morito and K. Iga, IEEE J. Quantum Electron., **27**, 1410 (1991).

[9] D. M. Kuchta, J.Gamelin, J. D. Walker, J. Lin, K. Y. Lau, and J. S. Smith, Appl. Phys. Lett., **62**, 1194 (1993).

[10] J. W. Scott, B. J. Thibeault, D. B. Young, L. A. Coldren, and F. H. Peters, Photonics Technol., Lett., 6, 678 (1994).

[11] E. Goobar, A. Karlsson, G. Bjork and P-J. Rigole, Phys. Rev. Lett., **4**, 437 (1993).

Realization of large subband separation and high power light output in GaAs/AlGaAs two-dimensional quantum well wire laser arrays

Yi Qian, Lianghui Chen, Jingming Zhang, Qiming Wang, Lianxi Zhen*, and Xiongwei Hu*

NIOEL, Institute of Semiconductors, Chinese Academy of Sciences, P.O.Box 912, Beijing 100083, China

*National Research Center for Optoelectronic Technology, P.O.Box 912, Beijing 100083, China

Tel: 86-1-2558131 ext. 511   Fax: 86-1-2562389

Incorporating lower-dimensional structures such as quantum well wires (QWWs) and dots into semiconductor laser structures is expected to result in improved laser performance[1]. The technique of fabrication QWWs on nonplanar substrates by metal-organic chemical vapor deposition (MOCVD) is much potential due to formation of defect-free interfaces entirely during the epitaxial growth process[2]. With this approach, enhanced optical gain[3,4] and ultralow threshold current[2,5] have been demonstrated in QWW lasers. However, large QWW subband separation greater than thermal energy $k_B T$ at room temperature (~25meV) is still desirable, which should be realized by reducing wire sizes. The small wire volume, however, is disadvantageous for achieving high power light output of QWW lasers for some practical applications.

Here reports realization of our GaAs/AlGaAs QWW laser arrays with not only large subband separation but also high power light output, which were grown by MOCVD on nonplanar substrates. Surface-emitting electroluminescence (EL) spectra indicate the subband separation as large as 27meV, which is almost equal to the thermal energy at room temperature. Even though the effective width of QWWs is estimated to be smaller than 6nm, the linear light output power of the laser arrays have reached up to 100mW under pulsed conditions (1μs pulses at 1kHz) at room temperature. To our knowledge, the above light output is the highest figure to date for all kinds of QWW lasers, and the subband separation is the largest reported to date for the GaAs/AlGaAs QWWs having been incorporated into laser structures.

In order to reduce the wire size to reach large subband separation , we used high Al mole fraction (40%) in barriers, appropriate thickness rate between GaAs wells and AlGaAs barriers, and low growth temperature (700°C). On the other hand, in order to circumvent the disadvantage of the small wire volume to obtain high power output, we adopted an array structure with QWW lasers lined along the direction not only parallel but also perpendicular to the growth direction, which we call as two-dimensional (2D) QWW laser structure.

As shown in Fig.1(a), a multiple quantum well (MQW) graded-index(GRIN) separate confinement heterojunction laser structure was grown on (100) n^+-GaAs substrates, which were patterned into sawtooth-shaped grating with a period of 6μm along [011] direction using conventional photolithography and chemical wet etching. The MQW active layer consisted of four 5nm GaAs wells separated by five 26nm $Al_{0.4}Ga_{0.6}As$ barriers. Four crescent-shaped QWWs are formed at the bottoms of the V-grooves, and each of them is 7nm thick at the centers and ~60nm wide totally, as shown in Fig. 1(b). However, the effective widths of these wires are considerably smaller than the total width due to lateral tapering in the thickness of each crescent[4]. In addition,
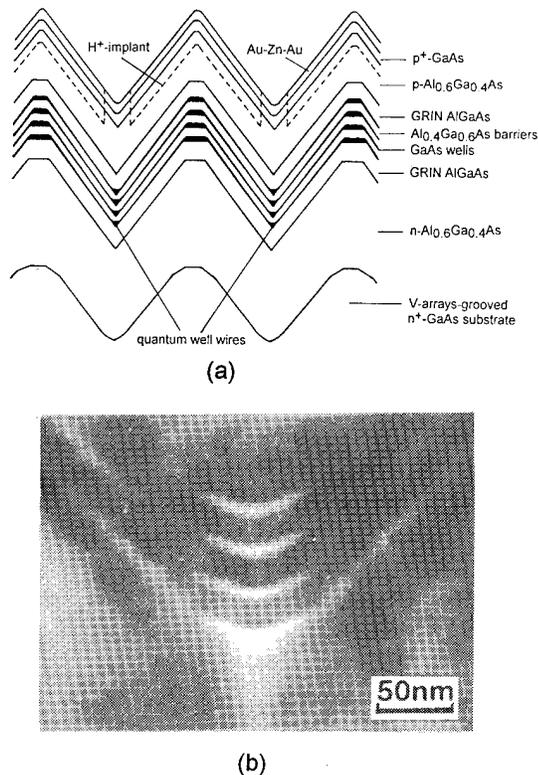
Fig. 1. (011) cross-section: (a) schematic illustration of 2D-QWW laser array structures, and (b) transmission electron micrography of four crescent-shaped QWWs at the bottoms of the V-grooves, where the bright stripes represent GaAs layers and the dark area AlGaAs.
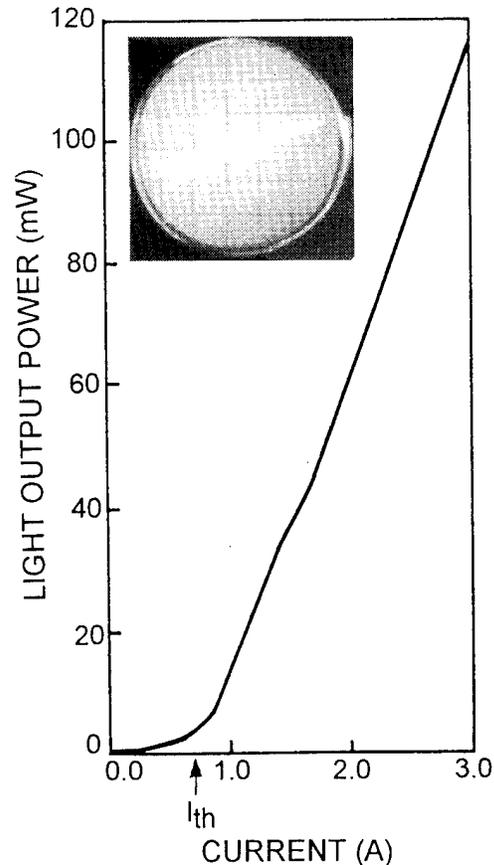
Fig. 2. L-I characteristic (L=200μm, W=120μm, uncoated, R.T. pulsed: 1kHz/1μs). The inset is a photography of the near-field pattern at 2.5A.

the QWs are 1.8nm thick on the sidewall (111) of the V-grooves and 8nm on the tops of the mesas, which are also derived from the transmission electron micrography.

Fig. 2 shows a light versus current characteristic of a typical 2D-QWW laser array operated at room temperature under pulsed conditions (1μs pulses at 1kHz). The linear pulse light output reaches up to 115mW at 3.0A. The light output should be more powerful if our current sources could afford bigger currents. The near-field pattern of the arrays shown in the inset indicates nineteen uniform circular spots. In Fig. 3, the lasing spectra of the 2D-QWW laser array feature multiple longitudinal mode structures, and the lasing wavelength is centered at 755.0nm.

Fig. 4 shows surface-emitting EL spectra at 10K. The samples measured were not processed by the H^+-implantation as shown in Fig. 1(a), and the EL emitted from a 50μm×50μm window etched on the p-side metallization. The laser array has been operated at 10K with threshold current of 4mA. The structure A, B, and C are attributed to the QWs on the tops of the mesas, the QWs on the (111) sidewalls, and the QWWs at the bottoms of the V-grooves, respectively. The three lowest subbands (l=0, 1, 2) of the QWWs observed at 736.8nm, 724.4nm, and 714.4nm,
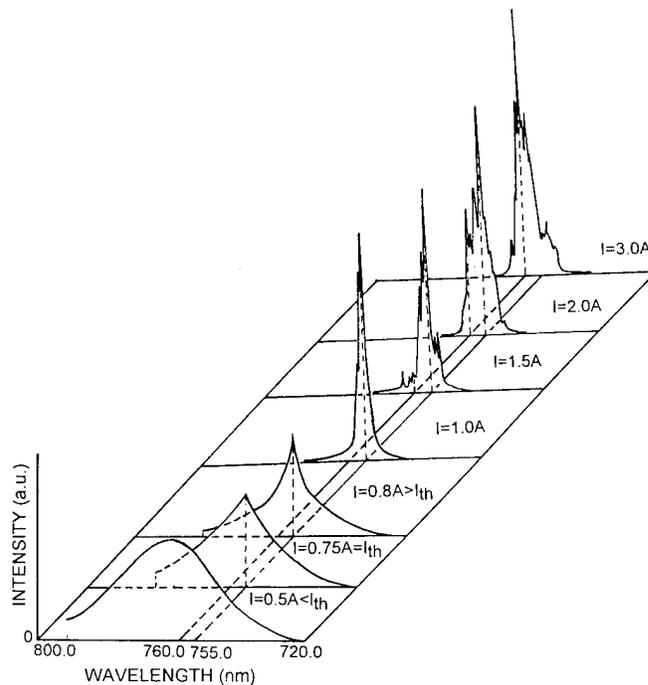
Fig. 3. Room temperature lasing spectra.
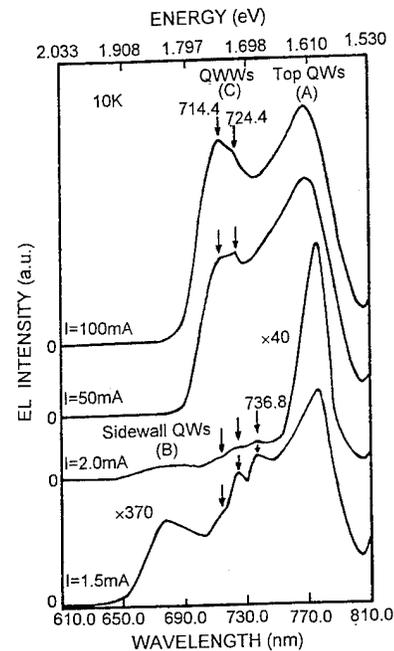
Fig. 4. Surface-emitting EL spectra (10K, CW, I_{th}=4mA).

respectively, which correspond to 780.0nm, 768.7nm, and 755.5nm at room temperature. Therefore, the 2D-QWW laser arrays are still operated at the high order (l=2) subband at room temperature, however, the separation between the two lowest subbands has reached up to 27meV, which is almost equal to the thermal energy at room temperature. Using the calculation model previously described[6], the effective width of QWWs is estimated to be smaller than 6nm. In addition, the wavelength positions of A and B are in agreement with the calculation results. Furthermore, the relative intensity of B decreases with the increase of injection current, which is different A and C and implies the efficient carrier capture from the sidewall QWs into the QWWs and the top QWs.

In conclusion, we have realized GaAs/AlGaAs 2D-QWW laser arrays with large subband separation by fabricating extremely small wires; nevertheless, the laser arrays have reached high power output, which is promising for further practical applications.

1.Y. Arakawa and H. Sakaki, Appl. Phys. Lett. 40, 939(1982); Y. Arakawa and A. Yariv, IEEE J. Quantum Electron. QE-22, 1887(1986).

2. S. Simhony, E. Kapon, E. Colas, D. M. Hwang, and N. G. Stoffel, Appl. Phys. Lett. 59, 2225(1991).

3. S. Tiwari and J. M. Woodall, Appl. Phys. Lett. 64, 2211(1994).

4. E. Kapon, D. M. Hwang, and R. Bhat, Phys. Rev. Lett. 63, 430(1989).

5. S. Tiwari, G. D. Pettit, K. P. Milkove, F. Legeous, R. J. Davis, and J. M. Woodall, Appl. Phys. Lett. 64, 3536(1994).

6.Yi Qian, Jingming Zhang, Junying Xu, Jianwei Xiao, Lianghui Chen, Qiming Wang, Xiaochuan Zhou, Jian Jiang, and Zhantian Zhong, Superlattices and Microstructures 13, 241(1993).

Novel Semiconductor Materials and Structures

QFA 8:30 am-10:00 am
Ballrooms VI-VIII

Nobuyuki Imoto, *Presider*
NTT, Japan

II-VI Semiconductor Nanocrystals as Isolated Quantum Dots and in Complex Structures

Moungi G. Bawendi

MIT, Department of Chemistry
77 Massachusetts Avenue
Cambridge, MA 02139

Tel: (617) 253-9796
FAX: (617) 253-7030
email: mgb@athena.mit.edu

Semiconductor crystallites which are 10's of Angstroms show a striking evolution of electronic properties with size.[1] These particles (quantum dots) are large enough to exhibit a crystalline core, but small enough that solid state electronic and vibrational band structure is not yet developed. We use a recently developed synthetic method for the fabrication of high quality nanometer size (1-10 nm) II-VI semiconductor crystallites with narrow size distributions ($\sigma < 5\%$), emphasizing CdSe.[2] Optical characterization of their electronic structure reveals both molecular and bulk-like characteristics as well as properties which are unique to nanometer size crystallites. We observe a number of discrete electronic transitions, assign them as coming from the creation of delocalized "particle-in-a-sphere" states using the theory of Ref. 3, and study their dependence on crystallite diameter.[4]

We then turn to structures of dots and describe the chemical manipulation of the dots into close packed glassy and ordered arrays, essentially "crystals" of quantum dots. We demonstrate control over dot-dot distance, dot size and structure (from glassy to perfectly ordered). We observe and study interdot

energy transfer (from small to large dot) by purposefully creating a close-packed structure of small dots with a few large dots interspersed in the structure.

We demonstrate electroluminescence from CdSe quantum dots embedded in a polymer film of PVK and PBD.[5] This shows that it is possible to electrically excite nanometer size quantum dots within a host matrix. The wavelength of the emitted light (bandwidth <40nm) is tunable from ~530 nm to ~650 nm by varying the size of the dots

1. For a review, see for example L. E. Brus, Appl. Phys. A **53**, *465* (1991).

2. C. B. Murray, D. J. Norris, and M. G. Bawendi, J. Am. Chem. Soc. **115**, *8706* (1993).

3. A. Ekimov, M. Hache, M. Schanne-Klein, D. Ricard, C. Flytzanis, I. Kudryavtsev, T. Yazeva, A. Rodina, and Al. Efros, J. Opt. Soc. Am. B **10**, *100* (1993).

4. D. J. Norris, A. Sacra, C. B. Murray, and M. G. Bawendi, Phys. Rev. Lett. **72**, *2612* (1994).

5. B. O. Dabbousi, M. G. Bawendi, O. Onitsuka, and M. F. Rubner, Appl. Phys. Lett. (in press).

Squeezed Light Generation in Semiconductors

A.M. Fox, J. J. Baumberg [a], M. Dabbicco, B. Huttner [b] and J.F. Ryan

Department of Physics, University of Oxford
Clarendon Laboratory, Parks Road, Oxford, OX1 3PU, U.K.
tel: +44 865 272200, fax: +44 865 272400

The signal to noise ratio of optical systems is ultimately limited by the shot noise due to the Poissonian statistics of the light field. In recent years there has been a considerable effort to find ways to overcome this limitation by generating non-classical light with sub-shot noise statistics. Several groups have demonstrated non-classical light generation in diode lasers or light emitting diodes, and the amplitude fluctuations have been reduced substantially below the shot noise level [1,2]. However, for phase-sensitive measurements it is necessary to generate the more general *quadrature* squeezed states. Such quadrature squeezed light can be generated either by second-order or third-order nonlinear processes provided the nonlinear material has very low losses at the optical wavelength. To date, the successful generation schemes for quadrature squeezed light have been restricted to atomic vapours, optical fibres, or second-order nonlinear crystals [3]. The possibility of using the large $\chi^{(3)}$ nonlinearities of semiconductors at frequencies below the band gap where the optical absorption is small has been discussed in the literature, but so far there have been no successful experiments [4-6]. In this paper we report measurements on GaAs/Al$_{0.3}$Ga$_{0.7}$As multiple quantum well waveguides and bulk ZnS in the wavelength range 750 - 890nm. Although we measure much larger nonlinearities in the quantum wells, the strong two-photon absorption is detrimental for squeezed light generation. However, in the ZnS where the laser frequency is below the two-photon absorption edge, we have succeeded in generating quadrature squeezed light in a semiconductor for the first time. On the basis of our results, we would expect that squeezed light could be generated in many other semiconductor systems provided the photon energy is less than half the band-gap energy.

The experiments on the GaAs quantum wells were performed at room temperature in the spectral region about 40meV below the heavy hole exciton line at 854nm. With this value of the detuning, there is still a resonant enhancement of the nonlinearity due to the AC Stark effect, but the linear absorption is weak because the detuning is greater than an LO-phonon energy from the exciton line. GaAs/Al$_{0.3}$Ga$_{0.7}$As superlattice rib waveguide samples were used with 80Å wells and 60Å barriers. The nonlinear refractive index n_2 was determined from self-phase modulation experiments to be -1×10^{-12}cm^{2}W^{-1} at 882nm [7]. At this wavelength the residual band tail absorption loss was only 1cm^{-1}. However, the limiting loss mechanism proved not to be the linear loss but the two-photon absorption. We measured a two photon absorption coefficient β of 19 cmGW^{-1} which gives rise to very high nonlinear absorption at the intensities required to obtain usable nonlinear phase shifts.

The problem of two-photon absorption can be overcome by working at photon energies below $E_g/2$, where E_g is the band-gap energy. ZnS, which has a band gap of 3.7eV at room temperature, meets this criterion when using a Ti:sapphire laser. Self phase modulation experiments were performed at 780nm with 125fs pulses from a mode-locked laser, and nonlinear phase shifts up to $\pi/2$ were measured with very small linear and nonlinear losses. These conditions are much more favourable for squeezing than in the GaAs quantum wells.

Squeezing experiments were performed using an anti-reflection coated ZnS sample at room temperature placed within a nonlinear Sagnac interferometer. The nonlinear interferometer separates the squeezed light from the large coherent component of the laser pulses [8]. The light is squeezed by the optical Kerr effect after a single pass through the sample. Balanced homodyne detection was used to observe the phase dependence of the quantum noise in the sidebands of the laser modes.

Fig. 1 shows the phase dependent noise at 35MHz observed with 3nJ 125fs pulses incident on the sample. Also shown is the shot noise level (SNL) of the local oscillator. As the local oscillator phase is varied, we observe that one quadrature phase drops 0.9dB below the SNL, while the other quadrature lies 2.0dB above SNL. The estimated detection efficiency for this measurement is 50%, and thus we deduce that the light is squeezed by approximately 2dB in the semiconductor material. Fig. 2 shows the frequency dependence of the noise power normalised to the shot noise level. We observe no significant variation within the bandwidth of our detection electronics. We expect that the noise will be squeezed over a very broad band of frequencies.

In conclusion, we have succeeded in generating quadrature squeezed light using semiconductor nonlinearities for the first time. Experiments exploiting the enhanced excitonic effects in quantum wells were hindered by strong two-photon absorption, but by using II-VI semiconductors with larger band gaps, we were able to overcome the two photon absorption problem and generate 2dB squeezing across a broad range of frequencies.

The quantum well waveguides were grown and fabricated by M.A. Pate and J.S. Roberts at the SERC III-V Semiconductor growth facility at Sheffield University.

(a) Present address: Hitachi Cambridge Laboratory, Cavendish Laboratory, Madingley Road, Cambridge CB3 0HE, U.K.
(b) Present address: NTT Basic Research Laboratories, 3-1 Morinosato Wakamiya, Atsugi, Kanagawa 243-01, Japan.

References

[1] W.H. Richardson, S. Machida, and Y. Yamamoto, Phys. Rev. Lett. **66** , 2867 (1991).
[2] P.R. Tapster, J.G. Rarity, and J.S. Satchell, Europhys. Lett. **4**, 293 (1987).
[3] See special issue on *Quantum noise reduction in optical systems - experiments* : edited by E. Giacobino and C. Fabre, Appl. Phys. B **55** , 189 - 303 (1992).
[4] R.E. Slusher, S.L. McCall, A. Mysyrowicz, S. Schmitt-Rink and K. Tai, in *Nonlinear Optics of Organics and Semiconductors*, Ed. T. Kobayashi, Springer Proceedings in Physics Vol. 36, p. 24, Springer-Verlag, Berlin (1989).
[5] R.E. Slusher, A. LaPorta, P. Grangier and B. Yurke, in *Squeezed and Nonclassical Light*, Edited by P. Tombesi and E.R. Pike, p. 39, Plenum, New York (1989).
[6] L. Hillico, J.M. Courty, C. Fabre, E. Giacobino, I. Abram, and J.L. Oudar, Appl. Phys. B, **55**, 202 (1992).
[7] A.M. Fox, B. Huttner, J.F. Ryan, M.A. Pate, and J.S. Roberts, Phys. Rev. A (to be published).
[8] M. Shirasaki and H.A. Haus, J. Opt. Soc. Am. B **7**, 30 (1990).
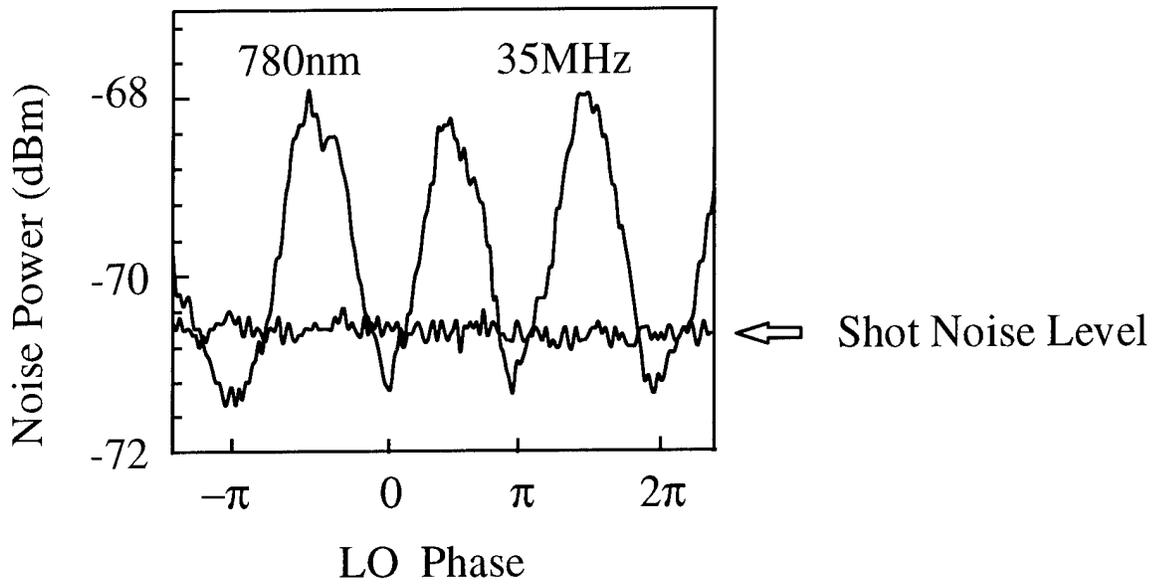
FIG. 1 Phase dependent noise from the ZnS sample at room temperature measured with a balanced homodyne detector. The laser wavelength was 780nm, and the pulse width was 125fs. The shot noise level of local oscillator is shown for comparison.
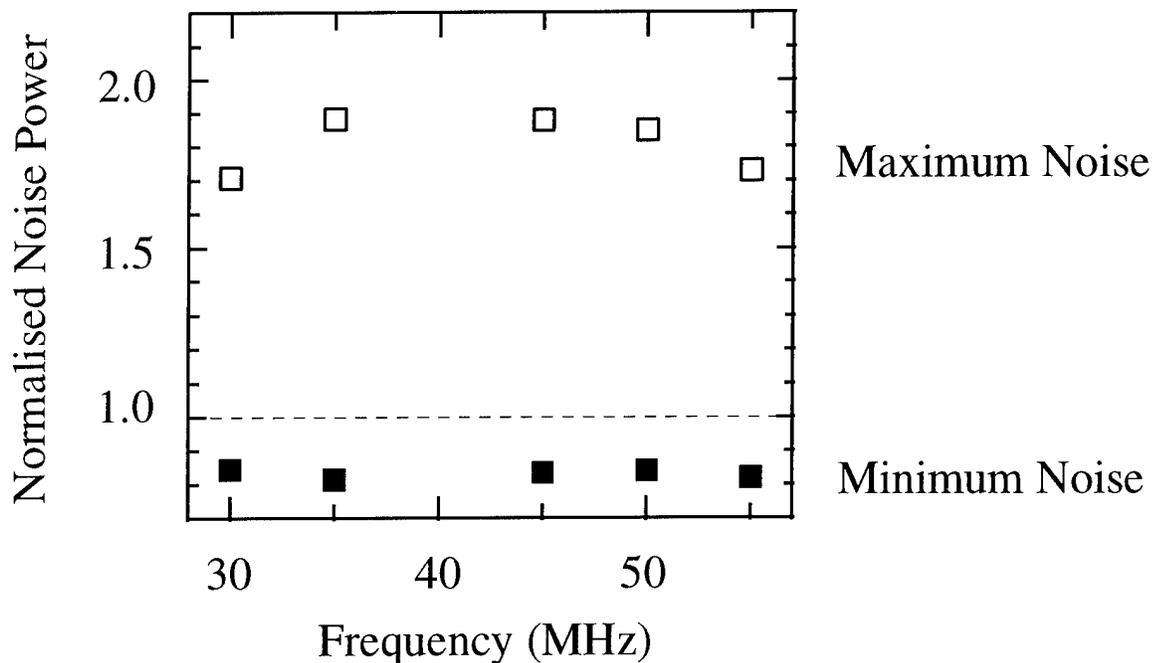
FIG. 2 Frequency dependence of the noise in the two phase quadratures normalized to the shot noise level. The sample was ZnS and the wavelength was 780nm. The spectrum analyser bandwidth was 3MHz. The upper and lower limits of the frequency range are determined by the detection electronics.

Blue-green laser diodes with improved crystal quality
by using a strained-layer superlattice for the optical guiding layer

Jun Gotoh, Shinnichi Nakatsuka, Kazuhiro Mochizuki,
Masayuki Momose, Akira Taike, and Masahiko Kawata
Hitachi Central Research Laboratory
1-280, Higashi-Koigakubo, Kokubunji-shi, Tokyo 185, Japan
Phone. +81-423-23-1111 (ext. 3014)
Fax.   +81-423-27-7747

Blue-green laser diodes (LDs) are attractive for such novel media applications as high-density optical recording systems and full color display devices. ZnSe-based II-VI semiconductor LDs have been developed in recent years[1], and room temperature continuous-wave operation has been achieved[2]. These developments have enabled us to examine the various laser structures using this II-VI semiconductor, e.g., a separate-confinement heterostructure (SCH) gain guide laser[1,2], and a ridge-waveguide laser[3].

The epilayers for these LDs have been grown by molecular beam epitaxy (MBE) which allows device quality p-type layers to be grown routinely. However, it is too difficult to change the composition of the alloys used in cladding and optical guiding layers. This is because II or VI group elements, whose vapor pressure is very high, are intractable materials in MBE. Therefore, the compositional deviations of these alloys are apt to arise, the crystal defects deteriorate these LDs are consequentially formed in these alloys.[4]

We have developed a superlattice optical guiding layer (SOGL), consists of a ZnCdSSe and ZnSSe strained-layer superlattice (SLS), that improves the crystallinity of the active region in SCH lasers. Superlattice buffer layers are widely used to improve the performance of quantum well lasers, in which very smooth interfaces are required.[5] Furthermore, this structure can be grown without any growth interruptions between the cladding layer and the optical guiding layer, which are inevitably necessary in changing the composition of the alloys.

Samples were grown at 300 °C on (100) GaAs substrates by MBE. The source materials were Zn, Se, Mg, Cd, and ZnS. The p-type layers were doped with nitrogen excited by a plasma source. $ZnCl_2$ was used as the n-type doping source.

A test structure was constructed to study the optical properties of single quantum well (SQW) on an SLS. It consisted of a ZnSe buffer layer (0.5 μm), a $Zn_{0.7}Cd_{0.3}S_{0.12}Se_{0.88}$ (10 nm)/$ZnS_{0.12}Se_{0.88}$ (10 nm) SLS layer, a $Zn_{0.7}Cd_{0.3}Se$ SQW layer (10 nm), and a $Zn_{0.7}Cd_{0.3}S_{0.12}Se_{0.88}$ (10 nm)/$ZnS_{0.12}Se_{0.88}$(10 nm) SLS layer. For comparison, a similar SQW structure in which ZnSe layers were used instead of the SLS layers was also grown. The effect of the SLS layers on the optical quality of a ZnCdSe SQW active layer as a function of the periodic number of SLS layers was examined by photoluminescence (PL) measurement with a 325-nm line from a He-Cd laser at 14 K.

Figure 1 shows the PL intensity and the full-width at half-maximum (FWHM) of PL spectra from an SQW structure plotted against the periodic number. The values for the periodic number zero are for the ZnSe layers instead of the SLS. The PL intensities of the samples with SLS layers were two orders of magnitude higher than the samples without SLS layers. This suggests that the nonradiative defects around the active region with SLS layers were reduced, and is not attributable to better carrier confinement . Because the barrier energy of an SLS layer for an SQW is almost equivalent to the energy of a ZnSe buffer layer. On the other hand, the FWHM of the PL spectra decreased as the periodic number increased. The

SLS therefore seems to reduce fluctuations in SQW thickness. These results indicate that SLS layers can remarkably improve the quality of an SQW structure.

An SCH laser with SLS layers as the optical guiding layers was prepared on an n-GaAs substrate. For comparison, a similar LD structure, in which $ZnS_{0.1}Se_{0.9}$ optical guiding layers were used instead of the SOGL layers, was also grown. A schematic cross section of the SOGL device is shown in Fig. 2. An epitaxial layer with them consists of (1) an n-$Zn_{0.9}Mg_{0.1}S_{0.15}Se_{0.85}$ cladding layer (1.2 µm), (2) an n-$Zn_{0.7}Cd_{0.3}S_{0.12}Se_{0.88}$/ $ZnS_{0.12}Se_{0.88}$ SOGL (90 nm), (3) a $Zn_{0.7}Cd_{0.3}Se$ active layer(6 nm), (4) a p-$Zn_{0.7}Cd_{0.3}S_{0.12}Se_{0.88}$/ $ZnS_{0.12}Se_{0.88}$ SOGL (90 nm), (5) a p-$Zn_{0.9}Mg_{0.1}S_{0.15}Se_{0.85}$ cladding layer (80 nm), (6) a p-$ZnS_{0.07}Se_{0.93}$ layer (50 nm), and (7) a p-ZnSe contact layer(100 nm). Each SOGL consists of seven pairs of 2.5-nm $Zn_{0.7}Cd_{0.3}S_{0.12}Se_{0.88}$ well layers and 10-nm $ZnS_{0.12}Se_{0.88}$ barrier layers. These quantum wells have to be combined with each other in order to prevent the carriers from trapping in the SOGLs. The critical thickness of an SOGL is regulated by the ratio of well and barrier layer thicknesses since the well and barrier layers were strained at compressive and tensile stress, respectively. The optical confinement factor at an active layer of an SOGL is about 1.3 times that of a $ZnS_{0.07}Se_{0.93}$ layer. A polyimide insulator defines a 15-µm wide stripe for the laser diodes, which have a 1-mm cavity length. The Au electrode is evaporated on the p-ZnSe contact layer, and the In serves as an n-metal contact to the n-GaAs substrate.

Figure 3 is a cross-sectional transmission electron microscopy (TEM) bright field image showing epitaxial layers with and without SOGLs. Without SOGLs, there are uneven interfaces and many misfit dislocations on the active layer. On the other hand, images of all observed areas of the epilayer with SOGLs show smooth interfaces free from misfit dislocations, indicating that the entire epilayer was successfully grown.

Figure 4 shows the light output-current (L-I) characteristics at 77 K for pulsed operation of an SQW-SCH laser with SOGLs. The pulse length was 100 ns at a repetition rate of 10 KHz. The inset lasing spectrum shows blue-green emission at a wavelength of 470 nm. The threshold current is 50 mA without facet coating. This corresponds to a threshold current density of 330 A/cm^2. The threshold current of a triple quantum well (TQW) active layer without SOGLs was 100 to 150 mA. The calculated value of the threshold current density in an SQW active layer is 0.7 to 0.8 times than that in a TQW active layer at 77 K.[6] Therefore, low threshold current of an SCH laser using SOGLs is achieved by improving the crystal quality of the ZnCdSe active layer and increasing the optical confinement factor.

In summary, we have investigated the effect of superlattice optical guiding layers in ZnMgSSe laser diodes grown by MBE. The photoluminescence property and the crystalline quality of an SQW are greatly improved by using SOGLs.

References

1) M. A. Hasse, J. Qiu, J. M. DePuydt, and H. Cheng, Appl.Phys.Lett. 59 (1991) 1272.
2) N. Nakayama, S. Itoh, T. Ohta, K. Nakano, H. Okuyama, M. Ozawa, A. Ishibashi, M. Ikeda and Y. Mori, Electron. Lett. 29 (1993) 1488.
3) A. Salokative, H. Jeon, M. Hovinen, P. Kelkar, A. V. Nurmikko, D. C. Grillo, L. He, J. Han, Y. Fan, M. Ringle and R. L. Gunshor, Electron.Lett. 29 (1993) 2041.
4) J. Petruzzello, R. Drenten, J. M. Gains, J.Cryst.Growth 138 (1994) 686.
5) T. Fujii, S. Hiyamizu, S. Yamakoshi and T. Ishikawa, J.Vac.Sci.Technol. B3 (1985) 776.
6) M. Kuramoto, T. C. Chong, A. Kikuchi and K. Kishino, Electron.Lett. 29 (1993) 1260.
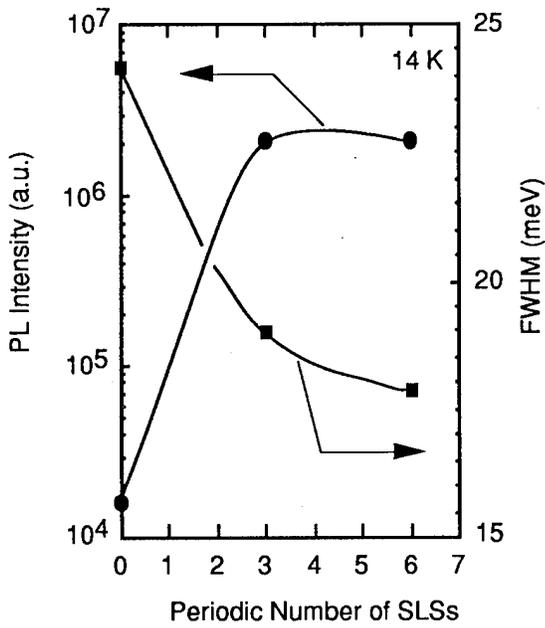
Fig. 1. PL intensity and FWHM
of PL spectra at 14 K from SQW
structure with a strained-layer
superlattice (SLS) vs.
periodic number of SLSs.
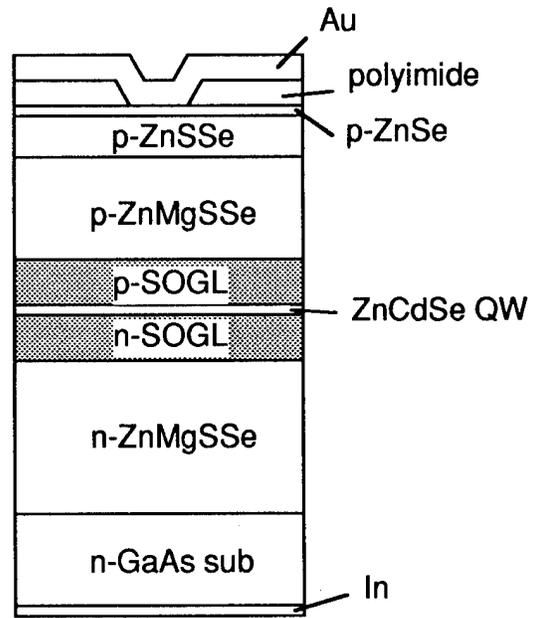
Fig. 2. Schematic cross section of
a ZnMgSSe laser structure with
superlattice optical guiding layers.
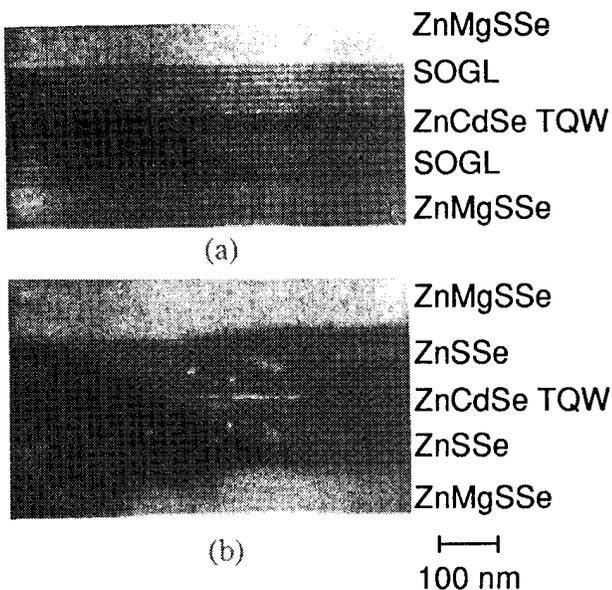
Fig. 3. Cross-sectional TEM bright-field
image of epilayer (a) with and (b) without
superlattice optical guiding layers.
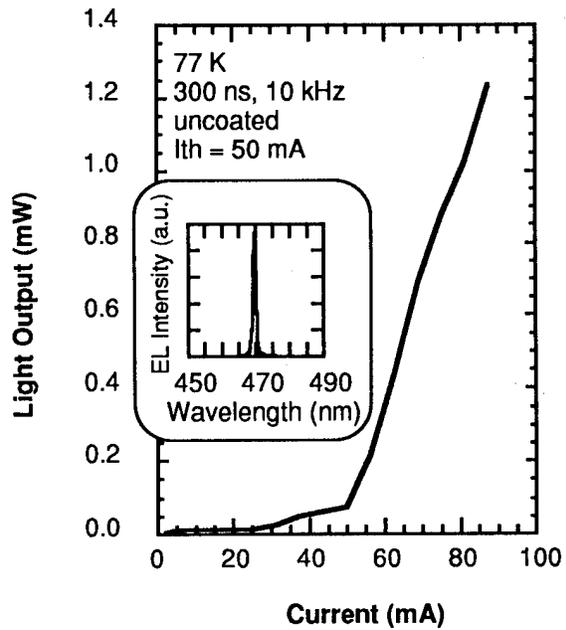
Fig.4. L-I characteristic and
emission spectrum of a blue-green laser diode.

Normal Incidence Intersubband Absorption in Vertical Quantum Wells.

V. Berger , Laboratoire Central de Recherches, THOMSON-CSF, Domaine de Corbeville, F-91400 ORSAY, FRANCE.
Telephone: 33 1 69 33 90 84   Fax: 33 1 69 33 07 40

G. Vermeire, P. Demeester, University of Gent, IMEC, Department of Information Technology, Sint-Pietersnieuwstraat 41, B-9000 GENT, BELGIUM.

C. Weisbuch, Laboratoire de Physique de la Matière Condensée, Ecole Polytechnique, F-91128 PALAISEAU, FRANCE.

For all applications involving intersubband transitions [1, 2] (ISBTs) (like Quantum Well Infrared Photodetectors[3]), the interaction between light and quantum confined electrons yields to the very stringent quantum mechanical selection rule governing intersubband transitions, which stipulates that the electric field is absorbed through its component normal to the direction of confinement. The most important consequence of this selection rule is the impossibility to excite intersubband transitions at normal incidence.

To overcome this stringent selection rule, n-doped vertical AlGaAs quantum wells have been fabricated by metalorganic vapor phase epitaxial growth of a single doped AlGaAs layer on a submicron grating. This technique is originating from the developments of the growth of quantum wires on non planar substrates[4], and was described with all the details in reference[5]. The principle of this new method of growth relies on the different migration properties of the Ga and the Al atoms, which form vertical layers of Ga-rich AlGaAs along the grooves of the grating. The structures were grown in an atmospheric pressure, horizontal MOVPE reactor using trimethylgallium, trimethylaluminium and undiluted arsine as group III and group V sources, respectively. The substrates were (100) undoped GaAs, 2° off-oriented to the nearest [110] direction. The submicron grating was defined by holographic lithography in a photoresist, followed by a wet chemical etching in citric acid. The period of the gratings was 660 nm, and they were oriented along the [011] direction. The vertical quantum wells VQWs were formed during the growth of a 1 μm $Al_{0.375}Ga_{0.625}As$ layer; the doping of the layer was in the order of 10^{18} cm^{-3} for sample A. Sample B was exactly the same structure, but was undoped, as a reference sample. The temperature of the growth was 700°C, and the velocity 5.5 μm/h, under a V/III ratio of 40. The SEM picture in figure 1 shows a stain-etched cross section of typical VQWs.
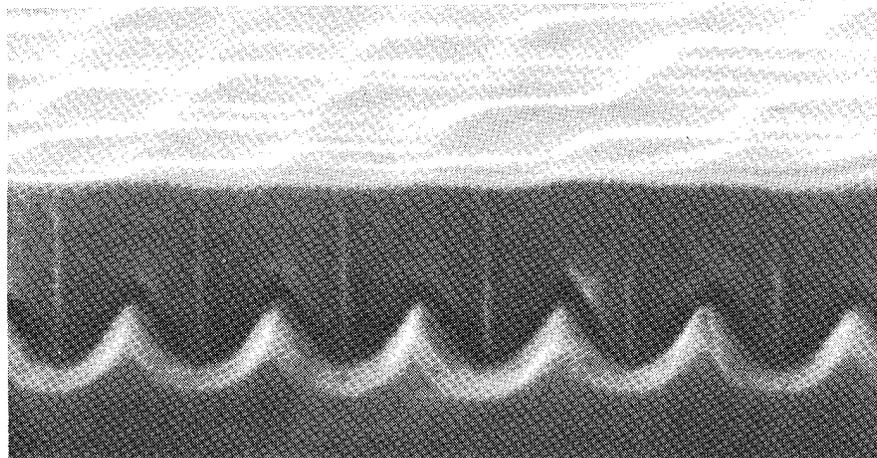
Figure 1: SEM picture of a typical stain-etched cross-section of VQWs grown on the submicron grating.

The infrared absorption experiments were performed in a Fourier transform infrared spectrometer. For each sample, the transmission was measured *at normal incidence*, at room temperature. Figure 2 shows the transmission spectra of sample A and B. Those two spectra are the ratio between the transmissions of the sample in the TM polarization and in the TE polarization, the latter being used as the background spectrum. Figure 2 shows clearly the huge intersubband absorption at 78 meV, present only on the spectrum of the doped sample, because the absorption requires the first QW level of the conduction band to be populated. This is the first direct demonstration of the quantization of the energy levels in VQWs, since it involves quantized levels of the same band (the conduction band).
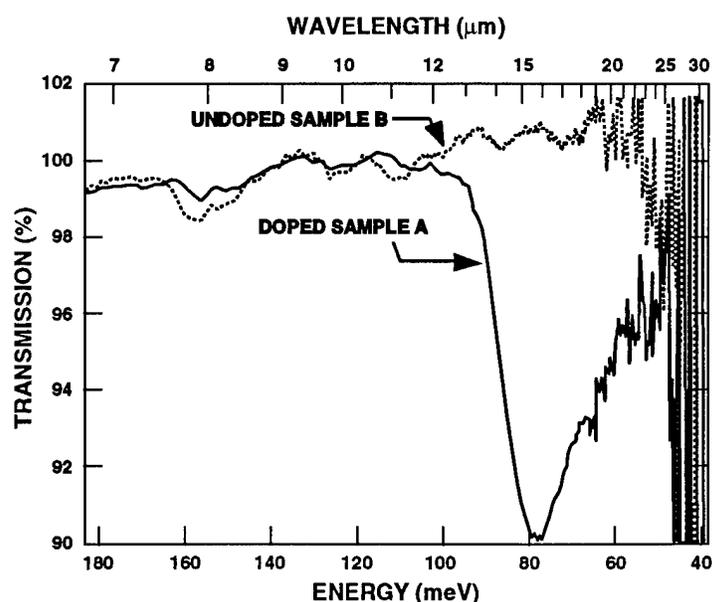
Figure 2: Transmission spectra of sample A and B.

We have checked the polarization angle dependance of this absorption peak, which is characteristic of ISBTs. The excellent agreement between the measured integrated absorption and the $\cos^2\varphi$ law proves the intersubband origin of the absorption reported on fig. 2.

Figure 3: Integrated intersubband absorption as a function of the angle of polarization of the incident light (white dots). The size of the dots represents the error bars. The theoritical $\cos^2$ law is shown (full line).
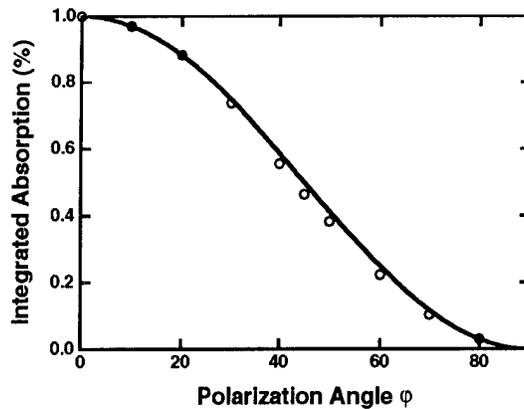
The low width of the absorption peak (only 25meV) shows the high quality of the two-dimensionnal confinement, and the surprisingly low inhomogeneity of the QW width during the vertical growth. The photoluminescence of sample B around 700nm at 77K shows that the Al concentration in the VQW equals about 18% ±1%. Taking 15 meV for the part of the ISBT width which is due to the inhomogeneity, intersubband energy calculations lead to a QW width between 79 and 91Å, assuming a square potentiel in the Shrödinger equation.

Potential applications for this new type of heterostructures concern all intersubband devices, which will be able to work at normal incidence, including quantum well infrared photodetectors. Another important point is the possibility to embed VQWs between two Bragg mirrors, forming a vertical microcavity. We could then associate the high dipole matrix elements of the ISBTs with the various effects provided by microcavities on the optical field[6]. For example, we could enhance the absorption coefficient (only 10% here) by the quality factor of the cavity, and then easily reach 100% of absorption. This possibility was forbidden with conventionnal QWs by the selection rule.

References:

(1) E. Rosencher, B. Vinter and B. Levine, eds., *Intersubband Transitions in Quantum Wells* (Plenum, London, 1992).

(2) H. C. Liu, B. F. Levine and J. Y. Andersson, eds., *Quantum Well Intersubband Transition Physics and Devices* 1994).

(3) B. F. Levine, Journal of Applied Physics **74**, R1-R81 (1993).

(4) M. Walther, E. Kapon, J. Christen, D. M. Hwang and R. Bhat, Appl. Phys. Lett. **60**, 521-523 (1991).

(5) G. Vermeire, Z. Q. Yu, F. Vermaerke, L. Buydens, P. V. Daele and P. Demeester, J. of Crystal Growth **124**, 513-518 (1992).

(6) C. Weisbuch and E. Burstein, eds., *Confined Electrons and Photons: New Physics and Applications* (Plenum, New York, 1994).

One-dimensional Exciton Diffusion in GaAs Quantum Wires

Y. Nagamune[1], H. Watabe[2], M. Nishioka[2], and Y. Arakawa[2]

[1]*Research Center for Advanced Science and Technology, University of Tokyo,*
4-6-1 Komaba, Meguro-ku, Tokyo 153, Japan
Tel.+81-3-3481-4464, Fax.+81-3-3466-8308

[2]*Institute of Industrial Science, University of Tokyo,*
7-22-1 Roppongi, Minato-ku, Tokyo 106, Japan
Tel.+81-3-3402-6231, Fax.+81-3478-1398

The newly developed micro-photoluminescence measurement at low temperature has revealed one-dimensional diffusion of excitons in GaAs quantum wires with the lateral width of 7 - 30 nm fabricated by the selective growth technique using metal-organic chemical vapor deposition. The observed diffusion length increased with decreasing the wire width from 30 to 15 nm, and decreased from 15 to 7 nm, where the maximum diffusion length was about 4 μm for the 15-nm quantum wire. The change of the diffusion length vs. the wire width is expected to be due to the competition between the one-dimensional character and the interface fluctuation.

1. Introduction

Two-dimensional (2D) confinement of carriers is an important phenomenon for fundamental study in physics as well as for quantum device applications[1], and there are many reports for fabrication of quantum wire structures and characterization[2-4]. Recently, strong 2D confinement of exciton is realized, which was evidenced by the observation of the blue-shift of the photoluminescence (PL) spectra[5] and the enhanced exciton binding energy deduced from the magneto-PL measurement[6].

It is important to investigate exciton transport in quantum wires in the next step, while realization of very high electron mobility is predicted in quantum wire structures[7]. However, there is no report in which such the high mobility was observed in the fabricated samples or at least indirect phenomena indicating high mobility were observed.

In this work we report on micro-PL (μ-PL) measurement of the GaAs/AlGaAs quantum wire structures at low temperature. Anisotropic diffusion in the quantum wires was observed. In addition, very long diffusion length along to the wire was observed, probably showing high mobility for exciton transport.

2. Experimental

2.1. Sample

Samples studied in this work were prepared by the selective growth technique using metal-organic chemical vapor deposition (MOCVD)[4,5]. The samples include quantum wires having triangular-shaped structures with a period of 200 nm, of which the lateral base width determined from high resolution scanning electron microphotographs are 7-30 nm, and the height was about half the base width.

We estimated 2D confinement energy of excitons to be in the range of 30 - 260 meV from the blue-shift values[5], and binding energy of the confined excitons to be 12 - 24 meV deduced from the magneto-PL measurement[8].

2.2. μ-PL measurement for optical transport

μ-PL measurements were carried out with a cw Ar$^+$ laser light which was focused onto the sample by an objective lens for an optical microscope. PL spectra from the sample were transferred to a spectrometer or a charge coupled device (CCD) camera operated at room temperature by using the same objective lens. The objective lens, of which the construction was designed including a window of a cryostat for better resolution, was placed out of the cryostat. Wavelength of the laser light was 514.5 nm and the beam diameter was 0.7 μm which is equal to the spatial resolution of the present measurement system. The laser beam shape and the size were checked by monitoring the reflection image with the CCD camera. The sample was cooled down at about 15 K in the cryostat by a closed He gas type refrigerator of which the vibration was carefully reduced. Spatial image of the PL spectra from the quantum wire was detected with the CCD camera through a band-pass filter passing only the PL spectral line of the wire.

If laser beam diameter is sufficiently smaller than the diffusion length of excitons, the PL image directly indicates behavior of the exciton diffusion because observed distribution of PL intensity is corresponding to the exciton density. This is a quite different point from the transient grating method[9] or the mask method[10], in which diffusion length is estimated by comparing experimental data with a model calculation. Diffusion length in the present experiment can be directly obtained as the distance between a illuminated position and a position where the PL intensity decreases to 1/e times as large as that at the illuminated position.

3. Results and Discussion

Figure 1 shows 3D plots of the image in a 12-μm^2 area detected by the CCD camera, where in Fig. 1(a) the vertical axis stands for intensity of the laser light reflected on the sample and in Fig. 1(b) it indicates the PL intensity from the 15-nm wire structure illuminated by the laser light. The spatial profiles of the PL intensity parallel and perpendicular to the wire structure are plotted as a function of distance in Fig. 2, where the laser beam profile is also shown for comparison.

As shown in Figs. 1 and 2, anisotropic PL distribution along to the wire direction is seen. It is considered that this PL distribution almost shows anisotropy of exciton diffusion because
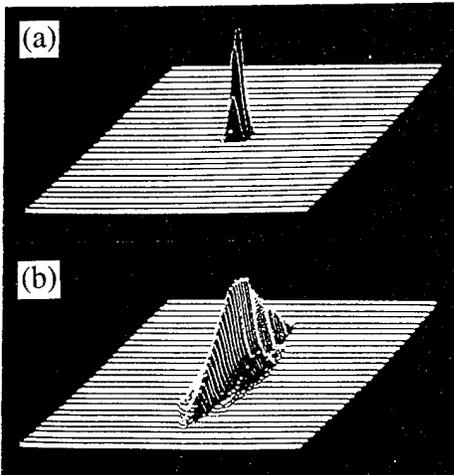
Fig. 1. Three-dimensional plots of spatial images of a laser beam (a) and the photoluminescence of the 15-nm wire structure illuminated by the laser (b).
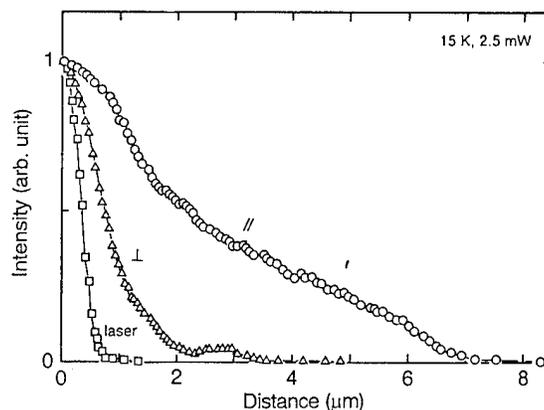
Fig. 2. Intensity profiles of the photoluminescence parallel and perpendicular to the 15-nm wire structure, where laser beam profile is also plotted for comparison.
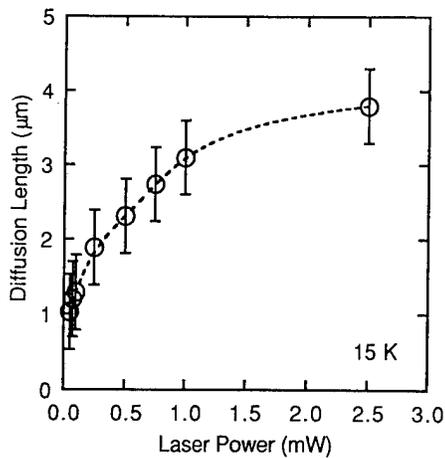
Fig. 3. Diffusion length of excitons in the 15-nm wire structure as a function of excitation laser power.
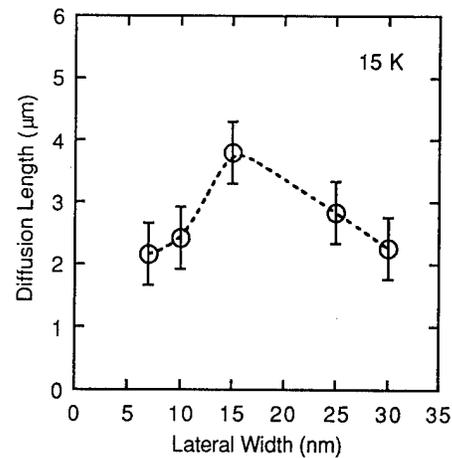
Fig. 4. Diffusion length of excitons as a function of the lateral size of quantum wires.

luminescence occurs after the relaxation into the quantum wire potential, and expansion of PL image perpendicular to the wires dose not almost take place, moreover this measurement was performed at low temperature so that carrier relaxation should be much faster than the radiative recombination of excitons.

Figure 3 shows diffusion length in the 15-nm wires along to the wire direction as a function of excitation laser power. As shown in this figure, diffusion length increases with increasing excitation laser power, and shows saturation at large excitation power region.

Diffusion length as a function of lateral wire width are plotted in Fig. 4. As shown in this figure, diffusion length increases with decreasing the wire width from 30 to 15 nm, and decrease from 15 to 7 nm. This change may demonstrate the competition between the 1D character enhancing electron and hole mobility and the interface fluctuation reducing the mobility, in particular, in narrower wires.

References

1. Y. Arakawa and H. Sakaki, Appl. Phys. Lett. **40**, 939 (1982).
2. T. Fukui, S. Ando, Y. Kokura, and T. Toriyama, Appl. Phys. Lett. **58**, 2018 (1991).
3. E. Kapon, K. Kash, E. M. Clausen, Jr., D. M. Hwang, and E. Colas, Appl. Phys. Lett. **60**, 477 (1992).
4. S. Tsukamoto, Y. Nagamune, M. Nishioka, and Y. Arakawa, J. Appl. Phys, **71**, 533 (1992).
5. S. Tsukamoto, Y. Nagamune, M. Nishioka, and Y. Arakawa,, Appl. Phys Lett. **63**, 355 (1993).
6. Y. Nagamune, Y. Arakawa, S. Tsukamoto, M. Nishioka, S. Sasaki, and N. Miura, Phys. Rev. Lett. **69**, 2936 (1992).
7. H. Sakaki, Japanese Journal Appl. Phys. **19**, L735 (1980) .
8. Y. Nagamune, T. Tanaka, T. Kono, S. Tsukamoto, M. Nishioka, Y. Arakawa, K. Uchida, and N. Miura, to be submitted.
9. A. Miller, R. J. Manning, D. C. Hutchings, D. W. Crust, and K. Woodbridge, J. Opt. Soc. Am. **B6**, 567 (1989).
10. H. Hillmer, A. Forchel, S. Hansmann, M. Morohashi, E. Lopez, H. P. Meier, and K. Ploog, Phys. Rev. **B39**, 10901 (1989).

Micro- and Vertical-Cavity Physics and Applications

QFB 10:30 am-12:00 m
Ballrooms VI-VIII

Connie Chang-Hasnain, *Presider*
Stanford University

Theory of Semiconductor Microcavities and Lasers

S.W. Koch, F. Jahnke and H.C. Schneider

Fachbereich Physik und Zentrum für Materialwissenschaften

Philipps-Universität Marburg,

35032 Marburg, Germany

A fully quantum mechanical theory for the coupled electron-hole-pair and photon dynamics of semiconductor microcavity systems is presented. Based on a nonequilibrium Green's functions approach, the carrier system is described by a generalized Boltzmann equation which includes contributions for carrier generation, carrier scattering by other carriers and phonons, as well as the spontaneous and stimulated recombination. The photon dynamics is described in terms of coupling to the carriers as well as by the mode confinement through the cavity. The many-body Coulomb effects are included on the level of a screened Hartree-Fock approximation.

This nonequilibrium quantum theory allows us to treat the carrier and photon dynamics in semiconductor microcavity resonators under various excitation conditions. As an example we have applied the theory to analyze semiconductor microcavity lasers. Assuming injection pumping of the carri-

ers we study the influence of Pauli blocking, hole burning and phonon cooling on the lasing process[1]. It is found that for not too high laser intensities the carrier distribution functions can be characterized by effective electron and hole temperatures, which can considerably exceed the lattice temperature. This plasma heating is determined by the balance between hot carrier injection under the influence of Pauli blocking and carrier cooling by phonon coupling. The plasma heating prevents the carrier density clamping above the laser threshold. We show that the increasing carrier density above the laser threshold is connected with increasing luminescence of the active material as well as index changes. This behavior is found in agreement mit experimental results[2].

The microcavity resonator modifies the photon density of states and the coupling efficiency of the spontaneous emission into the laser mode. A detailed numerical analysis based on our theory shows that for large spontaneous emission coupling the strong reduction of the laser threshold is connected with anomalous emission properies[2]. For dominant spontaneous emission we find deviations from the Schawlow-Townes behavior. These results and the influence of the spectral properties of gain, spontaneous emission and cavity loss are discussed.

Besides the application of our microscopic theory to laser situations we are also interested in excitonic effects and passive optical nonlinearities in microcavities. Recent results will be presented.

[1] U. Mohideen, R.E. Slusher, F. Jahnke and S.W. Koch, Phys. Rev. Lett. **73**, 1785 (1994).

[2] F. Jahnke and S.W. Koch, Optics Letters **18**, 1438 (1993).

Limitations of Surface Related Optical and Carrier Losses
in Microcavity Lasers

B. J. Thibeault, T. A. Strand, M. G. Peters, T. Wipiejewski, D. B. Young, J. W. Scott,
and L. A. Coldren

Electrical and Computer Engineeering Department, University of California,
Santa Barbara, 93106

There is much interest in exploring the physics associated with micro-cavity lasers. These lasers can have very low threshold currents because the number of cavity modes is limited and a large portion of the spontaneous emission must be coupled to the lasing mode. To achieve such a structure a very small (< 1 μm diameter) optical cavity must be used. The index-guided vertical-cavity surface-emitting laser (VCSEL) is a prime candidate for this goal. However, due to the effects of waveguide scattering loss, diffraction loss, and surface recombination, electrically pumped diameters have been limited to > 2 μm [1]. In this paper, we first explore the issues limiting size reduction of the index-guided VCSELs through modelling and experiment. We then show how the issue of surface-recombination can be resolved through in-situ etching and regrowth.

In order to explore the limitations of size reduction of VCSELs, a finite-element model of the VCSEL was developed to self-consistently solve for the lateral recombination and diffusion currents in the active region of the laser. For a given threshold gain (g_{th}), there is a corresponding radiative current density (J_{rad}). For the $In_{0.2}Ga_{0.8}As$ quantum wells we consider in this work, the relation has been experimentally derived [2]. To find the radiative current density, the threshold gain of the laser needs to be determined. This is experimentally determined by the following relation:

$$g_{th} = \frac{1}{\Gamma_{enh} d_{act}} \ln\left(\frac{1}{R}\right) \frac{\eta_i}{\eta_{ext}(r)} \tag{1}$$

where Γ_{enh} is the standing wave enhancement factor, d_{act} is the active region thickness, R is the mean mirror power reflectivity, η_i is the injection efficiency, r is the radius and $\eta_{ext}(r)$ is the radius dependent external quantum efficiency. η_{ext} is taken experimentally from pulsed measurements of devices of various diameters to account for the waveguide and diffraction losses. For a given surface recombination velocity S, the total uniform current density can be found from

$$\eta_i J_{th} = J_{rad} + \frac{2}{r} q d_{act} n(r) S \qquad (2)$$

where q is the electron charge and $n(r)$ is the carrier density at the edge of the pillar. By iteratively solving the continuity equation across the active region, families of curves for current density versus diameter are generated for given values of S.

Figure 1 shows such a family of curves for index-guided VCSELs (etched through the active region) of 20 μm in diameter and less. From the measurements, a surface velocity of 1.5e5 cm/s is inferred. The curves also point out several features. Even with no surface recombination, the threshold current density increases dramatically with decreasing width due to the surface related optical losses. With an assumed maximum gain of 5000 cm^{-1}, the smallest possible laser is only 5 μm in diameter for this material. Lasers smaller than this do not lase at due to the high required gain and current density. Since our devices are only waveguided in the top half of the structure, the simulation is also run with only diffraction loss present to determine the cause of the loss. The diffraction loss dependence used was modelled by Babic [3]. Figure 2 shows the simulation result. Even with diffraction loss, the device size is still limited with zero S, but at smaller diameters. This suggests that the devices are currently limited by waveguide scattering losses caused by the imperfect processing of the devices.

Assuming that the waveguide loss can be eliminated and diffraction loss is removed by waveguiding the entire structure, the issue of surface recombination then arises. As shown in figure 3, surface recombination has the effect of raising the threshold current density of the device to very high levels (> 40 kA/cm^2) for small devices, possibly limiting the ultimate size through device heating. It is therefore desirable to remove this recombination mechanism. In-situ etching and regrowth with molecular beam epitaxy (MBE) provides this tool.

In-plane lasers (IPLs) were used to evaluate the in-situ etch and regrowth technique. Figure 4 shows a plot of threshold current density versus IPL width for three different samples. One sample was simply etched through the active region using reactive ion etching. The two other samples were in-situ etched and regrown over by MBE. The model described above was used with this data to extract values of S. The data shows that levels of S below 3e3 cm/s are achievable by this technique.

In this paper, we have shown the effects of waveguide, diffraction loss, and surfaces on VCSEL size reduction. Surface recombination is effectively reduced through in-situ etching and regrowth by MBE. The focus now needs to be placed on waveguide loss reduction.
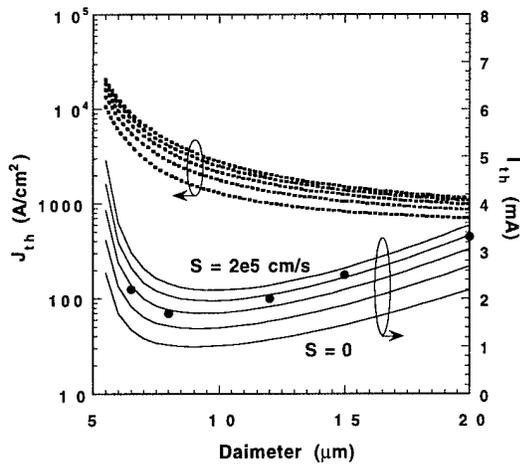
Figure 1: Measured (Dots) and modelled threshold currents vs. diameter.
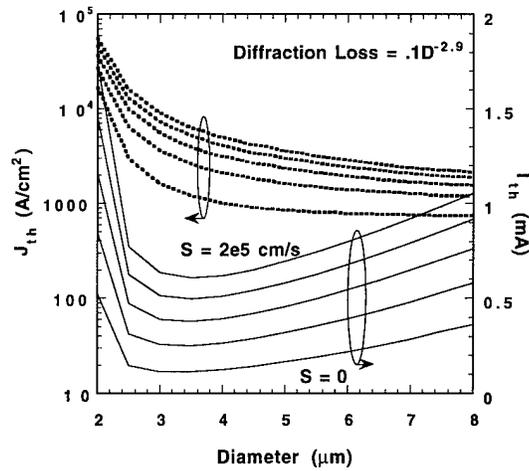
Figure2: Modelled threshold currents with no waveguide loss.
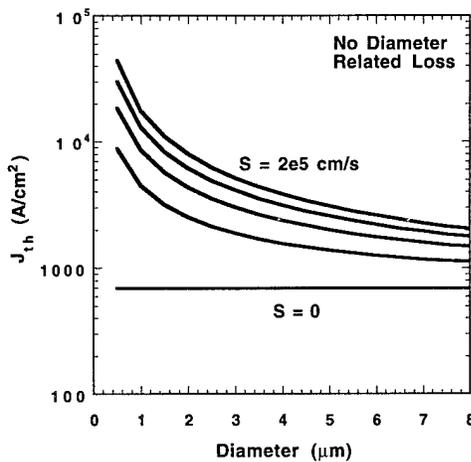
Figure 3: Modelled threshold currents with no size limiting optical loss.
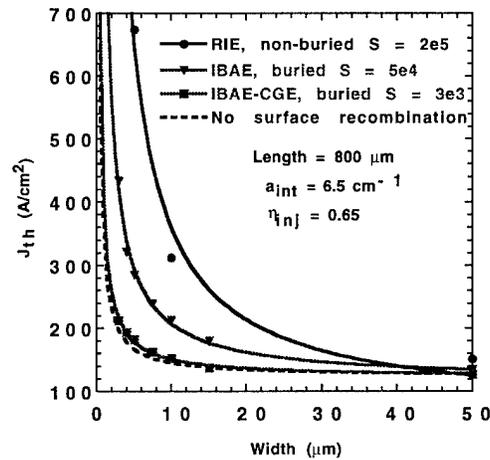
Figure 4: In-situ etched and regrown laser threshold currents to demonstrate reduction of S.

References:
[1]   F.H. Peters, G.D. Robinson, M.G. Peters, D.B. Young, and L.A. Coldren, "Small Electrically Pumped Index-Guided Vertical-Cavity Lasers," IEEE   Photonics Technology Letters, **6**, p. 1176.
[2]   S.W. Corzine, "Design of Vertical-Cavity Surface-Emitting Lasers with Strained and Unstrained Quantum Well Active Regions", Ph.D. Dissertation, Dept. of Electrical and Computer Engineering, Technical Report #93-09
[3]   D.I. Babic, Y. Chung, N. Dagli, and J.E. Bowers, "Modal Reflection of Quarter-Wave Mirrors in Vertical Cavity Lasers," Journal of Quantum Electronics, **29**, p. 1950.

Low Threshold Microcavity Lasers using a Half-Wave Cavity Spacer

D.L. Huffaker, J. Shin, and D.G. Deppe

Microelectronics Research Center
Department of Electrical and Computer Engineering
The University of Texas at Austin, Austin, Texas 78712-1084

Data will be presented characterizing a microcavity laser structure which uses a half-wavelength cavity (HWC) spacer layer surrounding a single quantum well (QW) active region. Initial results demonstrate a continuous-wave (CW) room-temperature lasing threshold current of $91\mu A$ for a $2\mu m$ device ($J_{th}=2.3kA/cm^2$), and $220\mu A$ for an $8\mu m$ device ($J_{th}=344A/cm^2$). The HWC laser, as illustrated in Fig.1, uses 26 pairs of n-AlAs/GaAs distributed Bragg reflectors (DBRs) for the bottom mirror, a half-wavelength cavity spacer composed of an n-AlAs layer beneath the QW and p-AlAs layer on top, and a p-GaAs cap layer.
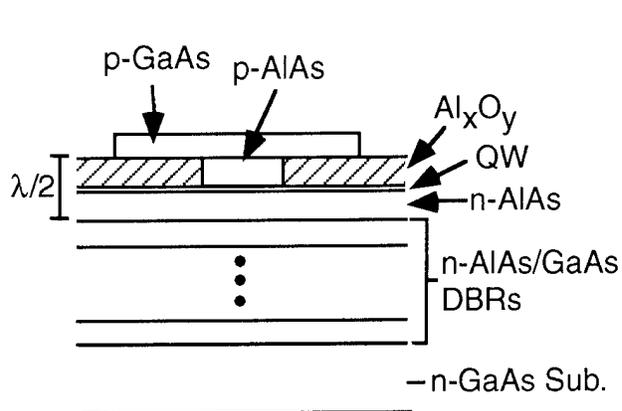
Figure 1: Schematic cross-section of half-wave VCSEL.
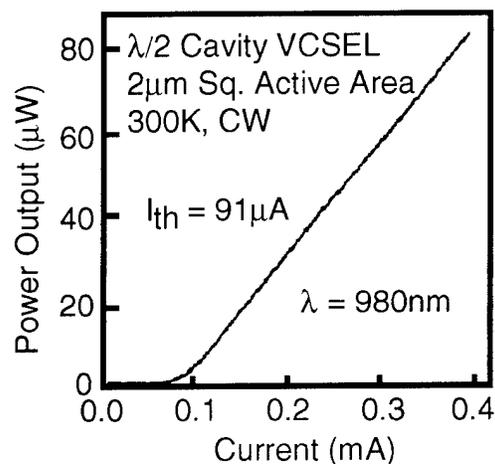
Figure 2: Light output versus current curve for $2\mu m$ square half-wave VCSEL.

The top mirrors (not shown in the figure) are five pairs of high contrast ZnSe/CaF DBRs. Current confinement to the active region is achieved through the selective lateral oxidation of the p-AlAs spacer layer to form an Al_xO_y ring beneath the p-GaAs layer.[1] The details of the Al_xO_y microcavity laser with a full wavelength cavity spacer have been discussed in Ref.2. An important difference in the HWC structure is that the low-index Al_xO_y ring is

only 200Å from the QW, due to GaAs/AlGaAs barriers, such that significant index-guiding may by expected. The lateral dimensions of the fabricated lasers range from 8μm to 2μm squares. Many of the 2μm square devices tested have CW thresholds in the 100μA range. The measured minimum room-temperature CW threshold current of 91μA for a 2μm square device is shown in Fig.2. To our knowledge, this is the lowest room-temperature threshold yet achieved in a semiconductor laser. The minimum CW room-temperature thresholds for the larger devices are 316 μA for a 5μm square active region. For an 8μm square active region a threshold current of 220μA is measured, as shown in Fig.3. The minimum CW threshold current density of 260 A/cm^2 is achieved for the 8μm device at 240K as shown in the threshold versus temperature characteristics, Fig.4, and to our knowledge represents the lowest threshold current density yet achieved in a vertical-cavity laser.
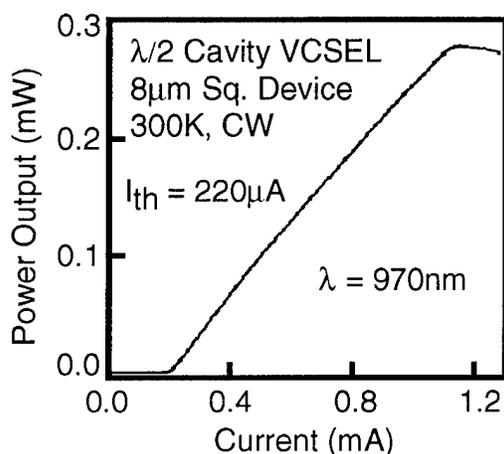
Figure 3: Light output versus current for 8μm square half-wave VCSEL.
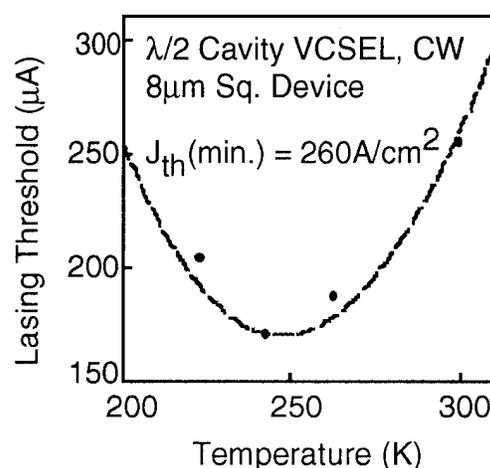
Figure 4: Lasing threshold versus temperature for 8μm square half-wave VCSEL

The advantages of high contrast DBRs such as the ZnSe/CaF$_2$ materials is the decreased effective cavity length which supports a smaller lasing active area compared to the p-AlAs/GaAs.[3] This is important in achieving low threshold operation in small area devices such as the 2μm square device. The high threshold current density for the 2μm square device is most likely due to a combination of current spreading and diffraction loss especially in the n-AlAs/GaAs DBRs for the small area lasing mode. Therefore, it may be possible to lower the threshold of the 2μm device by replacing the n-AlAs/GaAs DBRs with high contrast DBRs.

In our work on full-wave microcavity lasers with a single QW active region, we see stable lowest-order transverse mode operation for pump levels up to ten times threshold in a 5μm device.[4] In the HWC laser, stable lowest-order transverse mode behavior is observed in the 2μm and 8μm square devices, where the 5μm device operates in higher-order transverse modes, most likely due to index-guiding by the Al_xO_y ring in combination with cavity tuning. Significant reduction of the spontaneous emission linewidth is observed for the 2μm square device before the application of the upper e-beam deposited dielectric mirrors. Since the 2μm dimension is on the order expected for the lateral spontaneous mode (based on the spontaneous linewidth) expected in such a planar cavity, this may reflect the control of spontaneous emission due to the lateral index confinement. For the 8μm device, self-focusing is observed such that the beam waist is located outside of the active region. In the talk the experimental data describing these measured results will be presented.

References

1. J.M. Dallesasse, N. Holonyak, Jr., A.R. Sugg, T.A. Richard, and N. El-Zein, Appl. Phys. Lett. **57**, 2844 (1990)

2. D.L. Huffaker, D.G. Deppe, K. Kumar and T.J. Rogers, Appl. Phys. Lett. **65**, 97 (1994)

3. D.L. Huffaker, C.C. Lin, D.G. Deppe, and T.J. Rogers, IEEE Photon. Technol. Lett. **6**, 135 (1994)

4. D.L. Huffaker, J. Shin, and D.G. Deppe, Appl. Phys. Lett. **65**, #L-1839, 21 Nov. 1994

Cavity Characteristics of Selectively Oxidized Vertical-Cavity Lasers

K. D. Choquette, K. L. Lear, R. P. Schneider, Jr., G. R. Hadley, K. M. Geib, and S. P. Kilcoyne
Photonics Research Department
Sandia National Laboratories
Albuquerque, NM 87185

Vertical-cavity surface emitting lasers (VCSELs) are of interest from both scientific and technological points of view. For example, distributed Bragg reflector (DBR) mirrors used to produce microcavities with a single longitudinal mode have been employed to study novel optical phenomena and are critical to VCSEL performance. Optical and electrical confinement in the transverse direction has been commonly achieved using etched post index-guided structures, or ion implanted "gain-guided" devices. We report the optical and electrical properties of VCSEL diodes fabricated using a buried oxide layer with a current aperture within an all semiconductor DBR mirror. We show this oxide layer has profound implications, leading to new transverse optical effects in the cavity as well as significant advances in VCSEL performance.

The selectively oxidized VCSEL structure is shown in Fig. 1. VCSELs employing an oxide layer under a hybrid DBR mirror have been previously reported.[1] Here we exploit the high oxidation selectivity of AlGaAs alloys to form a single buried oxide layer under a monolithic top DBR.[2] Large area mesas are reactive ion etched in order to expose the AlGaAs layer for lateral oxidation. The lateral oxidation is done at 425-450°C in a water vapor atmosphere for 30 to 150 minutes.[3] The oxidized AlGaAs layer, which constitutes the low index layer of the DBR immediately adjacent to the active region, is oxidized partially through the mesa to form a current aperture. The current aperture thus minimizes current spreading, eliminates implantation damage, and enables fabrication of high performance ultra-small VCSELs.

Fig. 2 illustrates the spatially dependent cavity resonance in our oxidized VCSELs. Because the refractive index of the oxide layer is reduced from 2.89 to ≈ 1.55, the cavity resonance along the transverse direction is strongly modulated. Plotted in Fig. 2 is the calculated reflectance from the air side of cavities containing an oxide layer or the as-grown layer. Notice that with the oxidized layer, the cavity resonance is blue-shifted by ≈ 17 nm relative to the unoxidized resonance wavelength. In addition, we find the reflectivity is *increased* with the oxide layer compared to the as-grown layer. Superimposed on Fig. 2 is the observed lasing spectrum from a VCSEL located in a region of the wafer with blue-shifted peak gain offset. At threshold we observe lasing around the perimeter of the current aperture, which corresponds to the shorter wavelength emission in Fig. 2. At a higher injection current the region inside the aperture begins to lase, and a new lasing peak is observed at the expected cavity resonance wavelength. Hence, due to blue-shifted gain and the higher reflectivity under the oxidized layer, the oxide perimeter modes arise first at threshold; as the gain red-

shifts with increasing current injection, the gain comes into alignment with the unoxidized cavity resonance which leads to aperture lasing modes.

In Fig. 3 we show the calculated wavelength shift of the oxide cavity resonance relative to the as-grown cavity resonance. Notice that both blue- and red-shifted oxide cavity resonance wavelengths can be achieved by varying the thickness of the oxide layer. The magnitude of the shift can be controlled by inserting the oxide layer further into the DBR mirror away from the active region. The buried oxide layer also leads to index-guided optical confinement, as expected from the large transverse index variation. The index-guiding is evident in the many (>5) lasing transverse (aperture) modes separated by 0.23 nm, which arise in a small area oxidized VCSEL (214 μm^2). By comparison, for a similar sized implanted VCSEL (177 μm^2) from the same wafer we observe a few (2-3) lasing transverse modes separated by ≈ 0.4 nm, in agreement with the weaker optical confinement from its thermally-induced index profile.

In addition to these optical effects, the current aperture achieves enhanced electrical confinement as illustrated in Figs. 4 and 5. Fig. 4 compares the threshold voltage, V_{th}, of oxidized (area=400 to 1000 μm^2) and implanted VCSELs (area=707 μm^2) fabricated from a wafer with three InGaAs quantum wells. In Fig. 5 we similarly compare the threshold current density, J_{th}, which accounts for size variations in the current apertures of the oxide VCSELs. It is readily apparent in Figs. 4 and 5 that the oxidized VCSELs exhibit significantly lower V_{th} and J_{th}: the minimum values of 1.33 V and ≈ 90 A/cm^2 per quantum well, respectively, are the lowest values reported to date for VCSELs. Low J_{th} arises from strong electrical confinement (no current spreading) and optical confinement (index-guiding), while low V_{th} arises from low series resistance[4] and low J_{th}. The combination of achieving lower J_{th} and V_{th} with index-guiding leads to significant power conversion (wall plug) efficiency enhancements in these oxidized VCSELs. In Fig. 6 we plot the light output and the power conversion efficiency of an oxidized VCSEL (area=317 μm^2) from a wafer with greater output coupling. Fig. 6 shows a 33% maximum conversion efficiency, a dramatic improvement over the best reported results from implanted VCSELs.[4]

In summary, the selectively oxidized VCSELs exhibit record device performance, arising from the combination of efficient current injection and index-guiding, making them attractive for technological applications. Furthermore, this VCSEL structure allows one to engineer the off-axis cavity resonance independent of the as-grown cavity resonance, which may enable new physical phenomena in the cavity. This work is supported by the United States Department of Energy under contract No. DE-AC04-94AL85000.

[1] D. L. Huffaker, et al., Appl. Phys. Lett. 65, 97 (1994).
[2] K. D. Choquette, et al., Int'l Semi. Laser Conf., PD4 (1994); submitted to Electron. Lett.
[3] J. M. Dallesasse and N. Holonyak, Jr., Appl. Phys. Lett. 58, 394 (1991).
[4] K. L. Lear, et al., Photon. Technol. Lett. 6, 1053 (1994).
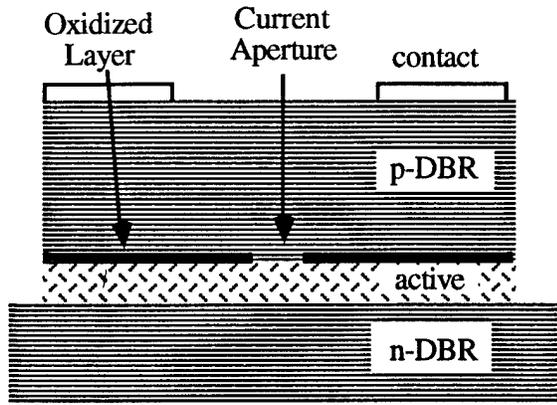
Fig. 1. Selectively oxidized VCSEL sketch.
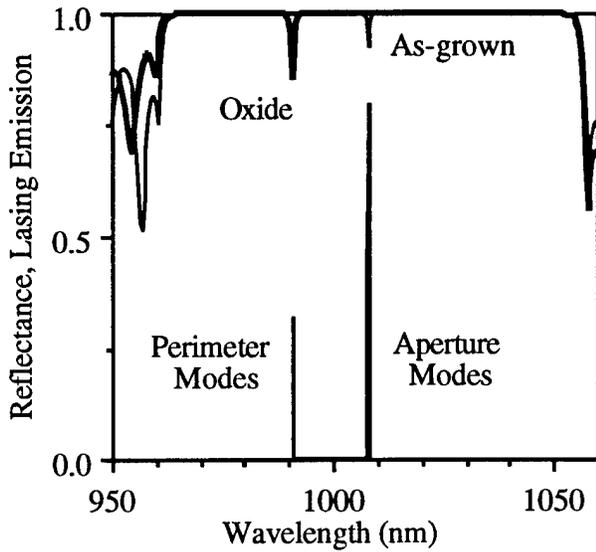
Fig. 2. Oxidized VCSEL cavity resonances and lasing emission.
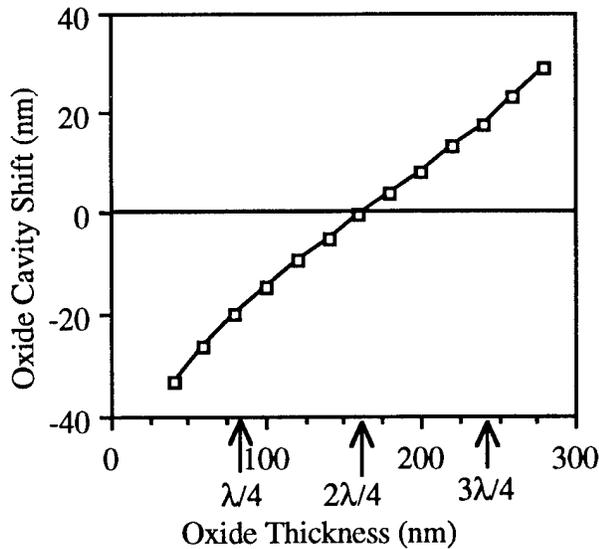
Fig. 3. Cavity shift vs. oxide thickness.
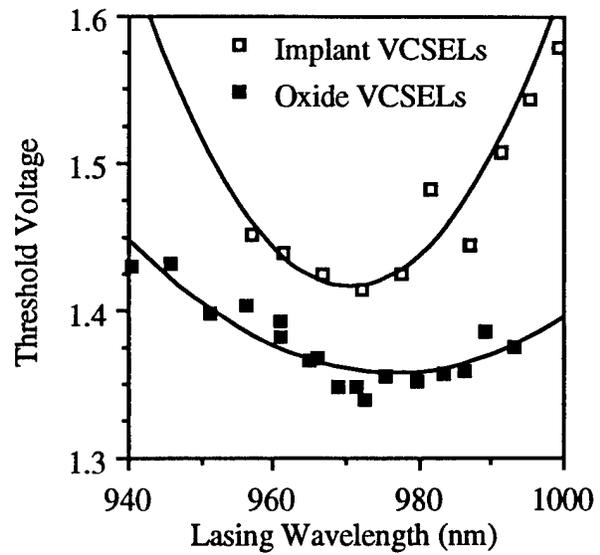
Fig. 4. V_{th} vs. threshold wavelength.
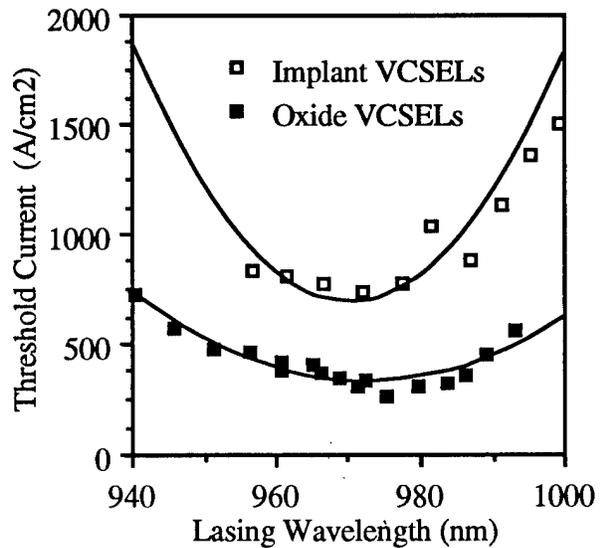
Fig. 5. J_{th} vs. threshold wavelength.
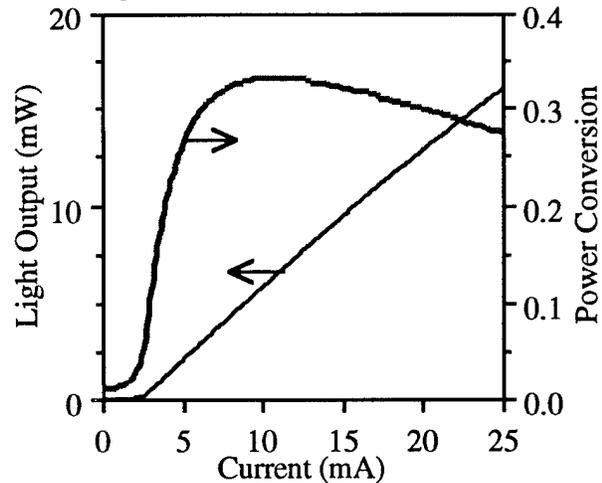
Fig. 6. VCSEL Output and power efficiency.

Complete Polarization Control of 8x8 Vertical-cavity Surface-emitting Laser Matrix Arrays

T. Yoshikawa, H. Kosaka, K. Kurihara, M. Kajita, Y. Sugimoto and K. Kasahara

Opto-electronics Research Laboratories, NEC Corporation
34 Miyukigaoka, Tsukuba, Ibaraki 305, Japan
Tel. +81-298-50-1168 fax +81-298-56-6140 e-mail t_yoshi@obl.cl.nec.co.jp

Polarization control in vertical-cavity surface-emitting lasers (VCSELs) is important because the devices in which VCSELs are used, such as magneto-optical discs or optical interconections, often use polarization-sensitive elements such as beam spliters. Additionally, a great advantage of VCSELs is that they can readily be used to form arrays; thus, polarization must be controlled for not only single VCSELs but also VCSEL arrays. However, since the VCSEL polarization direction is not determined, the polarization direction of the emitted light is random. In previous works, efforts have been made to control polarization, however, polarization still remains uncontrolled, especially in array form[1-3].

We show complete polarization control of 8x8 VCSEL matrix array. The diffraction loss of fundamental-mode emission is increased[4] in one direction by reducing the size of the post in one direction. This causes anisotropy of transversal mode selectivity, leading to pinning of the polarization direction.

An index-guided transversal-injected VCSEL (Fig. 1) was fabricated[5]. An InGaAs 3-QW-VCSEL wafer consisting of 15.5 and 18.5 GaAs/AlAs DBR pairs was grown by molecular beam epitaxy on a (001)-GaAs substrate misoriented 2° toward (111)A. Rectangular pattern resist masks were made with size varying (in 0.25 μm increments) from 6 x 6 μm to 6 x 3.5 μm. The shorter side was in the <110> direction (Fig. 1). Electron beam lithography was used to ensure accurate pattern size. Posts were then formed by Cl_2 reactive ion beam etching from the top layer to the 14th GaAs layer of the p-side DBR, while using *in situ* laser reflectometry to monitor the etching. The correct size of the rectangular posts was confirmed by optical microscopic observation after etching. The active layer beside the post was inactivated by proton implantation. The light output side was AR coated.

The light output power was monitored through a Glan-Thomson prism, and the prism angle at which the maximum output was obtained was classified into three polarization angles. These angles were 0°, which corresponded to 0° to <110>; 90°, which corresponded to 90° to <110>; and 45°, which corresponded to the rest. These types of VCSELs with a post size of less than 6.5x6.5 μm have a fundamental-single mode emission both in the longitudinal and transversal modes[9] and are linearly polarized. The direction of the polarization angle, however, can switch when the operating current increases, probably because of spacial hole burning or stress from heat expansion. In such cases, the angle observed first was defined as the polarization angle. The number of polarization-switched VCSELs was also counted. The operating current was varied from 0 to 10 mA, which roughly corresponds to 10 times the threshold current and a light output power of 3 mW.

The proportion of VCSELs for each polarization directions is shown in Fig. 2 as a

function of post size. The proportion of switched VCSELs is also shown. The proportion of VCSELs with 90° polarization increases, and the proportion of switched VCSELs decreases as the length of the shorter side decreases. These changes indicate that pinning of the polarization angle becomes rigid as the length of the shorter side decreases. When the length of the shorter side becomes less than 5 μm, the polarization of the 8x8 VCSEL matrix is 100% controlled. All of these VCSELs have fundamental single-mode emission with linear polarization and without switching. Figure 3 shows the distribution of polarization angles for a 6x6-μm polarization uncontrolled VCSEL array and a 6x5-μm polarization controlled array. The polarization angle distribution clearly decreases for the 6x5-μm array. Furthermore, the polarization angle distribution of all the 6x5-μm VCSELs is suppressed within only 12° with a deviation of 2.9°, which is comparable to the measurement error.

As this polarization control method uses the increase in diffraction loss, light output degradation becomes a concern. The average threshold current in fact increased as the post size decreased, but this change was small when the size exceeded 6x4 μm. Therefore, the average threshold current of the 6x5-μm polarization-controlled VCSEL array was 1.29 mA, which was only 1.17 times that of the 6x6 μm polarization-uncontrolled VCSEL array. However, this higher threshold current is negligible for conventional use. The I-L characteristics of the 6x6-μm VCSEL and 6x4 μm VCSEL were almost the same (Fig. 4). The difference in the higher current injection was probably caused by heating, since these measurements were performed without a heat sink. Although heat resistance can be high for a 6x4-μm VCSEL because of its small cross section, this can be reduced by proper bonding to a heat sink. The neatly round shape of the near field pattern of the 6x5-μm VCSEL indicates fundamental single-transversal-mode emission over the operating current range up to 10 mA. Distortion due to anisotropy of the rectangular post was not observed.

It is known that when a current probe is used to connect the electrode pad and current source, tension from the probe may change the polarization direction. Furthermore, when Pb-Sn is used for mounting VCSEL arrays, the tension from heat expansion can change the polarization direction. Both of these effects occurred with the 6x6-μm polarization-uncontrolled VCSEL array; however the polarization-controlled VCSEL array did not experience such problems, and maintained its polarization angles throughout the bonding and measuring processes. Such rigid polarization pinning is suitable for conventional use in mounted form.

We think this polarization control method is very simple and effective because it uses the small increase in diffraction loss by reducing the post size in one direction relative to the fundamental single-mode emission. This causes anisotropy in transversal mode selectivity. The 6 μm size, at which the smallest threshold current is obtained for the fundamental single mode, is the optimum size for polarization control. This is because if the post size is much larger than the fundamental mode size, the post structure does not affect mode selectivity. If the post size is much smaller than the fundamental mode size, the diffraction loss becomes too high for stable lasing at low current injection.

References
[1]T. Mukaihara, F. Koyama, and K. Iga, IEEE Photon. Tech. Lett. **5**, 133(1993)
[2]D. Vakhshoori, Appl. Phys. Lett. **65**, 259(1994)
[3]K. D. Choquette and R. E. Leibenguth, IEEE Photon. Tech. Lett. **6**, 40(1994)
[4]H. Kosaka, K. Kurihara, A. Uemura, T. Yoshikawa, I. Ogura, T. Numai, M. Sugimoto, and K. Kasahara, IEEE Photon. Tech. Lett. **6**, 323(1994)
[5]M. Kajita, T. Numai, K. Kurihara, T. Yoshikawa, H. Saito, Y. Sugimoto, M. Sugimoto, H. Kosaka, I. Ogura, and K. Kasahara, Jpn J. Apply. Phys. **33**, 859(1994)
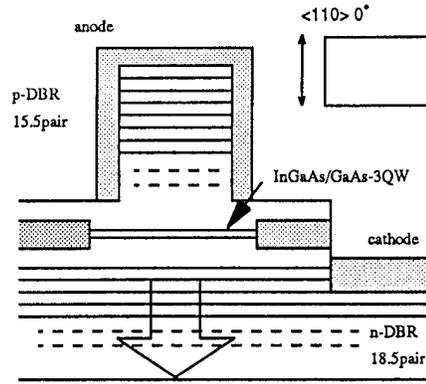
Fig.1: Structure of index-guided transversal injected VCSEL and upper view of rectangular post in <110> direction.
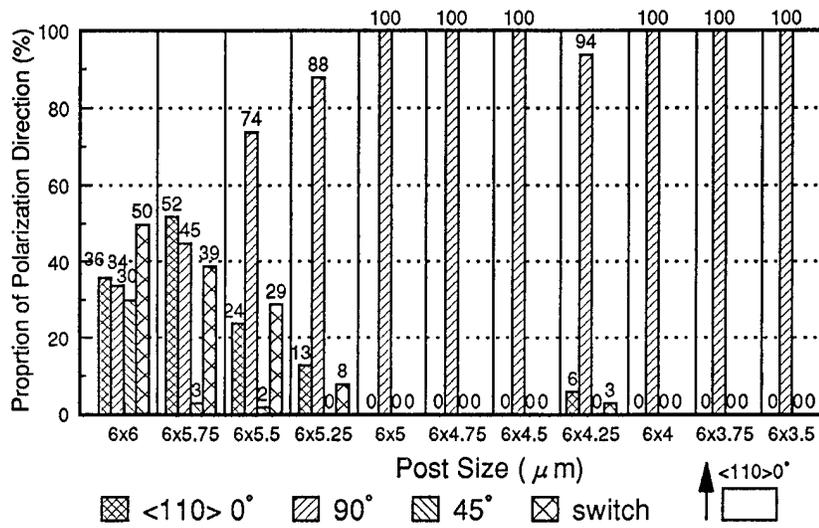
Fig.2: Proportion of polarization direction of 8x8 matrix array (64 VCSELs) vs. post size from 6x6 μm to 6x3.5 μm. Polarization was completely controlled for 6x5 μm - 6x3.5 μm sizes. Probably, the post structure was broken for 6 % of the 6x4.25 μm size array, which does not have 100 % polarization pinning.
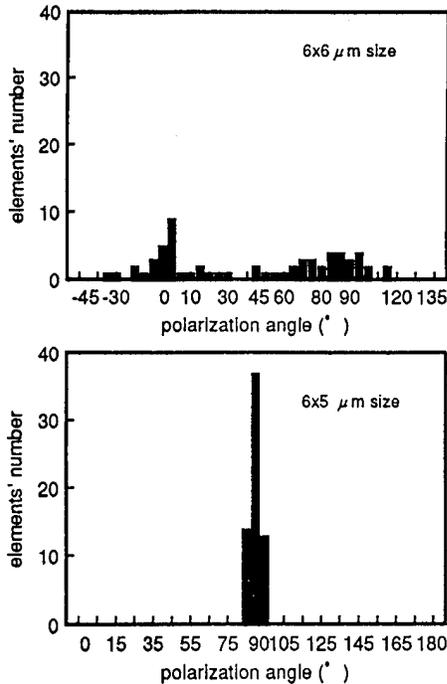
Fig.3: Polarization angle distribution of (a) the 6x6 μm size polarization uncontrolled VCSEL and (b) the 6x5 μm polarization controlled array. The deviation angle is only 2.9° for the 6x5 μm array.
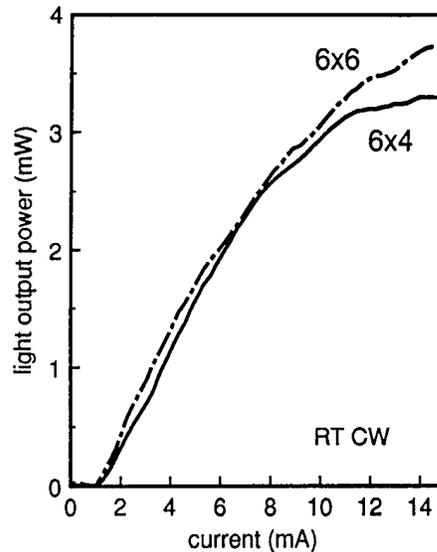
Fig.4: L-I characteristics of the 6x4 μm polarization controlled VCSEL and the 6x6 μm polarization uncontrolled VCSEL. The difference in the higher current range is probably caused by heating, and be reduced when a heat sink is used.

Ploog, K. — QWB1
Pommerehne, J. — QThB4

Qian, Yi — QThE19

Ram, Rajeev J. — QThA4
Reinhart, F. K. — QThE10
Rhee, J. K. — QThA3
Rivlin, L. A. — QThE17
Roberts, C. — QThE7
Robinson, Gerry — QThE18
Roskos, H. G. — JWA5
Rühle, W. W. — QWB1, QThE1
Ryan, John F. — QWA, QFA2

Sacedón, A. — QThE8
Saif, Babak N. — QThE15
Saito, Hisao — QThD1
Sakaki, H. — QWA4
Salmeron, M. — QWA3
Samarath, N. — QWA1
Sánchez-Rojas, J. L. — QThE8
Sato, T. — QThD3
Schmidt, K. — QThC2
Schneider, H. C. — QFB1
Schneider, R. P., Jr. — QFB4
Schultz, S. — QThE2
Schulze, A. — QThE14
Scott, Jeff W. — QThE18, QFB2

Seery, Bernard D. — QThE15
Shah, Jagdeep — QWB2
Shen, Z. — QThB2
Shin, J. — QThE6, QFB3
Shirai, M. — QThD3
Slusher, Richart E. — JWA2, QThB
Smirl, Arthur L. — JWB3, QThE8, QThE9
Smith, D. R. — QThE2
Smith, S. — QThE16
Stanley, R. P. — QThA2
Stark, Jason B. — JWA2
Stavrinou, P. N. — QThE7
Strand, T. A. — QFB2
Sugimoto, Y. — QFB5
Sugo, Mitsuru — QThD2
Sun, D. — QThE9
Suzuki, Toshio — QThE2

Taike, Akira — QFA3
Tajima, K. — JWB1
Takeuchi, Koichiro — JWA4
Tamamura, Toshiaki — QThD2
Temmyo, Jiro — QThD2
Thibeault, B. J. — QFB2
Towe, E. — QThE9
Tsuda, S. — QWB4
Tsybeskov, L. — QThB3
Tu, C. W. — QThE12

Ucer, K. B. — QThB3

van der Weide — QThD4
Vermeire, G. — QFA4
von Behren, J. — QThB3

Wa, P. Li Kam — QThE7
Wakana, Shinichi — JWA3
Wang, H. S. — QThE7
Wang, Hailin — QWB2
Wang, Qiming — QThE19
Watabe, H. — QFA5
Weisbuch, C. — QThA2, QFA4
Weiss, S. — QWA3
Wieder, H. H. — QThE12
Wipiejewski, T. — QFB2
Wood, Colin — QThE15

Yablinovitch, E. — QThA1
Yazawa, M. — QThD3
Yoshikawa, T — QFB5
Young, D. B. L. — QFB2
Yu, Paul K. — QThE2

Zapaskii, Valerii — QThC4
Zhang, Jingming — QThE19
Zhen, Lianxi — QThE19

QUANTUM OPTOELECTRONICS
TECHNICAL PROGRAM COMMITTEE